CHEMICAL REVIEWS

Review

pubs.acs.org/CR

Spectroscopic and Device Aspects of Nanocrystal Quantum Dots

Jeffrey M. Pietryga,[†] Young-Shin Park,[†,‡] Jaehoon Lim,[†] Andrew F. Fidler,[†] Wan Ki Bae,[§] Sergio Brovelli,[∥] and Victor I. Klimov*[,†]

[†]Nanotechnology and Advanced Spectroscopy Team, Chemistry Division, Los Alamos National Laboratory, Los Alamos, New Mexico 87545, United States

[‡]Center for High Technology Materials, University of New Mexico, Albuquerque, New Mexico 87131, United States

[§]Photo-Electronic Hybrids Research Center, Korea Institute of Science and Technology, Seoul 02792, Korea

[∥]Dipartimento di Scienza dei Materiali, Università degli Studi di Milano-Bicocca, I-20125 Milano, Italy

ABSTRACT: The field of nanocrystal quantum dots (QDs) is already more than 30 years old, and yet continuing interest in these structures is driven by both the fascinating physics emerging from strong quantum confinement of electronic excitations, as well as a large number of prospective applications that could benefit from the tunable properties and amenability toward solution-based processing of these materials. The focus of this review is on recent advances in nanocrystal research related to applications of QD materials in lasing, light-emitting diodes (LEDs), and solar energy conversion. A specific underlying theme is innovative concepts for tuning the properties of QDs beyond what is possible via traditional size manipulation, particularly through heterostructuring. Examples of such advanced control of nanocrystal functionalities include the following: interface engineering for suppressing Auger recombination in the context of QD LEDs and lasers; Stokes-shift engineering for applications in large-area luminescent solar concentrators; and control of intraband relaxation for enhanced carrier multiplication in advanced QD photovoltaics. We examine the considerable recent progress on these multiple fronts of nanocrystal research, which has resulted in the first commercialized QD technologies. These successes explain the continuing appeal of this field to a broad community of scientists and engineers, which in turn ensures even more exciting results to come from future exploration of this fascinating class of materials.

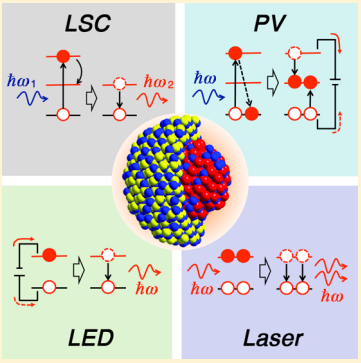

CONTENTS

1. Introduction 10514
2. Electronic States in Semiconductor Quantum Dots 10515
  2.1. Spherical Quantum Box Model 10515
  2.2. Absorption Spectra and Absorption Cross Sections 10517
  2.3. Valence-Band States 10518
  2.4. Fine Structure of Band-Edge Exciton States 10519
  2.5. Radiative Decay of Band-Edge Excitons 10520
3. Synthesis of Heterostructured Quantum Dots 10522
  3.1. Focus, Organization, and Scope 10522
  3.2. Single-Component Quantum Dots: The Starting Point 10523
  3.3. Heterostructured Quantum Dots 10524
  3.4. Engineering Carrier Localization 10527
    3.4.1. Type-I 10527
    3.4.2. Type-II 10528
    3.4.3. *quasi*-Type-II 10530
    3.4.4. Tuning Carrier Localization via Quantum Confinement 10531
  3.5. The Core/Shell Interface: Strain and Alloying 10532
  3.6. Summary and Outlook 10535
4. Auger Recombination and PL Intermittency in Individual QDs 10536
  4.1. Scaling of Auger Recombination Rates with QD Occupancy 10536
  4.2. Universal Volume Scaling of Auger Lifetimes 10537
  4.3. Auger Decay Engineering 10539
    4.3.1. Control of the Overlap of Electron and Hole Envelope Wave Functions 10540
    4.3.2. Control of Conduction- and Valence-Band Mixing 10540
    4.3.3. Control of the Strength of the Intraband Transition 10540
  4.4. PL Intermittency 10541
  4.5. Power Law Distribution of the ON and OFF Time Probabilities 10542
    4.5.1. Random Charging/Discharging 10542
    4.5.2. Fluctuating Nonradiative Decay 10543
  4.6. A- and B-Type Blinking 10544
  4.7. Suppression of PL Blinking and Lifetime Blinking 10544
  4.8. Summary and Impact on QD Applications 10545
5. Quantum Dot Lasing 10546
  5.1. History of Colloidal Quantum Dot Lasing 10546

Special Issue: Nanoparticle Chemistry

Received: March 10, 2016
Published: September 28, 2016

ACS Publications © 2016 American Chemical Society

DOI: 10.1021/acs.chemrev.6b00169
Chem. Rev. 2016, 116, 10513−10622

5.2. Optical-Gain and Lasing Thresholds in Relation to Auger Recombination 10549
5.3. Experimental Studies of the Effect of Auger Decay Suppression on Lasing Performance 10552
5.4. Single-Exciton Optical Gain 10555
5.5. Recent Advances and Future Challenges 10557
6. Quantum Dot-Based Light-Emitting Diodes (QD-LEDs) 10558
6.1. Electroluminescence (EL) from QDs 10558
6.2. Device Structure and Operational Mechanism 10559
6.3. Performance-Limiting Factors: A Spectroscopic Perspective 10562
6.4. Applications of QD-LEDs 10566
6.4.1. Full-Color QD Displays 10566
6.4.2. QD-Based White-Light LEDs 10567
6.5. Future Directions in QD-LEDs 10568
6.5.1. Heavy Metal-Free QD-LEDs 10568
6.5.2. Outcoupling Efficiency Improvement 10569
6.5.3. Long-Term Stability 10570
7. Carrier Multiplication 10571
7.1. Principles of Carrier Multiplication and Theoretical Considerations 10571
7.1.1. CM Fundamentals 10571
7.1.2. Theoretical Models 10572
7.1.3. Implications for Photovoltaics 10573
7.2. Carrier Multiplication Probed by Transient Optical Spectroscopies 10573
7.2.1. CM Signatures in TA and Time-Resolved PL 10573
7.2.2. Photocharging Artifacts in CM Measurements 10576
7.3. Carrier Multiplication in QDs versus Bulk Semiconductors 10577
7.4. Effects of Quantum-Dot Size and Composition in Carrier Multiplication 10578
7.4.1. Effect of QD Size 10578
7.4.2. Effect of Composition (Pb-Chalcogenide Family) 10580
7.4.3. Other Compositions 10580
7.5. Carrier Multiplication in Engineered Nanostructrues 10581
7.5.1. Shape Effects in CM 10581
7.5.2. Cooling-Rate Engineering in Core/Shell QDs 10582
7.6. Carrier Multiplication in Device-Grade Nanocrystal Films Evaluated by Electro-Optical Techniques 10584
7.6.1. Time-Resolved Microwave Conductivity Measurements 10585
7.6.2. Ultrafast Photocurrent Spectroscopy of QD Films 10585
7.6.3. Carrier Multiplication in Solar Cells and Photodetectors 10587
8. Quantum Dot Luminescent Solar Concentrators 10588
8.1. Introduction to Luminescent Solar Concentrators 10588
8.2. Operating Principles and Main Characteristics of Luminescent Solar Concentrators 10589
8.3. Quantum Dots as an Alternative to Organic Dyes for Applications in Luminescent Solar Concentrators 10591
8.4. Approaches to Stokes-Shift Engineering with QDs 10592
8.4.1. QD Heterostructures 10592
8.4.2. Doped QDs for LSC Applications 10595
8.4.3. Heavy-Metal-Free QDs for Highly Efficient LSCs 10598
8.5. QD-Polymer Waveguides: The Importance of the Nanocomposite Matrix 10599
8.6. Assessing the State-of-the-Art in LSC Technologies: QDs versus Organic Dyes 10601
8.7. Colorless QD LSCs for Building-Integrated PVs 10602
8.8. Addressing Remaining Challenges for QD-LSCs 10603
9. Nanocrystal Quantum Dots: Present Status and Outlook for the Future 10603
Author Information 10604
Corresponding Author 10604
Notes 10604
Biographies 10605
Acknowledgments 10605
References 10605

1. INTRODUCTION

One of the defining features of a semiconductor is an energy gap (E_g) separating a fully occupied valence band from the unoccupied conduction band. The color of light emitted by the semiconductor material and the spectral onset of optical absorption are both directly linked to the width of this gap. In semiconductors of macroscopic sizes, *i.e.*, bulk semiconductors, the gap width is a fixed parameter determined by the material's composition and structure. However, in sufficiently small semiconductor crystals (typical dimensions are less than 10−20 nm) the band gap is dependent on particle dimensions, which is a result of an additional contribution arising from tight spatial confinement of electron and hole wave functions. The size regime in which this effect becomes important is termed the regime of quantum confinement, and the nanocrystals that fall into this size range are often referred to as quantum dots (QDs). In the present review, we will restrict the use of the term QD to spherical nanocrystals, while the nanocrystals of other morphologies will be referred to based on their actual shapes, such as, *e.g.*, nanorods, nanocubes, tetrapods, *etc.*

In the first approximation, the electronic structures in a QD can be described using a simple spherical "quantum box" model in which the electron motion is restricted in all three dimensions by impenetrable walls.[1] For a QD with radius R, this model predicts that a size-dependent contribution to the energy gap is simply proportional to $1/R^2$, implying that the gap quickly increases as the QD size decreases. By employing effects of quantum confinement, it is possible to continuously tune E_g in many cases by hundreds of millielectronvolts, and even more than 1 eV for materials with small carrier masses (see the detailed discussion in Section 2.1).

Semiconductor nanocrystals emerged as a distinct research topic more than three decades ago with studies of semiconductor-doped glasses[1−4] and semiconductor colloids (see Section 3.2).[5−7] Glass-based samples were used to gain interesting initial insights into electronic and optical properties of strongly confined nanocrystals including the structure of electronic states,[8,9] electron−phonon interactions,[10−13] intraband relaxation,[14,15] nonlinear optical phenomena,[16] Auger

DOI: 10.1021/acs.chemrev.6b00169
Chem. Rev. 2016, 116, 10513−10622

processes,[17−19] and the physics of optical gain and lasing.[20] Eventually, however, most of the efforts in the nanocrystal field have shifted in the direction of colloidal samples that allowed for a more facile size control, narrower size distribution, and greatly improved surface passivation. Colloidal nanocrystals comprise a semiconductor core capped with a layer of organic molecules. The organic capping prevents uncontrolled growth and agglomeration of the nanoparticles and allows nanocrystals to be chemically manipulated like large molecules, with solubility and chemical reactivity determined by surface capping groups. In addition to defining chemical functionality of the nanocrystals, the capping molecules also provide "electronic" passivation of the nanocrystal surfaces, that is, terminate dangling bonds that otherwise would act as carrier traps leading to rapid nonradiative deactivation of electronic excitations.

A landmark result in the field of colloidal nanocrystal synthesis was the development of a highly effective organometallic route employing strongly coordinated ligands.[21] Originally demonstrated for II−VI QDs of three formulations (CdSe, CdTe, and CdS), it was eventually adapted for a large number of other compositions, including IV−VI, III−V, I−III−VI, and Group IV materials (see Section 3.2 for details). The next important milestone was the development of chemical techniques for fabricating high-quality heterostructures (Sections 3.3−3.5) that allowed for dramatic improvements in the emission efficiency[22] and opened new opportunities for controlling nanocrystal functionalities by means of "wavefunction engineering".[23−25] The development of methods for shape control[26,27] provided additional means for both tuning electronic and optical properties of nanocrystals as well as controlling their assembly into large-scale macroscopic structures.

The developments in the chemistry of the nanocrystals have been complemented by advances in understanding of their physical behaviors. The elucidation of the structure of the band-edge states helped clarify the mechanism for light emission from the nanocrystals.[28,29] Considerable progress has been made in understanding energy relaxation,[15,30−32] carrier recombination[33] and multicarrier phenomena.[34−36] The development of single-dot diagnostic techniques helped reveal intrinsic characteristics of individual QDs and elucidate the effects heterogeneities in ensemble samples.[37−40] More recent efforts have focused on the physics of electronically coupled QD assemblies and the development of methods for achieving large-range low-loss carrier transport in QD solids.[41−45]

Progress in the chemistry and physics of QD materials has culminated in the emergence of first nanocrystal-based technologies. The majority of demonstrated applications explore highly efficient, color-tunable emission from the nanocrystals. The development of highly emissive, biocompatible QDs allowed their use in biolabeling, bioimaging, and medical diagnostics.[46−48] Due to their narrow emission line width, QDs have been shown to provide an improvement in color quality compared to traditional phosphors, which stimulated their applications in display technologies.[49] Significant progress has been achieved in the area of electrically driven QD light-emitting diodes (LEDs). This research, which started more than two decades years ago with proof-of-principle demonstrations of electroluminescence from the QDs,[50,51] has led to recent demonstration of devices operating near the fundamental power-conversion limit.

QD researchers have long envisioned using nanocrystals in light-harvesting applications as well, such as in the active layers of photovoltaics (PVs).[52−54] Size-controlled spectral tunability could, for example, simplify realization of multijunction architectures.[55] An important milestone in this area was the demonstration of QD-based PV cells with certified performance, with the first such device reported in 2010 exhibiting ∼3% power conversion efficiency.[56] During the past 5 years, the efficiencies of nanocrystal-based PVs have more than tripled and now exceed 10%.[57,58] Interest in QDs as a novel PV platform has also been motivated by prospects for boosting the photocurrent of the devices via carrier multiplication (CM) or multiexciton generation (MEG), the process whereby multiple electron−hole pairs are generated by single photons.[53] Originally, this research relied mostly on spectroscopic observations;[59] however, more recently an increasing number of publications have reported observing current enhancement via this process in actual PV devices.[60,61]

At the same time, there has been a significant recent interest in applications of QDs in luminescent solar concentrators (LSCs) for the realization of semitransparent PV windows and high-efficiency collectors of diffuse solar radiation.[62−65] QDs provide several advantages over dyes in this type of devices, including enhanced environmental stability and photostability, and widely tunable emission and absorption spectra that allow for an improved coverage of the solar spectrum and reduced losses to reabsorption in large-area devices.

The focus of this review is on recent progress in nanocrystal research related to prospective applications of these materials in lasing, LEDs, advanced PVs, and LSCs. The review starts with a discussion of electronic and optical spectra of "standard" single-domain spherical QDs (Section 2). Then, it advances to chemical and spectroscopic aspects of more complex heterostructured QDs (Section 3), which includes chemical approaches to heterostructuring, and the classification of type-I, type-II, and *quasi*-type-II carrier localization regimes. In Section 4, we discuss the importance of Auger recombination in quantum-confined nanocrystals, and its relationship to the phenomenon of fluorescence intermittency (or "blinking"). In Section 5, we overview the fundamentals of QD lasing, analyze the effect of Auger recombination on the lasing performance of these materials, and discuss the suppression of Auger recombination via interfacial alloying in core/shell QDs. Then, in Section 6, we provide an overview of the history and recent progress in QD-LEDs with a focus on factors that limit their efficiency, and approaches seeking to reach industry-standard performance for this type of devices. This is followed by the discussion of the prospects of semiconductor nanocrystals as enablers of advanced PV schemes utilizing CM (Section 7). We further move on to the topic of QD-LSCs (Section 8), which is discussed in the context of the previous research of concentrators based on organic molecules. Special attention is paid to the concept of "Stokes-shift engineering" for reducing reabsorption losses and chemical aspects of incorporation of the nanocrystals into high-optical-quality, scattering-free transparent waveguides. Finally, in Section 9, we summarize the current status of research into semiconductor nanocrystals and discuss future prospects of these materials.

2. ELECTRONIC STATES IN SEMICONDUCTOR QUANTUM DOTS

2.1. Spherical Quantum Box Model

A distinct feature of the QD regime is the discrete structure of electronic states that replace the continuous energy bands of a bulk material (Figure 1). A common approach to a quantitative

DOI: 10.1021/acs.chemrev.6b00169
Chem. Rev. 2016, 116, 10513−10622

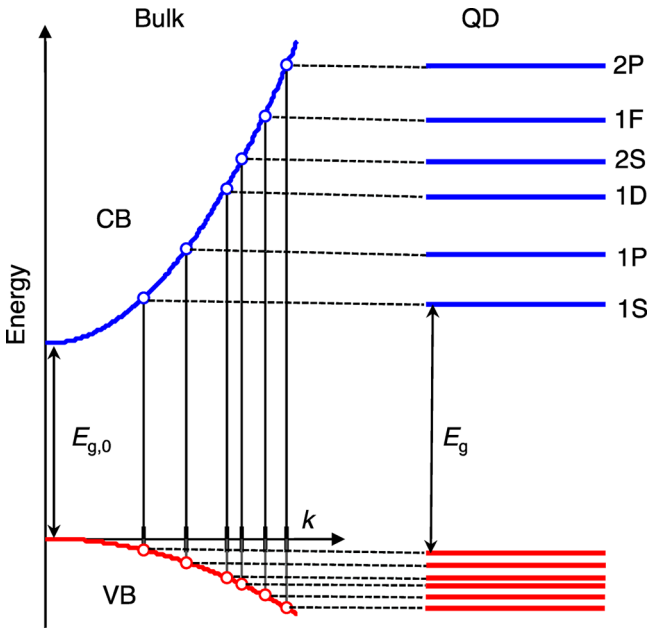

Figure 1. Idealized model of electronic states in a bulk semiconductor (left) and a spherical QD made of the same material (right). Continuous bands of a bulk semiconductor with parabolic dispersion of carrier kinetic energies ($E_k \propto k^2$; k is the wave vector) in the valence and conduction bands (denoted VB and CB, respectively) transform into discrete atomic-like levels in the case of the QD. The energies of the QD electronic states can be derived from those of the bulk semiconductor assuming discrete values of $k = \phi_{n,L} = \pi$ (1S), 4.49 (1P), 5.76 (1D), 2π (2S), *etc.* The vertical lines depict nominally allowed optical transitions according to the simple selection rules $\Delta n = 0$ and $\Delta L = 0$.[67]

description of these states employs the effective mass approximation, wherein the QD wave function is presented as a product of an envelope wave function and a Bloch wave function.[66] The envelope wave function describes the carrier motion in the QD confinement potential, while the Bloch function describes the carrier motion in the quickly oscillating potential of the underlying crystal lattice. In principle, the Bloch component comprises wave functions of multiple bulk semiconductor bands. However, if the interactions between different bands are weak (*e.g.*, in the case that the relevant band minima/maxima are widely separated in either energy or momentum space), each of them gives rise to an independent series of quantized levels. This corresponds to a so-called single-band approximation.

Applying this approximation to a spherical particle of radius R with an infinitely high potential barrier, we obtain that the envelope wave function is a product of the spherical Bessel (j_L) and spherical harmonic ($Y_{L,M}$) functions:[66]

$$\Phi_{n,L,M}(r, \theta, \varphi) = \frac{\sqrt{2}}{R^3}\frac{j_L(\phi_{n,L}r/R)}{j_{L+1}(\phi_{n,L})}Y_{L,M}(\theta, \varphi) \quad (1)$$

where r is the radial coordinate, θ and φ are the angular coordinates, and $\phi_{n,L}$ is the nth root of the spherical Bessel function of the Lth order. Quantities n, L, and M represent the quantum numbers of the corresponding quantum mechanical problem. The energies are degenerate with regard to M; therefore, in the notation of the quantized states, M is often omitted and the state is denoted by a pair of n and L, in which n is usually shown by the number and L by the letter (S, P, D, ... for L = 0, 1, 2, ..., respectively).

The energies of the quantized states can be derived from those of the parental bulk semiconductor using a set of discrete wave vectors (k) that are equal to ϕ_{nL} (Figure 1). This approach yields

$$E_{n,L} = \frac{\hbar^2\phi_{n,L}^2}{2mR^2} \quad (2)$$

where $\hbar$ is Planck's constant and m is the particle mass, which is replaced by the effective electron (m_e) or hole (m_h) mass in the case of the conduction or the valence band, respectively. The quantized states are ordered in energy according to the values of $\phi_{n,L}$ that form the following progression: π (n = 1, L = 0), 4.49 (n = 1, L = 1), 5.76 (n = 1, L = 2), 2π (n = 2, L = 0), *etc.* The corresponding states are 1S, 1P, 1D, 2S, *etc.* (Figure 1; at right). The energies of quantized states increase with decreasing radius as the inverse square of R. They also increase with decreasing effective mass. In II–VI and III–V semiconductors, the hole mass is typically much greater than the electron mass (in CdSe, *e.g.*, $m_h/m_e \approx 6$); therefore, the conduction-band levels in QDs of these materials are much more sparse than the valence-band levels.

The envelope function of the ground state (n = 1, L = 0, M = 0) has the form

$$\Phi_{1,0,0}(r, \theta, \varphi) = \frac{1}{\sqrt{2\pi R}}\frac{\sin(\pi r/R)}{r} \quad (3)$$

The corresponding energy is

$$E_{1,0} = \frac{\hbar^2\pi^2}{2mR^2} \quad (4)$$

In QDs, the band gap energy (E_g) is defined by the spacing between the band-edge electron ($1S_e$) and hole ($1S_h$) levels (Figure 1; at right), and it can be calculated as the sum of the bulk band gap ($E_{g,0}$) and the $E_{1,0}$ energies of the electron and the hole:

$$E_g = E_{g,0} + \frac{\hbar^2\pi^2}{2m_eR^2} + \frac{\hbar^2\pi^2}{2m_hR^2} = E_{g,0} + \frac{\hbar^2\pi^2}{2m_{eh}R^2} \quad (5)$$

where $m_{eh} = m_em_h/(m_e + m_h)$ is the reduced electron–hole (e-h) mass. The difference between the QD band gap and the band gap of the parental bulk material sometimes is referred to as the confinement energy, $E_c = E_g - E_{g,0}$. The value of E_c increases with decreasing QD size as R^{-2}, and in small particles it can approach the bulk band gap and even exceed it in the case of narrow-gap materials.

So far, we have neglected the Coulomb e-h interaction. The energy of this interaction is given by

$$V_{eh}(\mathbf{r}_e, \mathbf{r}_h) = -\frac{e^2}{\varepsilon|\mathbf{r}_e - \mathbf{r}_h|} \quad (6)$$

where e is the elementary charge, $\mathbf{r}_e$ and $\mathbf{r}_h$ are the electron and hole vector coordinates, and ε is the dielectric constant. In bulk materials, this term gives rise to the e-h bound states or excitons. In small size colloidal QDs, the confinement energy is usually much larger than the exciton binding energy. Therefore, the spatial extent of the electronic excitation is defined not by the Coulomb interaction but by the boundaries of the nanocrystal. In this case, the Coulomb interaction can be treated as a small correction to electronic energies, which can be calculated within the first-order perturbation theory. Applying this approach to the electron and hole band-edge states, we can obtain the following expression for the first-order Coulomb correction to the band gap:[68,69]

DOI: 10.1021/acs.chemrev.6b00169
Chem. Rev. 2016, 116, 10513–10622

$$\Delta_{eh} = \langle \Phi_{1,0,0}(\mathbf{r}_e)\Phi_{1,0,0}(\mathbf{r}_h)|V_{eh}(\mathbf{r}_e, \mathbf{r}_h)|\Phi_{1,0,0}(\mathbf{r}_e)\Phi_{1,0,0}(\mathbf{r}_h)\rangle \quad (7)$$

Since in colloidal QDs, the confinement energy greatly exceeds typical energies of lattice vibrations (i.e., phonon energies), the e-h interaction potential in eq 7 should be calculated using the high-frequency dielectric constant ($\varepsilon = \varepsilon_\infty$). Using eq 7 together with eq 3 and eq 6, we obtain $\Delta_{eh} = -1.765e^2/(\varepsilon_\infty r)$, which yields the following expression for the size-dependent QD energy gap, which accounts for both quantum confinement and Coulombic effects:

$$E_g = E_{g,0} + \frac{\hbar^2\pi^2}{2m_{eh}R^2} - \frac{1.765e^2}{\varepsilon_\infty R} \quad (8)$$

Additional corrections to electronic energies due to Coulomb interactions arise from polarization effects associated with image charges. The description of these effects can be found in, *e.g.*, refs 68 and 69.

2.2. Absorption Spectra and Absorption Cross Sections

Next, we will use the above formalism to calculate the absorption spectrum of QDs. The absorption coefficient can be found from

$$\alpha(\hbar\omega) = \frac{4\pi\omega}{n_m c}\chi''(\hbar\omega) \quad (9)$$

where χ'' is the imaginary part of the optical susceptibility χ, c is the light velocity, and n_m is the refractive index of the QD sample (at low QD loading factors, it is given by the index of a surrounding medium, *i.e.*, a solvent or a matrix). Using Fermi's golden rule, χ'' can be expressed as follows:[70]

$$\chi''(\hbar\omega) = \pi n_{QD}|\mathbf{e}\cdot\mathbf{d}_{cv}|^2 \sum_{\substack{n_v,L_v,M_v \\ n_c,L_c,M_c}} 2|\langle\Phi_{n_c,L_c,M_c}|\Phi_{n_v,L_v,M_v}\rangle|^2 \times \delta(\hbar\omega - E_{g,0} - E_{n_v,L_v} - E_{n_c,L_c}) \quad (10)$$

where δ is the delta function, $E_{n_vL_v}$ and $E_{n_cL_c}$ are the valence- and conduction-band energies given by eq 2 (here we do not account for Coulomb corrections to energies), n_{QD} is the concentration of the QDs in the sample, $\mathbf{e}$ is the unit-length polarization vector of incident light, and $\mathbf{d}_{cv}$ is the dipole matrix element of the interband transition of the parental bulk semiconductor. The term in the triangular brackets is the overlap integral between the envelope valence- and conduction-band wave functions; the factor 2 under the summation sign accounts for the 2-fold spin degeneracy of quantized states. Since the envelope functions with different quantum numbers are orthogonal, $|\langle\Phi_{n_cL_cM_c}|\Phi_{n_vL_vM_v}\rangle|^2 = \delta_{n_vn_c}\delta_{L_vL_c}\delta_{M_vM_c}$, where $\delta_{i,j} = 1$ when $i = j$ and $\delta_{i,j} = 0$ otherwise. Further, since electronic energies do not depend on M, the summation over M_v and M_c yields $(2L + 1)$, which leads to the following final expression for the absorption coefficient obtained by combining the above considerations with eq 9 and eq 10:

$$\alpha(\hbar\omega) = \frac{8\pi^2\omega}{n_m c}n_{QD}|\mathbf{e}\cdot\mathbf{d}_{cv}|^2 \sum_{n,L}(2L+1) \times \delta\left(\hbar\omega - E_{g,0} - \frac{\hbar^2\phi_{n,L}^2}{2m_rR^2}\right) \quad (11)$$

This expression indicates that the QD absorption spectrum consists of a series of sharp lines at the positions of the allowed optical transitions whose energies are given by (Figure 2a)

$$\hbar\omega_{n,L} = E_{g,0} + \frac{\hbar^2\phi_{n,L}^2}{2m_rR^2} \quad (12)$$

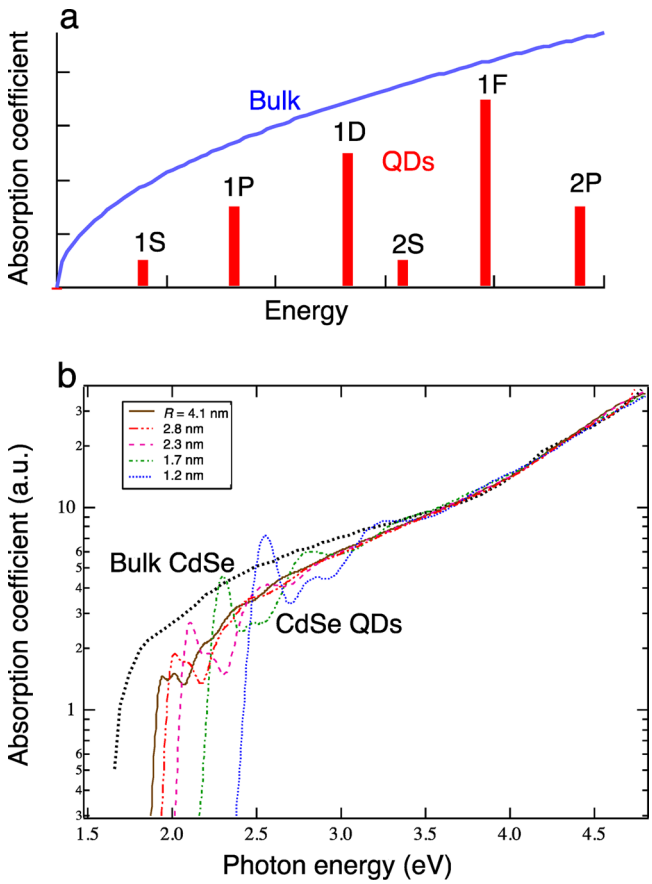

Figure 2. (a) Schematic representation of a continuous absorption spectrum of a bulk semiconductor ($\alpha(\hbar\omega) \propto (\hbar\omega - E_{g,0})^{1/2}$; blue line) in comparison to a discrete absorption spectrum of a QD (red bars). (b) Absorption spectra of CdSe QDs with mean radii from 1.2 to 4.1 nm in comparison to the absorption spectrum of bulk CdSe multiplied by a field-correction factor $|f(\hbar\omega)|$. Adapted with permission from ref 71. Copyright 2000 American Chemical Society.

With increasing QD radius, the spacing between absorption peaks decreases until they merge into a continuous spectrum of the bulk semiconductor[66] described by

$$\alpha(\hbar\omega) \propto |\mathbf{e}\cdot\mathbf{d}_{cv}|^2\sqrt{\hbar\omega - E_{g,0}} \quad (13)$$

Equation 11 also predicts that, for any fixed QD radius, the QD absorption spectrum should converge to that of the bulk semiconductor at high spectral energies for which $(\hbar\omega - E_g)$ is sufficiently large compared to the confinement energy E_c. Such a convergence has been demonstrated experimentally.[71] In order to conduct the comparison between QDs and the bulk, one should account for the dielectric screening effects that reduce the effective electric field applied to electronic excitations in the QD compared to the external field. The field-correction factor (f) depends on the shape of the nanocrystal. In the case of a spherical particle, the modulus of f can be expressed as

$$|f| = \left|\frac{3\varepsilon_m}{\varepsilon_\infty + 2\varepsilon_m}\right| = \frac{3\varepsilon_m}{\sqrt{(\varepsilon'_\infty + 2\varepsilon_m)^2 + (\varepsilon''_\infty)^2}} \quad (14)$$

DOI: 10.1021/acs.chemrev.6b00169
Chem. Rev. 2016, 116, 10513−10622

where ε'_∞ and ε''_∞ are, respectively, the real and imaginary parts of the high-frequency dielectric constant of the semiconductor, and $\varepsilon_m = n_m^2$ is the high-frequency dielectric constant of the medium surrounding the QD (it is assumed to be real). Taking into account the field-correction factor, and the fact that the semiconductor material occupies only a fraction (ξ) of the sample's volume, we can relate the high-spectral-energy absorption coefficient of the bulk semiconductor (α_0) to that of the QDs by

$$\alpha(\hbar\omega) = \xi |f|^2 \left(\frac{n}{n_m}\right) \alpha_0(\hbar\omega) \tag{15}$$

where $n = \sqrt{\varepsilon_\infty}$ is the refractive index of the semiconductor.[71]

In ref 71, the absorption spectrum of bulk CdSe corrected for dielectric screening was compared with absorption spectra of a series of CdSe QD samples with mean QD radii from 1.2 to 4.1 nm. As expected based on eq 13, all QD spectra closely overlapped with each other and the bulk spectrum at energies greater than 3.5 eV (Figure 2b), which was roughly twice the bulk CdSe band gap ($E_{g,0}$ = 1.75 eV). This indicated that eq 15 indeed accurately described the QD absorption at high spectral energies and, therefore, could be used to derive the high-spectral-energy absorption cross section, the quantity defined as $\sigma = \alpha/n_{QD}$. For this purpose, ξ can be expressed via the QD volume (V_{QD}) and QD concentration as $\xi = V_{QD}n_{QD}$, which together with eq 15 lead to the following relationship between σ and α_0:

$$\sigma(\hbar\omega) = V_{QD}|f|^2 \left(\frac{n}{n_m}\right) \alpha_0(\hbar\omega) = \frac{4\pi}{3} R^3 |f|^2 \left(\frac{n}{n_m}\right) \alpha_0(\hbar\omega) \tag{16}$$

This expression indicates direct linear scaling of the absorption cross section of the QD with its volume or cubic scaling with the radius. Equation 15 is general and applicable to nanocrystals of arbitrary shape; each nonspherical shape, however, requires a separate calculation of the field-correction factor, which might become anisotropic, *i.e.*, dependent on the direction of polarization of incident light.

A similar approach to derivation of QD absorption cross sections on the basis of bulk-semiconductor absorption coefficients has been used in numerous studies of light absorption properties of the QDs of various compositions.[72−74]

Some of these studies directly validated eq 16 via the measurements of QD absorption spectra and QD concentrations. The above approach can also be used in reverse, *i.e.*, applied for evaluating QD concentrations based on the measured absorption spectra and known absorption cross sections that are well documented in the literature for many types of the QDs.

2.3. Valence-Band States

The single-band model of electronic states provides a fairly accurate description of the conduction band of the QDs of many wide-gap semiconductors. However, because of the multi-sub-band character of the valence band typical of many materials, the structure of QD hole states is strongly affected by confinement-induced mixing between different sub-bands.[9,75−77] Below we provide an abbreviated description of the valence-band states of CdSe QDs, that have served as a model system in many early theoretical and experimental studies of strongly confined nanocrystals. A detailed theory of electronic states in II−VI QDs in the presence of interband coupling can be found, *e.g.*, in ref 9.

In bulk CdSe, the lowest-energy conduction minimum is derived from the S-type atomic orbitals and is 2-fold degenerate due to two possible orientations of the electron spin. The valence band is formed from the P-type wave functions and is split by the spin−orbit interaction into a 4-fold degenerate band with the Bloch-function angular momentum J = 3/2 and a 2-fold degenerate band with J = 1/2 (Figure 3a). Since the energy of

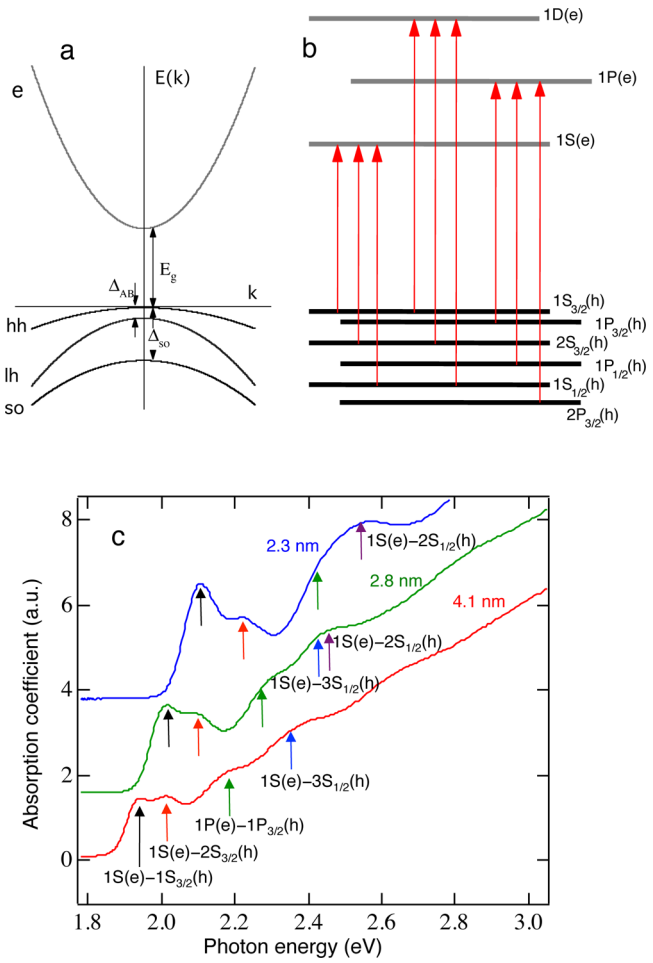

Figure 3. (a) Band structure of wurtzite CdSe near the Γ point of the Brillouin zone. In contrast to the simple single-valence-band model considered in Figure 1, the valence band of CdSe comprises three subbands. Two correspond to the light (lh) and heavy (hh) hole bands split by energy Δ_{AB} due to a crystal field of a hexagonal lattice. The third, spin−orbit split-off band is separated from the heavy-hole band by Δ_{so}. (b) The multi-sub-band character of the valence band leads to a more complex structure of hole states in CdSe QDs compared to the single-band model, which translates into a more complex structure of interband optical transitions (shown by arrows). (c) Some of the transitions shown in panel b can be easily discerned (approximate positions are shown by arrows) in the absorption spectra of CdSe QD samples (mean radii are shown in the figure). The arrows of the same color correspond to the same transitions.

the spin−orbit interaction in CdSe is fairly large (Δ_{so} = 433 meV), the effect of mixing of the band-edge states with the spin−orbit split-off band is not significant and, therefore, is neglected in our simplified description here. Instead, we will focus on mixing between states derived from the J = 3/2 bands.

The J = 3/2 band comprises the light- and heavy-hole sub-bands with angular momentum projections $J_m = \pm 1/2$ and $\pm 3/2$, respectively. At the Γ point of the Brillouin zone, the light−

DOI: 10.1021/acs.chemrev.6b00169
Chem. Rev. 2016, 116, 10513−10622

heavy-hole splitting is zero for the zinc-blende (cubic) form of bulk CdSe and nonzero (so-called crystal-field splitting; $\Delta_{AB} = 26$ meV) in the wurtzite lattice (Figure 3a). In the case of the QDs, where quantum confinement mixes different valence sub-bands, the hole states are characterized by the total angular momentum, **F**, which is a vector sum of the Bloch-function angular momentum and the orbital momentum of the hole envelope function: **F** = **J** + **L**. Given that the same total momentum **F** can be produced by using different combinations of **J** and **L**, the hole states represent a superposition of envelope wave functions with the orbital momenta L and $L + 2$, which is sometimes referred to as the "S-D mixing" effect. To label hole states, one usually indicates the lower of the two momenta and shows the projection of the total angular momentum (F) as a subscript. In this notation, the three lowest-energy hole states are $1S_{3/2}$, $1P_{3/2}$, and $2S_{3/2}$ (Figure 3b).

In addition to modifying the structure of hole states compared to the single-band model, band mixing also significantly alters the selection rules for optical transitions. Specifically, in this case the quantum numbers L and n are not strictly conserved in dipole-allowed transitions.[9] For example, transitions involving the 1S electron state are possible not only from the hole $1S_{3/2}$ and $1S_{1/2}$ states but also from the other S-type states with $n > 1$, because all of these states have a contribution from the spherical harmonic $Y_{0,0}$ and, therefore, are no longer orthogonal to the electron 1S state. Similarly, transitions to the 1P electron state are possible from all $nP_{1/2}$, $nP_{3/2}$, and $nP_{5/2}$ hole states with $n \geq 1$. Due to the S-D mixing, the transitions to the 1D electron level are possible from both S- and D-type hole states: $nS_{1/2}$, $nS_{3/2}$, $nD_{5/2}$, and $nD_{7/2}$.

The structure of the lower-energy dipole-allowed transitions in CdSe QDs is illustrated in Figure 3b. In Figure 3c, we display an example of how these transitions are manifested in the experimental absorption spectra of CdSe QDs. More details on band mixing and its effect on transition probabilities can be found in refs 9 and 76.

2.4. Fine Structure of Band-Edge Exciton States

In spherical QDs, the lowest-energy exciton comprises the 1S electron and the $1S_{3/2}$ hole. Because the spin 1/2 electron and the spin 3/2 hole have, respectively, 2 (=2 × 1/2 + 1) and 4 (=2 × 3/2 + 1) possible spin projections, this exciton is nominally 8-fold degenerate. However, the degeneracy is lifted if one accounts for the effects of the crystal field in the hexagonal lattice, deviations from a spherical shape, and the e-h exchange interaction that lead to a fine structure of the band-edge exciton.[28,29,78] Here, we briefly discuss it using wurtzite CdSe nanocrystals as an example.

As discussed in the previous subsection, the crystal field of the wurtzite lattice splits the $1S_{3/2}$ hole states with different projections (J_m) of the angular momentum into two levels with $|J_m| = 1/2$ and 3/2 that correspond to light and heavy holes, respectively (Figure 4a). This splitting (denoted here Δ_{lh}) is analogous to the A-B splitting in bulk semiconductors (see Figure 3a). It is independent of QD radius but is sensitive to the ratio (β) of the light (m_{lh}) and heavy (m_{hh}) hole masses in the direction parallel to the hexogonal **c** axis: $\beta = m_{lh}/m_{hh}$.[78] In the limit of $\beta = 0$, Δ_{lh} is $\sim 0.2\Delta_{AB}$; that is, the light–heavy-hole splitting in the QDs is five times smaller than that in the bulk semiconductor.[78]

In a nonspherical nanocrystal, the splitting between the hole states is further contributed by the term Δ_{sh} arising from shape asymmetry.[78] In ellipsoidal nanocrystals, the deviation from the spherical shape can be characterized by the parameter $\chi = a/b - 1$, where a and b are the major and the minor axes of the ellipsoid, respectively, that are assumed to be parallel with (a) and perpendicular to (b) the crystal **c** axis. In prolate nanocrystals ($a > b$), χ is positive, and it is negative in oblate particles ($a < b$). The

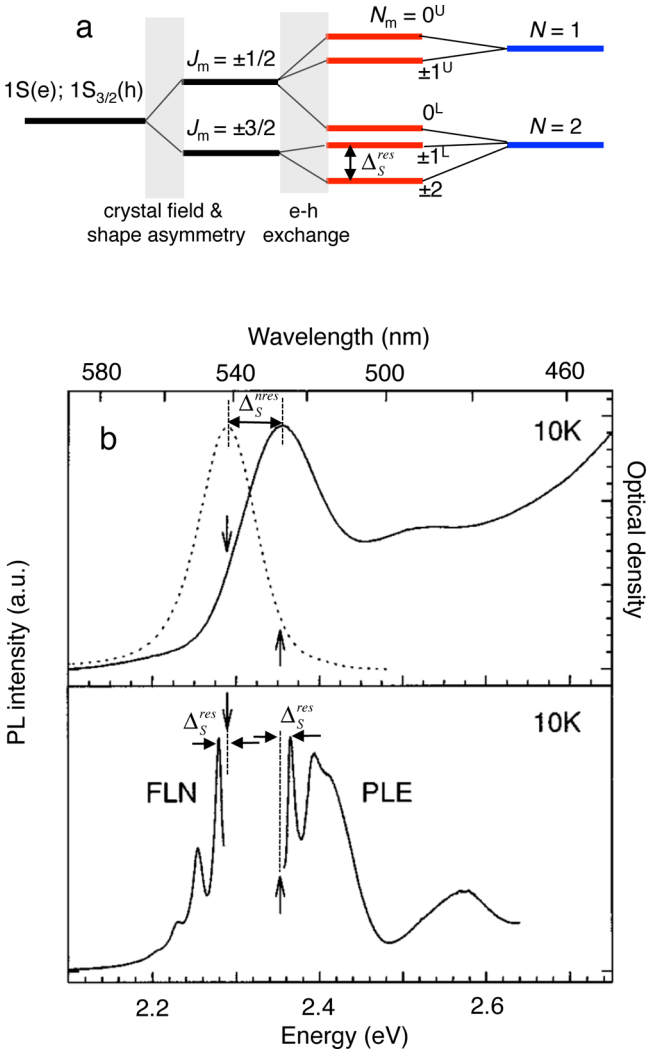

Figure 4. (a) Schematic representation of a fine structure of band-edge exciton states in CdSe QDs (red lines in the middle) in relation to the light- and heavy-hole valence-band states (black lines on the left), and "exchange-correlated" excitonic states with the total angular momenta N = 1 and 2 (blue lines on the right). The lower manifold of fine-structure states comprises excitons with $|N_m| = 2$ (optically passive), 1^L (optically active), and 0^L (optically passive). The two lowest states dominate the light emission properties of the QDs and are often referred to as "dark" ($|N_m| = 2$) and "bright" ($|N_m| = 1$) excitons. The energy spacing between these two states is observed in high-spectral-resolution measurements as a resonant Stokes shift (Δ_S^{res}). The upper manifold comprises optically active states with $|N_m| = 1^L$ and 0^L that are pronounced in absorption. (b) Absorption (solid line) and nonresonant emission (dotted line) spectra of CdSe QDs with the mean radius 1.9 nm (top) in comparison to their FLN and PLE spectra (T = 10 K). The downward arrow marks the spectral position of excitation in the FLN measurements, while the upward arrow corresponds to the spectral energy of detection in the PLE experiment. The resonant Stokes shift derived from the FLN/PLE measurements (Δ_S^{res}) is considerably smaller than the apparent (nonresonant) Stokes shift (Δ_S^{nres}) observed in the full PL and absorption spectra collected without spectroscopic size-selection. Adapted with permission from ref 29. Copyright 1996 American Physical Society.

DOI: 10.1021/acs.chemrev.6b00169
Chem. Rev. 2016, 116, 10513–10622

splitting Δ_{sh} can be expressed as $\Delta_{sh} = 2\chi u \beta E_{3/2}$,[78] where $E_{3/2}$ is the energy of the $1S_{3/2}$ hole state in a spherical QD with the effective radius $R_{eff} = (a^2 b)^{1/3}$, and u is the parameter dependent on the ratio between the light- and heavy-hole masses. In CdSe, $u < 0$;[78] therefore, in oblate nanocrystals ($\chi < 0$), Δ_{sh} is positive, and hence, the effects of shape anisotropy increase the light−heavy-hole splitting. On the other hand, in prolate nanocrystals ($\chi > 0$), Δ_{sh} is negative, and as a result, the effects of a nonspherical shape tend to reduce Δ_{lh}. In particles of small sizes where $E_{3/2}$ is large (it scales as $1/R^2_{eff}$), Δ_{lh} can even become negative, indicating the switching of the topmost valence-band-edge state from heavy-hole-like ($J_m = 3/2$) to light-hole-like ($J_m = 1/2$).

The effects of e-h exchange lead to additional splitting of the band-edge states (Figure 4a). This arises from the difference in the energy of e-h pairs with different total spins and is usually treated using excitonic terminology. A combination of the spin 1/2 hole with the spin 1/2 electron produces two excitonic states with the projection of the total angular momentum $N_m = 0$ (denoted usually as 0^L and 0^U) and the state with $|N_m| = 1$ (denoted as 1^U). Combining the $|J_m| = 3/2$ hole and the spin 1/2 electron, we obtain two excitonic levels with $|N_m| = 2$ and 1 (denoted as 1^L).

In spherical CdSe QDs, the lowest exciton state corresponds to $|N_m| = 2$. Since a photon cannot carry two units of angular momentum, this state is optically passive and often referred to as a "dark" exciton. The next state (1^L) is optically active and by analogy is called a "bright" exciton. The separation between the $|N_m| = 2$ and 1^L states defines the dark−bright exciton splitting Δ_{db}. In spherically shaped nanocrystals, Δ_{db} scales approximately as $1/R^3$ for larger sizes but eventually saturates at the value of $3\Delta_{lh}/4$ for smaller sizes.[78] The splitting manifests in optical measurements as a resonant Stokes shift (Δ_S^{res}) which can be detected by techniques such as size-selective fluorescence-line-narrowing (FLN) spectroscopy[29,79] or PL excitation (PLE) conducted either on a QD ensemble or at the single-dot level.[80] An example of FLN and PLE spectra that reveal Δ_S^{res} is shown in Figure 4b.[29] For CdSe QDs, the measured values of Δ_S^{res} range from ∼1 meV to ∼20 meV for QD radii from 4.3 to 1.2 nm.[28,29,79]

The apparent Stokes shift (denoted here as Δ_S^{nres}) observed in CdSe QD samples in the case of nonresonant excitation well above the band edge is considerably greater than Δ_S^{res} and ranges from 15−20 meV in large-size QDs to 80−100 meV in smaller particles.[79] The difference between Δ_S^{res} and Δ_S^{nres} arises from several effects. One is a contribution to optical absorption from the upper manifold of the fine structure states (1^U and 0^U) that are separated from the 1^L state by *ca.* 30−50 meV in small-size QDs. In larger QDs, the sum of the oscillator strengths of the 1^U and 0^U excitons is comparable to that of the 1^L state and it rapidly increases with decreasing QD size, while, at the same time, the oscillator strength of the 1^L exciton decreases. This leads to the increasing apparent Stokes shift in smaller QDs.

An additional contribution to the nonresonant Stokes shift arises from phonon-assisted processes that play an important role in both emission and absorption of light in the QDs, leading to the development of phonon replicas in optical spectra.[29,77,79] The most active role in these processes is played by longitudinal optical (LO) phonons. The LO-phonon energy in CdSe is 26 meV, which in terms of temperature (T) translates into 302 K. Based on this value, even at room temperature the LO mode is not heavily populated, and therefore, the processes with phonon emission prevail over those accompanied by phonon absorption. This implies that in emission the phonon replicas develop primarily on the red side of the zero-phonon PL band, while they emerge on the blue side of the absorption peak, leading to the increased apparent Stokes shift.

Polydispersity of a QD sample leads to a further increase of Δ_S^{nres}, which occurs due to the increasing influence of size on the absorption cross section with increasing photon energies. As was discussed earlier (Section 2.2), σ scales as R^3 at high spectral energies, while the scaling changes to linear ($\sigma \propto R$) at the band edge.[71] This implies that high-energy nonresonant excitation leads to a preferential selection of larger dots from the ensemble compared to near-resonant excitation at the band-edge energies, which results in the additional red-shift of the PL band and hence increased apparent Stokes shift.

This discussion of contributions to the apparent Stokes shift assumes that a singular entity is responsible for both absorption and emission, such as is the case with single-component, core-only QDs. In QDs comprised of more than one material (*e.g.*, heterostructured or doped QDs) that make unequal contributions to absorption and/or emission, the situation can be more complex. The concept of engineering the effective Stokes shift is discussed in detail in Section 8.4.

2.5. Radiative Decay of Band-Edge Excitons

The fine structure of band-edge states has a significant effect on exciton dynamics in the QDs and specifically leads to a strong effect of sample temperature on the radiative decay rate arising at least partially from the redistribution of the exciton population between the lower-energy dark ($|N_m| = 2$) and the higher-energy bright ($|N_m| = 1^L$) exciton states. To model T-dependent exciton decay, we limit our consideration to these two states and, as before, denote the difference in their energies by Δ_{db}. We further assume that the probability of an exciton residing in one of these states (p_d and p_b, for the bright and the dark states, respectively) is described by Boltzmann statistics, *i.e.*, $p_d = [1 + \exp(-\Delta_{db}/k_BT)]^{-1}$ and $p_b = [1 + \exp(\Delta_{db}/k_BT)]^{-1}$, where k_B is the Boltzmann constant. Then, the overall decay rate (Γ) can be related to the dark (Γ_d) and the bright (Γ_b) exciton decay rates by $\Gamma = p_d\Gamma_d + p_b\Gamma_b$, which leads to the following expression for the overall exciton lifetime $\tau = 1/\Gamma$:

$$\tau = \frac{\tau_b \tau_d}{\tau_b(1 + e^{-\Delta_{db}/k_BT}) + \tau_d(1 + e^{\Delta_{db}/k_BT})} \quad (17)$$

where $\tau_d = 1/\Gamma_d$ and $\tau_b = 1/\Gamma_b$ are the dark- and the bright-exciton lifetimes, respectively.

In Figure 5a, we show the temperature dependence of τ calculated using eq 17 for three values of the dark−bright splitting (11, 6, and 2 meV) that are characteristics of CdSe QDs with radii 1.3, 1.85, and 2.1 nm, respectively. In these calculations, we used $\tau_d = 1$ μs and $\tau_b = 8$ ns. These specific values of Δ_{db}, τ_d, and τ_b have been selected based on the measurements that are discussed next in this subsection.[33] The calculated curves show an expected trend; that is, at low temperature excitons are primarily in the dark state. Therefore, the corresponding lifetime is defined by a very long τ_d time constant. As temperature is increased, the lifetime shortens due to increasing probability for the exciton to be thermally activated into the bright state, which leads to the acceleration of exciton recombination. At sufficiently high temperature ($k_BT \gg \Delta_{db}$), the probabilities p_d and p_b become equal to each other ($p_d = p_b = 0.5$) and τ becomes close to twice the bright exciton lifetime ($\tau \approx 2\tau_b = 16$ ns). The temperature threshold for the activation of the

DOI: 10.1021/acs.chemrev.6b00169
Chem. Rev. 2016, 116, 10513−10622

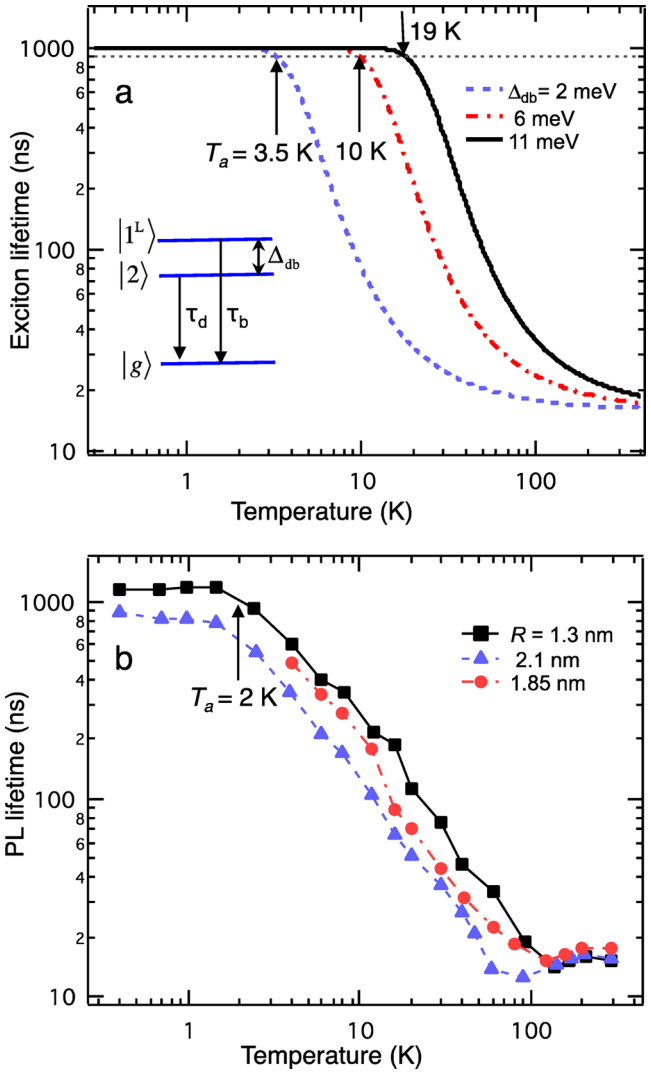

Figure 5. (a) Exciton lifetime (τ) as a function of temperature calculated using a dark–bright exciton model (inset) with τ_d = 1 μs, τ_b = 8 ns, and three different values of the dark–bright splitting shown in the figure. Arrows mark the activation threshold (T_a), defined as the temperature at which τ drops by 10% of its value in the $T \rightarrow 0$ limit. (b) Temperature-dependent PL lifetimes measured for CdSe QD samples with three different mean radii (shown in the figure). These measurements indicate an almost QD-size-independent activation threshold of ~2 K. Adapted with permission from ref 33. Copyright 2003 American Institute of Physics.

fast decay is controlled by the dark–bright exciton splitting and, therefore, is higher in smaller QDs with a larger value of Δ_{db}.

In Figure 5b, we display the experimental results[33] for the temperature dependence of exciton lifetimes in CdSe QDs of three sizes that are the same as those considered in the modeling in Figure 5a. These data were obtained by analyzing the PL relaxation time inferred from the "tails" of PL dynamics (after the signal drops to ~5% of the initial amplitude), where the decay was presumably dominated by radiative processes. In general, the observed T-dependent trends agree with the prediction of the two-state model. Specifically, τ_{PL} indeed saturates in the limits of both high- and low-temperatures. Based on the limiting values of τ_{PL}, the bright and dark exciton lifetimes in CdSe QDs are ~1 μs and ~8 ns, respectively. These are the values used in the modeling in Figure 5a.

Despite this general agreement, the measurements differ from the model in one important aspect. Specifically, instead of the size-dependent temperature activation threshold (T_a) predicted by the model, the activation threshold inferred from the experiment was nearly size-independent and corresponded to *ca.* 2 K. This is in contrast to expectations based on eq 17 according to which T_a is controlled by the dark–bright splitting ($T_a \propto \Delta_{db}/k_B$), which is a size-dependent quantity. Based on the two-state model, for the QD sizes studied in ref 33 T_a is expected to be 3.5, 10, and 19 K (Figure 5a). The behavior observed experimentally suggests the existence of an additional recombination pathway characterized by a small activation energy of the order of 1 meV. This decay channel governs exciton recombination dynamics between ~2 and ~20 K. Since no PL intensity drop is detected in this temperature range, it is primarily radiative and seems to be either independent or only weakly dependent on QD size. An explanation for this channel originally proposed in ref 33 was a weak exchange interaction of dark excitons with an ensemble of paramagnetic dangling bonds associated, *e.g.*, with surface defects. This interaction could, in principle, open a spin-flip assisted pathway for recombination directly from the dark state.

Similar T-dependent trends have been observed in other experimental studies of exciton recombination of the CdSe QDs.[81−84] Some of them also pointed toward the existence of the recombination channel with a small activation threshold, which was lower than typical energies of the dark–bright splitting.[81,83] In addition to the spin-flip mechanism proposed in ref 33, other alternatives have been considered. The authors of ref 81, for example, discussed the accuracy of determination of Δ_{db} from the FLN/PLE measurements and the validity of the overall picture of the exciton fine-structure splitting derived from the effective mass considerations. The overall conclusion of this discussion was that the previous studies of band-edge exciton states in CdSe QDs might have overestimated the dark–bright splitting in these nanostructures, while the T-dependent exciton lifetime studies allowed for a more accurate determination of this quantity.

Yet another explanation of the decay channel with a small activation energy invoked interactions with low-frequency confined acoustic modes.[83] Specifically, based on the measurements of size series of QDs of several compositions, the authors of ref 83 established the existence of a universal behavior of radiative lifetimes associated with a small activation energy of 0.5–4 meV. They attributed this energy to confined acoustic phonon modes that in most of the studied cases could be assigned to the lowest energy breathing mode with the angular momentum two. They further proposed that increasing the population of this mode with increasing temperature could open a decay pathway accompanied by phonon absorption. This would provide a necessary angular momentum for recombining from the $|N_m| = 2$ dark state, which would accelerate exciton recombination dynamics.

This short overview of experimental data indicates that there is a general agreement on the validity of the dark/bright exciton model for explaining temperature-dependent radiative recombination dynamics in CdSe QDs. There is also a consistency in opinions regarding the mechanisms for recombination in the extremes of low (<1–2 K) and high (>20–40 K) temperatures that have been attributed to dark- and bright-exciton decay, respectively. The time scales for these decay channels are in close agreement between different reports and are, respectively, ~1 μs and ~10 ns. On the other hand, the exact mechanism that governs radiative decay in the range of intermediate temper-

DOI: 10.1021/acs.chemrev.6b00169
Chem. Rev. 2016, 116, 10513–10622

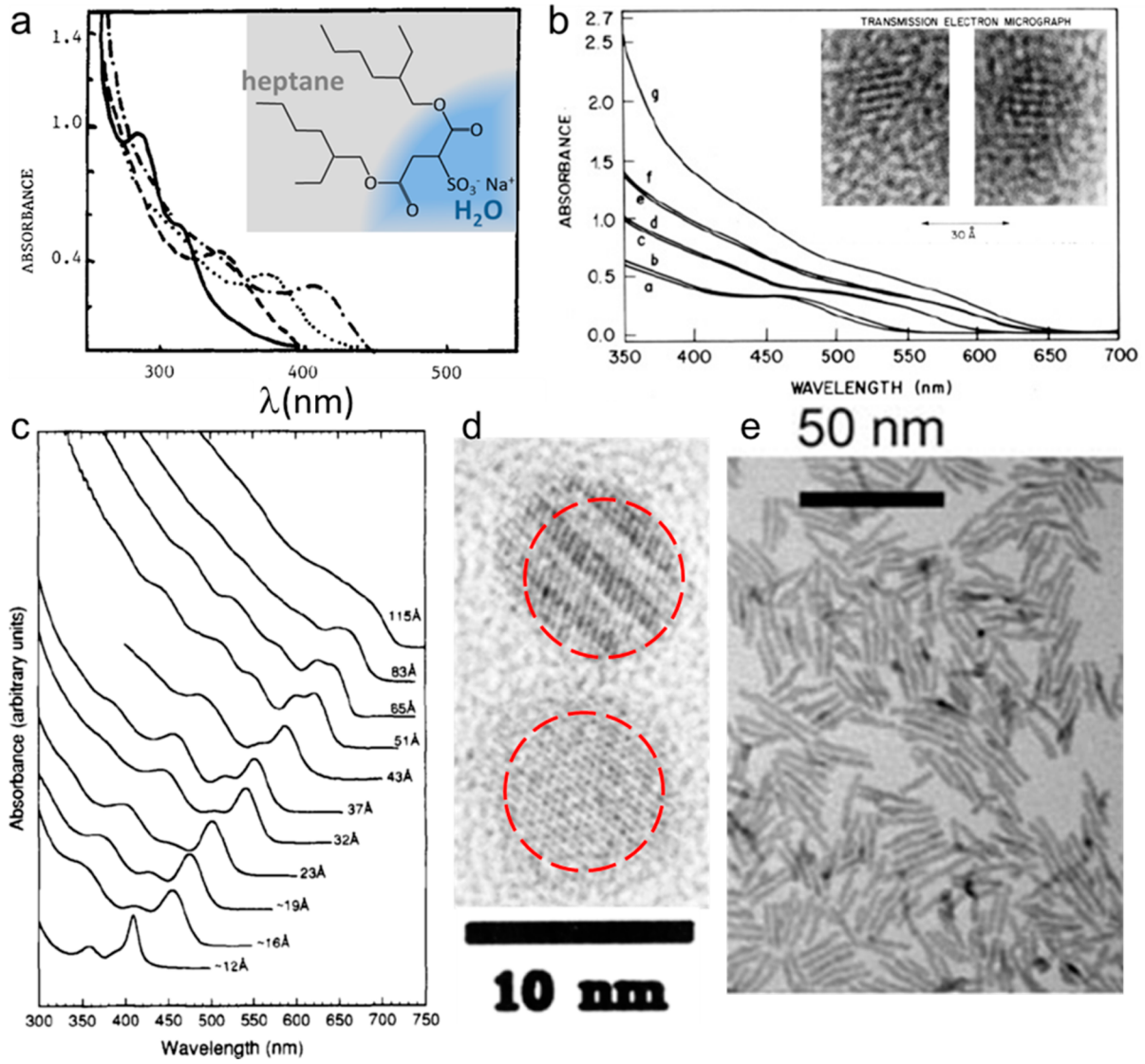

Figure 6. (a) Absorption spectra of CdS QDs synthesized via the inverse micelle approach with water:surfactant ratio varying from 1 (solid line) to 8.4 (dot−dash line). Adapted with permission from ref 108. Copyright 1986 American Chemical Society. Inset: The surfactant bis(2-ethylhexyl sulfosuccinate) stabilizes small water domains in a heptane medium. (b) Evolution of absorption spectra for inverse-micelle-synthesized CdSe QDs during atomic layer-by-layer growth via alternate addition of cation and anion precursors. Inset: Transmission electron microscopy (TEM) image of CdSe QDs. Figure and inset adapted with permission from ref 120. Copyright 1988 American Chemical Society. (c) Absorption spectra of a size series of CdSe QDs synthesized using the hot-injection method. (d) TEM image of CdSe QDs synthesized using the hot-injection method. Elongation along the (002) direction is evident in QDs for which this axis lies along the image plane (upper QD), but cannot be seen in QDs for which this axis is perpendicular to the image plane (lower). Adapted with permission from ref 21. Copyright 1993 American Chemical Society. (e) CdSe nanorods synthesized by modifying the hot-injection method to favor a fast growth regime. Adapted with permission from ref 26. Copyright 2000 Nature Publishing Group.

atures is less clear. Most of the experimental results point toward the existence of a recombination channel with a small activation energy of the order of 1−4 meV. However, the exact nature of this channel is still a subject of debates.

3. SYNTHESIS OF HETEROSTRUCTURED QUANTUM DOTS

3.1. Focus, Organization, and Scope

The focus of this section is on the development of engineered heterostructured QDs, which we define to be single nanostructures combining two or more semiconductor materials in a geometric arrangement (*e.g.*, core/shell) that is a direct result of the reaction pathway used to synthesize them. In the cases of most particular interest, the heterostructures are designed to exhibit electronic and optical properties meaningfully altered from those of simple, single-component QDs. This can be as simple as a core/shell QD exhibiting "inorganic passivation", resulting in a much improved photoluminescence (PL) quantum yield (QY) as compared to the core-only QD,[85] or more complex examples of what is now commonly called "wave-function engineering", which can result in advanced phenomena such as slowed radiative recombination,[23] reduced Auger recombination of multiexcitons[86] (Section 4.3), increased apparent Stokes shift (Section 8.2),[64] *etc.* In this review, the engineered heterostructures will often be discussed relative to single-component QDs, often in the context of a progression toward a specific application. Accordingly, we will discuss the synthetic develop-

DOI: 10.1021/acs.chemrev.6b00169
Chem. Rev. 2016, 116, 10513−10622

ment in a similar manner: we start with a look at the evolution of methods for simple QDs, and then examine how the chemical principles derived from these efforts were applied to the syntheses of heterostructures. We will then examine two major themes underlying the examples of QD engineering discussed in the subsequent sections, including structure-based control over carrier localization, and the nature of the heterostructure interface. To serve the larger purposes of this review, this section focuses on the centrosymmetric core/shell(s) motif and seeks to provide a limited number of primary or chemically edifying examples only, rather than to give a complete and up-to-date picture of the entire field of heterostructures today, vast and rapidly expanding as it is.

3.2. Single-Component Quantum Dots: The Starting Point

Given the huge diversity of materials that are commonly referred to as QDs, even when restricted to those that are chemically synthesized rather than physically fabricated, perhaps it is not too surprising that their emergence came about more as an evolution, rather than as a distinct event. Coming on the heels of decades of investigations into the use of semiconductors as catalysts or photocatalysts,[87] the seminal work of Fujishima and Honda on the photolysis of water on TiO_2[88] triggered a worldwide surge in research. The arrival of colloidal QDs came about from the amalgamation of two initially distinct lines of inquiry within this reinvigorated field: (1) investigations of aqueous suspensions of TiO_2 powders[89,90] that potentially offer higher photocatalytic activity than TiO_2 crystals or thin films; and (2) the use of semiconductors of narrower bandgap, such as cadmium chalcogenides, as photocatalysts that could be driven with lower-energy, visible light.[91−93] Thus, studies of suspended powders of visible-bandgap semiconductors such as CdS[94,95] followed as a natural combination. Gradually, the use of powder suspensions with relatively large (up to micron-sized) particles diminished in favor of much smaller particles synthesized using a "bottom-up" approach, either free-standing[96,97] or supported on silica nanoparticles.[5] These efforts used the slow reaction of ionic precursors in an aqueous or otherwise highly polar medium, based on chemistry used for solution deposition of thin-film electrodes,[98−100] but at very low concentrations in order to nucleate submicron-sized particles that would remain suspended during subsequent analysis and experiments.

At first, the drive to smaller particles was motivated largely by a desire to alleviate the light scattering that complicated optical studies, but the observation of PL from CdS nanocrystals[5,101,102] ultimately inspired the intentional synthesis of particles small enough to observe the effects of quantum confinement.[68,103−108] On the basis of these landmark examinations of the effect of crystallite size and chemical environment on their optical properties, including PL, these CdS nanocrystals are the first of what we now recognize as colloidal QDs. By combining "colloidal" as a term used to describe dispersions of inorganic materials in solution,[109] with "quantum dot" referring to a system with complete spatial confinement,[1,68,110,111] this name captures both of the defining characteristics of this unique class of materials.

A flood of nanocrystals of other materials soon followed, including ZnS;[112] PbS;[113] Cd_3P_2 and Zn_3P_2;[114] Cd_3As_2;[115] PbSe and HgSe;[116] and even Si.[117] Collectively, considered simply in terms of composition, an impressive fraction of the current assortment of colloidal QDs finds precedent within a narrow window of time in the mid-1980s. However, the single methodological development that has had the most far-reaching impact across the entirety of the field was the use of bis(2-ethylhexyl sulfosuccinate)-stabilized inverse micelles[118] (Figure 6a inset) for the growth and dispersion of high-quality CdS[108,119] and (for the first time) CdSe[120] QDs. Among the varying chemical methods described in the references above, the inverse micelle approach provides the best combination of fine control over size and narrow size distribution upon initial synthesis, achieved through varying the water:surfactant stoichiometry (Figure 6a). In comparison to the highly successful use of hexametaphosphate-stabilized micelles to make the first redispersible CdS nanocrystals,[105] it ultimately represents a more impactful change in the chemistry of QDs. Specifically, it brings these inorganic colloids into nonpolar solvents, in these cases heptane,[108,119,120] by fundamentally changing the physical nature of the nanocrystal surface and interparticle interactions. Rather than relying on Coulombic repulsion of highly charged surfaces in a polar medium to prevent (or more accurately, slow down) agglomeration and ripening, a robustly associated surfactant layer and nonpolar solvent environment keeps the inorganic particles quite well separated and much more stable relative to ripening in solution at room temperature.[119] As with the hexametaphosphate-stabilized nanocrystals, it also allows them to be reduced to a solid form in which the particles remain isolated and can be redispersed in solvent; however, in this case the surfactant shell is retained even during repeated chemical precipitation,[120,121] such as would be used for size-selection.[122] Importantly, each individual inorganic particle in solution remains reactive toward chemicals intentionally diffused in from the nonpolar phase, allowing useful chemistry, including atomic layer-by-layer growth[85,120] (Figure 6b) and the first examples of "ligand" passivation and exchange[108,120] according to the modern use of the terms.

By establishing the benefits of keeping nanocrystals more strictly isolated during growth, and by opening the door to a broad range of more weakly interacting and potentially high-boiling solvents, the inverse micelle approach caused a shift in the type of chemistry used for QD synthesis. Instead of relying on low-temperatures and limited concentrations to coax mainly ionic precursors into reacting slowly, so as to nucleate small particles without running away to bulk solids (so-called "arrested precipitation"), fast, high-temperature reactions could be applied while relying on the extra stabilization/hindrance of surfactant ligands to moderate particle growth and agglomeration. The promise of this shift in mind-set was evinced by demonstrations that thermolysis of organometallic precursors in organic solution can be used to synthesize dispersible nanocrystals of both cadmium chalcogenides[123,124] and III−V compounds.[125]

The true benefits of using fast reactions, however, were finally realized with the development of the "hot-injection" method, as demonstrated by Murray et al., for the synthesis of CdS, CdSe, and CdTe QDs.[21] The success of this method is based on finding a combination of metal and chalcogen precursors that will react quickly to form a product that will, in turn, thermolyze to yield the desired semiconductor material. If this is done using a suitable concentration of precursors, and in the presence of appropriate ligands, the product will be a stable colloid. The use of high temperatures also offers further unique benefits over arrested precipitation. In the widely applied model of colloid formation by LaMer and Dinegar,[126] the separation of a solution into a colloid occurs when a critical degree of supersaturation is achieved, which triggers "nucleation" of a homogeneous, finely dispersed phase (which in this case is the inorganic nanocrystals) out of the solution phase. Because for each newly formed particle,

DOI: 10.1021/acs.chemrev.6b00169
Chem. Rev. 2016, 116, 10513−10622

nucleation is followed by growth, the key to achieving size monodispersity is to alleviate the critical supersaturation as instantaneously as possible in a discrete nucleation event, so as to give every particle the same temporal starting point for growth. Slow, low-temperature reactions make this difficult to achieve, as at concentrations necessary for particle growth, local fluctuations have the potential to trigger nucleation of new particles. Rapid injection of precursors into a hot bath of ligand and solvent, on the other hand, results in a fast reaction, producing a huge surge in supersaturation that in turn triggers a singular nucleation event. Growth of each particle, then, proceeds from a very nearly identical starting time and chemical environment, leading to minimal size dispersity across the population. In addition, high temperatures also favor highly crystalline and shape-regular nanocrystals.

The benefits of this new approach are most clearly demonstrated by considering its impact on CdSe QDs, which from the time of the publication of Murray et al.,[21] would go on to surpass CdS QDs as the most studied, applied and ultimately commercialized nanocrystal material. In this work, CdSe QDs were synthesized via the injection of a solution containing dimethyl cadmium and trioctylphosphine selenide into a flask containing hot (>250 °C) trioctylphosphine oxide; after an immediate nucleation, particle growth then proceeds at elevated temperatures for as long as desired up to a few hours. The resulting QDs exhibit PL QYs of ∼10%, with as-synthesized size dispersities as low as 10%, which could be improved to ∼5% after sequential size-selective precipitations.[21]

These advances in material quality had impact far exceeding the immediate benefit of improvements to a single type of QD. The narrow size distributions allowed the discernment of fine features in the absorption spectra (Figure 6c); because of this, and their high QYs of band-edge emission (particularly at low temperature[127]), these samples allowed advanced spectroscopic probes of exciton structure and dynamics of CdSe QDs[28,33,78,127,128] that laid the groundwork for the modern understanding of QDs in general. In addition, the excellent size and shape regularity also allowed the confident assertion not only of the prolate nature of these wurtzite CdSe nanocrystals (Figure 6d) but also of the crystal direction of the elongation; this observation was the underpinning for later methods for synthesizing elongated CdSe nanorods (Figure 6e),[26] which essentially launched the field of nanocrystal shape control.

The hot-injection paradigm was successfully extended to numerous other QD systems, including zinc chalcogenides,[129−132] various II−V[133−135] and I−III−VI[136,137] compounds, and the lead chalcogenides.[138−141] As these methods became more and more widely used, a better understanding of the chemistry led to a greater diversity in choice of precursors, some of which offered their own advantages. In a particularly important example, Peng and co-workers prepared high-quality cadmium chalcogenide QDs without using highly toxic and pyrophoric dimethyl cadmium,[142,143] an advancement that expanded the accessibility of these materials to a much wider community of researchers.

While elevated synthesis temperatures have been found to lead to high crystallinity in general for these and many other types of colloidal QDs, hot-injections are not generally used for some specific material families. These include for III−V[144−147] and Group IV[148−153] materials, for which fast injection yields no particular benefits, due to very high crystallization energies, and for mercury chalcogenides,[154−156] which grow too fast at high temperatures. Finally, even for many materials popularly made by hot-injection methods, alternative routes to narrow size distributions have been demonstrated. Cao and Wang devised a one-pot, noninjection method for synthesizing high-quality CdS QDs,[157] and later CdSe and CdTe,[158] which avoided the dimethylcadmium used in a previously reported method for CdTe.[159] Intriguingly, the noninjection methods tend to result in nanocrystals evincing the zinc-blende cubic crystal structure for all three materials instead of the wurtzite phase that is more typically formed in injection syntheses. This can potentially be ascribed to the nucleation occurring at relatively low temperature, although a subsequent alternative preparation of zinc-blende CdSe found that temperature was less important than choice of ligands.[160]

Driven by potential advantages in scalability, large-yield noninjection (or low-temp injection with subsequent heating) methods were subsequently developed for other QDs, including of PbS[161] and $CuInS_2$;[162,163] this continues to be an active field of development.[164]

3.3. Heterostructured Quantum Dots

The preceding subsection describes a selection of the many methods for producing single-component colloidal QDs of a variety of materials. Though the chemistries, band gaps, stabilities, and other properties vary with formulation, they possess a defining commonality in that their optical characteristics (especially absorption) can be understood by imposing the perturbation of quantum confinement on the known properties of the related bulk materials. This is true to a large extent for QDs comprised of alloyed materials as well, for example, $Zn_xCd_{1-x}Se$,[165] $CdS_{1-x}Se_x$[166] or $InGaP_2$[147] QDs, although a study of $CdSe_{1-x}Te_x$ alloy QDs demonstrates that both bulk factors (*e.g.*, nonlinearities in the dependence of band gap on composition due to so-called "optical bowing") and uniquely nanoscale effects (*e.g.*, variations in composition along the QD radius) can have unanticipated effects on observed properties.[167] For heterostructured QDs, *i.e.*, those comprising two or more distinct material regions in intimate contact, the situation is much more complex, and the potential for observing and/or intentionally achieving novel properties or carrier behavior is correspondingly greater. In the subsections that follow, we will define and examine the categorization of heterostructured QDs based on their optical properties. Here, we will describe the development of the chemistry of core/shell heterostructures in general.

Studies of heterostructuring in colloidal particles started almost contemporaneously with those of single-component aqueous semiconductor colloids, originally in the mindset of seeking enhanced catalyst effects, such as with nominally core/shell combinations of CdS and ZnS.[112,168,169] Later, again as in simple QDs, focus shifted more toward the effect of heterostructuring on optical absorption and PL for a wider range of combinations, particularly pairs of materials with very different bandgaps like CdS/Ag_2S,[170] AgI/Ag_2S,[171] CdS/PbS,[172] and HgS/CdS (and the reverse)[173] and CdS/HgS/CdS core/shell/shell[174,175] nanocrystals. A consistent difficulty with these early efforts is that the determination of how the two materials were arranged (*e.g.*, an alloy-like mixed phase, vs a mixture of separate crystallites vs core/shell embedding of one phase in the other) was based on an extrapolation of the synthesis procedure (i.e., precursors for core and shell were added in a respective order, and in selected relative amounts) coupled with rationalization of the observed spectra and/or photocatalyst activity. Assertions made in this way varied in strength; however, the

DOI: 10.1021/acs.chemrev.6b00169
Chem. Rev. 2016, 116, 10513−10622

relative stability of inverse-micelle nanocrystals allowed synthesis of a two-component colloid with somewhat less experimental uncertainty, as was accomplished in a report of CdSe/ZnS and ZnS/CdSe core/shell QDs[85] (a structural assertion later verified independently by a similar synthesis of CdSe/ZnSe QDs[176]).

The key for successful shell growth, as would become standard in future efforts, was to introduce the precursors for the shell material in such a way that homogeneous nucleation separate from the already formed cores was suppressed. In the inverse-micelle syntheses of core/shell structures,[85,176,177] borrowing a page from the atomic layer-by-layer growth protocol of Steigerwald et al. (Figure 6b),[120] small amounts of separate shell cation and anion precursor solutions were added alternately to a micellar dispersion of cores. This method promotes reaction of each successively added precursor with the surfaces of the existing nanocrystals while avoiding a large concentration of both precursors at the same time, which can trigger a homogeneous nucleation.

As the field moved into high-temperature organometallic syntheses, gains in size and shape regularity in core/shell heterostructures were realized, and the variety of material combinations eventually matched and surpassed those in heterostructures grown via low-temperature methods. In the prototypical example, again the key is to add shell precursors to a solution of cores in a controlled manner that avoids nucleation. In perhaps the earliest hot-injection core/shell synthesis, fully purified 4 nm diameter CdSe cores are redispersed and heated to 150 °C, whereupon a solution containing a diethylzinc and trioctylphoshpine selenide solution are added slowly and continuously using a syringe pump.[178] The progress of formation of CdSe/ZnSe core/shell QDs is monitored using absorption and PL spectroscopy, as would become standard practice. Although average shell thicknesses of ∼1.3 nm are reached, the heterostructured particles are much less regular in shape than the original CdSe cores, indicating that the shell is highly nonuniform in thickness; X-ray diffraction further suggests that the shell is at least polycrystalline and perhaps partly amorphous.

Greater regularity is observed in a synthesis of CdSe/ZnS reported at nearly the same time.[22] In this case, 3 nm diameter CdSe cores were not isolated, but rather a solution of diethylzinc and hexamethyldisilathiane was added in small, periodic injections directly to the CdSe growth solution at the surprisingly high temperature of 300 °C, after which the reaction mixture is allowed to stir at 100 °C for 1 h. The resulting CdSe/ZnS QDs feature a thinner shell (∼0.6 nm on average) but retain a more regular shape. A more complete range of core diameters (2.3 to 5.5 nm) and shell thicknesses (up to 1.6 nm) for the CdSe/ZnS system, and the first organometallic synthesis of CdSe/CdS QDs, were obtained by dropwise addition of corresponding precursors to purified and redispersed CdSe cores at temperatures of 140−220 °C.[179] Shortly after, growth of CdS shells on CdSe cores was demonstrated at the even lower temperature of 100 °C.[180] Finally, the model originally used for inverse-micelle growth of heterostructures,[85] specifically the iterative, separate addition of cation and anion precursor solutions, was applied to organometallic synthesis, resulting in what has been named the "successive ion layer adsorption and reaction" (SILAR) method.[181] Interestingly, because the method uses less reactive precursors (cadmium oleate, and elemental sulfur dissolved in 1-octadecene) and keeps precursor concentrations at a minimum throughout the reaction, shell growth can be carried out at high temperatures (240 °C) while maintaining very fine control over shell thickness, and without homogeneous nucleation.

The outcome of this explosion in development of CdSe/ZnS and CdSe/CdS QD syntheses was a versatile class of fluorophores exhibiting QYs regularly over 50% over a large portion of the visible spectrum. But in addition, as in the simple QDs, the methods developed for cadmium chalcogenides inspired syntheses of heterostructures based on cores of other common semiconductor systems, including the zinc chalcogenides,[25,182,183] silver chalcogenides,[184] III-Vs,[185,186] II-Vs,[135] and I−III−VIs.[163,187,188] The growth of core/shell nanocrystals by sequential addition of appropriate precursors is not limited to binary combinations of pure compounds: although new examples are developed regularly and are already too numerous to cover adequately in this review, this method can also be used to create well-defined heterostructures including multiple shells[189−191] and alloyed compounds.[192,193] A conceptually related alternative to the slow addition of shell precursors to a solution of core nanocrystals is the "one-pot" method, in which all precursors are present at or near the beginning of the reaction, and differences in reactivity lead to the desired heterostructuring. Although it does not offer the same level of fine control over core and shell dimensions, this approach has been successfully applied to, for instance, II−VI heterostructures.[194]

A strikingly different approach to heterostructuring is the use of cation exchange reactions. Like ligand exchange or typical nanocrystal growth/shell formation, cation exchange takes advantage of Le Chatelier's principle that when a system at equilibrium is perturbed, it will react in a manner to return to equilibrium. For a colloidal QD in solution, when a new ligand or reactive precursor species is introduced, the system seeks a new equilibrium by engaging in chemistry at the nanocrystal surface (*e.g.*, ligand exchange or reactive material deposition). In cation exchange, the reaction to an excess amount of a new cation precursor is a replacement reaction with surface and near-surface cations from the nanocrystal lattice (leaving the anion sublattice intact). Cations formerly in solution are now in the nanocrystal solid, forming a heterostructure, and displaced cations are pulled into solution. In order for significant cation exchange to occur, as with any reaction in a *quasi*-equilibrium environment like a colloidal QD solution, a thermodynamic driving force is required. In this case, the favorability of an exchange reaction is based primarily on the sum of two major energetic contributions: the stability of the ionic solid phase, and the stability of the solvated ions in solution. These principles have been used in a number of examples of the total transformation of nanocrystals by complete cation exchange,[195] driven by either the formation of a much more stable solid phase, as in the reaction of CdSe nanocrystals with methanolic Ag^+ solution to form Ag_2Se nanocrystals,[196] or by the efficient solvation of ions in the presence of specific ligands, as in the formation of PbSe nanocrystals by reaction of PbI_2 with either CdSe[197] or ZnSe[198] nanocrystals in oleylamine.

Stoichiometry can be used to stop the replacement reaction before it reaches totality, i.e., by simply not adding enough new cation, one can end up with a partial replacement. The result can be either an alloy[199] or a heterostructure; facet-selective, fast-propagating exchange starting from a point or face of first exchange typically produces not core/shell heterostructures, but instead more complex structures that feature separate material domains met at essentially flat interfaces.[200−205] In a few cases, a slower, self-limiting exchange can result in a core/shell heterostructure. Cation-exchange was invoked in the description of the synthesis of CdS/HgS[173] and subsequent CdS/HgS/CdS[175] QDs, where exposure of CdS nanocrystals in aqueous colloid to Hg^{2+} ions resulted in replacement of only one

DOI: 10.1021/acs.chemrev.6b00169
Chem. Rev. 2016, 116, 10513−10622

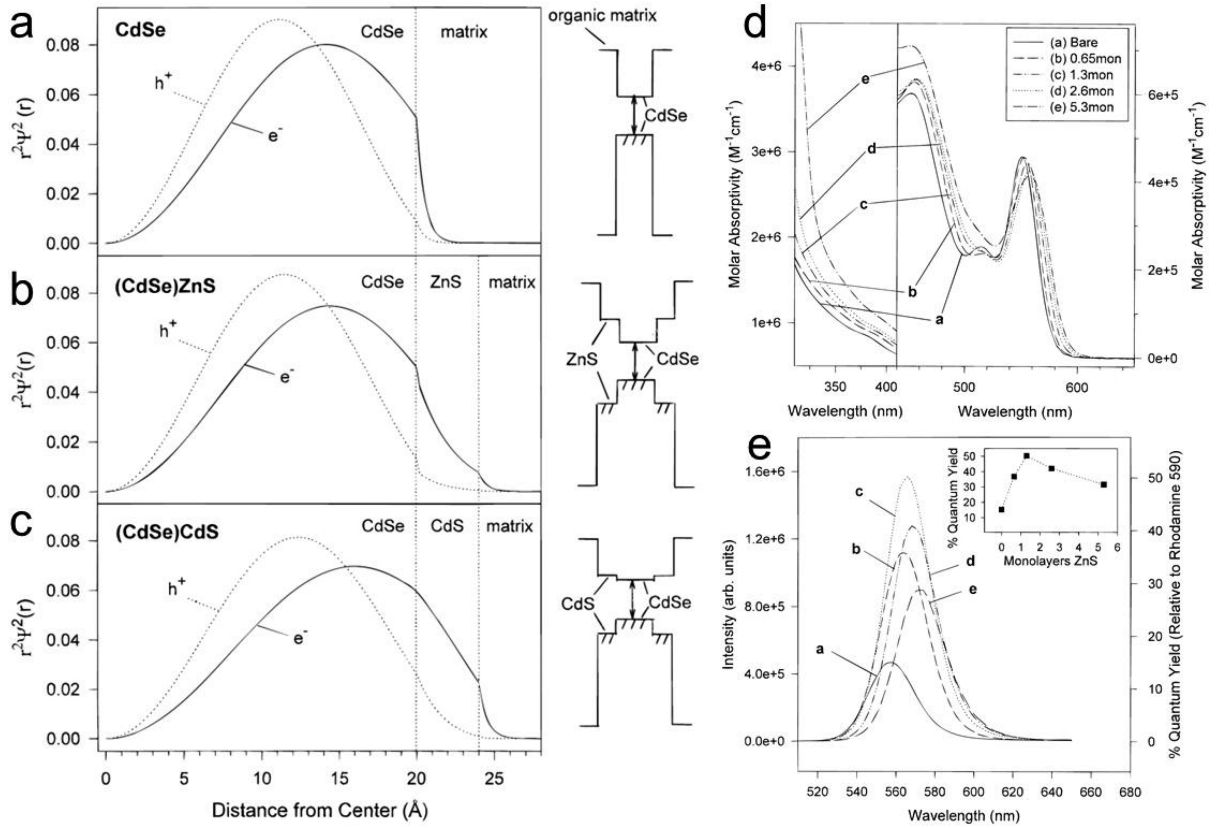

Figure 7. (a–c) Radial probability functions for the band-edge electron and hole wave functions in (a) bare 2 nm diameter CdSe QDs, (b) CdSe/ZnS and (c) CdSe/CdS core/shell QDs, each with a 2 nm diameter core and a 0.4 nm shell. The approximate band offsets between the various components are depicted to the right of each. (d) Absorption and (e) PL spectra for a series of CdSe/ZnS QDs featuring a 4.2 nm core and varying thicknesses of ZnS shell (expressed in monolayers). ZnS shell growth has little effect on absorption near the band edge, but strongly enhances QD emission QY (inset of e). Adapted with permission from ref 179. Copyright 1997 American Chemical Society.

monolayer of Cd^{2+} cations; nevertheless, because of the very large difference in bandgaps, the red-shift of the optical absorption and PL spectra was substantial. Another example is the synthesis of $CuInS_2/ZnS$[206] and $CuInSe_xS_{2-x}/ZnS$ or $CuInSe_xS_{2-x}/CdS$[207,208] QDs, wherein the I–III–VI material core is exposed to a solution of zinc or cadmium carboxylate at elevated temperatures, resulting in formation of a thin (<2 monolayers), fairly uniform shell of II–VI material. Because the formation of a shell of wider bandgap material comes at the expense of core material, the spectral features of the core/shell nanocystals shift to higher energies as the reaction proceeds.

A particularly notable example of self-limiting cation exchange resulting in a core/shell structure is that of the lead chalcogenide nanocrystals, if only because no other method described above has proven effective at creating such heterostructures due largely to the instability of lead chalcogenide nanocrystals at elevated temperatures. Exposure of PbS or PbSe QDs to a solution of excess cadmium oleate results in formation of a uniform shell of the corresponding cadmium chalcogenide whose thickness depends on the duration and the temperature of the reaction. At low temperatures (20–100 °C), the thickness can be controlled from nearly imperceptible submonolayer (<0.3 nm) thicknesses up to ∼1.5 nm;[209] exchange performed on PbTe QDs tends to produce somewhat thicker shells.[210] As the shell is formed, the lower band-gap core is effectively consumed, moving spectral features to the blue. If the original QD is large enough to support it, applying elevated temperatures up to 200 °C allows for access to shell thicknesses as high as 4 nm;[211] prolonged heating at or above this temperature leads to delamination of the shell and formation of either separate homogeneous lead and cadmium chalcogenide particles (if in solution), or fused bihemispherical "Janus" particles (if in vacuum).[212] Despite evidence of facet selectivity,[213] due to the highly symmetrical rock-salt crystal structure, the reaction proceeds nonselectively more-or-less across the entire nanocrystal surface, even for elongated or star-shaped particles,[213] retaining the original anion lattice and total shape of the particle even as the lead-containing domain shrinks away to one or more tiny and highly faceted cores. Throughout the process, the interface between the cadmium and lead regions remains absolutely abrupt, with no evidence of intermixing or alloying.[211] Finally, it has been shown that these core/shell heterostructures are more robust than the original lead chalcogenide QDs toward ripening at elevated temperatures, allowing subsequent shell growth by more conventional methods to create PbSe/CdSe/ZnS[209] and PbSe/CdSe/CdS[214] heterostructured QDs.

Ion-exchange reactions with nanocrystal systems dominantly involve cations, as they are generally much smaller and more mobile than anions, but there are exceptions. A particularly interesting example of anion exchange is the reaction of 10 nm spherical CdS nanocrystals with trioctylphosphine telluride at 260 °C.[215] Complete exchange involves the transformation of spherical wurtzite-phase CdS into spherical zinc-blende CdTe, but considerable strain and the relatively high mobility of cations means that at intermediate stages, shape is not preserved, and particles are actually "dimers" of two quasi-spherical domains

DOI: 10.1021/acs.chemrev.6b00169
Chem. Rev. 2016, 116, 10513–10622

meeting at a plane. While for most binary semiconductors, these factors can be expected to always make shape retention difficult, it has been shown that the more open and purely ionic perovskite structure of cesium lead halides ($CsPbX_3$; X = Cl, Br, or I) allows for the straightforward, reversible interexchange of halide anions in nanocrystals of these materials at low temperature with complete retention of lattice and nanocrystal shape.[216,217] Although partial exchange is possible, no evidence of a distinct heterostructure has been observed.

3.4. Engineering Carrier Localization

As stated in the introduction to the previous subsection, a major motivation for the development and study of heterostructured QDs is the emergence of electronic and optical properties beyond those that arise from the influence of quantum confinement on the bulk band structure of a material. One of the sources of these new properties stems from the new possibilities open to excited carriers in a heterostructure for how they interact with the physical confines of the nanocrystal, as well as with other carriers. To demonstrate what this means, we can compare the localization of excited carriers in typical single-component QDs (CdSe, 2 nm radius) to that in two types of heterostructured QDs (CdSe/ZnS and CdSe/CdS, both 2 nm core radius plus 0.5 nm shell) according to a simple particle-in-a-box model (Figure 7a–c).[179] In Figure 7a, we see that even though the different electron and hole effective masses change the shape of the radial probability function of each respective carrier in a CdSe QD, they both necessarily sample a very similar space overall (defined by the entire physical extent of the QD), and both extend at least somewhat into the exterior of the QD (noted as "matrix"). In contrast, while the extent of either carrier into the matrix is reduced in heterostructured QDs (Figure 7b and c) the electron extends significantly into the shell of both the CdSe/ZnS and especially the CdSe/CdS QD. These features have several ramifications for the optical properties of the QD. First, this model predicts a reduction in the interaction between either carrier and the QD surface, suggesting that carriers in the heterostructures should have a reduced probability of finding nonradiative recombination centers, or "traps," on the surfaces. This in turn implies a higher probability of the carriers recombining radiatively, i.e., well-synthesized heterostructures should have higher emission QYs. Second, the increased electron probability function in the shell for the CdSe/CdS QD in particular means a greater volume extent for the electron wave function overall, and correspondingly weaker confinement: the spectral features of this QD should be at lower energy than those of the CdSe QD. Finally, the overall spatial localization of hole and electron are most different in the case of CdSe/CdS QD, suggesting that electron–hole overlap function will be reduced, leading to a lower oscillator strength for the radiative transition and longer radiative lifetime.[218,219]

Because the respective carrier spatial localization is heavily influenced by the relative positions of the valence and conduction bands of the materials making up the core/shell QD, we use these positions (as determined, to a first approximation, by applying the expected effects of size-based quantum confinement on the bulk positions) to categorize the main types of heterojunctions (Figure 8). The type-I and type-II descriptors themselves are conventions used for describing semiconductor heterojunctions in general, but additional nuances arise when they are applied to heterostructured nanocrystals, as their small size means that the entire material becomes defined by the junction behavior. A discussion of the major categories and subcategories, and their properties along with illustrative examples, follows below.

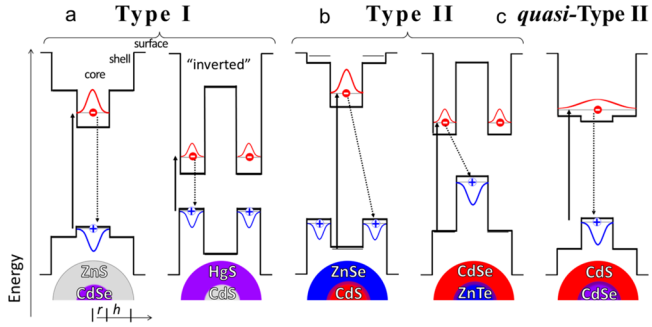

Figure 8. Band alignments between the materials in core/shell QDs result in three major carrier localization regimes, depicted using the qualitative alignments for known examples of each (at bottom) based on the bulk band alignments (heavy horizontal lines) modified by quantum confinement (thin horizontal lines) for arbitrary combinations of core/shell size. The localizations of the wave function for band-edge electrons and holes are depicted in red and blue, respectively. The principal absorbing (solid arrows) and emitting (dotted arrows) transitions are also shown for each example. (a) Type-I QDs feature a nested alignment, causing both the electron and hole to reside principally in either the core (left) or the shell (right). (b) In Type-II QDs, a staggered alignment of conduction and valence bands pulls band-edge electrons and holes into separate parts of the core/shell QD. (c) In *quasi*-type-II QDs, one carrier remains localized in a single component of the heterostructure (here, the hole), while the other is largely delocalized throughout the entire QD.

3.4.1. Type-I. Type-I heterostructures (Figure 8a) usually combine two semiconductor materials with bandgaps of significantly different size, as it is defined by a "nested" arrangement of band positions, i.e., one material has a higher-lying valence band and lower-lying conduction band than the other. As a result, both excited carriers are colocalized within the material with the narrower bandgap. Accordingly, as can be seen in the widely studied CdSe/ZnS QDs, optical properties such as the structure of the absorption spectrum near the band-edge (Figure 7d), the PL energy (Figure 7e) and the radiative lifetime[33] are largely determined by the smaller bandgap material. The CdSe/ZnS QD represents the most popular manifestation of the type-I heterostructure, wherein the narrower gap material is the core (Figure 8a, left). This arrangement is commonly referred to as "inorganic passivation," because as predicted in Figure 7b, the shell serves as a barrier suppressing the interaction of excited carriers with surface trap sites, thus effectively taking on the former role of the passivating ligand in increasing emission QYs (Figure 7e). The concept of improving fluorescence yield by encapsulating a QD with a higher bandgap material has precedents in the practice of "activation" of aqueous nanocrystals, *e.g.*, the formation of a $Cd(OH)_2$ layer on the surface of CdS QDs by exposing them to excess Cd^{2+} ions at high pH.[170] The effect can be profound, especially for QDs with poor surface quality such as many of those produced by low-temperature methods,[85] and is accompanied by enhanced environmental stability, making Type-I heterostructured QDs the original fluorophores of choice for applications like LEDs (see Section 6).

The "inverted" arrangement, in which the narrower bandgap material serves as the shell (Figure 8a, right), does not provide the same isolation of carriers from the surface. However, the formation of an inverted type-I QD is very easy to follow spectroscopically, as the absorption and PL (if measurable)

DOI: 10.1021/acs.chemrev.6b00169
Chem. Rev. 2016, 116, 10513–10622

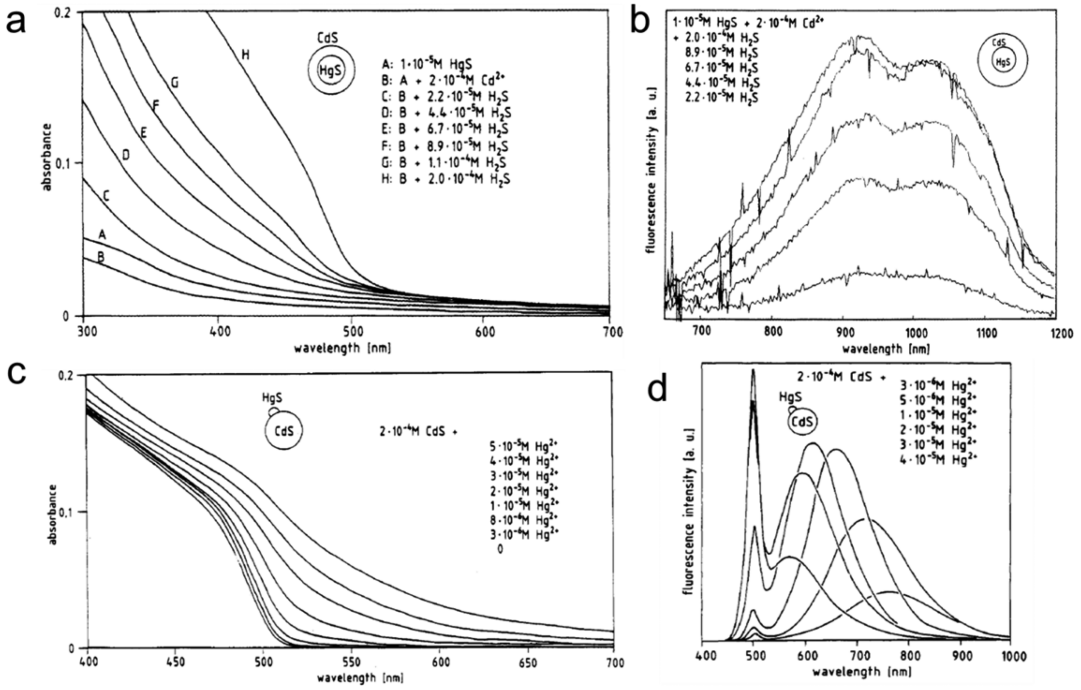

Figure 9. Evolution of (a) absorption and (b) PL spectra of type-I HgS/CdS core/shell QDs as first Cd^{2+} ion and then successive amounts of H_2S are added to the growth solution, resulting in an increasingly thick shell. The infrared band-edge absorption onset and PL remain constant in energy. In contrast, the absorption (c) and PL (d) of inverted type-I CdS/HgS QDs shift dramatically with increased shell thickness as more Hg^{2+} ion is added in the presence of excess sulfur precursor. Adapted with permission from ref 173. Copyright 1993 American Chemical Society.

spectra shift strongly to the red as the shell forms and thickens. For this reason, heterostructures of this geometry were studied extensively early in the development of colloidal QDs.[171,172,220,221] An illustrative comparison of the progressive shifts in spectra during formation of both standard and inverted type-I heterostructured QDs can be carried out on the CdS/HgS (HgS/CdS) system (Figure 9).[173]

An interesting extrapolation upon the type-I motif occurs when an additional shell of the core material is grown onto the shell. Starting with the CdS/HgS inverted Type-I QD, the result is a CdS/HgS/CdS so-called "quantum dot quantum well"[174,175] wherein the carriers are confined to a hollow spherical HgS domain of controllable thickness sandwiched between an inner core and outer shell both made of CdS (Figure 10a). On the other hand, building the related structure onto a conventional type-I CdSe/ZnS QD, one can realize instead a CdSe/ZnS/CdSe "dual quantum system."[190] When the ZnS barrier layer is thin (1 monolayer), the two CdSe regions are fully coupled, exhibiting a single PL peak consistent with lower confinement energy than in the original CdSe/ZnS QD. However, when the ZnS is 2 or more monolayers thick, in addition to the original core-based emission, a second emission peak emerges whose energy depends on the thickness of the outer CdSe shell (Figure 10b).

3.4.2. Type-II. In variance to most type-I heterostructures, type-II heterostructures tend to be comprised of materials featuring bandgaps that are both at least moderately wide (>1.3 eV). This is because it makes the defining characteristic, a staggered band-alignment in which both the conduction and valence bands of one material are higher-lying than those of the other (Figure 8b), easier to attain. The most important consequence of this alignment is that excited carriers are energetically pulled into separate material domains within the QD. Specifically, the electron will be localized in the material (whether core or shell) with the lower-lying conduction band, and the hole will be in that with the higher-lying valence band. The spectroscopic consequences of this spatial separation are manifold. First of all, while the onset of strong absorption for such nanocrystals is still determined by whichever material possesses the narrower bandgap, the emission (if any) comes from a spatially indirect transition of considerably lower energy (Figure 8b, dashed line), resulting in a large apparent Stokes shift. Because of reduced overlap between the carriers, this transition has lower oscillator strength, meaning longer radiative lifetime and typically lower QY, as in this case even slow nonradiative processes can effectively compete with radiative decay.[23] In cases when the core/shell interface and surface of the type-II QD have really low defect densities, the heterostructure may actually show higher QY than the original single-component QD, for the same reasons as in the case of a type-I heterostructured QD.[223,224] Finally, separation of carriers of opposite sign fundamentally changes the Coulomb interactions within multiexciton states,[225,226] which has dramatic consequences for QD lasing, as will be discussed later in Section 5.

The creation and characterization of type-II QDs is somewhat more challenging than other types of heterostructures for a number of reasons, including that the influence of quantum confinement effects on both domains puts a very high premium on fine control over core- and shell-size precision. Indeed, distinguishing type-II localization from type-I (especially inverted) often relies on time-resolved spectroscopy coupled with computational analysis. As such, unlike other heterostructure classes, there is not an appreciable history of type-II QDs before the advent of organometallic syntheses. Like the others, though, it has been dominated by combinations of II–VI semiconductors, including CdTe/CdSe[23,223,224] (and CdSe/CdTe[227]), CdSe/ZnTe[23,228] (and ZnTe/CdSe[182,229]), CdS/ZnSe[230] (and ZnSe/CdS[231]), and ZnTe/ZnSe;[232] but type-II InP/CdS QDs have also been reported.[233]

DOI: 10.1021/acs.chemrev.6b00169
Chem. Rev. 2016, 116, 10513–10622

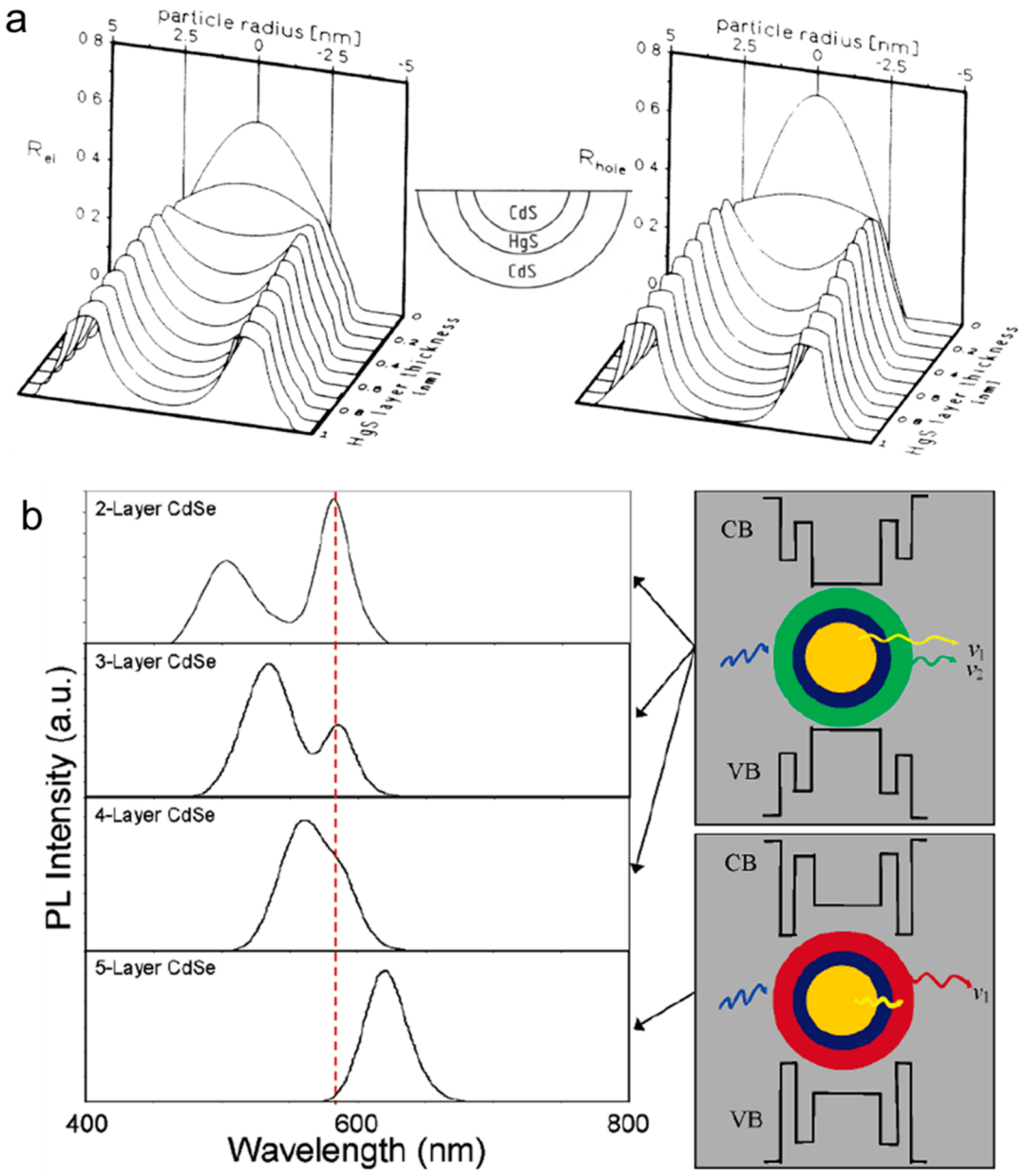

Figure 10. (a) Radial wave functions of electrons (left) and holes (right) for CdS/HgS/CdS core/shell/shell "quantum well quantum dots" with a 4.7 nm CdS core, 0.9 nm outer CdS shell, and variable HgS intermediate shell thickness. Adapted with permission from ref 222. Copyright 1994 American Physical Society. Inset adapted with permission from ref 175. Copyright 1994 American Chemical Society. (b) Evolution of the PL spectrum of CdSe/ZnS/CdSe "dual quantum systems" (left) as the outer CdSe shell gets progressively thicker (in monolayers of CdSe), showing stationary core emission and red-shifting shell emission. As shown at the right, at a critical thickness, the shell band gap becomes lower than that of the outer core, and efficient energy transfer from the core to the shell results in observation of only shell-based emission. Adapted with permission from ref 190. Copyright 2005 American Chemical Society.

Figure 11 depicts how the major spectral characteristics of typical type-II QDs evolve with growth of an increasingly thick shell. In ZnTe/ZnSe, as the ZnSe shell gets thicker, the primary absorption feature diminishes, and the spectrum begins to "tail" increasingly to the red, due to a small contribution from the spatially indirect transition (Figure 11a). The PL from this feature (Figure 11b) also moves to lower energies and can remain strong in well-passivated QDs (or if a second shell is applied, as in CdTe/CdSe/ZnS[224] or CdSe/CdTe/ZnSe[234] QDs). Similar trends are observed in the spectra of CdTe/CdSe QDs in Figure 11c, and in Figure 11d we see the accompanying pronounced lengthening of PL lifetime.

It is worth noting that, in many cases, high-quality type-II nanostructures can be synthesized out of many of the material pairs in either order, *i.e.*, starting with a core of either material. Often there are reasons for preferring one configuration over the other, beyond just ease of synthesis, depending on what is required for a given use. For instance, in the context of light emission applications, the range of PL energies achievable in CdS/ZnSe[230] QDs lies further to the red than those of ZnSe/CdS QDs,[231] while, for QD-sensitized solar cells[235] or as a photocatalyst,[236] CdTe/CdSe would be preferable to CdSe/CdTe because, in the former, the excited electron is localized in the shell, making extraction potentially faster. The order of core

DOI: 10.1021/acs.chemrev.6b00169
Chem. Rev. 2016, 116, 10513−10622

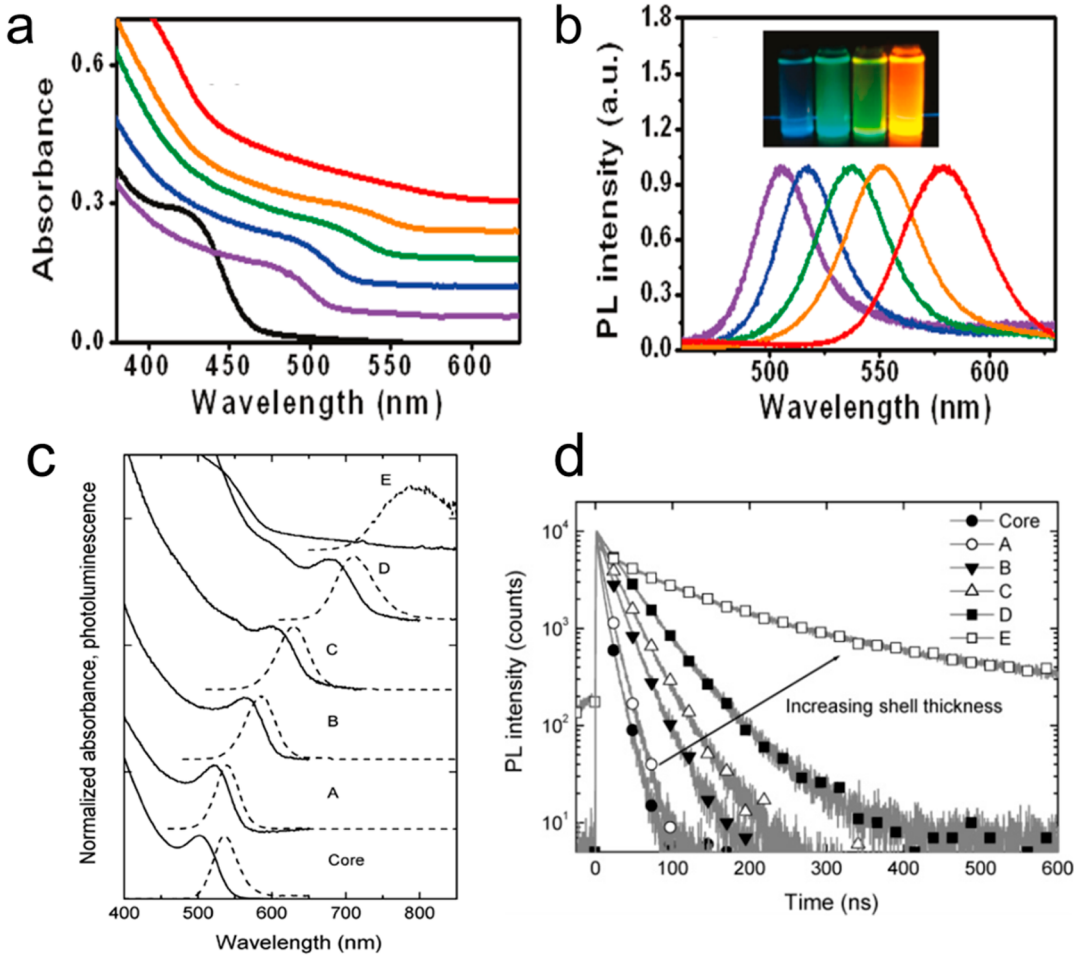

Figure 11. (a) Absorption and (b) PL spectra of ZnTe/ZnSe QDs that have 2.2 nm radius cores and shells ranging from 0 (black) to 5 (red) monolayers thick. Inset: various ZnTe/ZnSe QD samples under UV illumination. Adapted with permission from ref 232. Copyright 2010 American Chemical Society. (c) Absorption (solid) and QD (dashed) spectra of colloidal CdTe/CdSe QDs with a 2.6 nm CdTe core and CdSe shell thickness ranging from 0 to 1.6 nm; spectra labeled "E" are of branched "multipods". (d) PL decay traces of the samples shown in (c), demonstrating the increased lifetime typically observed in type-II QDs. Adapted with permission from ref 223. Copyright 2007 American Chemical Society.

and shell materials is particularly important in multishell heterostructures. As mentioned previously, a second shell of high-bandgap material can provide inorganic passivation;[224,234] alternatively a second shell can be used to increase the degree of separation between carriers, such as in CdSe/CdTe/ZnTe QDs featuring what is referred to as "cascade band edges" (Figure 12a).[237] A progressive staggering of both the conduction and valence band positions pulls excited holes in these heterostructures all the way into the outer ZnTe shell, while electrons remain largely in the CdSe core; the result is emission well into the infrared (Figure 12b) with extremely long radiative lifetimes claimed to be ∼10 ms.

3.4.3. *quasi*-Type-II. In between carrier co-localization (type-I) and complete carrier separation (type-II) is the situation in which one carrier is localized within a single material, but the other is delocalized across multiple materials. This requires that the material pair for a core/shell heterostructure have either conduction bands or valence bands similar in energy. This condition is met for relatively few bulk material pairs, but among the few known nanocrystal examples[180,209,238,239] are a couple that are particularly widely studied. The organometallic synthesis of CdSe/CdS core/shell heterostructures[179,180] was developed only a short time after those of CdSe/ZnSe[178] and CdSe/ZnS.[22] Although they exhibit very high emission QYs similar to those of type-I heterostructures, it was recognized that the absorption and emission spectral features shift to lower energies during shell growth (Figure 13a), which was attributed to substantial delocalization of the electron into the shell (Figure 13b).

A second prominent quasi-type-II nanocrystal is the PbSe/CdSe QD. As in the case of CdSe/CdS, the formation of a CdSe shell on PbSe results in increased QYs, much as with type-I QDs. Moreover, the very large difference in band gap (bulk difference of ∼1.5 eV) further leads to the expectation of a nested arrangement of band positions. The tell-tale signature of carrier delocalization in the shell seen in CdSe/CdS (red-shifted spectral features), however, is not evident in the PbSe/CdSe system due to the cation-exchange synthesis[209] used to create it: the formation of the shell comes at the expense of the core material, leading to a very strong spectral blue-shift masking any effects of delocalization. Time-resolved spectroscopy also does not provide a strong indication of delocalization: the typical PL lifetime of PbSe/CdSe nanostructures is ∼1 μs, which is not notably different than that observed for high-quality PbSe QDs (see Section 7.2). Instead, chemical proof was used. It was noted that PL efficiency varied widely during the growth of an additional shell on the PbSe/CdSe to make PbSe/CdSe/ZnS QDs, implying that at least one of the carriers was delocalized into the CdSe shell enough to be sensitive to surface trap

DOI: 10.1021/acs.chemrev.6b00169
Chem. Rev. 2016, 116, 10513−10622

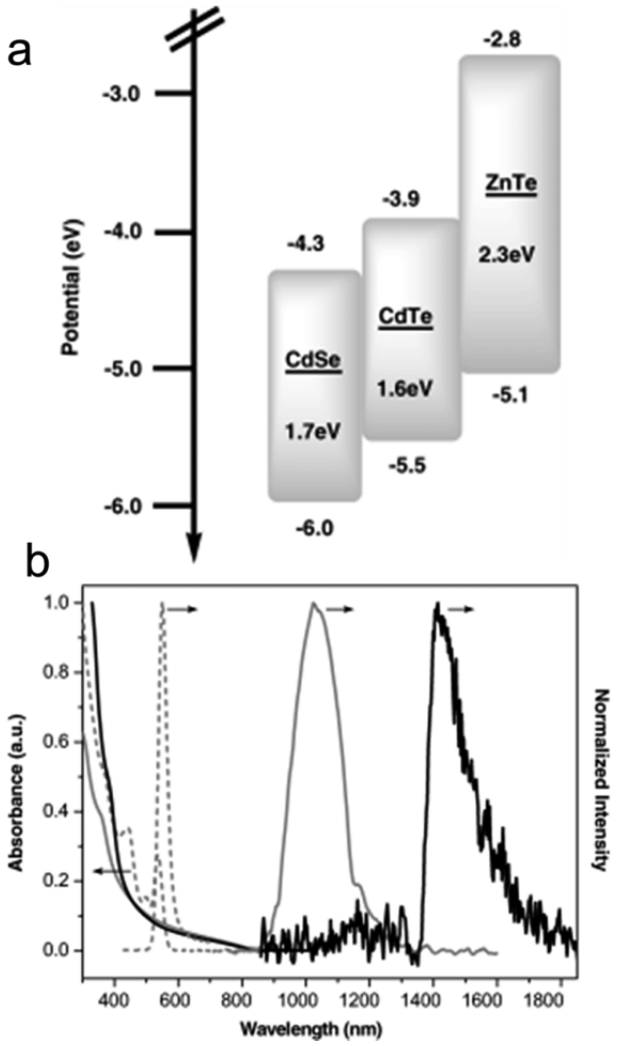

Figure 12. (a) "Cascaded" bulk band alignments within CdSe/CdTe/ZnTe core/shell/shell QDs. (b) Normalized absorption and emission spectra of 3.4 nm CdSe core QDs without shell (dashed gray line), with 1.8 nm CdTe shell (solid gray line), and with 1.8 nm CdTe shell plus 1.3 nm ZnTe outer shell (black), showing extreme emission red-shifting. Adapted with permission from ref 237. Copyright 2005 Wiley-VCH.

states.[209,214] On the other hand, growth of a shell of CdS onto the PbSe/CdSe QD led to lengthening of radiative lifetime by nearly 2 orders of magnitude (Figure 13c).[214] Since we know from the preceding paragraph that electrons (and not holes) delocalize in a CdSe/CdS heterostructure, it follows that electrons must also be delocalized across PbSe/CdSe heterostructures as well. In a less circumstantial approach, it was later shown that while hole-scavenging thiols do not quench the PL of PbSe/CdSe QDs, electron acceptors do, again showing that the electron reaches the surface, as supported by simple effective mass modeling of the carrier wave functions (Figure 13d).[238]

3.4.4. Tuning Carrier Localization via Quantum Confinement. The strong and sometimes even dominant role of quantum confinement in determining the energies of electronic states in each component of a heterostructured nanocrystal gives rise to tuning possibilities that are not available in bulk heterojunctions. Specifically, the carrier localization regime adopted by a given material combination can change with the size of each domain. An illustration of this can be seen in the ZnSe/CdSe heterostructure during shell growth (Figure 14).[25,240] At early stages, a very thin shell (<1 nm) of CdSe possesses a band gap substantially wider than the ZnSe core due to strong quantum confinement. Therefore, despite a nominally inverted type-I bulk alignment, both electrons and holes remain confined to the ZnSe core, as in a standard type-I heterostructure (Figure 14a, left).[25] As a result, the absorption spectrum of thin-shell ZnSe/CdSe QDs shows a band-edge excitonic feature (Figure 14b, lavender)[240] consistent with absorption dominated by the ZnSe core. When the shell is thick (>1.6 nm), the band gap of CdSe becomes much narrower than that of the ZnSe core, and both carriers are localized in the shell, as in an inverted type-I configuration (Figure 14a, right). Again, the absorption spectrum presents a clear excitonic feature (Figure 14b, red), but it is much lower in energy, as it is attributable now to the CdSe shell. In a very specific intermediate shell thickness range (1.1−1.5 nm) the carrier localization exhibits features typical of the type-II regime, i.e., the absorption spectrum lacks a well pronounced band-edge excitonic feature, showing instead the typical tailing toward low energies (Figure 14b, green). Within this regime, the electron is substantially delocalized into the shell while the hole remains in the core (Figure 14a, middle). For such QDs, a two-band effective mass model has been used to analyze the spatial distribution of the density functions of the respective carrier ground states. The evolution of those distributions for a 1.5 nm radius ZnSe core-based heterostructure as the shell gets thicker is depicted in Figure 14c; a detailed look at the differential distributions of the hole and electron wave functions in the intermediate thickness regime (outlined in green) is shown to the right of the panel.[24]

As mentioned in Section 3.4.2, the localization regime experienced by excited carriers within a heterostructured QD affects their spectroscopically observable behavior in many ways, including in some that can be attributed to a modification of the strength and nature of carrier−carrier interactions. An example is a consideration of the Coulombic contributions to the energy of multiexciton states within a heterostructure. In general, in type-I heterostructures, the interaction between two excitons is attractive, *i.e.*, the system energy of a biexciton state is lower than the sum of energies of two noninteracting excitons. On the other hand, in type-II systems, the contribution of Coulomb forces between like carriers can cause the interaction of two excitons to be repulsive (*i.e.*, higher in energy).[225,226] Such effects and their importance to the problem of QD lasing are discussed in Section 5.4. Because of examples like this, the assignment of localization regime can be more than a mere semantic concern, especially for systems like those of the preceding paragraph which may display a transition between regimes based on size parameters. In response to this concern, in a theoretical examination of generalized core/shell heterostructures, Piryatinski et al. proposed a so-called "energy criterion" to distinguish different regimes based on identifying the preferred localization of each carrier individually, which can then be combined to determine the overall localization regime.[226]

To demonstrate this method, we can first consider the case of a heterostructure that, based solely on bulk energy levels, possesses a type-II alignment wherein the core material conduction and valence bands are both lower in energy than those of the shell material (Figure 15a). The energy criterion can then be applied to determine the localization of either carrier for an arbitrary combination of core radius, R, and shell thickness, H, within the quantum-confined size regime. By this formalism, an electron will be primarily localized in the core if its lowest-energy level is located below the conduction band offset presented by the core/

DOI: 10.1021/acs.chemrev.6b00169
Chem. Rev. 2016, 116, 10513−10622

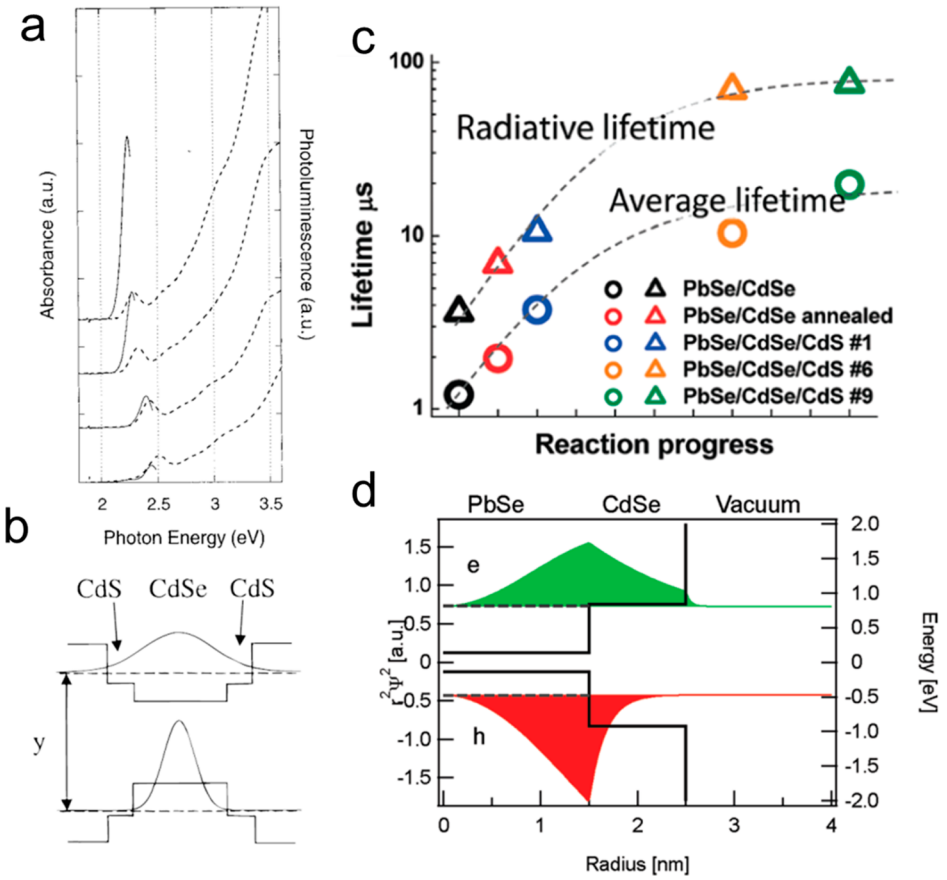

Figure 13. (a) Absorption (dashed) and PL (solid) spectra of a series of CdSe/CdS *quasi*-type-II QDs with 2.3 nm diameter core and shell thickness ranging from 0 (bottom) to 2.1 (top) monolayers. Both absorption and emission spectra red-shift with increasing shell thickness. (b) Electron and hole wave functions computed via an effective mass approximation for CdSe/CdS QDs featuring a 3.4 nm diameter core and 0.9 nm thick shell, superimposed on a representation of the core and shell band potentials according to a particle-in-a-box model. In similarity to the calculation shown in Figure 7c, the electron is substantially delocalized into the shell. Adapted with permission from ref 180. Copyright 1997 American Chemical Society. (c) The evolution of average excited-state and radiative lifetimes for PbSe/CdSe/CdS core/shell/shell QDs as the CdS outer shell gets progressively thicker. The striking lengthening of lifetimes is consistent with delocalization of excited electrons throughout the entire nanostructure, which become increasingly separated from the core-localized holes. Adapted with permission from ref 214. Copyright 2010 American Chemical Society. (d) Electron (green) and hole (red) for PbSe/CdSe QDs (core radius 1.5 nm and shell thickness 1 nm) according to a simple effective mass model, showing delocalization across the entire heterostructure. Adapted with permission from ref 238. Copyright 2011 American Chemical Society.

shell interface (denoted U_0^e in Figure 15a); otherwise, it is delocalized across both core and shell. In a similar way, the hole localization can be determined by the corresponding relationship between the lowest-energy hole level relative to the valence band offset (U_0^h). Taken together, the independently established localizations can then be used to define the overall localization regime, whether type-II, *quasi*-type-II, or type-I. The same formalism can be applied to the reverse situation (*i.e.*, when the conduction and valence bands of the core material are higher than those of the shell material; Figure 15b). Figure 15c shows how, in response to quantum confinement-induced changes in core energy states, localization regime depends on R and H for a hypothetical heterostructured QD with the alignment depicted in Figure 15a, with $U_0^e = U_0^h = 0.5$ eV, and other material parameters chosen to resemble those of typical II–VI semiconductors.[226]

3.5. The Core/Shell Interface: Strain and Alloying

Along with alignment of band positions, another important consideration in determining the optical properties of a heterostructured nanocrystal is lattice matching. As in planar thin films, strain from epitaxial contact between two materials with significantly different lattice constants can have a strong effect on the electronic structure of both materials, and consequently on the entire heterostructure. In core/shell colloidal nanocrystals, highly curved surfaces further complicate the prediction of the effects of lattice mismatching, but some trends have been noted. Interestingly, the prototypical stable and brightly emissive type-I QD, CdSe/ZnS, is a combination of materials with a substantial lattice mismatch (12%).[22] As a result, the maximum QD emission QY is reached at a relatively thin shell thickness (typically a little more than a monolayer); above this point, the accumulating strain leads to defects that serve as trap states, reducing PL efficiency. The mismatch problem is one of the reasons why especially thick-shell QDs, such as the so-called "giant QDs", employ CdS shells, with only 6% lattice mismatch,[181] instead of ZnS shells.

As described above, CdS is not necessarily a perfect replacement for ZnS for overcoating CdSe for every application, as it has a *quasi*-type-II alignment instead of a type-I. Another method for mitigating the strain problem in CdSe/ZnS heterostructures borrows a page from thin film systems by inserting an additional layer of intermediate lattice parameter to mitigate the strain; here, using a layer of either CdS or ZnSe are obvious starting points. In a direct comparison,[189] it was found

DOI: 10.1021/acs.chemrev.6b00169
Chem. Rev. 2016, 116, 10513–10622

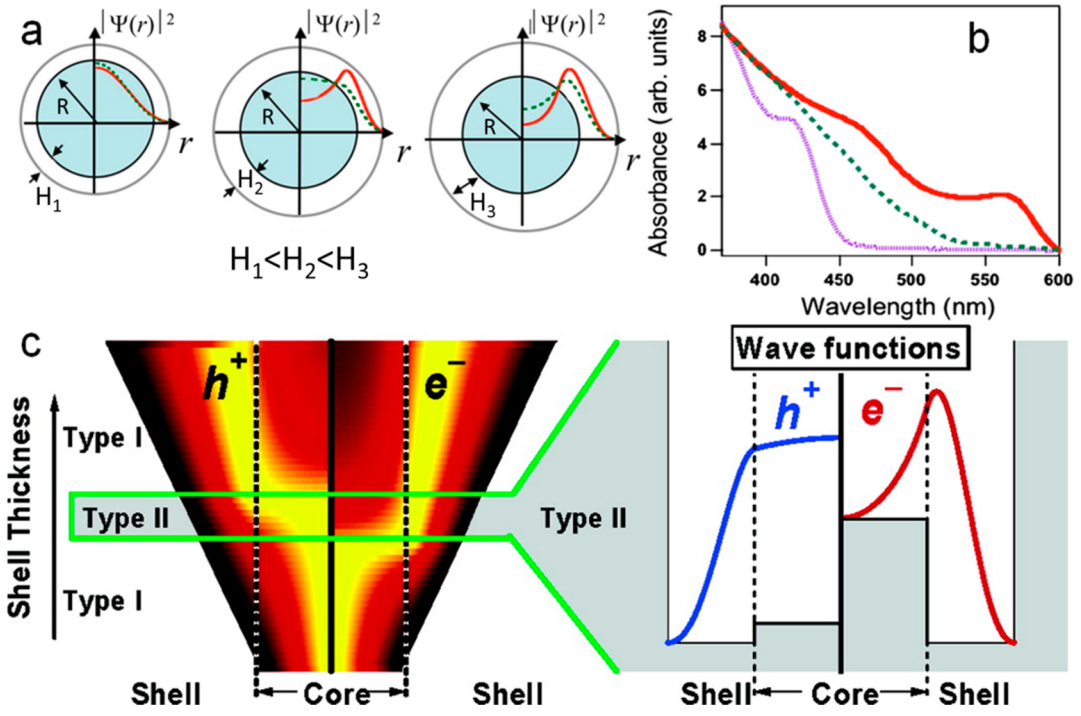

Figure 14. (a) Evolution of carrier localization in ZnSe/CdSe QDs with a 1.5 nm radius core as band-edge state positions of the shell shift in response to changes in quantum confinement, according to an effective mass model. When the shell is thin (0.5 nm, left), both electron (red) and hole (green) wave functions are colocalized in the core (type-I). At intermediate shell thickness (1.3 nm, middle) the electron is preferentially drawn into the shell while the hole remains core-localized (type-II). Finally, for thick shells (1.9 nm, right), the hole joins the electron in the shell, resulting in an inverted type-I localization regime. (b) Absorption spectra for samples corresponding to the type-I (lavender), type-II (green), and inverted type-I (red) localization regimes depicted in (a). Adapted with permission from ref 240. Copyright 2006 American Chemical Society. (c) False-color plot demonstrating how the radial distributions of the electron (right) and the hole (left) density functions change with shell thickness (vertical axis) for the same system. Highlighted is the regime of intermediate shell thickness in which type-II localization is observed. Adapted with permission from ref 24. Copyright 2004 American Chemical Society.

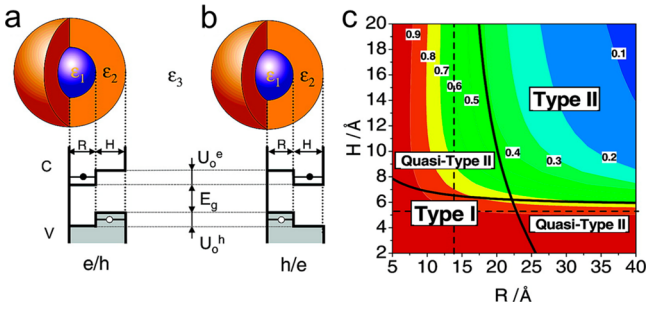

Figure 15. (a) Depiction of the key parameters for a hypothetical type-II heterostructured QD with core-localized electrons and shell-localized holes (e/h), including the core radius (R), shell thickness (H), and conduction and valence band offsets (U_0^e and U_0^h, respectively). (b) Same for the case of core-localized holes and shell localized electrons (h/e). (c) Localization phase diagram, showing how the carrier localization regime evolves with R and H for the system depicted in (a) where $U_0^e = U_0^h = 0.5$ eV. The color contours indicate regions of structural parameter space producing the same calculated electron-hole overlap integral (small numbers). Adapted with permission from ref 226. Copyright 2007 American Chemical Society.

that both CdSe/CdS/ZnS and CdSe/ZnSe/ZnS QDs offered better overall emission QYs, better rentention of emission efficiency for thicker shells, and consequently better photostability than CdSe/ZnS; moreover, perhaps because it is closer to the midpoint of the lattice constant between CdSe and ZnS, the QDs featuring a ZnSe layer performed 5−10% better than those with CdS (~80% QY).[189] A study published at nearly the same time, in this case reporting CdSe/CdS/$Zn_{0.5}Cd_{0.5}$S/ZnS core/shell/shell/shell QDs, described very similar ultimate QYs,[192] demonstrating that there is perhaps a complexity "point-of-diminishing-returns" after which adding more shells with finer compositional grading no longer produces any obvious benefit in PL efficiency. Nevertheless, this concept of enhancing PL efficiency by mediating lattice mismatch using an intervening layer has found general use in heterostructured QDs. It has been shown to be effective in enhancing the emission of the type-II CdS/ZnSe QDs, in which a very thin intermediate layer of CdSe results in PL QYs up to 50%.[230] Strain relief has proven especially important for heterostructures that combine both III−V and II−VI materials, such as $InAs_xP_{1-x}$/InP/ZnSe,[193] InAs/CdSe/ZnSe,[191] and InP/GaP/ZnS.[241]

While intentional inclusion of a strain-relieving layer has been proven effective, other studies have found similar benefits from incidental alloying that can happen simply by prolonged heating of a heterostructure during or immediately after growth. After shell growth at 190 °C, heating CdSe/ZnSe QDs to 300 °C causes alloying between the layers that leads to a more than 50% relative increase in emission QY.[242] Likewise, inward diffusion of Zn ions into the core during the high-temperature synthesis of $Cd_{1-x}Zn_xS$/ZnS QDs also boosts emission QY to up to 80%.[243] The benefits of heat-induced alloying have been found to extend to other properties of QDs as well: the long heating times involved in the SILAR preparation of thick-shell CdSe/CdS QDs[219,244] result in alloying (Figure 16a) between the core and shell that has a large effect on fluorescence intermittency and

DOI: 10.1021/acs.chemrev.6b00169
Chem. Rev. 2016, 116, 10513−10622

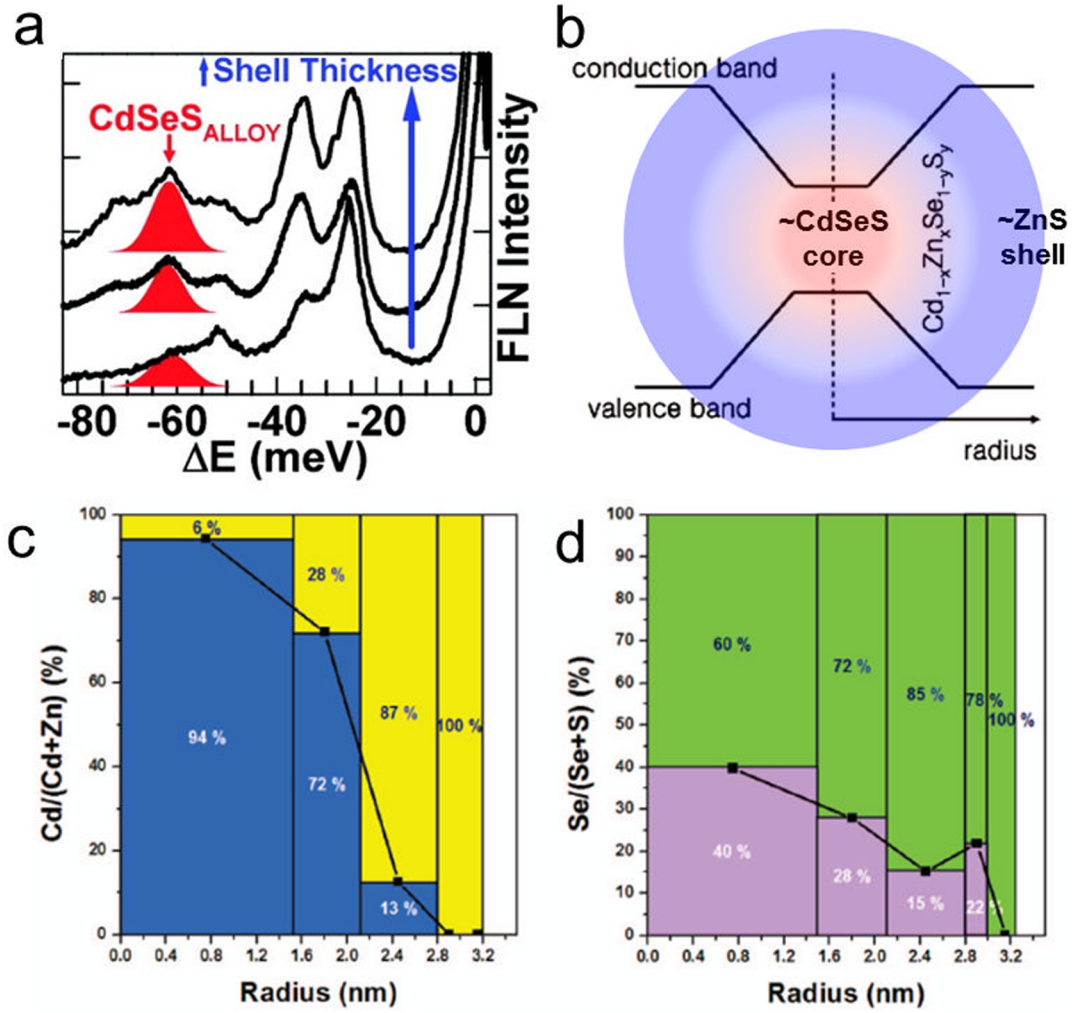

Figure 16. (a) A distinct CdSeS alloy-related longitudinal optical (LO) phonon replica at ~60 meV to the red of the zero-phonon line appears in the fluorescence line-narrowing spectra of thick-shell CdSe/CdS QDs, growing in intensity as the shell gets thicker. This is consistent with spontaneous alloying between the core and shell as a result of the prolonged heating required for SILAR growth. Adapted with permission from ref 218. Copyright 2011 American Chemical Society. (b) Cartoon depiction of the idealized band diagram for a CdZnSeS graded alloy QD synthesized by single-pot reaction of metal and chalcogen precursors chosen for their differential reactivities. (c) and (d) show the experimentally determined radial cation (cadmium in blue; zinc in yellow) and anion (selenium in lavender; sulfur in green), respectively, atomic distributions for the graded alloy CdZnSeS QDs. Adapted with permission from ref 194. Copyright 2008 American Chemical Society.

multiexciton processes (see Sections 4.3−4.4 and 5.3 for details).[218]

An important aspect of heating-based alloying is that rather than creating a single layer of a fixed composition, as is typical in intentional strain-relief layers, it creates a chemically (and therefore lattice constant) graded region. As a finely and constantly changing composition is anticipated to offer the most comprehensive suppression of defects caused by lattice-mismatch, there have been a number of efforts to intentionally create such gradients during synthesis. A common approach is to use a mixture of precursors of varying reactivity, for instance, a single-injection of a fast-reacting selenium precursor and a slow-reacting sulfur precursor into excess cadmium can be used to produce a CdSe/CdS gradient core/shell QD with 85% PL QY.[166] A similar method was used to create a graded ZnSeS shell on InP QDs to create InP/ZnSeS QDs with over 50% emission QYs.[246] In an interesting extreme example of this technique, a single mixture of cadmium, zinc, selenium and sulfur were reacted at high temperatures, and based on the natural differences in reactivity, a fully graded CdZnSeS composite QD was formed spontaneously (Figure 16b-d), with high emission QYs at wavelengths tunable by controlling the stoichiometry.[194]

Finally, while focusing on strain's relationship to emission QY in cores/shell heterostructures has led to marked progress in reproducible synthesis of efficient QD fluorophores, some reports have shown that intentionally strained nanocrystals can produce unusual effects that further demonstrate how different nanoscale systems can be from bulk or thin-film heterojunctions. Slow growth of ZnSe[247] or ZnS[248] onto CdTe results in a core/shell interface between materials for which the lattice mismatch is 14% and 19%, respectively. In both cases, the structures retain high PL QYs, but despite firmly type-I bulk band alignments, shell growth causes significant red-shifting in spectral features (Figure 17a). This is caused by a strain-induced transition to type-II band alignment: strain on the CdTe core increases its band gap, while, near the interface, the ZnSe (or ZnS) experiences a slight decrease in band gap. Because the effect is stronger on the conduction bands, a crossover is induced in

DOI: 10.1021/acs.chemrev.6b00169
Chem. Rev. 2016, 116, 10513−10622

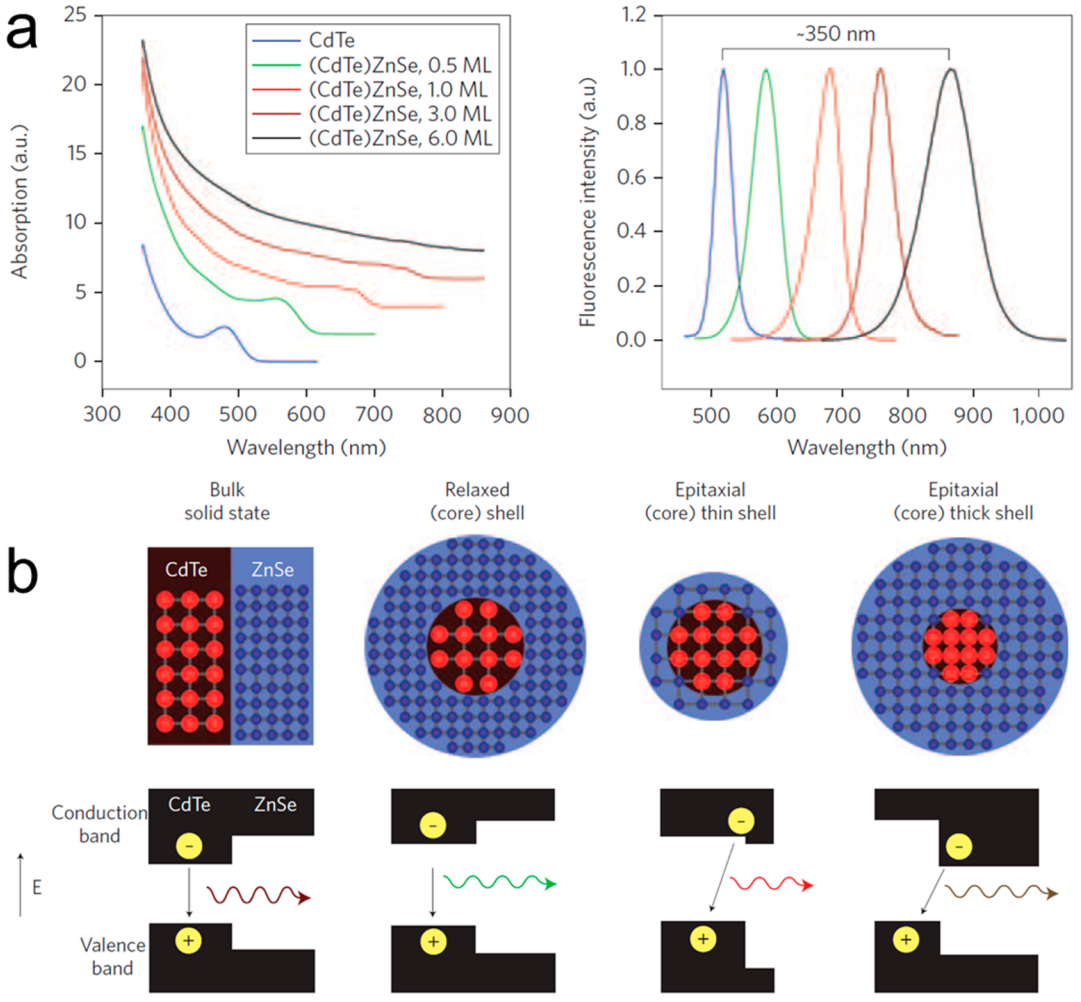

Figure 17. (a) Evolution of absorption (left) and fluorescence (right) spectra of CdTe/ZnSe QDs with 1.8 nm CdTe cores and increasing ZnSe shell thickness (in monolayers). The pronounced red-shift of spectral features suggests type-II carrier localization. (b) Depiction of band alignment changes in CdTe/ZnSe QDs of varying shell thickness induced by lattice strain. From a consideration of either the strain-free bulk (far left) or quantum-confined (second from left) junctions, a type-I alignment is predicted. However, for a small (<4 nm diameter) CdTe core, both thin and thick ZnSe shells create considerable strain. Calculations using the model-solid theory and a continuum elasticity model predict that this should shift both the conduction (primarily) and valence band positions to produce a type-II alignment consistent with the spectra in (a). Adapted with permission from ref 247. Copyright 2009 Nature Publishing Group.

which the electron delocalizes into the shell, resulting in a type-II heterostructure (Figure 17b).

3.6. Summary and Outlook

Considered as a whole, the potential offered even only by the relatively straightforward chemical methods examined in this section is extremely rich. The examples provided above are a mere sample of the massive realm of possibilities for both profound and nuanced modification of the optical and electronic properties of nanomaterials afforded by control over their structure at the level of single atoms. A suggestion of the extent of this field can be arrived at simply by considering the multiplicative effect of material choice and various well-established types of complexity. The *CRC Handbook of Chemistry and Physics*, for instance, lists the properties of more than 100 basic multinary semiconductors;[249] though the methods will necessarily vary drastically, most of these materials are (or likely can be rendered) amenable to colloidal synthesis at some level of quality. Various subsets of these materials will be intercompatible enough to allow the construction of heterostructures containing 2, 3, or even more components, conservatively allowing 1000s of combinations, and potentially orders of magnitude more. Each of these combinations can, in turn, yield a wide range of exact geometries that offer strikingly different properties depending upon the ordering and relative size of material domains; when one then adds in control over alloying, crystalline polytypism, and variations to the exact structures of interfaces, quickly it becomes apparent that even within a fixed combination of materials, the number of spectroscopically distinguishable heterostructures likely grows by additional orders of magnitude. Finally, one could apply additional types of complexity that are too expansive to be adequately covered here (such as shape control[26,27,250−252] and impurity doping[253,254]), and, further, allow the heterostructures themselves to be used as building blocks along with, *e.g.*, metal, dielectric and other semiconductor nanoparticles to arrive at larger yet still discrete hybrid nanoconstructions with truly diverse functionalities.[255,256] At this point, the idea of enumerating such entities becomes, to say the least, impractical.

As the above exercise demonstrates, the full scale of opportunities for chemically fabricated nanostructures is truly vast. In the sections that follow, we will examine how the ever-

DOI: 10.1021/acs.chemrev.6b00169
Chem. Rev. 2016, 116, 10513−10622

expanding toolbox provided by advanced colloidal synthesis has been put to use to push the frontiers of our understanding of basic and exotic physical phenomena in nanoscale semiconductors (Sections 4 and 7), as well as to optimize and exploit such phenomena in an array of technological applications (Sections 5, 6, and 8). Necessarily, the included examples constitute only a selection out of a much larger field of opportunity; there are many other current directions for QD exploration, and many more are waiting to be thoroughly considered or even fully articulated. In our view, the ultimate extent of this field is limited only by the motivation, creativity, patience, and (to some extent) luck of nanoscientists around the world.

4. AUGER RECOMBINATION AND PL INTERMITTENCY IN INDIVIDUAL QDS

4.1. Scaling of Auger Recombination Rates with QD Occupancy

As discussed in Section 2.5, the recombination dynamics of single excitons in well-passivated QDs are dominated by intrinsic radiative recombination. The situation dramatically changes in the case when one or more extra carriers are introduced into the nanocrystal, which opens a new nonradiative pathway associated with Auger recombination. In this process, the recombination energy of the e-h pair is not converted into radiation, but instead is used to excite a third charge carrier (an electron or a hole) into a higher energy level.[34] In bulk semiconductors, as a result of the demands of simultaneous conservation of both energy and translational momentum (summed over all three carriers), Auger recombination is a temperature-activated process whose rate can be expressed as $r_A \propto \exp(-\gamma_A E_g/k_B T)$, where γ_A is a constant dependent on the electronic structure of a particular semiconductor.[257] Based on this expression, the rate of Auger decay quickly decreases with increasing band gap. As a result, Auger recombination is considerably less efficient in bulk wide-gap (*e.g.*, CdSe and CdS) compared to narrow-gap (*e.g.*, PbSe and PbS) materials. This expression also predicts that the rate of Auger recombination decreases with decreasing temperature, and tends to zero in the zero-T limit. This can be understood by considering two electrons and a hole within a model two-band semiconductor with parabolic valence and conduction bands (Figure 18a). At $T = 0$, all three carriers have zero kinetic energy, and hence are characterized by zero translational momentum. In such a case, the total initial translational momentum of the electronic system is also zero. In the course of Auger decay, the energy released during the e-h pair recombination event is transferred to the extra electron. But since this carrier transits to a higher-lying energy level by following a parabolic dispersion curve, it gains a net momentum and the system as a whole violates the law of translational momentum conservation. Thus, such a process cannot occur and the corresponding rate is zero.

However, in QDs influenced by the effect of strong spatial confinement, the translational momentum conservation is relaxed, being replaced by less stringent angular momentum conservation.[258−260] In addition, the forced proximity among particles contained within the nanometer-sized QD boundary significantly increases the magnitude of Coulomb coupling among the charge carriers, which is further enhanced by reduced dielectric screening resulting from significant penetration of electric-field lines into the matrix/solvent medium normally characterized by a lower dielectric constant than the QD itself. All of these factors make Auger recombination exceptionally strong

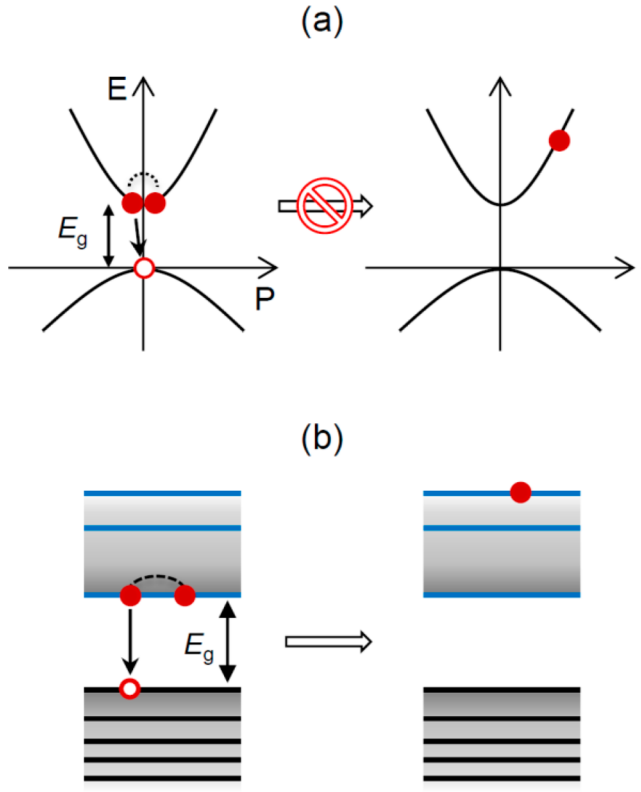

Figure 18. (a) In a bulk semiconductor, at $T = 0$ when the kinetic energies of all three charge carriers are zero, Auger recombination is not possible, as it violates translational momentum conservation. (b) In QDs, translational momentum conservation is relaxed, resulting in efficient Auger recombination even at $T = 0$.

in QDs (Figure 18b), which becomes one of the determining factors in the dynamics of their multicarrier states. Depending on the QD size and the exciton multiplicity, the characteristic times of multicarrier Auger recombination vary from a few to a few hundreds of picoseconds,[258] which is orders of magnitude shorter compared to radiative lifetimes,[33] resulting in very low PL efficiencies of multicarrier states. It is well-known that PL quenching by Auger recombination complicates a range of QD-based applications that require high emissivity of multicarrier states in QDs, including QD lasers[261,262] (Section 5) and QD LEDs[50,263] (Section 6).

The simplest form of multicarrier states in a QD is a charged exciton composed of one exciton plus an extra electron or hole, which is referred to as a negative (X^-) or a positive (X^+) trion, respectively (Figure 19a,b). Taking into account all possible recombination pathways, the radiative decay rate of a QD state which comprises N_e electrons and N_h holes [the (N_e, N_h) state] can be calculated from $k_r(N_e,N_h) = N_e N_h k_{r,1X}$, where $k_{r,1X}$ is the single-exciton radiative decay rate.[264,265] On the basis of this scaling, often called "statistical", the radiative rate of a charged exciton is twice as high as that of a single exciton, *i.e.*, $k_{r,X^+} = k_{r,X^-} = 2k_{r,1X}$. Accordingly, the emission efficiency of charged excitons should be greater than or equal to that of a single exciton if there is no additional nonradiative loss in a charged exciton state. However, charged excitons can also decay via nonradiative Auger recombination where the exciton recombination energy is transferred to an electron for X^- or a hole for X^+. In fact, nonradiative Auger decay rates of charged excitons outpace their radiative decay rates by orders of magnitude, resulting in

DOI: 10.1021/acs.chemrev.6b00169
Chem. Rev. 2016, 116, 10513−10622

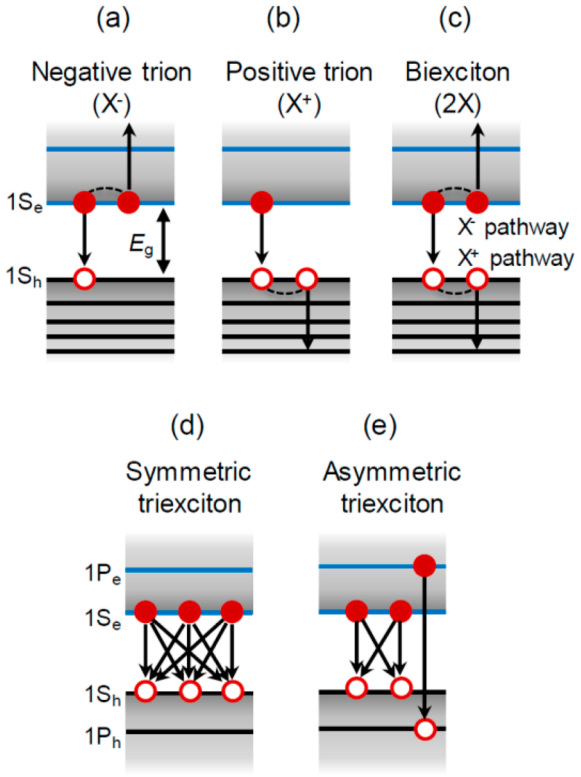

Figure 19. Auger recombination of (a) a negative trion (X^-), (b) a positive trion (X^+), and (c) a biexciton (2X). The energy released during e-h recombination is transferred to an electron for X^- or to a hole for X^+. In the case of biexciton Auger recombination, the energy of the e-h pair can be transferred to either an electron (X^- pathway) or a hole (X^+ pathway). Possible recombination pathways of (d) a symmetric triexciton, in which all charge carriers reside in the 1S conduction- or valence-band state, and (e) an asymmetric triexciton realized in QDs with 2-fold degenerate 1S levels when the third carrier resides the 1P state.

extremely low emission QYs of charged excitons (only a few percent relative to the single-exciton PL QY).

In a similar way, the nonradiative Auger process is also the dominant recombination mechanism of a biexciton, which is a neutral state consisting of two e-h pairs. Although, according to statistical scaling, the radiative decay rate of a biexciton ($k_{r,2X}$) is four times faster than that of a single exciton (*i.e.*, $k_{r,2X} = 4k_{r,1X}$), the PL QY of biexcitons in QDs is extremely poor (even smaller than that of a charged exciton), again due to nonradiative Auger recombination. Auger decay of a biexciton can occur via one of the two independent pathways wherein either an electron or a hole is excited within the same band in the course of e-h pair recombination. These two decay channels are commonly referred to as the negative and positive trion pathways, respectively (Figure 19c). Correspondingly, the biexciton Auger recombination rate ($k_{A,2X}$) can be expressed as twice the sum of Auger decay rates of X^- (k_{A,X^-}) and X^+ (k_{A,X^+}), *i.e.*, $k_{A,2X} = 2(k_{A,X^-} + k_{A,X^+})$.[259,266] Based on this relation, in QDs with mirror symmetric conduction and valence bands, where the Auger decay rates of X^- and X^+ are the same, the biexciton Auger decay rate is four times that of the trion: $k_{A,2X} = 4k_{A,X^-} = 4k_{A,X^+}$. The experimental validation of the direct correspondence between the biexciton Auger decay rate and those of trions has been conducted for QDs with both mirror-symmetric (PbSe[267]) and strongly asymmetric (CdSe[266]) band structures.

Auger decay rates of multiexciton states are expected to progressively increase with the number of charge carriers in a QD due to the increase in both the number of recombination pathways (given by N_eN_h) and pathways whereby the e-h recombination energy is transferred to the third carrier [given by $(N_e + N_h - 2)$]. If all recombination and energy-transfer pathways have identical rates (Figure 19d), the Auger decay rate of the (N_e,N_h) states can presented as $k_A(N_e,N_h) = (1/8)N_eN_h(N_e + N_h - 2)k_{A,2X}$, where $k_{A,2X}$ is the biexciton Auger decay rate.[268] As in the case of radiative recombination of multicarrier states, this scaling of Auger lifetimes is often referred to as "statistical." When applied to a neutral N-exciton state ($N \geq 2$), it yields $k_{A,NX} = (1/4)N^2(N - 1)k_{A,2X}$. We can see that the Auger recombination rate of a triexciton is 4.5 times faster than that of a biexciton, and $k_{A,NX}$ increases very rapidly with N, approximately proportional to the cube of N for large N. On the other hand, according to statistical scaling the radiative decay rate of multiexcitons increases quadratically with N and is given by $k_{r,NX} = N^2k_{r,1X}$. Assuming that nonradiative loss of multiexcitons is determined primarily by Auger recombination and the single-exciton PL QY is equal to one, the PL QY of the N-exciton state (Q_N) can be calculated as $Q_N = 4(k_{r,1X}/k_{A,2X})/(N - 1)$, showing a gradual diminishing of Q_N with exciton multiplicity due to strong Auger recombination.

Despite its simple underlying assumptions, the statistical argument serves as a good approximation for the scaling of both radiative and nonradiative multicarrier dynamics and has been frequently used to describe the experimental observations, especially when investigating the pump intensity dependence of PL.[266−268] For example, statistical scaling was able to explain multiexciton processes in PbSe QDs that can accommodate up to 8 electrons in the band-edge levels; the overall 8-fold degeneracy of the band-edge states originates from the existence of the 4 equivalent band minima at the L-points of the Brillouin zone and the 2-fold spin degeneracy.[269] Based on pump intensity dependence of PL dynamics in PbSe QDs, the ratio of radiative decay rates between the biexciton (or the triexciton) and the single exciton was found to be close to 4 (or 9),[264] as expected from the statistical scaling. The ratio of Auger decay rates between the biexciton and the triexciton in PbSe QDs with a radius of 4 nm was measured to be ~4, which also agrees reasonably well with a value of 4.5 predicted by statistical scaling.[268]

In the case of a 2-fold degeneracy of the 1S band-edge level, the scaling of Auger rates needs to be modified, as for states with $N >$ 2 the electron and the hole of the third exciton (and other additional excitons) should be in the 1P state (Figure 19e). In this case, assuming that no S−P interband transitions are allowed, the ratio of Auger decay rates between a triexciton and a biexciton is estimated to be 2.5.[268] This explains the observations for CdSe QDs for which the experimental values of the $k_{A,3X}/k_{A,2X}$ ratio (~2.3−3.4)[34,268] are lower than those expected based on purely statistical scaling.

4.2. Universal Volume Scaling of Auger Lifetimes

As discussed above, Auger recombination is a fairly inefficient process in bulk semiconductors (especially in wide-gap materials) but it becomes increasingly efficient as the dimensions of a semiconductor structure become reduced such that electronic states develop atomic-like QD features. Consequently, the Auger lifetimes are expected to vary with QD size, although it is difficult to predict the exact size-dependence of the Auger decay rate based on theoretical considerations alone. However,

DOI: 10.1021/acs.chemrev.6b00169
Chem. Rev. 2016, 116, 10513−10622

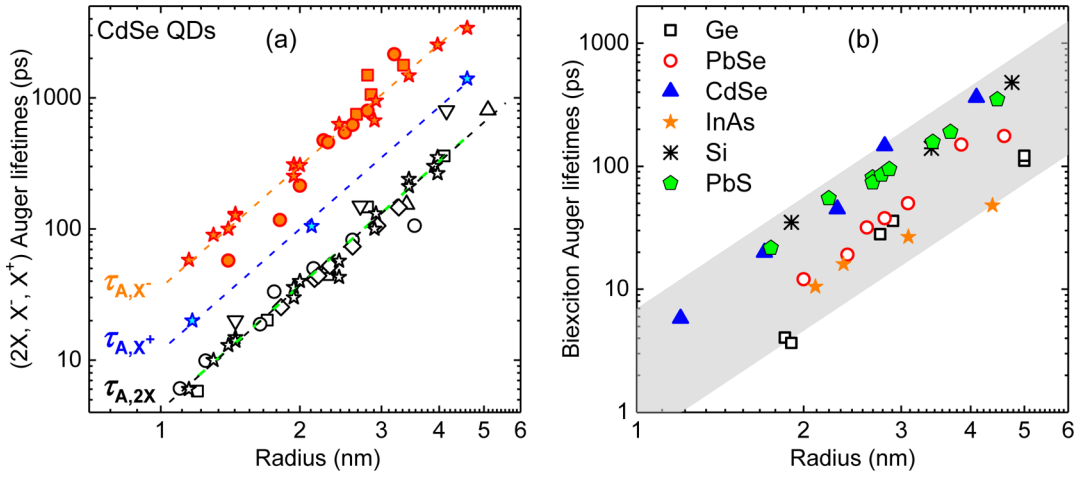

Figure 20. (a) QD size dependence of Auger lifetimes of biexcitons (black open symbols), negative trions (orange solid symbols), and positive trions (blue symbols). Biexciton Auger lifetimes are from refs 34 (squares), 272 (circles), 35 (up-triangles), 36 (diamonds), 268 (down-triangles), and 273 (stars). Auger lifetimes of negative trions are from refs 270 (squares), 271 (circles), and 273 (stars). Auger lifetimes of positive trions are from ref 273. Fits to the experimental data are shown by dashed lines of orange (X^-) and blue (X^+) and black (2X) colors. (b) Size dependence of biexciton Auger lifetimes for QDs of different compositions: Ge (black open squares), PbSe (red open circles), CdSe (blue solid triangles), InAs (orange solid stars), Si (black "snow flakes"), and PbS (green solid pentagons).

starting from the first systematic QD-size-dependent study of Auger recombination,[34] there have been numerous spectroscopic investigations of this process that in combination reveal a universal trend of linear scaling of Auger lifetimes with nanostructure volume. This trend, known as a "volume scaling," is illustrated in Figure 20a, where we display a broad collection of data for Auger lifetimes of the negative (orange) and positive (blue) trions and the biexcitons (black) measured for CdSe QDs as a function of QD radius. Along with previously reported experimental data,[34−36,268,270,271] in this figure, we also plot a new data set (denoted by stars) over a wide range of QD radii from $R \sim 1$ nm to over 5 nm that were obtained from recent transient absorption (TA) measurements.

For biexcitons, the size dependence of Auger lifetimes can be described as scaling with the cube of the QD radius.[34,274] The newer data[273] (black stars) also follows this trend, closely overlapping with the previous results through all QD sizes. Indeed, the linear fit (dashed black line) to all data sets plotted in a log−log representation yields the dependence $\tau_{A,2X} = 1/k_{A,2X} \propto R^m$ with $m = 3.13 \pm 0.1$. The "volume scaling" seems to be a very robust trend which is observed not only for CdSe QDs but also for nanocrystals of other materials with widely varying bulk band gap energies and electronic structures. Figure 20b displays biexciton Auger lifetimes observed for a wide range of QDs, including direct- (CdSe, InAs, PbSe, PbS) and indirect- (Ge, Si) gap QDs.[274,275] We can see that despite a vast difference in intrinsic physical properties among the QDs, and their bulk Auger constants, the biexciton Auger lifetimes are similar for the same size nanocrystals and they all increase as the cube of R, hence, volume scaling.[274] This indicates that the key parameter defining Auger decay rates in QD materials is the QD size rather than the energy gap or specific band structure of a parental bulk semiconductor.

A similar linear scaling of Auger lifetimes with QD volume is also observed for charged excitons (Figure 20a). The measurements of charged exciton dynamics are not as extensive as those of biexcitons, which is mostly due to experimental difficulties in the control of the degree of charging. In previous studies, extra charges were introduced into single QDs or QD ensembles via electrochemical injection,[270,276] chemical treatment with reducing species,[267] or a photochemical reaction.[271] Latter approaches produce preferentially negatively charged QDs, which are suitable for spectroscopic studies of negative trions. In Figure 20a, Auger lifetimes of negative trions in CdSe QDs from refs 270 (orange solid squares) and 271 (orange solid circles) are displayed along with a newer set of data (orange solid stars) from pump-intensity-dependent TA dynamics.[273] Apart from a minor discrepancy that occurs for small-size QDs (radius <2 nm), the overall size-dependent trend of Auger lifetimes of negative trions from all of the measurements is again consistent with direct volume scaling. Specifically, the X^- Auger lifetimes closely follow the dependence $\tau_{A,X^-} = 1/k_{A,X^-} \propto R^m$ with $m = 3.20 \pm 0.1$. While displaying similar scaling with R, the Auger lifetimes of negative trions are significantly longer (by a factor of *ca.* 10) than those of biexcitons when compared for the same QD size.

In Figure 20a, we also present a new data set of Auger lifetimes for the positive trions (blue stars) obtained from ensemble TA measurements.[273] The X^+ data points are located roughly in the middle between those for negative trions and biexcitons, and also follow a volume scaling: $\tau_{A,X^+} = 1/k_{A,X^+} \propto R^m$ with $m = 3.11 \pm 0.2$. As was discussed earlier, for QDs with mirror symmetric conduction and valence bands, the Auger lifetimes of negative and positive trions are expected to be identical and equal to four times of the biexciton lifetime.[267] However, based on the data in Figure 20a, in CdSe QDs, the lifetimes of negative trions are much longer than those of positive trions. This disparity is likely attributable to a considerable difference in the spectral density of valence- and conduction-band states in II−VI materials. The existence of multiple valence subbands along with a large hole mass results in a quasi-continuum character of the hole energy spectrum, while the electron energy spectrum derived from a single conduction band with a small effective mass is sparse. As a result, it is easier to meet the energy conservation requirement during the Auger process accompanied by excitation of a hole (X^+ decay channel) compared to that involving excitation of an electron (X^- decay channel).

It should be noted that, even with the disparity between Auger lifetimes of negative and positive trions, the biexciton Auger lifetimes can still be described by a superposition of independent (that is, uncorrelated) negative- and positive-trion pathways; that

DOI: 10.1021/acs.chemrev.6b00169
Chem. Rev. 2016, 116, 10513−10622

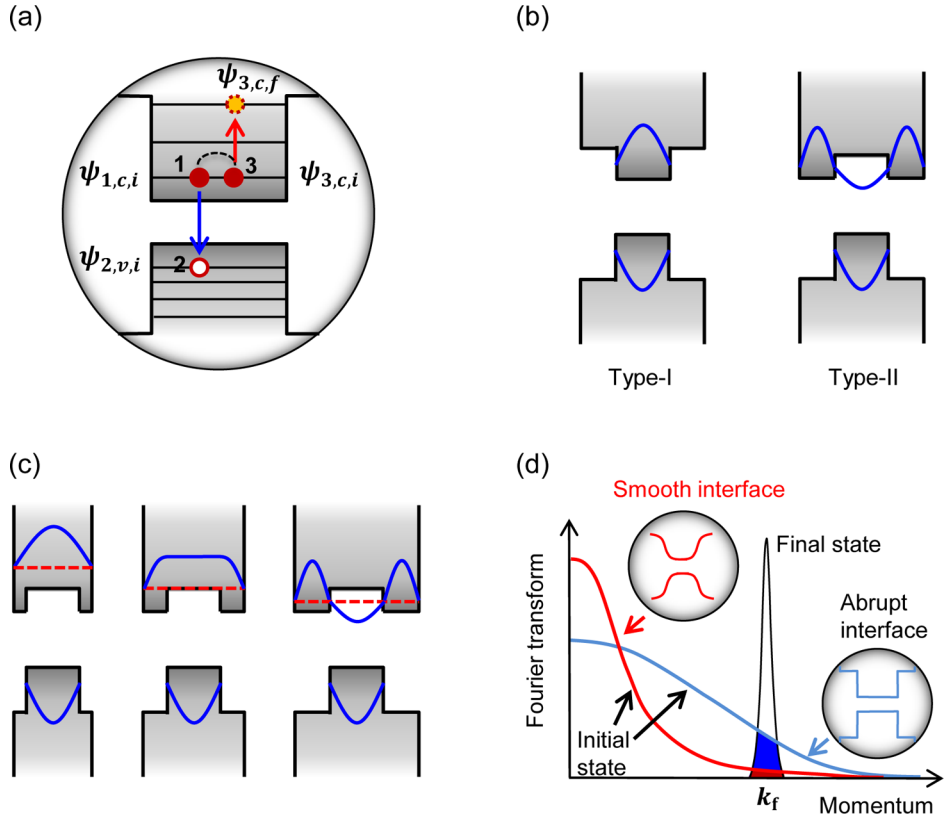

Figure 21. (a) Auger recombination of two electrons and a hole involves an interband transition (e-h recombination) and an intraband transition (electron excitation to a higher energy state within the conduction band). (b) Schematics of band diagrams of Type-I and Type-II structures. (c) Illustration of control of conduction and valence band mixing using a core/shell QD with a type-II heterointerface. For a certain shell thickness (middle diagram), the energy level of an electron is lined up with the bottom of the conduction band of the core material, which corresponds to the situation when the electron wave vector in the core is zero and hence the term describing the mixing between the conduction and the valence band is also zero. Adapted with permission from ref 280. Copyright 2014 American Chemical Society. (d) A qualitative representation of the Fourier transforms of the final (gray shading) and initial (ground-state) wave functions involved in Auger recombination for the case of the abrupt (blue line) vs smooth (red line) confinement potentials. The wave function overlap for the initial and the final states is reduced in the case of the smooth-confinement potential.

is, $\tau_{A,2X}$ can be related to τ_{A,X^-} and τ_{A,X^+} by $1/\tau_{A,2X} = 2(1/\tau_{A,X^-} + 1/\tau_{A,X^+})$. Indeed, the size dependence expected for the biexciton lifetime obtained from this expression and the fits to the measured X^- and X^+ lifetimes describes well the measurements for $\tau_{A,2X}$ (green solid line in Figure 20a). The validity of representing biexciton decay in terms of two independent X^- and X^+ channels was also confirmed by single-dot studies of CdSe/CdS core/shell QDs,[266] in which lifetimes of negative and positive trions were obtained from the analysis of the PL lifetime and PL intensity trajectories.

4.3. Auger Decay Engineering

As we have seen, Auger recombination dominates the dynamical behavior of multicarrier states in QDs, which we will see is a major complication for lasers (Section 5) and LEDs (Section 6). We will also examine the role this process plays in QD PL intermittency, where it can be responsible for the low emissivity of the "OFF" state, in detail in Section 4.4. In light of the drawbacks Auger recombination presents for a broad range of applications, approaches for its suppression (and even complete elimination) are the goal of vigorous theoretical and experimental efforts.

The volume scaling of Auger lifetimes of multicarrier states suggests that Auger decay rates can be controlled by changing particle dimensions. Indeed, as illustrated in Figure 20, biexciton and trion Auger lifetimes increase linearly with the QD volume. However, even in large dots, they are still considerably shorter (especially, in the case of biexcitons) compared to corresponding radiative lifetimes. Furthermore, even though allowing for reduction of Auger rates, the increase in the QD size also leads to a simultaneous decrease in the band gap, which diminishes the ability for controlling, *e.g.*, the emission wavelength. This highlights the need for approaches that would allow one to decouple (at least partially) the control of Auger decay rates from the control of the emission wavelength. The strategies for such control, often described as "Auger decay engineering", explore different methods for modifying the matrix element of Auger recombination while still maintaining a considerable degree of spatial confinement.

To understand the physics underlying the control of Auger recombination, we can recall that this process involves two transitions (Figure 21a): one interband, responsible for e-h recombination, and the other intraband, whereby the third carrier (an electron in Figure 21a) is promoted to a higher-energy state. Correspondingly, the rate of Auger decay depends on two overlap integrals, one involving the initial conduction- ($\Psi_{1,c,i}$) and valence- ($\Psi_{2,v,i}$) band states ($\langle\Psi_{1,c,i}|\Psi_{2,v,i}\rangle$; see Figure 21a for notations) and the other the initial and final states of the third carrier, which captures the energy released in the course of Auger decay ($\langle\Psi_{3,c,i}|\Psi_{3,c,f}\rangle$; Figure 21a). The first of these integrals can be modified by modifying the spatial overlap between either the envelope[225] or the Bloch[66] components of the wave function, while the second can be manipulated by tuning the envelope

DOI: 10.1021/acs.chemrev.6b00169
Chem. Rev. 2016, 116, 10513−10622

wave functions, since the Bloch function is usually assumed to stay unchanged during the intraband transition. Below, we provide literature examples of all three approaches to "Auger decay engineering".

4.3.1. Control of the Overlap of Electron and Hole Envelope Wave Functions. A common approach to reducing the spatial overlap between the electron and hole envelope wave functions utilizes heterostructured nanocrystals with type-II or quasi-type-II localization regimes in Figure 21b (see Section 3). Previously, it was explored, for example, using type-II core/shell CdTe/CdSe[23,223−225] and CdS/ZnSe[230] QDs (discussed earlier in Section 3.4.2), in which the electron and the hole are confined to different regions (the shell and the core) of the nanostructure. Large spatial separation between the electron and the hole in these QDs leads to a considerable lengthening of both the single-exciton lifetime and the biexciton Auger lifetime that in the case of CdTe/CdSe QDs, for example, reach ∼150 ns and ∼2 ns, respectively, when the shell becomes ∼2.3 nm thick.[225]

Reduction in the spatial overlap between the electron and hole envelope wave functions can also be obtained with quasi-type-II thick-shell CdSe/CdS QDs[86,219,244] and CdSe/CdS dot-in-rod nanostructures[277−279] (Section 3.4.3). In both cases, the hole is confined within the CdSe core (the core−shell valence-band offset is ∼0.3 eV), while, because of a small (<100 meV) band offset in the conduction band, the electron is delocalized over the entire nanostructure. For CdSe/CdS QDs, it was observed that, as the shell thickness increases, the resulting reduction of the e-h overlap leads to a significant lengthening of lifetimes of both the biexciton (up to ∼350 ps) and the negative trion (up to ∼5 ns), indicating a suppression of Auger recombination.[86]

4.3.2. Control of Conduction- and Valence-Band Mixing. An interesting approach to suppressing Auger decay by manipulating the overlap integral between the Bloch components of the conduction- and valence-band wave functions was proposed by Guyot-Sionnest and co-workers.[280] The idea behind this approach is derived from the $k\cdot p$ method used to describe interband mixing within the effective mass approximation. Without mixing, the conduction- and the valence-band Bloch functions are orthogonal, and hence, their overlap integral is zero, which implies that the matrix element of the Auger transition is also zero.

Normally, however, interband-mixing is nonzero, which leads to a nonzero probability of the Auger transition. In the effective mass approximation, the interband interaction is described by the term $H_{int} = (\boldsymbol{k}\cdot\boldsymbol{p})/m_0$, where $\boldsymbol{p}$ is the momentum operator, $\boldsymbol{k}$ is the Bloch function wave vector, and m_0 is the free electron mass. As was discussed in Section 2, in QDs, k is quantized ($k = k_i$; i denotes the set of quantum numbers specific for a given electronic state), and the energies of quantized states (E_i) are proportional to k_i^2, *i.e.*, $E_i \propto k_i^2$. If for a certain state, $E_i = 0$, when k_i is also zero, it is implied that the interband interaction described by H_{int} is removed.

To realize the situation when the band-mixing is reduced or even completely eliminated, ref 280 proposed to use type-II core/shell CdTe/CdSe QDs in which the bands are aligned in such a way as to favor separation of an electron and a hole between the shell and the core, respectively, for a sufficiently large shell thickness (Figure 21c). Further, by selecting a certain value of shell thickness, it is possible to produce a regime wherein the lowest level of the electron in the CdSe shell is lined up with the bottom of the conduction band of the CdTe core (diagram in the middle of Figure 21c). This produces the desired situation when the energy of the electron in the core region is zero, which eliminates the contribution from a core-localized valence-band state to the electron wave function, and thus leads to the zero value of the overlap integral between the electron and hole band-edge states. This should lead to complete suppression of Auger decay for this specific arrangement of electronic states.

The authors of ref 280 did report on the observation of a considerable lengthening of the negative trion Auger lifetime for one specific shell thickness, which seemed to indicate the achievement of suppression of Auger recombination. However, the puzzling result of these studies was a nonmonotonous size dependence of the X^- lifetime, which was observed simultaneously with a monotonous size dependence of the biexciton lifetime, which exhibits a typical volume scaling (Section 4.2). This observation was surprising, as the $k\cdot p$ calculations also predicted a nonmonotonous size dependence for the X^+ lifetime. Together with the theoretical predictions for the negative trions, this should have resulted in the nonmonotonous size dependence for the biexcitons. To explain the discrepancy between the measurements and the calculations, the authors of ref 280 invoked hole−hole correlations, without, however, specifying their nature. Thus, while being very interesting, the idea of Auger decay control via the manipulation of the interband mixing still requires additional experimental validation.

4.3.3. Control of the Strength of the Intraband Transition. One more interesting approach to suppressing Auger recombination was proposed in the theoretical work by Cragg and Efros,[245] and later re-examined by Climente et al.[281] These studies indicated that, in addition to the QD size, the shape of the confinement potential also has a significant effect on the rate of Auger decay. As was discussed earlier, apart from the strength of the e-h interband transition, the rate of Auger decay also depends on the strength of the intraband transition wherein the third carrier (assumed to be an electron in Figure 21a) is excited to a higher-energy state. Due to its large energy ($\sim E_g$), this state is characterized by a quickly oscillating wave function, which corresponds to a Fourier transform narrowly distributed around a specific k-vector of a large value (k_f in Figure 21d). The Fourier transform of the ground-state wave function, on the other hand, is centered around $k = 0$, and its spread in the wave-vector space depends on the shape of the confinement potential, as determined by the structure of the QD itself. For example, in the case of the square-shaped "abrupt" potential, it extends to large values of k, while the spread is reduced in the case of a smooth (*e.g.*, parabolic) profile (Figure 21d). As a result, the overlap between the initial and the final states involved in the intraband transition is smaller in the case of a more gradual change in the confinement potential.

The considerable effect of the shape of the confinement potential on the rate of Auger decay was confirmed by several recent experimental studies of core/shell CdSe/CdS QDs, wherein interfacial alloying (intentional or unintentional) can lead to grading (smoothing) of the confinement potential. In ref 282, single-dot measurements of the pump-intensity dependence of the PL signal and the second-order intensity correlation function, $g^{(2)}$, in thick-shell "giant" CdSe/CdS QDs were used to evaluate the PL QY of biexcitons and, thus, the degree of suppression of the nonradiative Auger recombination; stronger suppression of Auger decay was expected to lead to higher biexciton emission efficiencies. In pulsed measurements, the low-intensity limit of the ratio between the areas of the center and the side peaks of the $g^{(2)}$-function yields a direct measure of the ratio of the biexciton (Q_2) and the single-exciton (Q_1) PL QYs.[282,283] Figure 22a displays the summary of the measurements of the Q_2/

DOI: 10.1021/acs.chemrev.6b00169
Chem. Rev. 2016, 116, 10513−10622

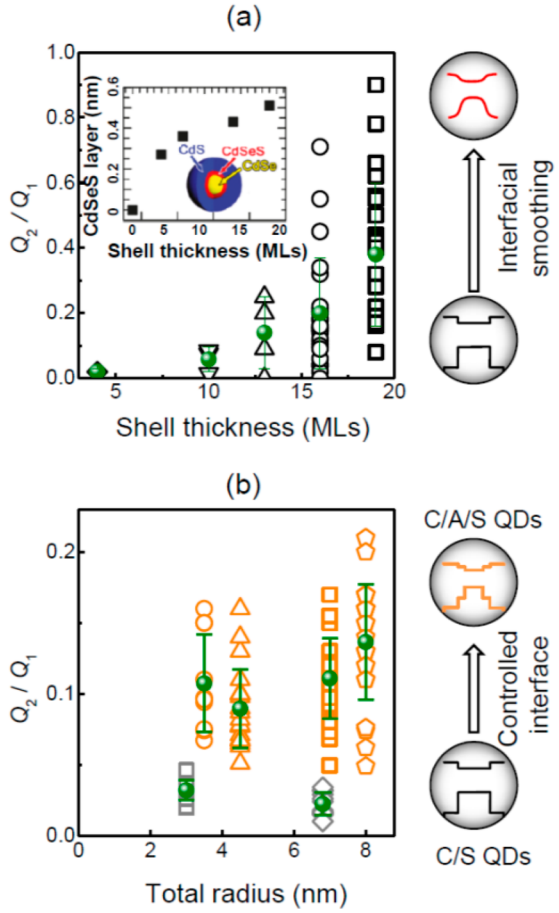

Figure 22. (a) Ratio between the biexciton and single-exciton PL QYs (Q_2/Q_1) as a function of shell thickness derived from single-dot measurements of CdSe/CdS QDs with $H = 4$ MLs (diamonds), 10 MLs (down-trianges), 13 MLs (up-triangles), 16 MLs (circles), and 19 MLs (squares). Average values of Q_2/Q_1 for dots with the same shell thickness are shown by green solid circles. Adapted with permission from ref 282. Copyright 2011 American Physical Society. The inset shows that the thickness of the alloy $CdSe_xS_{1-x}$ layer gradually increases as the shell thickness is increased. Adapted with permission from ref 218. Copyright 2011 American Chemical Society. (b) Comparison of Q_2/Q_1 for C/S (gray symbols) and C/A/S CdSe/CdS QDs (orange symbols) for various shell thicknesses. Green circles show the average values of Q_2/Q_1. Adapted with permission from ref 284. Copyright 2014 American Chemical Society.

Q_1 ratio for more than 100 individual CdSe/CdS QDs with varied shell thicknesses.[282] These data indicate that as the shell thickness is increased, the average value of Q_2/Q_1 (shown by green circles with error bars) gradually increases from ~2% in the case of the 4-monolayer (ML) shell to ~20% for the 16-ML shell, and then to ~40% for 19-ML shell. This increase can be attributed to a combination of effects that include the increased QD volume, the reduction of the e-h overlap in a *quasi*-type-II structure, and finally the increasing grading of the core−shell interface. The importance of the last factor is specifically indicated by a large distribution of the Q_2/Q_1 ratios for the dots with a nominally identical shell thickness (*e.g.*, from <10% to 90% for the thickest shells). Given a fairly tight size dipersion of the QDs indicated by TEM studies, the observed spread in the Q_2/Q_1 values cannot be explained by variations in the QD shell or core dimensions, suggesting that it results primarily from the different degree of alloying at the core/shell interface.

One might indeed expect a considerable degree of alloying for thick-shell dots studied in ref 282. These dots were synthesized via the SILAR process (discussed earlier in Section 3.5), which required elevated temperatures (~240 °C) and several days of growth. These conditions facilitate a compositional alloying between Se and S at the core−shell interface, which leads to grading of the confinement potential. Since the grading process is largely uncontrolled it likely results in large variations in the shape of the confinement potential, which translates into a spread of the Q_2/Q_1 values.[282] The formation of the alloyed layer at the core−shell interface during the SILAR growth was directly observed in low-temperature FLN measurements of giant QDs by analyzing the intensity of an LO-phonon replica associated with the mixed CdSeS phase[218] (the inset of Figure 22a).

More direct evidence of the role of interfacial alloying in suppression of Auger decay was provided by studies of refs 86 and 284 that compared two types of giant CdSe/CdS QDs: one with a sharp core−shell boundary (C/S sample), prepared by a fast shell growth method,[86,218,285] and the other with a thin $CdSe_{0.5}S_{0.5}$ alloyed layer (thickness L = 1.5 nm) incorporated between the core and the shell (C/A/S sample). Assuming that the height of the potential barrier depends linearly on the CdS fraction, the alloyed layer could be schematically described by an intermediate step in the confinement potential. Figure 22b shows the results of the $g^{(2)}$ measurements of Q_2/Q_1 for ~100 individual CdSe/CdS QDs with the alloyed (orange symbols) and the sharp (gray symbols) interface for several shell thickness.[284] In the C/S QDs, Q_2/Q_1 is lower than 0.05 regardless of the shell thickness. On the other hand, the C/A/S QDs show a substantial increase in the Q_2/Q_1 ratio (up to ~0.2), which is indicative of a considerable suppression of Auger decay. Figure 22b also shows that the CdS shell thickness has only a minor effect on the biexciton PL QY, which is in sharp contrast to the dramatic effect of the incorporation of even a thin interfacial alloy layer leading to a manifold increase in Q_2/Q_1. Significant suppression of Auger decay rates in C/A/S QDs is also indicated by independent single-dot measurements of biexciton dynamics that show a considerable extension in biexciton lifetimes upon interfacial alloying.[284]

The above examples demonstrate that even an imperfect "smoothening" of the interfacial potential with a single intermediate alloy layer still allows for appreciable suppression of Auger recombination. The benefits of this approach for practical applications of QDs have been recently tested in studies of QD-LEDs[285] and optical amplification.[261] In the case of LEDs, the use of the C/A/S QDs improved device characteristics such as the quantum efficiency and the onset of the efficiency roll-off (see Section 6). This type of structure was also used to demonstrate record-low thresholds of amplified spontaneous emission and lasing as discussed later in Section 5.3. A more complete suppression of Auger decay in core/shell QDs with an associated improvement of their device performance should be possible via a finer grading of the interfacial potential employing, *e.g.*, a continuous variation in the composition of the intermediate alloy layer.

4.4. PL Intermittency

A well-known property of individual QDs is a random fluctuation in the emission intensity, known as PL intermittency or "blinking." This process has been among the most studied research topics in the QD field both experimentally and theoretically since its discovery in 1996.[37] Fluorescence intermittency is common to nearly all nanostructures including

DOI: 10.1021/acs.chemrev.6b00169
Chem. Rev. 2016, 116, 10513−10622

single molecules,[286−290] carbon nanotubes,[291,292] semiconductor nanorods,[293,294] and even μm-long semiconductor nanowires.[295] Random switching between the high- ("ON") and low- ("OFF") emissivity states in single-dot emission is of great interest by itself, but it also represents a considerable drawback in some QD-based applications including, for example, single-photon (or photon-pair) generation that requires a stable photon stream from single QDs with no interruptions. Furthermore, it is apparent that the appearance of OFF-periods in single-dot emission is at least one of the reasons for the deviation of the PL QY of a QD ensemble from the ideal value of unity. Despite extensive investigations on PL intermittency, the physical mechanisms that are responsible for it still remain a subject of intense debates. Below we discuss some of the models proposed for explaining this phenomenon.

The first experimental observation of PL intermittency in semiconductor QDs was reported in 1996 by Nirmal et al., who studied single CdSe QDs under continuous wave (*cw*) excitation at room temperature (Figure 23a).[37] Random switching between the ON and the OFF states was found to be more frequent at higher pump intensities, resulting in longer average OFF times (the upper panel in Figure 23a). In this report, the ON-to-OFF state transition was attributed to photoionization whereby one of the photoexcited charge carriers (an electron or a hole) escapes into the surrounding medium, leaving the QD in a charged state. Subsequent photoexcitation of this QD produces a charged exciton (a trion) whose emission intensity is greatly reduced by fast nonradiative Auger recombination (Section 4.1). The OFF-state persists until the QD is neutralized (Figure 23b), and then the ON-OFF cycle is repeated again in a random fashion. This mode, relating the OFF periods to QD charging, was supported by the observation of a partial suppression of PL blinking in CdSe QDs capped with a ZnS shell manifested in the increase of the average ON time in the PL intensity trajectories (the lower panel in Figure 23a). In this case, a wider-band gap semiconductor layer likely served as a barrier inhibiting charge carrier escape from the QD, which helped maintain the charge neutrality of the QD.

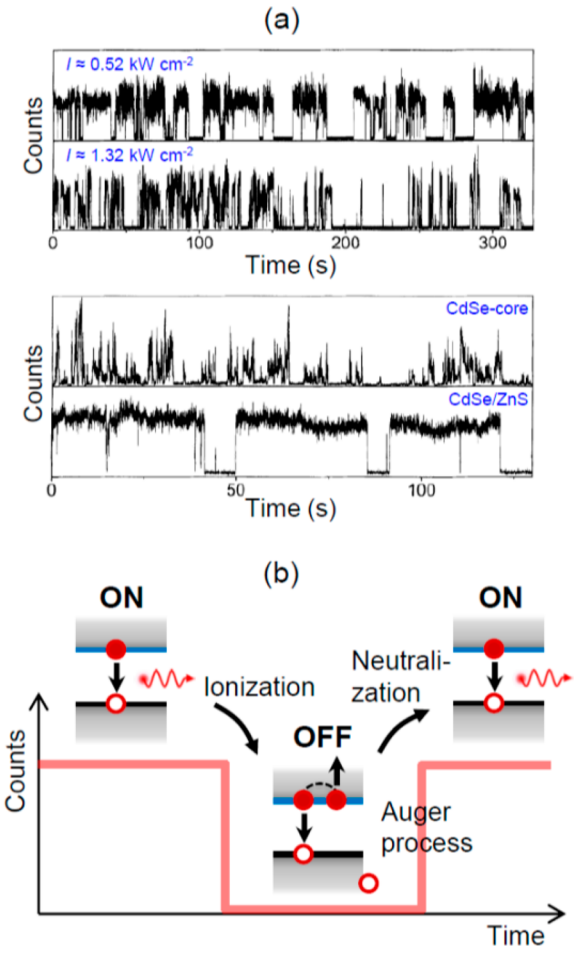

Figure 23. (a) First observation of PL intermittency ("blinking") in single CdSe QD measurements. Upper panel: PL intensity trajectories as a function of pump intensity (indicated in the figure). Lower panel: the dependence of PL blinking on QD structure. QDs with a ZnS shell show reduced blinking compared to core-only samples. Adapted with permission from ref 37. Copyright 1996 Nature Publishing Group. (b) Schematic description of the charging/discharging model of PL blinking. The ON state corresponds to a neutral exciton, and the OFF state to a charged exciton (trion). In the latter case, QD emission is quenched by fast nonradiative Auger recombination.

A theoretical background of the charging/discharging model of PL intermittency was developed by Efros and Rosen[296] who proposed that a QD can acquire a net charge as a result of either thermal or Auger-assisted ionization. In the latter process, it is assumed that even under low-intensity excitation there is a nonzero probability of a biexciton forming within a QD via sequential absorption of two photons. The biexciton decays via Auger recombination, and occasionally, the carrier which captures the energy released during e-h recombination is ejected from the QD leaving behind an uncompensated charge. Until the QD is reneutralized, the luminescence is quenched by non-radiative Auger recombination, as was originally suggested in ref 37. Numerical simulations based on the charging/discharging model successfully reproduced the random telegraph-like signals from a single QD usually detected under *cw* excitation.[296] Although the charging/discharging model has undergone several revisions to explain some specific experimental observations such as the power-law statistics of the ON/OFF times (see below), it still remains the most commonly accepted concept used in explaining PL intermittency in QDs.

4.5. Power Law Distribution of the ON and OFF Time Probabilities

4.5.1. Random Charging/Discharging. In the original charging/discharging model,[37,296] it was assumed that the ionization and reneutralization rates were given by single constants, which naturally led to the exponential distribution of the ON and OFF time probabilities. However, experimentally measured probability distributions (P) of both ON and OFF time periods usually do not follow exponential behavior, but instead exhibit an inverse power-law dependence expressed by $P(t) = t^{-\alpha}$ (Figure 24a,b).[40,297] This implies that the transition rates between the ON and the OFF states continuously change during PL blinking. The exponent $\alpha_{ON(OFF)}$ derived from single-dot measurements varies from 1 to 2 but is typically close to 1.5 and is virtually independent of QD composition.[298,299] The observed inverse power law is an extremely robust trend, especially as applied to the OFF time probabilities, and extends over a very large range of time durations that span over 5 orders of magnitude (from ∼200 μs to ∼200 s), with corresponding probability densities varied by 9 orders of magnitude.[40]

Experimental observations[297,299−301] have led to the consensus that the OFF time probability distribution is virtually insensitive to environmental conditions such as temperature,[301] identity of surrounding matrix,[302] pump intensity,[300,302] and

DOI: 10.1021/acs.chemrev.6b00169
Chem. Rev. 2016, 116, 10513−10622

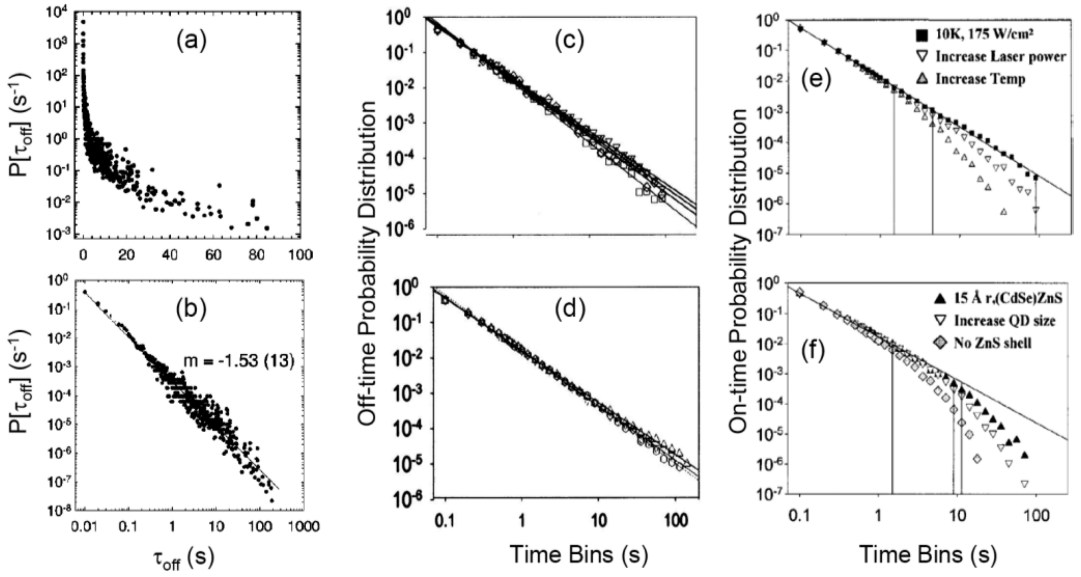

Figure 24. OFF time probability distributions are plotted using (a) a semilog and (b) a log−log representation. The data fall on a straight line (with a negative slope) in the log−log plot, indicating the inverse power law distribution of the OFF time probability. Adapted with permission from ref 40. Copyright 2000 American Institute of Physics. (c) Temperature dependence of the OFF time probability distribution observed from a 2.5 nm CdSe/ZnS QD: T = 10 K (up-triangles), 30 K (diamonds), 70 K (squares), and 300 K (down-triangles). (d) Size dependence of the OFF time probability distribution at room temperature: R = 1.5 nm (down-triangles; CdSe/ZnS QDs), R = 2.5 nm (diamonds; CdSe/ZnS QDs), and R = 2.5 nm (up-triangles; CdSe QDs). (e) Pump-intensity and temperature dependence of the ON time probability distribution for the 2.5 nm radius CdSe/ZnS QDs. Solid up-triangles, open down-triangles, and solid squares correspond, respectively, to 300 K and 175 W/cm^2, 10 K and 700 W/cm^2, and 10 K and 175 W/cm^2. (f) QD size and structure dependence of the ON time probability distribution at room temperature for pump power 100 W/cm^2: 1.5 nm radius CdSe/ZnS QD (black up-triangles), 2.5 nm radius CdSe/ZnS QD (open down-triangles), and 2.5 nm radius CdSe QD (black diamonds). Panels c−f are adapted with permission from ref 301. Copyright 2001 American Physical Society.

excitation wavelength,[303] and also to QD characteristics including QD size, composition (*e.g.*, CdSe, ZnCdSe, InP, or CdTe) or surface properties (*e.g.*, purely organic vs inorganic surface capping); see illustration in Figure 24c,d. Specifically, the fact that the OFF time probability distribution is insensitive to temperature (experimental studies covered the range from 400 K down to 10K)[297,300,301] has led to suggestions that tunneling-like mechanisms are involved in QD intermittency.

The distribution of the ON time probability also follows the inverse power law with an exponent α_{ON} of ~1.5. However, this behavior is usually limited to short ON time intervals, while, on longer time scales, the ON time probability develops an exponential cutoff, which is not observed for the OFF times (Figure 24e,f). The overall trend can be well described by a truncated power law, given by $P_{ON}(t) = t^{-\alpha_{ON}}e^{-t/t_c}$. Here, t_C is the truncation time which turns out to be sensitive to temperature,[301] pump intensity,[293,304] excitation wavelength,[303] and surface properties (Figure 24e,f). In particular, the dependence of t_C on the intensity and spectral energy of excitation implies that some photoinduced processes such as Auger photoionization[296,297] are involved in the development of the exponential cutoff in the distribution of the ON time probability.[293,304]

Based on experimental observations, several modifications have been proposed to the charging/discharging model mostly focusing on the mechanisms for ionization and reneutralization of the QD to explain the power law statistics of the ON and OFF time probabilities. Kuno et al.[297] suggested that QD quantized states are separated from external traps by a potential barrier which randomly fluctuates in its height and/or width. Because of the exponential dependence of tunneling rates on the barrier parameters, even moderate fluctuations in barrier height/width can lead to very large changes in the ON and OFF time probabilities, comparable to those observed in experiments. Another model[301,305] assumes that carrier transitions from and back to the QD occur via resonant tunneling involving a trap site outside the QD, when both the original and the final state undergo spectral diffusion in the energy domain. In yet another model, a charge carrier escapes from the QD via tunneling involving a uniform distribution of trap sites around the QD with a constant trap density.[306] In the case of the $1/r$ dependence of the carrier wave function, this model predicts the power-law distribution of the OFF times, however, leaves unexplained the distribution of the ON times. Spatial diffusion has been also considered as a reason for inverse-power-law statistics of PL blinking.[307] In this model, the ejected carrier undergoes a three-dimensional diffusion in space and returns to the QD due to Coulomb attraction. We note that all of the above models focus on details of how a charge carrier is ejected from (and returns to) a QD; however, in all of these models it is nonradiative Auger recombination that is responsible for the low emission efficiency during the OFF periods in the single-QD PL trajectories.

4.5.2. Fluctuating Nonradiative Decay. In addition to Auger quenching of QD emission in the OFF state other models have been considered for explaining low emissivity during the OFF periods. The development of these models has been at least partially motivated by some experimental observations that have been difficult to explain in terms of the traditional charging/discharging mechanism. One such observation was a very large contrast between the ON and the OFF emission levels, which seemed to be inconsistent with what was expected for emission intensities from a neutral and a singly charged exciton.[308] Another observation was the inconsistency between the

DOI: 10.1021/acs.chemrev.6b00169
Chem. Rev. 2016, 116, 10513−10622

measured OFF-state PL lifetime and the Auger lifetimes (specifically, their size dependence) expected for trions.[309]

A mechanism, alternative to Auger quenching, proposed by Franstuzov and Marcus[310] invokes a fluctuating nonradiative decay rate of a photoexcited exciton. Specifically, this model assumes that a photogenerated hole can be trapped at a deep intragap state via an Auger-assisted process whereby an electron is excited from the 1S to the 1P state, which preserves the overall energy of the system. Following relaxation back into the 1S state, the electron recombines nonradiatively with the trapped hole, which leads to the reduced emissivity of the QD without involvement of Auger recombination. In this model, the fluctuation of the PL intensity occurs due to the fluctuating 1S-1P energy spacing, which leads to a varied trapping rate, and hence, a varied PL intensity.

4.6. A- and B-Type Blinking

A wide diversity of documented PL blinking behaviors suggests the possibility of multiple mechanisms that can be responsible for this process. The single-dot spectroelectrochemical measurements of Galland et al.[276] identified at least two such mechanisms that could coexist in the same QD and could be observed in the same PL intensity/lifetime trajectory. The two distinct blinking behaviors observed in this work were termed A- and B-type blinking, and they were ascribed to a traditional charging/discharging process and hot-electron trapping, respectively.

To identify different blinking behaviors, the studies of ref 276 analyzed correlations between PL intensity and PL lifetime fluctuations. In the traditional charging/discharging model, the ON periods correspond to emission from a neutral exciton state, which decays ideally via radiative recombination. In the case of, for example, conventional CdSe QDs, the corresponding PL lifetime is ~20 ns.[33] On the other hand, during the OFF period, PL relaxation is controlled by recombination of a charged exciton (a trion).[296] As discussed earlier, in standard QDs, trion decay is dominated by fast nonradiative Auger recombination, which hence defines the OFF-state PL lifetime. Thus, during PL blinking due to charging/discharging, the fluctuation in the PL intensity should be accompanied by correlated fluctuation in the PL lifetime

A convenient way to analyze PL intensity/lifetime fluctuations involves the use of a fluorescence lifetime-intensity distribution (FLID) representation. In the example of FLID in Figure 25a,[276] the data points are distributed along a diagonal curve that has two end clusters corresponding to a neutral and a charged exciton (Figure 25a). This is exactly the behavior expected for PL intermittency due to charge fluctuations, which has been termed A-type blinking.[276]

A different type of PL blinking behavior is displayed in Figure 25b. Here, the two clusters observed in the FLID are displaced vertically, indicating a usual binary switching between the two PL intensity levels, which, however, is not accompanied by changes in the PL lifetime. This behavior, termed B-type blinking,[276] can be explained by invoking nonradiative recombination centers that can capture a "hot" electron prior to its relaxation into the emitting band-edge state. The intensity level of the OFF state in this case is determined by the ratio of the probabilities for the hot electron to either reach the emitting level or get trapped at the recombination center. In the case of B-type blinking, the PL intermittency arises from the fluctuating occupancy of hot-electron traps caused, *e.g.*, by the fluctuating Fermi level in the QD environment. Importantly, while these fluctuations lead to changes in the emission intensity they do not modify the PL

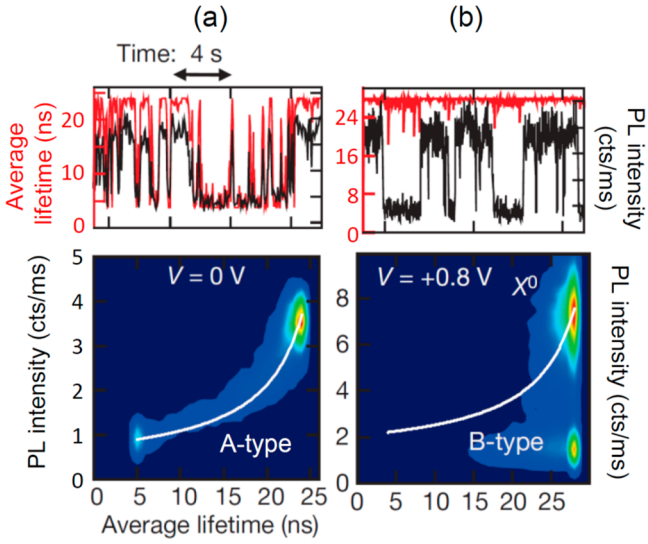

Figure 25. (a) A- and (b) B-type PL blinking observed for CdSe QDs with an intermediate thickness (7–9 MLs) of a CdS shell under electrochemical control. The A-type blinking was observed with no bias voltage (0 V), while the B-type blinking was recorded with a positive bias (+0.8 V) when the Fermi level was shifted down in energy, which resulted in "unblocking" hot-electron traps. The upper panels display single-dot trajectories of the PL intensity (black) and the PL lifetime (red). The difference between the A- and B-type blinking behaviors is visualized with a so-called fluorescence lifetime-intensity distribution representation used in the lower panels. Adapted with permission from ref 276. Copyright 2011 Nature Publishing Group.

lifetime as hot-electron trapping does not affect recombination dynamics of the band-edge states. This explains a peculiar blinking behavior when the PL intensity fluctuations are not accompanied by PL lifetime fluctuations. Strong evidence in support of this model was provided by spectroelectrochemical measurements that indicated that lowering the Fermi level, which reduced the occupancy of trap states, led to increased blinking. On the other hand, raising the Fermi level led to blinking suppression and even allowed for obtaining blinking-free PL trajectories, which corresponded to the situation when all of the hot-carrier trap centers were blocked.

4.7. Suppression of PL Blinking and Lifetime Blinking

Numerous applications would benefit from the availability of QDs with the PL quantum efficiency near the ideal value of 100%. A necessary condition for achieving this goal is the development of approaches for complete suppression of PL intermittency. Independent of a specific blinking model, the occurrence of OFF periods during PL blinking is associated with a trapping of one of the carriers at the sites located either at the surface or outside the QD. In some models, these sites serve as long-lived traps that facilitate the formation of long-lived charged QD states with resulting quenching of emission by nonradiative Auger recombination. In other models, the trapping sites serve as recombination centers that introduce recombination channels competing with radiative decay. In either case, realization of nonblinking emission can be achieved by blocking trap sites responsible for the escape of charge carriers from the QD.

One source of trapping centers is internal imperfections within the QD. However, because of the phenomenon of "self-purification," characteristic of nanoscale particles,[254] the internal defects are typically expelled toward the QD surface. Another source of defects are unpassivated dangling bonds that also reside

DOI: 10.1021/acs.chemrev.6b00169
Chem. Rev. 2016, 116, 10513–10622

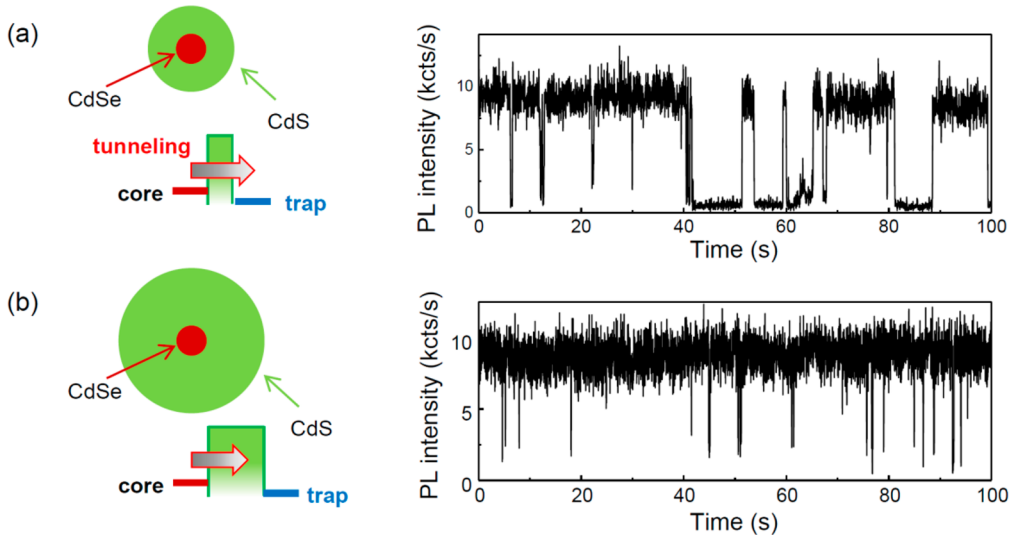

Figure 26. (a) PL blinking for a thin-shell (H = 1.0 nm) CdSe/CdS QD. (b) A nearly blinking-free PL intensity trajectory (ON time fraction >95%) of a thick-shell (H = 5.5 nm), giant CdSe/CdS QD.

on the QD surface. Thus, the problem of the elimination of PL intermittency has commonly involved by developing improved QD surface treatment procedures.

Earlier attempts to suppress PL blinking focused on direct chemical treatments of the QDs with so-called "anti-blinking" agents such as β-thioethanol[311] or thiopropionic acid,[312] or passivating the QDs with appropriate ligands such as oligo-phenylenevinylene.[313] It was demonstrated that PL blinking could be partially or even completely suppressed when these chemical species were introduced into the QD solutions or directly attached to the QD surfaces. In these examples, the "anti-blinking" additives serve as electron donors that help deactivate trap sites by filling them with electrons. While being an important research tool for unraveling the mechanisms for PL intermittency and devising approaches for its suppression, the chemical approaches are not well suited for implementation in practical devices.

An alternative approach to reducing the incidence of trapping of photogenerated charges is to physically separate them from the QD surface by introducing a barrier in the form of an especially thick shell of a wide-gap material. This idea was first realized independently by two research groups using similar nanostructures that had a CdSe core overcoated with a very thick (>10 ML) CdS shell.[219,244] These structures, often dubbed giant QDs, were discussed earlier in Section 3.5. The QDs reported by Chen et al.[244] had shells with up to 19 CdS MLs (~6.7 nm shell thickness), and more than 20% of individual QDs studied in single-dot measurements exhibited virtually nonblinking PL with the ON time fraction of greater than 99%. Mahler et al.[219] made a similar observation: more than 68% of the CdSe/CdS QDs with a 5 nm-thick-shell studied in their measurements showed essentially nonblinking emission for observation times in excess of 5 min. In Figure 26b, we show a representative example of virtually nonblinking emission (ON time fraction >95%) from a CdSe/CdS QD with the core radius r = 1.5 nm and the shell thickness H = 5.5 nm. In this trajectory the PL intensity stays nearly constant and exhibits only rare, short fluctuations toward the OFF state. Apart from producing strong suppression of PL blinking, a thick CdS shell greatly improves longtime environmental and photostability of PL properties of the QDs, making them well suited for applications as, *e.g.*, downconverting phosphors,[314−316] and active elements in LEDs[50,317−323] (Section 6) and LSCs[64,324,325] (Section 8).

In addition to improved isolation of photogenerated carriers from surface defects, another factor contributing to reduced blinking in giant QDs is a considerable suppression of Auger recombination, which is especially strong for negative trions[86,284] (see Section 4.3). Indeed, according to single-dot spectroelectrochemistry studies,[276,326] photoionization of giant QDs occurs primarily via ejection of a hole and the blinking OFF state is associated with a negative trion. In the case when Auger recombination for negative trions is significantly suppressed their emission QY become comparable to that of neutral excitons, and thus, the switching between these two states does not lead to large changes in the PL intensity. While not being pronounced in PL intensity trajectories, charge fluctuations in this case can still be resolved in PL lifetime trajectories. This phenomenon of lifetime fluctuations for a nearly constant PL intensity was observed for the first time in ref 326, where it was termed "lifetime blinking." An example of a FLID illustrating this process is displayed in Figure 27.

4.8. Summary and Impact on QD Applications

The dominance of Auger recombination in the relaxation dynamics of QDs with multiple or charged excitons is a point of strict departure from the established behavior of bulk semiconductors. As such, studies of the fundamentals of this process have been ongoing for nearly three decades, yet still constitute a rich and vigorous field of inquiry, particularly for theorists and spectroscopists. To date, extensive investigations of QDs of a wide variety of compositions, structures and shapes have advanced our understanding of the physics underlying Auger recombination tremendously. This has, in turn, allowed the larger nanocrystal research community to evolve from simply quantifying the phenomenon,[34,258,327] to actively manipulating it through nanocrystal engineering.[245,278,281,284,328] Among several established approaches for accomplishing this, engineering of the interface in heterostructured QDs to control the shape of the confinement potential seems to offer significant promise. In addition to its effectiveness, compared to suppressing Auger by changing particle shape[278,327] or volume,[274] it offers the potential for much less perturbation of other important properties of the QD, such as band gap or single-exciton PL QY. The open

DOI: 10.1021/acs.chemrev.6b00169
Chem. Rev. 2016, 116, 10513−10622

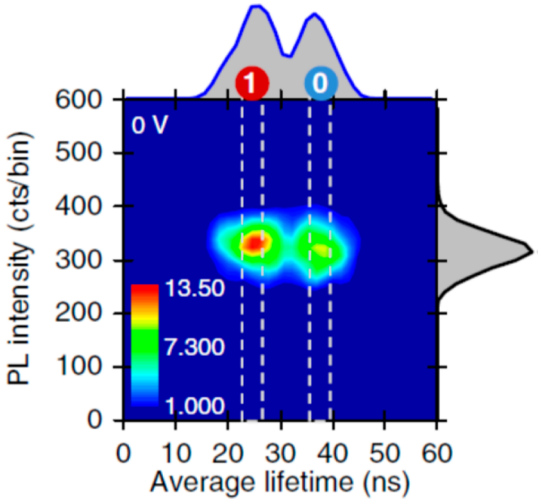

Figure 27. FLID representation of "lifetime blinking" observed for an individual giant CdSe/CdS QD with a 15-ML-thick CdS shell. A distinct feature of this blinking regime is that the PL lifetime fluctuations occur without noticeable changes in the PL intensity. Adapted with permission from ref 326. Copyright 2012 Nature Publishing Group.

question in this direction is whether the chemical control over the structure of the interface (Section 3.5) can allow one to realize the ultimate goal of complete suppression of Auger decay.

Meanwhile, the push to demonstrate manipulation of Auger recombination rates has gained heightened significance because of its increasingly recognized impact on device applications, which is a theme that will be repeated throughout the remainder of this review. The first example of this is the impact of fast Auger recombination, which dramatically reduces the lifetime of biexcitons in QDs,[34] on the ability to achieve population inversion for QD lasing (Section 5). More recently, the importance of Auger recombination on the performance of QD-LEDs (Section 6) has been increasingly recognized. In this case, the dominant factor is not the shortening of multiexciton lifetimes, but rather Auger recombination's role in rendering charged QDs dark because of the fast nonradiative relaxation of trions; charged QDs can form during QD-LED operation if electron and hole injections are not perfectly balanced. In a similar way, the presence of charged QDs due to chemical damage to QD surfaces during the fabrication of LSCs (Section 8) also reduces the efficiency of these sunlight collecting devices because of fast trion Auger recombination. Finally, while the impact of Auger recombination on the efficiency of QD solar cells operating under direct or concentrated sunlight is not fully appreciated at this time, it is well established that the inverse process of CM (Section 7) can have a substantial positive effect on their photocurrent. Interestingly, because of the relationship between Auger recombination and CM, the specific application of CM-enhanced solar cells could benefit from QDs in which the efficiencies of both of these proceses is actually enhanced, rather than suppressed.

An indirect way in which Auger recombination impacts technological applications is by its role in PL blinking (Section 4.4). This phenomenon is obviously detrimental to the use of QDs in many applications outside the scope of this review. This includes biolabeling, where it leads directly to loss of signal, and even more the use of QDs in single-photon or entangled photon-pair generation schemes that are still on the horizon. To date, studies of blinking in QDs have revealed a surprisingly complex picture, wherein blinking is not definitively associated with only a single process. Nonetheless, it has been shown that the charging of QDs, which opens the door to Auger recombination, plays a key role in at least some types of blinking. A potentially valuable advance in resolving the mystery of PL intermittency could be the concerted use of single-QD optical spectroscopy and high-resolution TEM to look for correlations between the blinking behavior and structural details of individual QDs.[329]

5. QUANTUM DOT LASING

5.1. History of Colloidal Quantum Dot Lasing

Lasers made from bulk semiconductor materials were first introduced several decades ago.[330,331] Following upon numerous advances during the early history of diode lasers, performance improved dramatically with the introduction of so-called quantum well lasers, in which charge carriers (electrons and holes) were confined within a common plane.[332] Quantum wells have a two-dimensional (2D), step-like density of electronic states that is nonzero at the band-edge, enabling a higher concentration of carriers to contribute to the band-edge emission. Consequently, it takes less intense "pumping" to get a quantum well laser to lase, which corresponds to a lower lasing threshold. Additionally, quantum well lasers show improved temperature stability, and a narrower emission line.

In QDs, the charge carriers are confined in all three dimensions, with the result that the electrons exhibit a discrete atomic-like energy spectrum. In very small QDs, the spacing between these atomic-like states is much greater than the available thermal energy, so thermal depopulation of the lowest electronic states is inhibited. This effect should result in optical gain that is temperature insensitive at an excitation level of just above one electron−hole (e-h) pair per dot on average in the case of the 2-fold degenerate band-edge states. These advantages were expected to translate into strong lasing performance superior not only to that of bulk semiconductors, but also to that of other types of low-dimensional nanostructures,[333] based on a theoretical analysis of various types of gain media (Figure 28a).

Lasing in QDs was first reported in 1991 in an optically pumped device using relatively large (approximately 10 nm) CdSe nanoparticles.[20] The QDs studied in this work were fabricated via high-temperature precipitation in molten glass.[334] These samples were incorporated into a Fabry−Pérot cavity and shown to lase at the temperature of liquid nitrogen (Figure 28b). Three years later, lasing was observed in QDs grown by epitaxial techniques using optical and then electrical pumping.[335,336] Follow-up efforts have resulted in considerable improvements in the performance of lasers based on epitaxial QDs leading to demonstrations of record-low lasing thresholds (in terms of the driving current) that surpass those of quantum well lasers.[337]

These successes provided strong motivation for the development of lasers based on strongly confined colloidal QDs with sub-10 nm diameters. In this size range, spacing between electronic levels can exceed hundreds of meV, considerably larger than the room temperature thermal energy (~24 meV), which was expected to lead to exceptional temperature stability not achievable with other types of nanostructures. An additional attractive feature of colloidal QDs as potential lasing media was a prospect of wide ranging spectral tunability on the order of 1 eV, in principle achievable within a single material system through the influence of quantum confinement. However, after a decade of research that provided some tantalizing hints of optical gain,[338,339] colloidal QDs failed to demonstrate lasing action.

DOI: 10.1021/acs.chemrev.6b00169
Chem. Rev. 2016, 116, 10513−10622

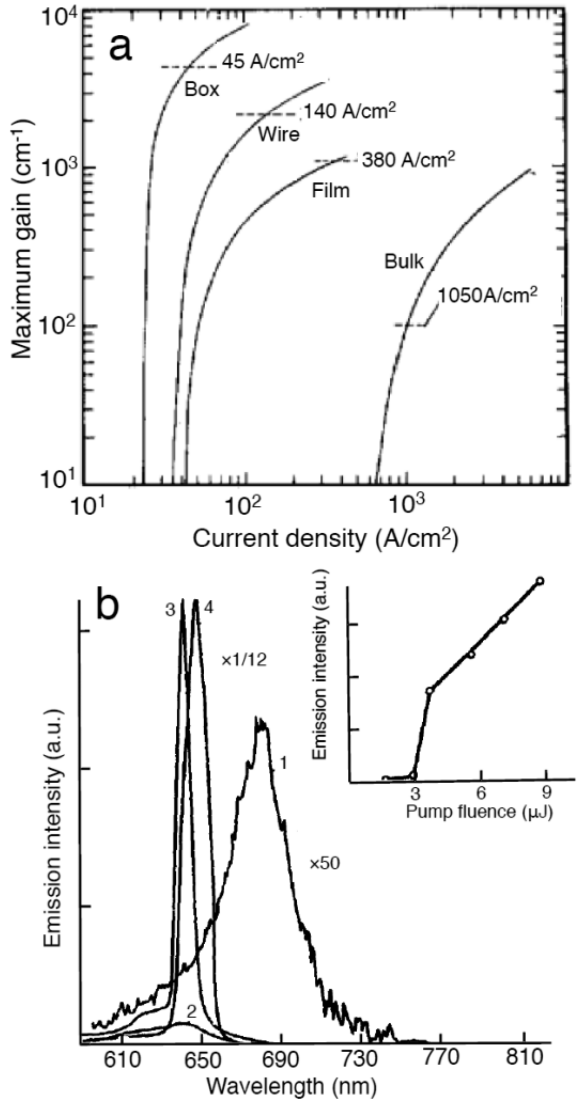

Figure 28. (a) Maximum gain as a function of injection current density calculated for the $GaAs/Ga_{0.8}Al_{0.2}As$ quantum box (i.e., QD), quantum wire, quantum film (*i.e.*, quantum well), and bulk crystal (conventional double heterostructure). Dashed lines mark the lasing threshold for each material. These plots illustrate a dramatic reduction in the threshold current density with decreasing dimensionality of the structure, that is, going from the bulk, to the 2D, 1D, and ultimately 0D material. Adapted with permission from ref 333. Copyright 1986 IEEE. (b) Emission spectra of 4-nm-radius CdSe QDs in a glass slab prepared as a Fabry–Pérot cavity with two dielectric mirrors reflecting 100% and 95% in the range 600–700 nm. The measurements were conducted at 80 K using 20 ps pump pulses at 532 nm. Before the onset of the lasing regime, emission was dominated by intragap defects, as often observed for poorly passivated QDs (spectrum 1, per pulse pump fluence w_p = 0.5 μJ). As the pump fluence was increased, the emission intensity sharply increased (inset), which was accompanied by a dramatic narrowing of the emission band, which became peaked at the position of the QD band-edge transition (around 650 nm). These were clear signatures of the transition to the lasing regime. Spectrum 2 was taken near the lasing threshold (w_p = 3 μJ; see inset), while spectra 3 and 4 were measured above it with w_p = 5 μJ and 100 μJ, respectively. Adapted with permission from ref 20. Copyright 1991 American Institute of Physics.

Originally, difficulties in achieving lasing were often attributed to high nonradiative carrier losses due to trapping at surface defects, a direct consequence of the large surface-to-volume ratio characteristic of sub-10 nm particles. Another concern raised in several theoretical papers was the strongly reduced efficiency of electron–phonon interactions in the case of discrete, atomic-like energy structures, which were characteristic of small-size dots.[340,341] For discrete spectra, the availability of pairs of electronic states satisfying energy conservation in phonon-assisted processes is drastically reduced compared to the *quasi*-continuous spectra of bulk materials. This deficiency has been expected to significantly lower the rate of carrier cooling by phonon emission (an effect known as a "phonon bottleneck"), leading to reduced carrier flows into the lowest "emitting" states and hence reduced PL efficiencies. However, the difficulties anticipated due to carrier surface trapping and the "phonon bottleneck" turned out to be much less important compared to such largely unforeseen problems as nonradiative multiparticle Auger recombination[34] (Section 4) and interference from photoinduced absorption due to carriers trapped at QD interfaces.[342,343]

The topic of intraband relaxation in QDs was addressed by several studies conducted on chemically synthesized[15,31] and epitaxial[344] QDs. These studies revealed that in contrast to predictions of "phonon-bottleneck" models, electron relaxation in QDs was extremely fast and occurred on picosecond to sub-picosecond time scales. This rapid relaxation was attributed to an Auger-type mechanism involving intrinsic e-h interactions.[30] In this process, excess electron energy is transferred to a hole, followed by fast hole relaxation through the dense spectrum of valence-band states. Several follow-up studies provided supporting evidence in favor of this relaxation mechanism by directly resolving dynamics of holes re-excited via the Auger process[345] and examining the effect of hole withdrawing species on the rate of electron cooling.[31,346] Other effects have been also suggested to influence the rate of carrier intraband relaxation in QDs including coupling to surface ligands[347,348] and intrinsic multiphonon emission.[32,349] The role of the non-Auger processes is likely especially important in situations when the holes are not present in the QDs[347,350] or the semiconductor material is characterized by sparse and mirror symmetric electronic states in the conduction and valence bands (as in, *e.g.*, PbSe and PbS),[349] conditions under which the e-h energy transfer is expected to be suppressed. The overall conclusion of all of these studies is that regardless of a specific mechanism for intraband relaxation, this process is extremely fast (sub-picosecond to picosecond time scales) in colloidal QDs, and thus does not represent an obstacle for QD lasing.

The photoinduced absorption turned out to be a more serious problem. For example, TA measurements[342,343] showed that in the case of many common solvents (*e.g.*, hexane, toluene, chloroform, or heptamethylnonane), CdSe QDs under optical excitation in solution, instead of absorption bleaching (required for observing optical gain) might exhibit *increased* absorption. The amplitude of the photoinduced absorption feature was found to be dependent on the type and quality of QD surface passivation, as well as the solvent identity; therefore, it was attributed to optical transitions involving interface states. It was further observed that the amplitude of photoinduced absorption rapidly increased with decreasing QD size, leading to complete suppression of the band-edge bleach. QDs of larger sizes did exhibit optical gain, however, without any signature of amplified spontaneous emission (ASE) a prerequisite for the lasing action.[342,343]

An important milestone in the quest for nanocrystal lasing was the realization that optical gain in these nanostructures relies on emission not from single excitons but biexcitons and other

DOI: 10.1021/acs.chemrev.6b00169
Chem. Rev. 2016, 116, 10513–10622

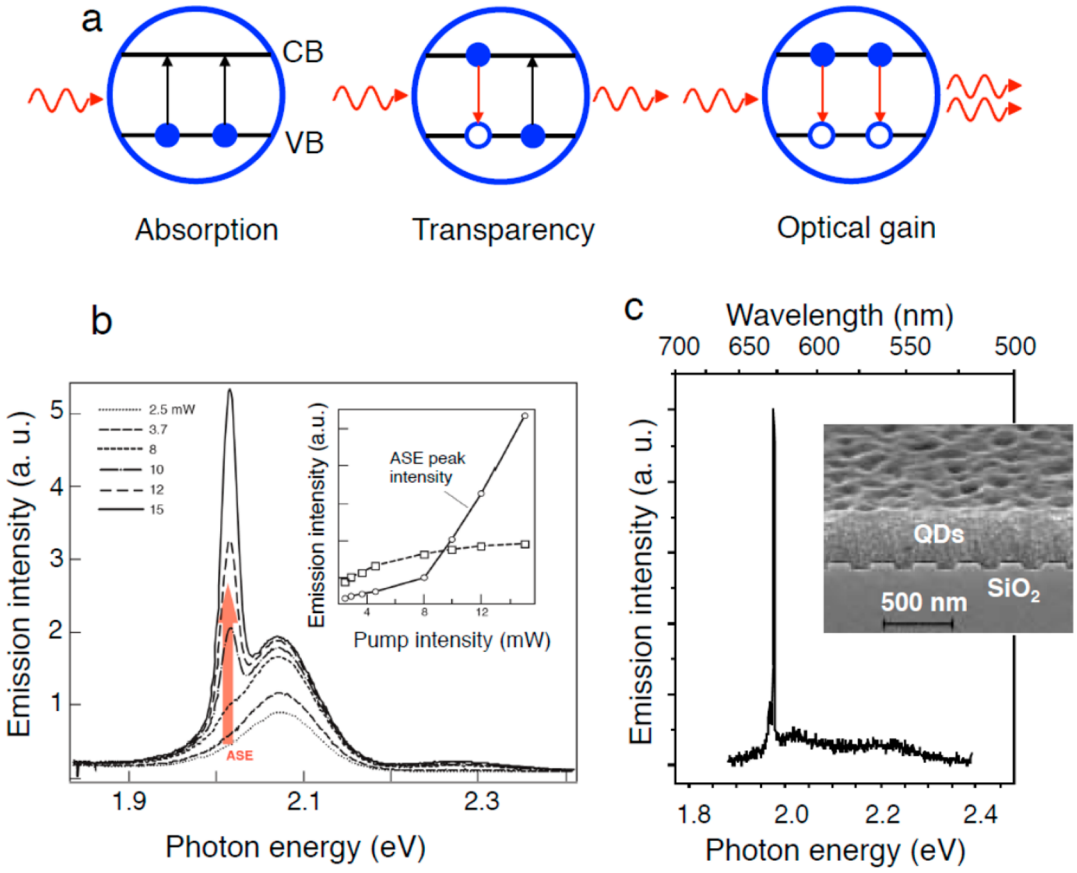

Figure 29. (a) Simplified scheme illustrating three different interaction regimes of a semiconductor QD with a photon resonant with the band-edge transition, which couples 2-fold spin-degenerate conduction- and valence-band levels (labeled CB and VB, respectively). In the ground state (left), both electrons are in the valence band, and as a result, the QD can only absorb a photon (arrows pointing upward). When one electron is promoted across the band gap (single-exciton state; middle), the QD is "transparent" to light, as absorption due to the valence-band electron (arrow pointing upward) is exactly balanced by stimulated emission produced by the conduction-band electron (arrow pointing downward). When both electrons are in the conduction band (biexciton state; right), the incident photon triggers stimulated emission by one of the electrons (arrows pointing downward), which produces an identical second photon. This corresponds to the optical-gain regime. (b) A series of PL spectra of the CdSe QD film (2.1 nm dot radius, 80 K sample temperature), recorded as a function of the pump intensity (shown in the legend), illustrating the development of a sharp ASE band on the low-energy side of spontaneous emission. Inset: The intensity of the ASE peak (circles) as a function of pump intensity in comparison to the PL signal outside the ASE feature (squares). The onset of the ASE regime indicated by a sharp rise of the PL intensity is around 8 mW. Adapted with permission from ref 262. Copyright 2000 The American Association for the Advancement of Science. (c) Room-temperature lasing spectrum of a distributed feedback (DFB) laser fabricated using CdSe/ZnS QDs with the 2.5 nm CdSe-core radius. Inset: a scanning electron microphotograph of a DFB structure. Adapted with permission from ref 351. Copyright 2002 American Institute of Physics.

multiexcitons of higher orders, which leads to a largely unforeseen complication associated with very fast nonradiative Auger recombination.[34] To illustrate this problem, we will approximate the lowest-energy "emitting" transition in the QDs by a simple 2-fold, spin-degenerate, two-level system. In the ground state of this system, two electrons with opposite spins occupy the valence band level (Figure 29a, left). If one electron is promoted to the conduction-band level, the resulting single-exciton state does not produce optical gain since stimulated emission due to radiative relaxation of the conduction-band electron is precisely balanced by absorption associated with the electron remaining in the valence band (a more complex case when these processes are not balanced is discussed in Section 5.4). This situation corresponds to the regime of optical transparency (Figure 29a, middle). In order to realize optical-gain, one must excite the second electron to the conduction band and thus generate a biexciton state (Figure 29a, right). The multiexciton nature of optical gain in QDs leads to a serious complication arising from highly efficient Auger recombination (Section 4), which leads to rapid depletion of optical gain.

Fast Auger recombination is the major obstacle preventing lasing in QD solution samples. Indeed, for lasing to occur the buildup of stimulated emission must outpace optical-gain relaxation. The rate of the ASE buildup is directly proportional to the gain coefficient, which in turn scales directly with the concentration of the QDs in the active medium. In solution-based samples, the QD density is constrained by solubility limits and cannot reach critical values for which the rate of stimulated emission outcompetes Auger recombination (see a quantitative discussion of this issue in Section 5.2). This explains failures of numerous early experiments that utilized dye-laser-like configurations for achieving nanocrystal lasing.

As was first realized in ref 262, the problem of Auger recombination could be resolved by employing densely packed QD films that allowed for much greater gain coefficients than the solution samples. A further important element of these studies was the use of femtosecond pulses for exciting the QD films, which allowed for minimizing carrier losses due to Auger decay at the pumping stage. These were two key components of the experiments that led to the first successful demonstration of ASE

DOI: 10.1021/acs.chemrev.6b00169
Chem. Rev. 2016, 116, 10513−10622

from colloidal QDs[262] (Figure 29b). Soon after these proof-of-principle studies, several research groups were able to demonstrate true lasing action using different cavity designs.[342,351−353] Figure 29c displays an example of a distributed feedback (DFB) laser[351] which demonstrated the facile tunability of emission wavelength allowed by simply varying the QD size.

In the subsections that follow, we provide a more in-depth analysis of principles of colloidal QD-based lasing in the presence of fast Auger recombination, the efforts on suppression of Auger recombination in relation to the problem of continuous-wave (*cw*) lasing, and novel lasing concepts such as single-exciton optical gain. We will finally conclude this Section with an overview of the recent progress in the QD-lasing field, and remaining problems and challenges.

5.2. Optical-Gain and Lasing Thresholds in Relation to Auger Recombination

To analyze optical gain and lasing thresholds, we update the simplified model of Figure 29a to account for the difference in degeneracies of the ground ($|0\rangle$), single-exciton ($|X\rangle$), and biexciton ($|XX\rangle$) states derived from the difference in their spin configurations.[261] The modified model is displayed in Figure 30a where the $|0\rangle$, $|X\rangle$, and $|XX\rangle$ states are placed along a vertical "energy" axis. Here we do not specify how carriers are injected into the QDs. Experimentally, the most common approach is optical excitation with short laser pulses tuned to an above-band-edge spectral energy.

In the ground state of the system displayed in Figure 30a, both valence-band spin sublevels are occupied with electrons; as a result this state is nondegenerate. The biexciton is also nondegenerate as it comprises two occupied conduction-band spin sublevels. On the other hand, the single-exciton state is 4-fold-degenerate due to four different spin configurations that can be assumed by the conduction and the valence band electrons. Because of optical selection rules, two of these configurations are optically active and two are passive. It is assumed that all of these configurations are in mutual thermal equilibrium implying that in a macroscopic system only half of the single excitons are optically active. This allows one to express the per-dot rate of stimulated emission due to the transition from the single exciton to the ground state as $W_{10} = (\gamma/2)\phi$ (Figure 30b) where ϕ is the density of photons accumulated in the cavity mode, and γ is the parameter proportional to the oscillator strength of the individual spin-allowed transition (shown by black arrows in Figure 30a), which is analogous to the well-known Einstein coefficient of stimulated emission (a so-called "*B*-coefficient"). The same rate characterizes the transition from the $|X\rangle$ to the $|XX\rangle$ state via absorption of a photon ($W_{12} = (\gamma/2)\phi$), implying that single-excitons are gain-neutral species, that is, their net contribution to the gain coefficient is zero. Thus, the only source of optical gain in this system is stimulated emission by biexcitons ($|XX\rangle-|X\rangle$ transition), which competes with photon losses arising from absorption due to the $|0\rangle-|X\rangle$ transition (Figure 30b). The corresponding per-dot rates are equal to each other and can be expressed as $W_{21} = W_{01} = 2\gamma\phi$. In this model, the relationship between emission rates by biexcitons and single excitons is 4 to 1, which is consistent with quadratic scaling of radiative rates with exciton multiplicity typically observed for QDs of various compositions.[264,354,355]

To characterize the behavior of an excited QD ensemble, we introduce probabilities for the QD to be in the ground (P_0), single-exciton (P_X), or biexciton (P_{XX}) states that are constrained by the condition $P_0 + P_X + P_{XX} = 1$. In this case, the net rate of photon generation per unit volume can be presented as $r_{SE} = n_{QD}(W_{21} - W_{01}) = 2\gamma n_{QD}(P_{XX} - P_0)$, where n_{QD} is the concentration of the QDs in the sample. This leads to the following expression for the gain coefficient $G = (c/n)r_{SE} = 2(c/n)\gamma n_{QD}\rho = G_0\rho$, where c is the speed of light in vacuum, n is the index of refraction of the QD sample, $\rho = P_{XX} - P_0$ is the per-QD population inversion, and $G_0 = 2(n/c)\gamma n_{QD}$ is the saturated gain obtained for $\rho = 1$, which corresponds to the complete population inversion when all QDs in the ensemble contain biexcitons.

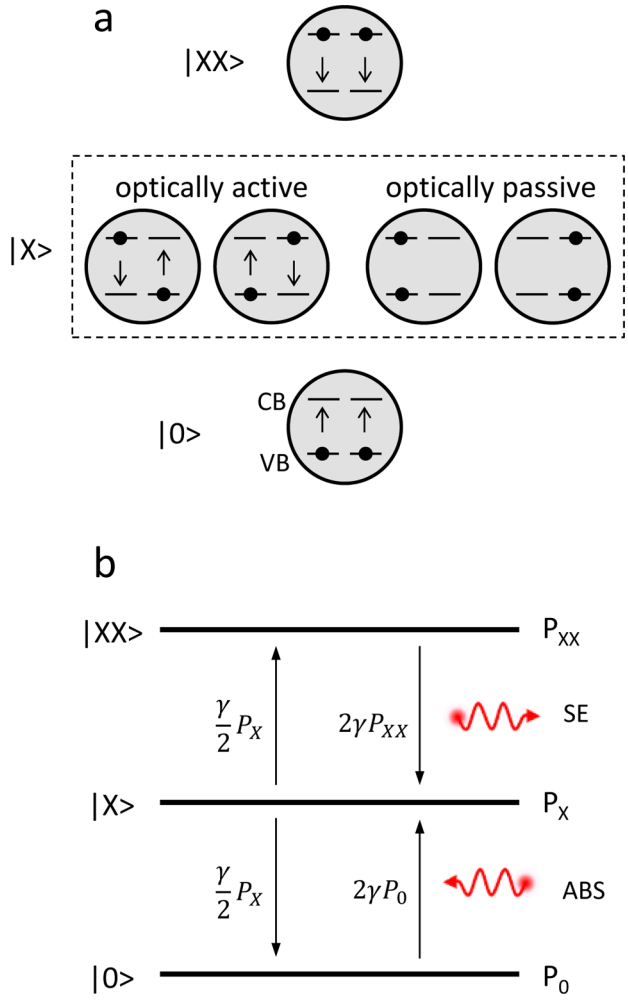

Figure 30. (a) Three-state model of optical gain in QDs, which comprises a nondegenerate ground state ($|0\rangle$, bottom), a 4-fold degenerate single-exciton state, ($|X\rangle$, middle), and a nondegenerate biexciton state ($|XX\rangle$, top). (b) These states are coupled by optical transitions leading to photon absorption (up arrows) or stimulated emission (down arrows). The rates of these transitions per unit photon density are indicated in the figure; γ is the transition probability per single spin-allowed transition (shown by black arrows in panel a). Adapted with permission from ref 261. Copyright 2015 American Chemical Society.

Based on the above considerations, the optical gain threshold (defined by the condition $G = 0$) is realized when $\rho = 0$ or $P_{XX} - P_0 = 0$. An example of an excited system where this condition is satisfied is a QD ensemble wherein every particle contains a single exciton. This corresponds to $P_X = 1$ and $P_{XX} = P_0 = 0$. However, a more realistic situation is a Poisson distribution of QD occupancies, which is typically realized following the above-band-edge excitation of the sample with a short laser pulse.[71] In

DOI: 10.1021/acs.chemrev.6b00169
Chem. Rev. 2016, 116, 10513−10622

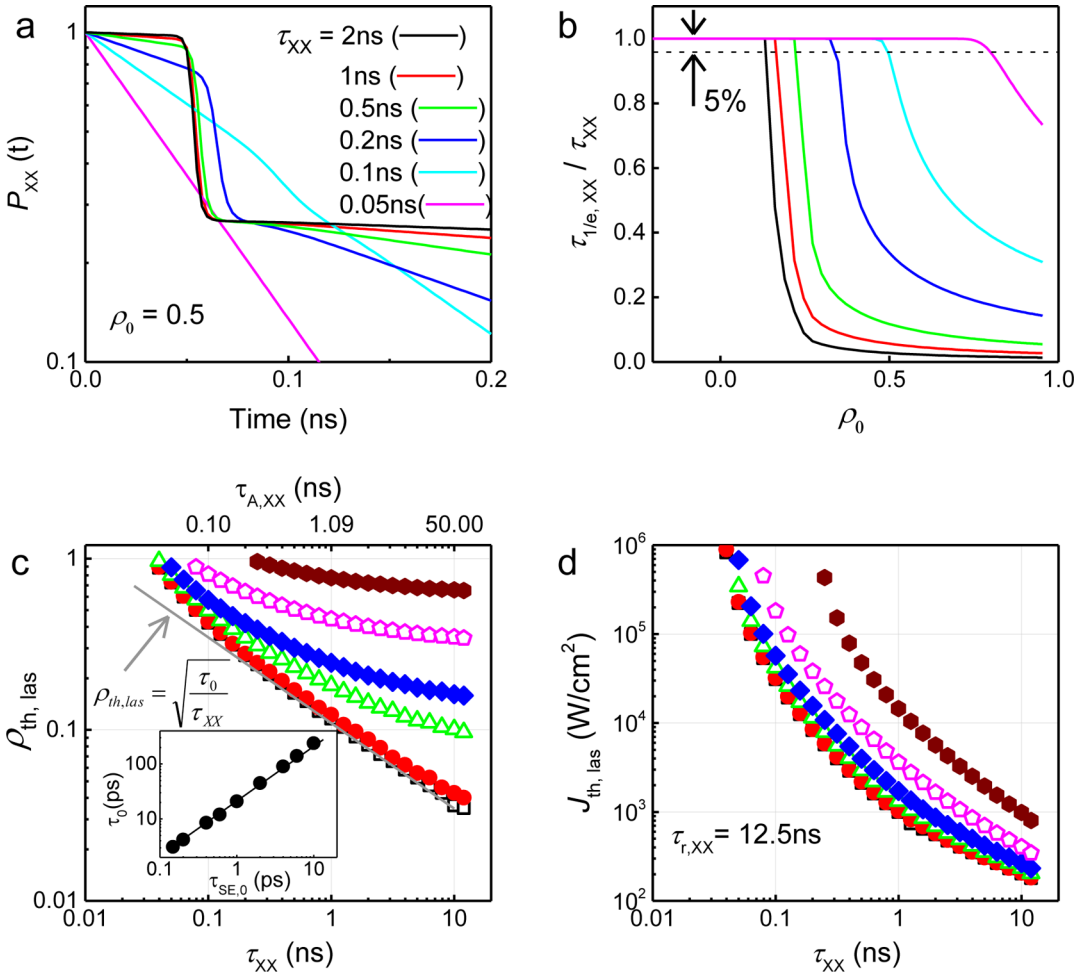

Figure 31. (a) Normalized decay of the biexciton population, $P_{XX}(t)$, for varied biexciton lifetimes (τ_{XX} = 50 ps to 2 ns) and a fixed initial per-QD population inversion ρ_0 = 0.5. Cavity lifetime τ_c = 10 ps. Transition to lasing is indicated by the development of a sharp step in biexciton dynamics, which signifies the regime when biexciton decay is dominated not by Auger recombination but by stimulated emission. (b) The 1/*e* biexciton lifetime (obtained from dynamics in panel a, using corresponding colors) normalized by τ_{XX} is shown as a function of ρ_0; the same values of τ_{XX} as in part b (same color coding). Lasing thresholds, $\rho_{th,las}$, are defined as the value of ρ_0 at which $\tau_{1/e,XX}$ drops by 5% from its maximum (dashed line). (c) Lasing threshold $\rho_{th,las}$ as a function of τ_{XX} for varied cavity photon lifetimes: τ_c = 1 ns (squares), 0.1 ns (circles), 0.01 ns (triangles), 0.005 ns (diamonds), 0.002 ns (pentagons), and 0.001 ns (hexagons). In the lossless cavity limit, $\rho_{th,as}$ is proportional $(\tau_0/\tau_{XX})^{1/2}$ (gray line). The inset shows that τ_0 scales linearly with $\tau_{SE,0}$. (d) The *cw* lasing threshold ($J_{th,las}$) as a function of τ_{XX} for the same values of τ_c as in panel c. Adapted with permission from ref 261. Copyright 2015 American Chemical Society.

this case, the probability of finding an *N*-exciton state in a QD ensemble is given by $p_N = \langle N\rangle^N (N!)^{-1} e^{-\langle N\rangle}$, where $\langle N\rangle = \sum_{i=1}^{\infty} i p_i$ is the average QD excitonic occupancy. To relate these Poisson probabilities to those introduced in the three-state model considered here, we take into account that all multi-excitons have the same contribution to the band-edge optical gain as a biexciton, and hence, the P_{XX} probability can be calculated from $P_{XX} = \sum_{i=2}^{\infty} p_i = 1 - p_0 - p_1$, while the probabilities P_0 and P_X can be directly related to p_0 and p_1 by $P_X = p_1$ and $P_0 = p_0$. Now, we can rewrite the condition for optical gain onset as $1 - 2p_0 - p_1 = 0$ or $\langle N\rangle + 2 = e^{\langle N\rangle}$. The solution of this equation indicates that in the case of the Poisson statistics of QD occupancies, the gain threshold expressed in terms of the average QD occupation factor is given by $\langle N_{th,g}\rangle \approx 1.15$, which is slightly higher than the threshold for the case of the uniform distribution of the excitonic population across the QD ensemble when $\langle N_{th,g}\rangle = 1$.

At the gain threshold, the population inversion ($\rho_{th,g}$) must be sufficiently high to ensure that stimulated emission exactly compensates losses due to photon absorption originating from the gain medium itself. As we showed above, this condition is realized when $\rho_{th,g} = 0$. However, achievement of the lasing regime requires higher values of population inversion ($\rho_{th,las} > \rho_{th,g}$) in order to allow for stimulated emission to compensate for additional losses arising from a finite lifetime of cavity photons. The critical value of ρ required for lasing is further increased if the optical gain is short-lived and hence the buildup of the cavity mode must be faster than the optical-gain relaxation time (τ_g). This latter factor is especially important in colloidal QDs where optical gain dynamics are controlled by extremely fast Auger decay, which leads to very short values of τ_g on picosecond to tens-of-picosecond time scales.[264,356]

The effect of Auger recombination on ASE and lasing thresholds was first discussed in ref 262 and recently studied more rigorously in ref 261. The latter study analyzed carrier and photon population dynamics in a QD gain medium incorporated into a single-mode optical cavity using a gain-switching model.[357] The initial population inversion (ρ_0) was assumed to be generated instantaneously at time t = 0 by a δ-function-like optical pulse, and a set of coupled rate equations was used to

DOI: 10.1021/acs.chemrev.6b00169
Chem. Rev. 2016, 116, 10513−10622

analyze temporal evolutions of the populations of the gain-active biexciton states ($P_{XX}(t)$) and the cavity mode ($\phi(t)$) as a function of ρ_0, the cavity photon lifetime (τ_c), and the single-exciton (τ_X) and biexciton (τ_{XX}) lifetimes. It was further assumed that the single-exciton decay was purely radiative ($\tau_X = \tau_{r,X}$), while the biexciton decay had contributions from both radiative ($\tau_{r,XX}$) and nonradiative Auger recombination ($\tau_{A,XX}$), which resulted in the expression $\tau_{XX} = \tau_{r,XX} \times \tau_{A,XX}/(\tau_{r,XX} + \tau_{A,XX})$. In the model, the value of $\tau_{r,X}$ was fixed to 50 ns. This led to a fixed value of $\tau_{r,XX}$, which was calculated from $\tau_{r,XX=} \tau_X/4 = 12.5$ ns based on the quadratic scaling of radiative rates with exciton multiplicity.[264,354,355]

Figure 31a displays the calculated dynamics of the biexciton population for $\rho_0 = 0.5$ and the biexciton lifetime tuned from 50 ps to 2 ns by varying $\tau_{A,XX}$. These data indicate a dramatic effect of τ_{XX} on both the quantitative characteristics of biexciton decay and its qualitative character. For the shortest Auger lifetime ($\tau_{A,XX} \approx \tau_{XX} = 50$ ps; trace shown in magenta), P_{XX} decays exponentially with a time constant defined by Auger recombination. When τ_{XX} is increased to 100 ps (light blue trace), the P_{XX} dynamics exhibit a kink at around 90 ps, indicating the increased influence of radiative recombination via stimulated emission. For longer values of τ_{XX}, the kink evolves into a sharp step-like drop indicating the transition to the regime where stimulated emission outpaces Auger recombination. This is a signature of the onset of the lasing action.

To better understand this behavior, one should take into account that the development of lasing is not instantaneous but is characterized by a certain time (τ_{SE}) which scales inversely with the gain coefficient, *i.e.*, $\tau_{SE} \propto n/(cG)$. For short Auger decay times, optical gain relaxation occurs faster than the buildup of the cavity mode and lasing does not occur. On the other hand, if optical gain is sustained for a time period longer than τ_{SE}, the lasing action can, in principle, develop if the gain coefficient is sufficiently large to compensate for cavity losses. These considerations imply that the lasing threshold, in addition to the characteristic cavity lifetime, is also directly linked to the Auger time constant.[354]

To analyze the relationship between $\rho_{th,las}$ and τ_{XX}, a calculation similar to those in Figure 31a was performed for a series of ρ_0 from 0 to 1,[261] and these data were used to obtain the dependence of the biexciton population lifetime (expressed in terms of the $1/e$ time constant, $\tau_{1/e,XX}$) on ρ_0 for varied τ_{XX} (Figure 31b). These calculations indicate that, at lower values of ρ_0, $\tau_{1/e,XX}$ stays constant and is virtually unperturbed compared to the nominal biexciton lifetimes. For a certain critical value of ρ_0, $\tau_{1/e,XX}$ sharply shortens, which signifies the onset of the lasing regime. As a quantitative measure of $\rho_{th,las}$, the authors of ref 261 used the value of ρ_0 at which $\tau_{1/e,XX}$ drops by 5% below the nominal biexciton time constant τ_{XX}.

Figure 31c displays $\rho_{th,las}$ as a function of τ_{XX} for several cavity photon lifetimes from 1 ps to 1 ns. For the shorter values of τ_c, the effect of τ_{XX} on lasing threshold is weak. However, it progressively increases as τ_c becomes longer, and the limit of the lossless cavity ($\tau_c \to \infty$), $\rho_{th,las}$, is directly linked to τ_{XX} by an approximately inverse-square-root scaling:

$$\rho_{th,las} = \sqrt{\tau_0/\tau_{XX}} \tag{18}$$

Here, τ_0 is a parameter directly proportional to the characteristic time of the stimulated emission buildup under gain-saturation conditions: $\tau_0 = \beta\tau_{SE,0}$, where $\tau_{SE,0} = n/(cG_0)$. As illustrated in the inset of Figure 31c, for the parameters of the model of ref 261, the proportionality constant β is *ca.* 20.

Equation 18 indicates the existence of the minimal (critical) value of the saturated gain ($G_{0,c}$) below which lasing is impossible even in a lossless cavity. Indeed, since ρ cannot exceed 1 (achievable under complete population inversion), for lasing to occur, τ_0 must be shorter than or at least equal to τ_{XX}, which indicates that the gain coefficient must be not lower than

$$G_{0,c} = \beta n(c\tau_{XX})^{-1} \tag{19}$$

Since the gain coefficient scales directly with the concentration of QDs in a sample (n_{QD}), eq 19 indicates a minimal density of QD emitters in the gain medium ($n_{QD,c}$) required for lasing. Specifically, defining the gain cross section as $\sigma_G = G_0/n_{QD}$, we obtain

$$n_{QD,c} = G_{0,c}/\sigma_G = \beta n(c\tau_{XX}\sigma_G)^{-1} \tag{20}$$

A useful benchmark for evaluating the suitability of a QD-based material for lasing applications is the critical volume fraction of active semiconductor (ξ_c) required for the lasing action. This quantity is linked to $n_{QD,c}$ by $\xi_{QD,c} = V_{QD}n_{QD,c}$, where V_{QD} is the QD volume. As was discussed in Section 4, in standard core-only QDs, the biexciton lifetime is controlled by Auger recombination ($\tau_{XX} \approx \tau_{A,XX}$), and further, it scales directly with the QD volume as $\tau_{XX} = \kappa V_{QD}$, where κ is a proportionality constant that is nearly independent of QD composition and is *ca.* 1 ps nm^{-3}. Based on these considerations, we obtain the following expression for $\xi_{QD,c}$:

$$\xi_{QD,c} = \beta n(c\kappa\sigma_G)^{-1} \tag{21}$$

For the purpose of illustration, we will estimate $\xi_{QD,c}$ using the parameters of core-only CdSe QD samples. On the basis of the literature ASE measurements,[261,353] the optical gain cross section of these QDs is $\sim 5 \times 10^{-17}$ cm.[2] The typical refractive index of close-packed CdSe QD films is ~1.8.[353] Using these two values along with $\beta = 20$ (see above) and $\kappa = 1$ ps nm^{-3}, we obtain $\xi_{QD,c} = 0.024 = 2.4\%$. While this value is not especially high, it is not accessible with QD solutions, which points toward the need for denser samples, such as close-packed QD films[353,356] or, for example, cross-linked QD-sol–gel composites[353,358,359] for the observation of ASE and lasing action.

In addition to imposing a strict limit on the minimal density of the QDs in the medium intended for lasing applications, Auger recombination also has a direct effect on the lasing threshold. In the pulsed-excitation regime, when the pulse duration is much shorter than the Auger lifetime, carrier losses at the photogeneration stage are small. In this case, the influence of Auger decay on the threshold population inversion can be directly evaluated from eq 18, which suggests an appreciable but a fairly slow change of $\rho_{th,las}$ with τ_{XX} described by the inverse square-root scaling.

The effect of Auger decay on lasing threshold is much more dramatic in the case of *cw* excitation as it requires very high pumping rates that could outpace Auger decay. Figure 31d displays a calculation of such dependence for the case of above-band-edge *cw* excitation assuming a QD absorption cross section at the pump wavelength of 10^{-15} cm^2.[261] These calculations indicate that the threshold intensity ($J_{th,las}$) rapidly decreases as the biexciton lifetime becomes longer, which makes it easier to achieve the lasing regime. For example, in the case of $\tau_{XX} = 50$ ps and low cavity losses ($\tau_c = 1$ ns), the lasing threshold is on the order of 1 MW/cm^2, which is too high for making a practical

DOI: 10.1021/acs.chemrev.6b00169
Chem. Rev. 2016, 116, 10513−10622

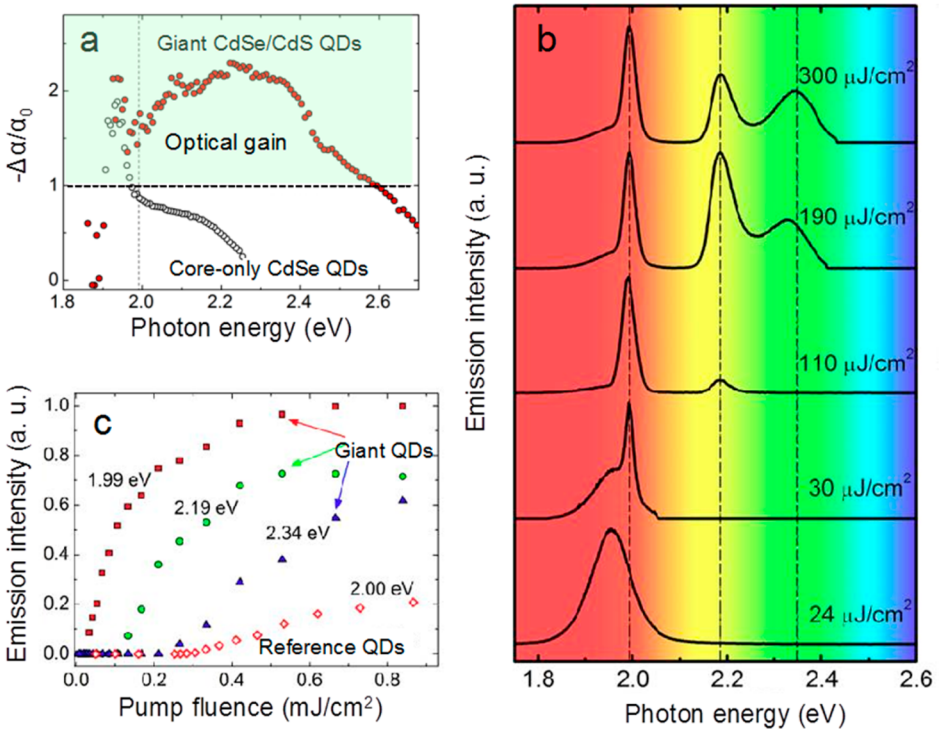

Figure 32. (a) Normalized TA spectrum (plotted as $-\Delta\alpha/\alpha_0$ vs photon energy) of giant CdSe/CdS QDs (11 MLs shell) recorded at 2 ps after excitation with 3.1 eV, 1.2 mJ cm^{-2} pulses (red solid circles). Due to contributions of higher-order multiexcitons to stimulated emission, optical gain (corresponding to $-\Delta\alpha/\alpha_0 > 1$) spans a wide range of energies of more than 500 meV. Black open circles show the same spectrum for the core-only CdSe QDs recorded under similar excitation conditions. In this case, optical gain is almost purely due to biexcitons (no contributions from higher-order multiexcitons), and as a result, it is limited to a narrow range of band-edge energies. (b) Emission spectra of a close-packed film of giant QDs that exhibit a progression of three ASE peaks at 1.99, 2.19, and 2.34 eV emerging one by one with increasing pump level. These bands span a wide range of colors from red to green. The multiband structure of the ASE spectrum indicates that, in addition to the band-edge transition, the regime of population inversion is achieved for the two higher-energy transitions involving excited electronic states. This further points toward a considerable suppression of Auger recombination in giant QDs, leading to extended lifetimes of higher-order multiexcitons. (c) Emission intensity as a function of pump fluence at the positions of the three ASE peaks for the giant CdSe/CdS QDs (solid symbols) in comparison to the similar dependence for the reference thin-shell CdSe/ZnS QDs (hollow diamonds). Adapted with permission from ref 328. Copyright 2009 American Chemical Society.

lasing device. However, if the biexciton lifetime is increased to 1 ns, $J_{th,las}$ drops by 3 orders of magnitude to around 1 kW/cm^2. This pump level is readily achievable with available coherent and even incoherent (*e.g.*, high-intensity commercial LEDs) *cw* pump sources, which could greatly simplify the achievement of *cw* QD lasing.

Despite significant progress in the area of colloidal QD lasing in general, a reliable demonstration of ASE and true lasing action under *cw* pumping still remains an important challenge. As illustrated above, the main difficulty in achieving this regime is very fast depletion of optical gain due to nonradiative Auger decay. Therefore, the development of methods/structures for effective suppression of Auger recombination is an important element of efforts on transforming QD lasing from the laboratory stage to a practical technology. Below we overview some of the work in this area with focus on experimental studies.

5.3. Experimental Studies of the Effect of Auger Decay Suppression on Lasing Performance

As was discussed in Section 4.3, one approach to suppressing Auger decay involves shaping (specifically "smoothening") of the confinement potential, for example, by introducing an alloyed layer at the core−shell interface in heterosturctured QDs. The beneficial effect of interfacial alloying for lasing was first demonstrated in an investigation of optical gain and ASE in samples of thick-shell, giant CdSe/CdS QDs.[328] The samples studied in this work comprised a 1.5 nm radius CdSe overcoated with the 5 nm CdS shell by the SILAR method,[181] for which it was speculated that the long multihour reaction times could result in unintentional alloying of the core/shell interface accompanied by the formation of the intermediate $CdSe_xS_{1-x}$ layer[328] (see Section 3.5). This conjecture was confirmed by a follow-up study of phonon replicas in giant QDs using low-temperature fluorescence line narrowing measurements which indicated the emergence of a distinct $CdSe_xS_{1-x}$ alloy mode at long growth times (Figure 16a).[218]

Giant QDs showed a considerable improvement in optical gain properties compared to standard QDs, which was at least partially due to suppression of Auger recombination induced by interfacial alloying. Specifically, these structures exhibited a remarkably large optical gain line width of more than 500 meV, which was not limited to just band-edge energies, as in standard core-only nanocrystals, but also reached to higher-lying electronic states (red solid circles in Figure 32a). The large spectral extent of optical gain allowed for the realization of an unusual regime of a low-threshold, multiband ASE (Figure 32b) with three distinct peaks spanning a wide range of colors from the red to the green. These observations indicated that in addition to band-edge biexcitons, optical gain was contributed by higher-order multiexcitons involving carriers in the above-band-edge electronic levels. In giant QDs, these multiexcitons were apparently sufficiently long-lived to support the development of ASE, which was a direct consequence of extended Auger

DOI: 10.1021/acs.chemrev.6b00169
Chem. Rev. 2016, 116, 10513−10622

lifetimes occurring at least partially due to unintentional alloying. In standard nanocrystals with more efficient Auger decay, high-order multiexcitons are very short-lived, which makes optical gain and ASE primarily "biexcitonic" in nature and limits their spectral extent to the band-edge energies (black open circles in Figure 32a).

In addition to suppressed Auger recombination, the giant QDs exhibited a very large absorption cross section for spectral energies above the onset of absorption of the CdS shell. This allowed for a considerable reduction of the ASE threshold compared to standard core-only or thin-shell QDs. In a reference thin-shell CdSe/ZnS QD sample, the ASE threshold was ~300 μJ cm^{-2} (red open diamonds in Figure 32c) versus only ~26 μJ cm^{-2} in giant QDs (red solid squares in Figure 32c).[328] Interestingly, in giant QDs, the excitation thresholds for the higher-energy ASE features (~100 μJ cm^{-2} and ~220 μJ cm^{-2}; green open circles and blue solid triangles in Figure 3c, respectively) were still lower than the ASE threshold in the reference sample.

Recent progress in the synthesis of core−shell structures allows for controlled incorporation of a well-defined alloyed layer at the core−shell interface.[86] Such intentionally alloyed QDs have essentially the same single-exciton properties as the structures with a sharp unalloyed interface, but they are characterized by considerably slower Auger recombination, as indicated by both ensemble[86] and single-dot[284] measurements. It was observed that the Auger lifetime lengthening directly translated into improved LED performance manifested as increased quantum efficiency and delayed onset of efficiency roll-off (also known as "droop") at increased drive current[285,360] (see Section 6.3 for details).

Recently, the effect of interfacial alloying on the lasing characteristics of heterostructured QDs was evaluated on the basis of a side-by-side comparison of core/shell CdSe/CdS QDs with a sharp core/shell interface (C/S sample) versus QDs with a thin (1.5-nm thickness) $CdSe_{0.5}S_{0.5}$ alloy layer separating the core and the shell (C/A/S sample).[86] These samples had the same core (r = 1.5 nm) and overall (R = 7 nm) radii, and they exhibited nearly identical single-exciton properties (*e.g.*, emission wavelengths, PL QYs, absorption cross sections, and single-exciton lifetime) but distinctly different Auger lifetimes.[261] This allowed for the isolation of the effect of Auger recombination on QD optical-gain properties from other factors such as absorption and gain cross sections, and the rate of defect-related nonradiative recombination. In this study, the single-exciton lifetime in both samples was ~50 ns, while, due to the presence of a graded interface, the biexciton lifetime was considerably longer in the C/A/S QDs compared to the C/S samples. In fact, single-QD measurements found that τ_{XX} for the majority of the C/A/S dots was longer than 1 ns, while most of the C/S QDs showed a resolution-limited τ_{XX} < 0.7 ns[261] (Figure 33a). Higher temporal resolution ensemble studies of PL from the C/S samples[86] indicated a biexciton lifetime of 0.35 ns, which was at least three times shorter than τ_{XX} in the C/A/S QDs.

Lengthening of the Auger lifetime in the alloyed QDs translated into appreciable improvement in their optical-gain performance as evaluated by measuring ASE and random lasing in spin-cast films excited by the frequency-doubled output (400 nm wavelength) of an amplified femtosecond Ti:sapphire laser (100 fs pulse duration).[261] Specifically, while both types of samples showed a transition to ASE and then random lasing with increasing pump level, the threshold pump fluences for observing these processes ($w_{th,ASE}$ and $w_{th,las}$, respectively) were systemati-

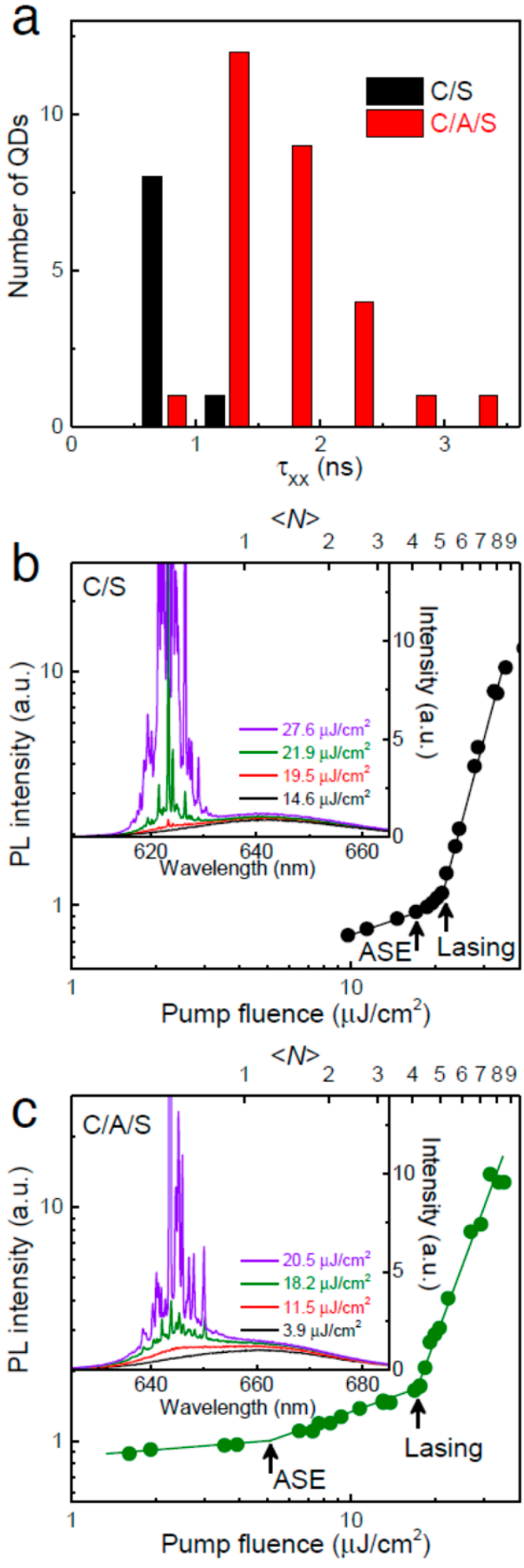

Figure 33. (a) Histogram of biexciton lifetimes for 37 individual C/S (black) and C/A/S (red) QDs. The majority of the C/S dots showed the resolution-limited (700 ps) biexciton time constant, while most of

DOI: 10.1021/acs.chemrev.6b00169
Chem. Rev. 2016, 116, 10513−10622

Figure 33. continued

the C/A/S dots had τ_{XX} longer than 1 ns. In fact, in some of the alloyed QDs, τ_{XX} was as long as ~3 ns. (b) Spectrally integrated emission intensity as a function of per-pulse pump fluence for the C/A/S QD film (~300 nm thickness); arrows mark onsets of the ASE and lasing regimes. Inset: pump-fluence-dependent emission spectra. Films were excited at 3.1 eV with frequency-doubled 100 fs pulses from an amplified femtosecond Ti:sapphire laser operating at 1 kHz repetition rate. The laser beam was focused with a cylindrical lens onto the QD film into a narrow stripe (73 μm wide, 1.36 mm long), and the emission was collected at the end of the stripe. (c) Same for the film (~300 nm thickness) of a C/S QDs. Adapted with permission from ref 261. Copyright 2015 American Chemical Society.

cally lower in C/A/S QDs than in C/S QDs. For example, for the samples shown in Figure 33b,c, $w_{th,ASE}$ was 6 and 19 μJ/cm^2, and $w_{th,las}$ was 17 and 21 μJ/cm^2 for the alloyed and nonalloyed QDs, respectively.

It is instructive to translate the threshold fluences at the ASE onset into effective three-state per-dot population inversions ($\rho_{th,ASE}$; see previous subsection), which yields $\rho_{th,ASE} \approx 0.19$ and 0.93, for the C/A/S and C/S QDs, respectively. These values correspond to the two opposite extremes allowed for ρ in the lasing regime ($0 < \rho \leq 1$). In the case of the C/A/S QDs, $\rho_{th,ASE}$ is close to the onset of optical gain ($\rho_{th,g} = 0$), while for the C/S QDs it approaches the maximum value achievable only under complete population inversion ($\rho_{max} = 1$). This illustrates that the ASE and lasing regimes can be much more readily realized with

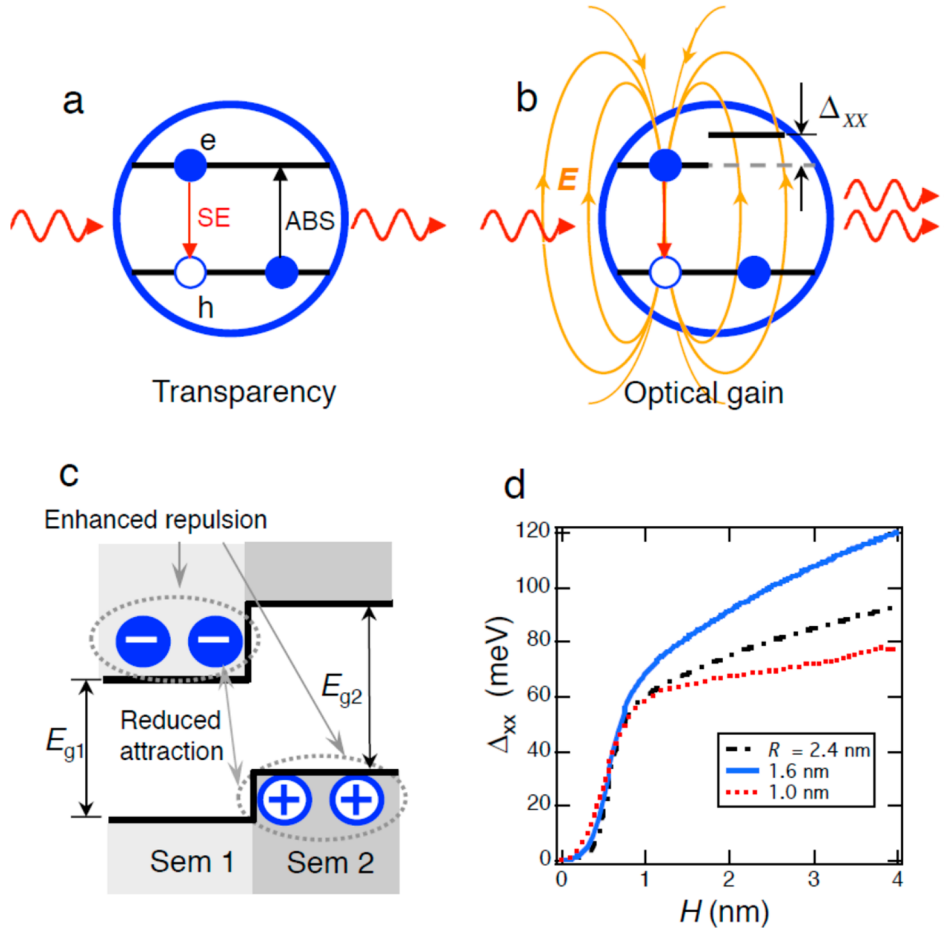

Figure 34. (a) Without exciton−exciton interactions, excitation of a single electron−hole pair in a QD does not produce optical gain but results in optical transparency, *i.e.*, the regime wherein stimulated emission is balanced by absorption. (b) In the presence of exciton−exciton interactions, the transition involved in the second absorption event is displaced from that whereby the original electron−hole pair was excited by a value represented by the exciton−exciton interaction energy Δ_{XX}. This effect can be interpreted in terms of a Stark shift associated with an electric field, ***E***, generated by the first electron−hole pair. As a result, the balance between stimulated emission and absorption becomes broken and lasing can, in principle, occur with single excitons. Adapted with permission from ref 361. Copyright 2007 Nature Publishing Group. (c) Strong exciton−exciton repulsion required for the realization of single-exciton gain can be obtained with type-II heterostructures, characterized by a so-called staggered band alignment, which drives spatial separation of electrons and holes across the heterointerface (Section 3.4.2). In the case of multiple electron−hole pairs, this type of spatial arrangement of charges boosts the repulsive part of the Coulomb interaction energy and, at the same time, decreases its attractive component. The overall effect of these trends is the development of net exciton−exciton repulsion with $\Delta_{XX} > 0$. Adapted with permission from ref 229. Copyright 2007 American Chemical Society. (d) The calculated dependence of the exciton−exciton interaction energy on shell thickness (H) in type-II core/shell CdS/ZnSe QDs with three core radii (R) of 1.0, 1.6, and 2.4 nm; these QDs were used in the first experimental demonstration of single-exciton ASE.[361] For all core radii, Δ_{XX} increases with shell thickness as a result of the increasing degree of spatial separation between electrons and holes. The nonmonotonic dependence of Δ_{XX} on core radius is due to the interplay between size-dependent changes in the electron−hole charge imbalance and the absolute values of charge density. On the basis of these calculations, out of the three considered core radii, the largest Δ_{XX} can be realized with the intermediate radius R = 1.6 nm.

DOI: 10.1021/acs.chemrev.6b00169
Chem. Rev. 2016, 116, 10513−10622

the alloyed samples, which is a direct consequence of suppressed Auger recombination in this type of QDs.

5.4. Single-Exciton Optical Gain

An attractive approach for the complete elimination of the detrimental effect of Auger recombination on QD lasing is achieving optical gain with single excitons, *i.e.*, without the involvement of the multiexcitons at all. The concept of single-exciton gain along with ideas of "giant" exciton−exciton repulsion in type-II heteronanocrystals for its practical implementation were first discussed in 2004.[25] This report also described the first experimental observation of spectral signatures of exciton−exciton repulsion in ASE of so-called inverted ZnSe/CdSe QDs that allow for partial spatial separation between electrons and holes for a certain range of core and shell dimensions (Section 3.4.4). Later, the effect of exciton−exciton repulsion of energy up to ∼30 meV was reported for type-II CdTe/CdSe QDs.[225] In 2007, ASE due to single excitons was successfully demonstrated experimentally using specially designed type-II CdS/ZnSe QDs.[361]

The concept of single-exciton gain due to "giant" exciton−exciton repulsion is illustrated in Figure 34a,b, which considers the competition between absorption and stimulated emission in a QD in the absence (a) and the presence (b) of the exciton−exciton interaction. In the former case, excitation of a single e-h pair (single exciton) does not produce optical gain but induces the regime of optical transparency (Figure 34a). As was discussed earlier in Section 5.1, in this case, stimulated emission associated with the electron in the conduction band is exactly balanced by absorption associated with the valence-band electron. The balance between these two processes is broken if one accounts for the exciton−exciton interaction, which displaces the "absorbing" transition with respect to the "emitting" one in the presence of a single excited e-h pair. This displacement can be interpreted as being due to the effective electric field created by the first exciton, which leads to a Stark shift of the transition involved in the generation of the second e-h pair.[361]

The effect of Coulomb interactions on optical gain, however, can be both negative and positive depending on the sign of the exciton−exciton interaction energy (Δ_{XX}). In the case of exciton−exciton attraction, Δ_{XX} is negative and the absorbing transition moves downward in energy. This can be detrimental for lasing, as it effectively diminishes optical gain due to increasing interference from strongly absorbing, above-band-edge transitions (not shown in the simplified diagram of Figure 34a,b). On the other hand, exciton−exciton repulsion ($\Delta_{XX} > 0$) can be beneficial for lasing because it shifts the absorbing transition upward in energy, which effectively places the emitting transition in the absorption-free intragap region (Figure 34b). Furthermore, if the transition shift (defined by Δ_{XX}) is greater than the emission line width, optical gain can be obtained with single excitons, which removes any complications associated with Auger recombination.

Standard core-only and type-I thin-shell nanocrystals exhibit exciton−exciton attraction;[272,362] therefore, they are unsuitable for the practical implementation of the single-exciton gain concept. However, the sign of the exciton−exciton interaction energy can be reversed in type-II heterostructured nanocrystals, in which electrons and holes reside in the distinct parts of the structure (Section 3.4.2).[226] In core/shell QDs with the type-II alignment of the band-edge states, electrons and holes become separated between the core and the shell. If such a QD is excited with a biexciton, same-sign charges are forced to share the same part of the nanostructure (both electrons are in the core, both holes are in the shell, or *vice versa*), which enhances the repulsive component of the exciton−exciton interaction (Figure 34c). On the other hand, the attractive component is decreased, since the charges of the opposite sign are separated by a heterointerface. The net result of these trends is the development of strong exciton−exciton repulsion with energies on the order of 10s or even 100s of meV.[225,226,229,361]

To quantify the onset of the single-exciton optical gain, we will apply a modified version of the model from Figure 30, in which we assume that the energy of the $|X\rangle-|XX\rangle$ transition is different from that of the $|0\rangle-|X\rangle$ transition by the energy of the exciton−exciton interaction. We will consider here the simplest case when Δ_{XX} is greater than the transition line width. Under this assumption, absorption leading to generation of a biexciton ($|X\rangle-|XX\rangle$ transition) does not interfere with stimulated emission arising from single excitons ($|X\rangle-|0\rangle$ transition) and *vice versa*; that is, ground state absorption ($|0\rangle-|X\rangle$) transition) does not interfere with stimulated emission by biexcitons ($|XX\rangle-|X\rangle$ transition). In this situation, the optical gain splits into two distinct bands (attributed to single-exciton and biexcitons) separated by Δ_{XX} and having two different gain thresholds.

To analyze the single-exciton gain, we can limit our consideration to the two lowest states in the diagram of Figure 30 ($|0\rangle$ and $|X\rangle$) and assume that the QD ensemble contains only unexcited QDs and dots populated with single excitons, implying that the probabilities P_0 and P_X are restricted by the condition $P_0 + P_X = 1$. Using the transition rates shown in Figure 30b, we can express the single-exciton gain as $G = (c/n)\gamma n_{QD}\rho(P_X/2 - 2P_0) = (c/n)(\gamma/4)n_{QD}(5P_X - 4)$. This expression indicates that the gain onset is achieved when $P_X = 4/5$, which also defines the threshold average QD occupancy: $\langle N_g\rangle = P_X = 4/5$. Since $\langle N_g\rangle$ is less than 1, the nonzero gain coefficient required for the lasing action can be obtained without involvement of biexcitons. The maximum value of single-exciton gain is realized when $P_X = 1$, and it is given by $G_{0,X} = c/n(\gamma/4)n_{QD}$.

The latter expression indicates that $G_{0,X}$ is eight times lower than the saturated biexciton gain. However, despite being smaller in magnitude, single-exciton-gain has the advantage of being long-lived because its relaxation is controlled by fairly slow single-exciton recombination instead of fast Auger decay. This could simplify the realization of *cw* lasing because the threshold pump intensity scales as the inverse of the gain lifetime. If, for example, the single-exciton gain strategies could be applied to standard CdSe QDs, it would allow for the reduction of the *cw*-lasing threshold by a factor of *ca.* 100−1000 (defined by the ratio of τ_X and τ_{XX}) compared to biexciton gain. In the case of type-II QDs that have been used in practically realized single-exciton gain schemes, the improvement in the lasing threshold can be even greater, as spatial separation between electrons and holes reduces the overlap integral between their wave functions and, as a result, leads to extended single-exciton lifetimes.

The above considerations have neglected the broadening (Γ) of optical transitions, which can be quite large in QD samples due to size nonuniformity. The effects of a nonzero line width on the single-exciton gain threshold were first quantitatively analyzed in ref 361 and then in greater detail in ref 229. These analyses produced the expected trend, *i.e.*, no effect of Γ on the threshold in the weak-broadening limit ($\Gamma/\Delta_{XX} \ll 1$), and a convergence to the biexciton-gain threshold in the limit of a large line width ($\Gamma/\Delta_{XX} \gg 1$). The studies of refs 229 and 361 assumed that the biexciton radiative lifetime was half of the single-exciton lifetime (at that time, the scaling factor between $\tau_{r,XX}$ and $\tau_{r,X}$ was not well

DOI: 10.1021/acs.chemrev.6b00169
Chem. Rev. 2016, 116, 10513−10622

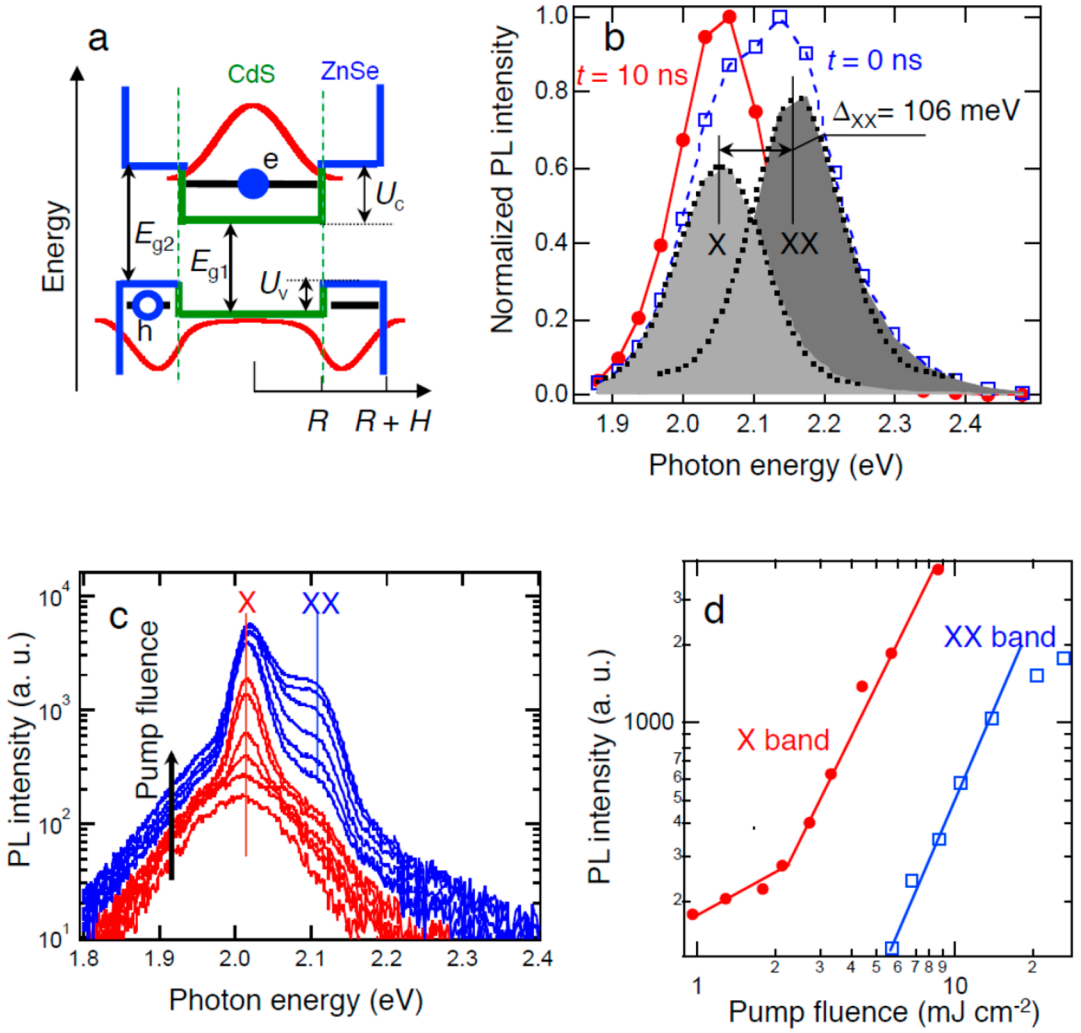

Figure 35. (a) Approximate band diagram of the type-II core/shell CdS/ZnSe QDs. The green and blue lines show bulk CdS and ZnSe band-edges, respectively, while black lines show electron and hole quantized levels in the QD case. Red lines are approximate distributions of electron and hole charge densities in this nanostructure. Arrows indicate bulk parameters: E_{g1} = 2.485 eV (CdS band gap), E_{g2} = 2.72 eV (ZnSe band gap), U_c = 0.795 eV (conduction-band offset), and U_v = 0.56 eV (valence-band offset). (b) Room-temperature PL spectra of CdS/ZnSe QDs with R = 1.6 nm and H = 2 nm recorded at time t = 0 (open squares) and t = 10 ns (solid circles) after excitation with a 100 fs laser pulse at 400 nm, which injects approximately 1.5 exciton per dot on average. The deconvolution of the early time spectrum into the two bands (shown by shaded areas; dotted lines are Gaussian fits) revealed the short-lived biexciton feature (labeled XX), which was blue-shifted from the single-exciton band (labeled X) by Δ_{XX} = 106 meV. These are a clear signature of giant exciton−exciton repulsion. (c) Pump-intensity-dependent emission spectra of the film of the same QDs as in panel b, indicating the development of a narrow ASE peak exactly at the center of the single-exciton emission band. At higher fluences, a second ASE band emerges, located at the position of the biexciton feature observed in time-resolved PL measurements of panel b. This evolution of the ASE spectra indicates that the onset of optical amplification was due to single-exciton gain, which was additionally contributed by biexciton gain at higher pump levels. (d) Both ASE features showed superlinear pump dependence above the onset of optical amplification that occurred at ~2 mJ cm^{-2} and ~6 mJ cm^{-2} for the single-exciton and biexciton gain mechanisms, respectively. Adapted with permission from ref 361. Copyright 2007 Nature Publishing Group.

established), which resulted in the gain threshold of $\langle N \rangle$ = 2/3 for the weak-broadening case. In our present analysis, we have used $\tau_{r,XX} = 1/4\tau_{r,X}$, which yields the threshold of 4/5.

The first examination of the idea of single-exciton optical gain using exciton−exciton repulsion also provided the first pieces of experimental evidence that it could be practically realized using so-called inverted ZnSe(core)/CdSe(shell) QDs (Section 3.4.4).[25] For a certain range of shell thicknesses, these structures exhibit partial spatial separation between an electron (localized primarily in the shell) and a hole (delocalized over the entire QD), a regime corresponding to *quasi*-type-II carrier localization, which in principle could produce exciton−exciton repulsion much as in true type-II QDs.[328,361] Some signatures of this effect, including a blue-shift of the ASE band from the peak of single-exciton emission and reduced ASE thresholds compared to standard core-only QDs, were observed in spectroscopic studies of ZnSe/CdSe QDs.[25]

Unambiguous evidence for optical amplification in the single-exciton regime was observed in studies of true type-II CdS/ZnSe QDs that favored localization of the electron in the core and the hole in the shell (Figure 35a).[361] Ultrafast PL measurements indicated that these QDs exhibited very strong exciton−exciton repulsion (Δ_{XX} of ~100 meV; Figure 35b) and, therefore, were well-suited for exploring the single-exciton-gain concept. Indeed, this effect was clearly observed in the ASE spectra of the close-packed CdS/ZnSe QD films (Figure 35c,d). As the pump fluence was ramped up, a sharp ASE peak emerged right at the center of the spontaneous emission band, indicating that it was due to

DOI: 10.1021/acs.chemrev.6b00169
Chem. Rev. 2016, 116, 10513−10622

stimulated emission from single excitons. Importantly, at higher fluences, a second ASE feature appeared on the blue side of the single-exciton band (Figure 35c,d), which was due to the usual biexctonic gain mechanism. The blue-shift of the biexciton ASE band from the single-exciton line provided yet another confirmation of strong exciton−exciton repulsion in these type-II QDs. As expected, the lifetime of the single-exciton gain band was considerably longer than the biexciton Auger lifetime (τ_g = 1.7 ns versus τ_{XX} = 210 ps),[229] indicating the significant promise of single-exciton gain strategies for the realization of QD-based lasing devices that do not require pumping with very short optical pulses, and instead can operate with more readily available long-pulse lasers and potentially *cw* pump sources. As discussed in the next subsection, the use of a single-exciton gain approach recently allowed for the realization of multicolor, low-threshold ASE and the first demonstration of a vertical-cavity surface-emitting laser (VCSEL) based on colloidal nanocrystals,[363] as well as single-mode lasing using spherical microspheres.[364]

5.5. Recent Advances and Future Challenges

Following initial experiments that established the principles of colloidal-QD lasing (Section 5.1), and introduction of advanced lasing concepts such as single-exciton gain (Section 5.4), this topic has captured the attention of many researchers attracted by the opportunity for the realization of solution processable lasing media with widely tunable emission wavelengths. Earlier efforts in this area focused on achieving true lasing action using various types of optical resonators including, for example, microring cavities[352,353] and distributed feedback (DFB) structures.[351] More recently, researchers explored QD-based VCSELs,[363] microsphere resonators,[364] and self-assembled resonators produced via a "coffee-stain" effect.[365] Several recent reports realized random lasing in films of colloidal QDs.[261,366]

In addition to using above band gap excitation, researchers also explored sub-band gap excitation using nonlinear two-photon[367,368] and even three-photon[368] absorption. Despite the expected increase in the threshold pump fluences for ASE and lasing, these excitation schemes may provide certain advantages including a more uniform excitation across the gain medium due to the increased penetration depth, and potentially reduced photodamage of the nanocrystals themselves as well as the capping layer and the matrix material.

However, the most common approach still remains traditional one-photon excitation. Over the years, considerable progress has been achieved in reducing the lasing thresholds in this pumping regime. As was discussed in previous subsections, in standard core-only or thin-shell QDs, the gain threshold in terms of the QD occupancy is close to one exciton per dot on average. However, if defined in terms of per-pulse fluence it can vary from one type of nanocrystal to another depending on their absorption cross sections. Since the latter scales directly with the nanostructure volume, it is not surprising that reduced thresholds have been shown for larger volume nanostructures such as nanorods,[369,370] thick-shell QDs,[328] tetrapods,[371] dot-in-rod particles,[372,373] and nanoplatelets.[374−376]

In Figure 36, we plot the ASE thresholds ($w_{th,ASE}$) versus nanocrystal volume (V_{NC}) for a large collection of nanostructures reported in the literature. This plot indicates the existence of a direct correlation between $w_{th,ASE}$ and V_{NC}. In fact, a "guide for the eye" described by the simple power dependence $w_{th,ASE} \propto (V_{NC})^{1.25}$ captures fairly closely the general trend. This confirms our earlier conjecture that in most of the cases the reduced ASE

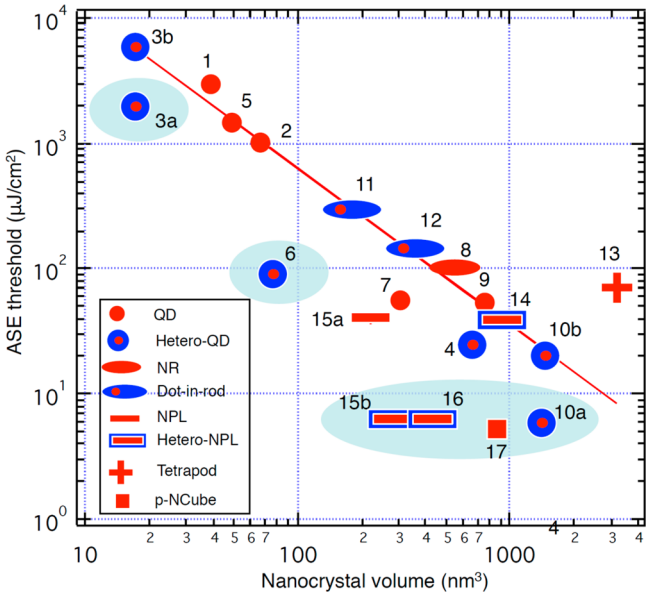

Figure 36. Survey of lasing thresholds versus nanostructure volume based on literature studies of nanocrystals of different morphologies including QDs (core-only and type-I heterostructures),[262,353,377−379] hetero-QDs (type-II and *quasi*-type-II),[261,328,361,363] nanorods (NRs),[370] dot-in-rods,[372,373] tetrapods,[371] nanoplatelets (NPLs),[374,375,380] and perovskite nanocubes (p-NCubes).[381] Points 3a and 3b correspond to onsets of single-exciton and biexciton ASE, respectively, measured for the same type-II CdS/ZnSe QDs (the volume is assumed to be that of the core, since the ZnSe shell did not provide a significant contribution to absorption at the pump wavelength).[361] Points 10a and 10b are for the core/shell CdSe/CdS QDs with a sharp and an alloyed interface, respectively.[261] Points 15a and 15b are for "core-only" CdSe and "core/shell" CdSe/CdS nanoplatelets, respectively.[375] The line is the dependence $w_{th,ASE} \propto (V_{NC})^{1.25}$, which reflects the general trend of decreasing lasing thresholds with increasing nanostructure volume.

thresholds have been primarily due to increased absorption cross sections at the pump wavelength.

The outliers in Figure 36 warrant closer inspection; we will focus on those that are below the general trend line (highlighted by light-blue shading). One, on the small-volume side (point 3a), corresponds to the first demonstration of the single-exciton ASE.[361] In this case, a favorable deviation from the general trend was achieved by employing a new gain mechanism. In fact, the ASE threshold for the biexciton gain in the same nanostructures (point 3b) remains in line with expectations based on the simple volume scaling.

The ideas of single-exciton lasing were taken further in very dense films (semiconductor volume fraction of ∼50%) of high PL QY (>80%) CdSe/ZnCdS QDs.[363] Using these structures, room-temperature ASE was demonstrated for three different emission colors (red, green, and blue) with a threshold as low as 90 μJ/cm^2 in the red (point 6 in Figure 36). This is roughly an order of magnitude lower compared to the values on the trend line of Figure 36.

The outliers in the plot of Figure 36 in the large-volume group comprise three different types of colloidal nanocrystals: nanoplatelets (points 15 and 16), perovskite nanocubes (point 17), and intentionally alloyed CdSe/CdSeS/CdS QDs (point 10a). As was discussed in Section 5.3, in the third case, deviation from the general trend originates from the suppression of Auger recombination due to the interfacial alloy. This assessment is

DOI: 10.1021/acs.chemrev.6b00169
Chem. Rev. 2016, 116, 10513−10622

supported by the fact that the same-volume QDs but without interfacial alloying reside right on the general trend line (point 10b).

In the case of perovskite nanocrystals (point 17 in Figure 36),[381] several factors may have contributed to the reduced thresholds, including high packing density allowed by the nanocube geometry and large gain cross sections resulting from fast radiative rates. Based on recent single-dot[382] and ensemble[383] measurements, Auger recombination in perovskite QDs is as fast as in, *e.g.*, II−VI QDs; therefore, the improvement in the ASE threshold was probably not related to modifications in the Auger decay rate. Similar arguments also apply to the nanoplatelets. Auger decay is still fast in these nanostructures;[375,376] therefore, the improved ASE performance is likely derived from the improved packing and faster radiative rates compared to the QD samples.

Recently, nanoplatelets were reported to exhibit lasing under *cw* pumping.[376] This result, while intriguing, still requires additional validation. Specifically, the same study also reported ASE and lasing under pulsed excitation (point 16 in Figure 36). Based on the per-pulse threshold fluence ($w_{th,ASE}$ = 6 μJ/cm^2) and the measured biexciton lifetime (τ_{XX} = 124 ps), the expected threshold intensity for *cw* pumping can be estimated from $J_{th,las} = w_{th,ASE}/\tau_{XX}$, which yields ~5 × 10^4 W/cm^2, a value considerably higher than that reported for cw lasing in ref 376 ($J_{th,las}$ = 6.5 W/cm^2).

The above literature overview indicates that most of the improvements in the ASE and lasing performance of colloidal nanocrystals have so far been achieved through a trivial control of the absorption cross sections using larger volume nanostructures. This approach, however, limits the range of spectral tunability to energies close to the parental bulk semiconductor band gap, and also is unlikely to allow for achieving the important milestone of *cw* lasing, as even large-volume nanostructures (*e.g.*, nanoplatelets) still exhibit large rates of Auger recombination.

Instead, a promising route toward a practical demonstration of lasing under *cw* excitation involves "interface-engineering" as a means for suppressing Auger decay.[261] The biexciton Auger lifetimes in existing alloyed nanocrystals are already on the nanosecond time-scale, approaching those of radiative decay. Further work in this area may focus on boosting the emission efficiency of interface-engineered QDs and increasing the degree of Auger-decay suppression by fine-tuning the composition and the thickness of the intermediate alloyed layer. Improvements in QD packing density and the optical quality of the QD solid may also help in reducing ASE thresholds to practical levels achievable with *cw* pumping. Interesting opportunities are also associated with extension of Auger-decay engineering strategies to perovskite nanocrystals and 2D nanoplatelets. These nanostructures already show strong ASE/lasing performance, which can be further boosted by suppressing parasitic carrier losses via Auger recombination.

After *cw* lasing under optical excitation, the next important milestone is the realization of lasing under electrical injection. This line of research might be facilitated by recent advances in QD-LEDs (Section 6). An important intermediate result would be the demonstration of stable devices with a very high injection current sufficient for exciting the majority of the QDs in the emitting layer with multiexcitons. This challenge directly relates to the problem of the EQE droop at high currents, and its resolution might again lie in the development of methods for effective control of Auger recombination.

The development of injection-based QD lasers may also require new LED architectures, as at present, the active emitting layers are too thin to serve as effective waveguides. The existing charge injection strategies, however, are not readily adaptable to thicker QD multilayers. On the other hand, the QD community involved in solar-relevant research has developed effective strategies for fabricating thick absorbing layers of the QDs that exhibit excellent charge transport properties. Perhaps a combination of expertise, materials, and approaches from the LED and solar QD communities will converge upon a viable route toward practical realization of highly emissive, droop-free LEDs with thick emissive layers suitable for implementing ideas of QD laser diodes.

6. QUANTUM DOT-BASED LIGHT-EMITTING DIODES (QD-LEDS)

6.1. Electroluminescence (EL) from QDs

Electroluminescence (EL) is the phenomenon of light emission from a material excited by electric current. EL in semiconductor structures (such as diodes) is the result of radiative recombination of charge carriers (electrons and holes) that are injected into an emissive material from contact electrodes, often through interceding charge transport layers (CTLs) possessing suitable band positions (Figure 37a). Photons produced by the EL process have an energy that is equivalent to the energy difference between the electron and hole states in the emissive material, *i.e.*, the valence-band (VB) edge and conduction-band (CB) edge in inorganic semiconductors, or the highest-occupied molecular orbital (HOMO) and lowest-unoccupied molecular orbital (LUMO) in organic semiconductors. This spectrally specific and narrow emission distinguishes EL from other light generation mechanisms, such as the broadband blackbody radiation of incandescent bulbs, or fixed, multiline atomic emission spectra of sodium or mercury vapor lamps. The advantages of colloidal QDs for use in EL devices are derived from their narrow emission bandwidth and the freedom of band gap tunability achievable by changing QD size, chemical composition and internal structure.

Similar to conventional light-emitting diodes (LEDs), QD-LEDs typically have a *p*-i-*n* structure, which comprises an anode, a hole transport layer (HTL), a QD emissive layer (EML), an electron transport layer (ETL), and a cathode (Figure 37a). Under forward bias, electrons and holes are injected from opposite electrodes and delivered by charge transport layers (CTLs) toward a QD EML, in which the injected carriers recombine to generate light. Since the first demonstration,[50] QD-LEDs have continued to evolve, which has resulted in steady improvement in their optoelectronic performance. Many specific advances in QD-LEDs have been produced by successful adaptation of materials, architectures, and processing techniques borrowed from the more mature field of organic LEDs (OLEDs). Because of similarities between QDs and organic molecules, particularly in how they are processed into device architectures, QD-LEDs can offer many of the same beneficial features as OLEDs, such as compatibility with a variety of rigid and flexible substrates (*e.g.*, glass, plastics, or fabric), and potential for ultrathin profile, lightweight, and large-area devices.

A large number of established synthesis protocols (Section 3) provide access to colloidal QDs with narrow and finely tunable emission spectra spanning an extremely wide energy range from the UV into the IR. Spectral tunability and narrow emission peaks are the primary motivations for the development of QD-

DOI: 10.1021/acs.chemrev.6b00169
Chem. Rev. 2016, 116, 10513−10622

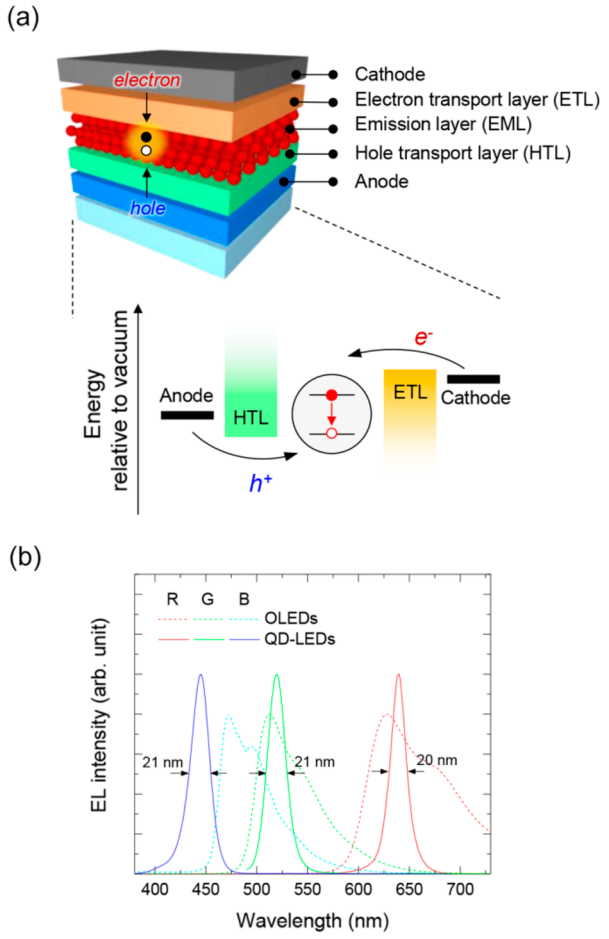

Figure 37. (a) General schematic of a *p*-i-*n* QD-LED structure (top) along with the corresponding energy band diagram (bottom). Electrons (holes) from a cathode (an anode), transported by electron (hole) transport layers, are injected into an active QD layer, where they recombine to produce light. (b) Typical EL spectra of red-, green-, and blue-emitting QD-LEDs (solid lines) and OLEDs (dashed lines). Reproduced with permission from ref 360. Copyright 2013 Material Research Society.

LEDs as potential replacements for OLEDs. Figure 37b compares representative EL spectra of LEDs based on red-, green, and blue-emitting QDs (solid lines) with those of OLEDs (dashed lines). The EL spectra of OLEDs comprise multiple emission peaks owing to the strong electron−phonon coupling in organic semiconductor materials; as a result, the overall EL spectral width is large, typically exhibiting a full-width at half-maximum (fwhm) of 40−60 nm. On the other hand, the spectral width of QD emission is controlled by the distribution of size, shape, and composition within a given QD ensemble, and for the best samples it approaches the line widths observed for individual QDs in single-dot measurements of ∼20 nm (Figure 37b).[381,384,385] This exceptional color purity is particularly important for applications in displays with an extended color gamut (see Section 6.4.1 for details).

Another large advantage of QDs over organic molecules is the absence of intrinsic limits on the maximum EL efficiency imposed by spin selection rules. In OLEDs, electrically injected electrons and holes can form an exciton with a total spin state of either 0 (singlet, 25% probability) or 1 (triplet, 75%). Since organic semiconductors strictly obey the spin selection rules that forbid radiative recombination of triplet states, statistical considerations limit their internal quantum efficiency (IQE) to 25% (IQE is defined as the ratio of the number of photons emitted inside the active layer to the number of injected e-h pairs). Therefore, for the past two decades, a major focus in the OLED area has been on a molecular design seeking to utilize the triplet states for radiative recombination. The explored strategies include the use of heavy-metal containing molecules with strong singlet−triplet mixing[386−388] or molecules with a small splitting between the singlet and triplet states (on the order of room-temperature thermal energy, ∼26 meV), which facilitates reverse intersystem crossing and leads to so-called thermally activated delayed fluorescence.[389−391] In contrast to organic molecules, semiconductor QDs typically exhibit only a small dark−bright exciton splitting (1−15 meV),[33,78,392] which allows for efficient thermal excitation of dark excitons into the bright state at room temperature (see Section 2.5). As a result, QDs are not affected by statistical limitations existing in OLEDs.

Since 1994, when the first prototype QD-LED was demonstrated,[50] a considerable improvement in the peak external quantum efficiency (EQE, defined as the ratio of the number of photons extracted from the device to the number of injected e-h pairs) has been achieved via continuous improvements in both the device architecture as well as the quality of QD emitters (Figure 38). Early QD-LEDs utilized a device architecture similar to that of OLEDs, but the resulting performance, including efficiency, brightness, and stability, was by far inferior to that of structrues based on organic emiters.[393] A leap in the performance of QD-LEDs was achieved by adopting inorganic CTLs,[394] and specifically metal oxides (*e.g.*, ZnO) as ETL materials.[317] Recent high-performance QD-based devices have utilized hybrid CTLs, *i.e.*, an inorganic ETL and an organic HTL.[285,318−320,391,395,396] This type of architecture allows for obtaining efficiencies and brightnesses that are comparable to those of state-of-the-art OLEDs. The demonstrated record peak EQEs for QD-LEDs are 20.2% for red,[318] 14.5% for green,[319] and 10.7% for blue.[319] The highest reported brightnesses are 106,000 cd m^{-2} for red,[320] 218,800 cd m^{-2} for green,[317] and 7,600 cd m^{-2} for blue[321] (see Section 6.3 for a discussion of the factors that determine EQE); these values exceed the requirements for use in both displays and lighting (see Section 6.4). Furthermore, prototype QD-LED-based monochromatic[322] and full-color displays[323] have also been demonstrated. These advances collectively evince the significant potential of colloidal QDs as a materials platform for the realization of the next generation of displays and solid-state lighting devices.

6.2. Device Structure and Operational Mechanism

Brightness, lifetime, and efficiency are the critical performance characteristics of LEDs. Requirements for LED brightness depend on the specific application; in general, 100−1,000 cd m^{-2} is adequate for displays, and 1,000−10,000 cd m^{-2} is required for lighting.[397] The typical industry standard for the LED lifetime is over 10,000 h of operation. The efficiency should be as close as possible to the ideal values of 100% IQE and ∼20% EQE within the application-specific brightness range. The high efficiency is particularly important for application in portable electronics where low energy consumption is essential. Low quantum-efficiency devices also produce an abundance of excess heat, which can further affect both device performance and lifetime.

High PL QYs, narrow line widths, and the inherent stability of their inorganic cores make QDs very promising for applications in EL devices. However, a considerable obstacle has been the

DOI: 10.1021/acs.chemrev.6b00169
Chem. Rev. 2016, 116, 10513−10622

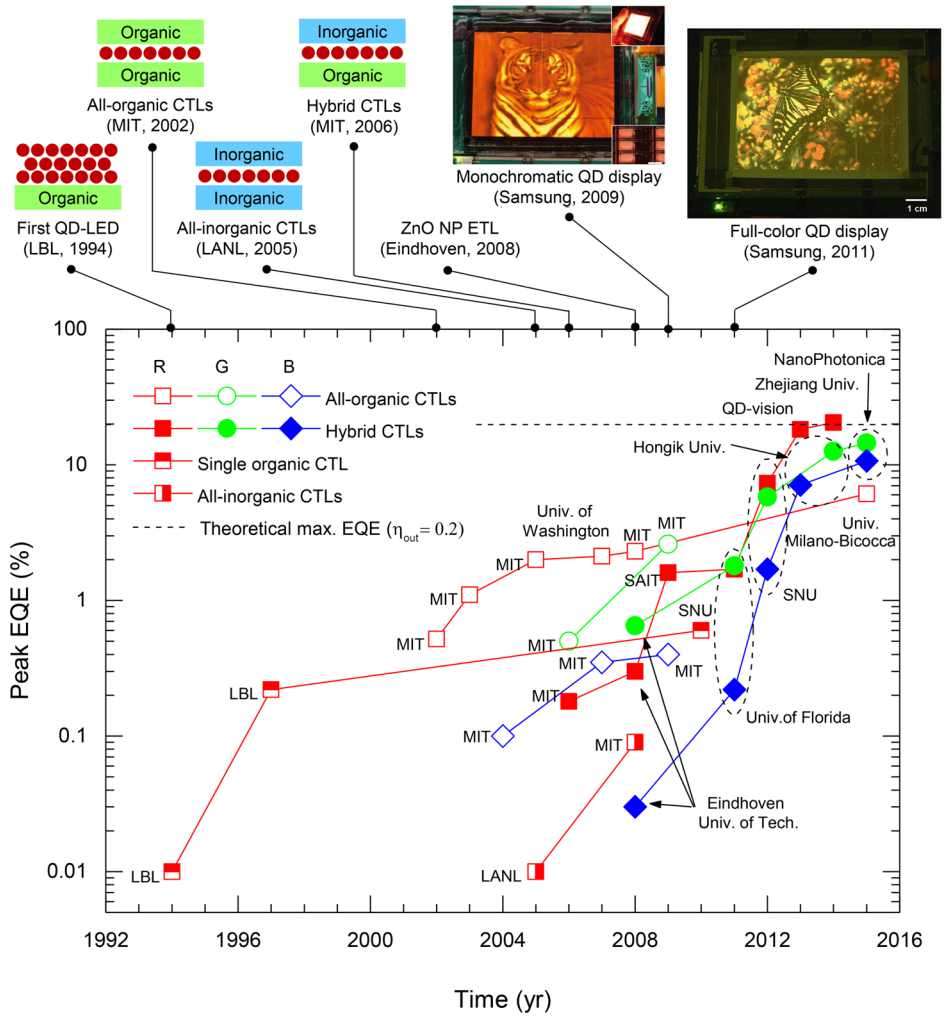

Figure 38. Progress in the performance of QD-LEDs evaluated in terms of the peak external quantum efficiency (EQE) from 1994 to 2015. The devices are categorized according to the emission color (R for red, G for green, and B for blue) and the type of charge transport layers (CTLs). Notable developments in the evolution of QD-LEDs are highlighted at the top of the chart. Figures reproduced with permission from ref 322 (monochromatic QD display) and ref 323 (full-color QD display). Copyright 2009 and 2011 Nature Publishing Group.

development of a device architecture that is compatible with QDs, specifically one that for a given QD formulation allows for balanced injection of electrons and holes over a wide range of operational currents. QD-LEDs to date can be categorized by the types of CTLs used for electron and hole injection. The earliest generation of devices used an "organic/QD" bilayer structure (Figure 39a),[50] combining a conjugated polymer [*e.g.*, poly(p-phenylenevinylene), PPV] as a HTL and a QD multilayer serving as both ETL and EML. These devices showed very low efficiencies (EQE = 0.001−0.01%), poor brightness (~100 cd m^{-2}), and considerable parasitic polymer-related emission observed in addition to QD emission. The deficiencies of these devices likely originated from charge imbalance, more specifically an excessive amount of electrons injected into the EML, which led to the formation of charged excitons decaying not by radiative processes but by nonradiative Auger recombination (Section 4).[285,360] Furthermore, as a result of the excessive electron injection, a considerable fraction of electrons could pass through the EML and eventually form excitons within the polymer layer instead of the QDs. This resulted in "contamination" of the EL spectra by polymer emission observed together with the emission from the QDs. Interestingly, as was suggested by several studies,[393,398] at least a portion of the excitons formed in polymer molecules could be redirected into the QD layer by Förster resonant energy transfer, which would recover some of the efficiency losses associated with the "leakage" of the current through the QD layer (Figure 39a, bottom).[393,398] An interesting possibility of using such energy transfer as an alternative method for efficient, noncontact excitation of the QDs was examined by Achermann et al.,[399] using structures combining an InGaN quantum well and a proximal layer of CdSe QDs.

Some additional problems of the earlier devices wherein the QD layer played the role of both an EML and a CTL were associated with the poor conductivity of QD solids. To resolve this issue, the next generation of devices explored architectures wherein QDs played solely the role of light emitters. In the first demonstration of this type of LED, a single monolayer of QDs was sandwiched between the organic ETL and the HTL (Figure 39b).[393] To fabricate these devices, Coe et al.[393] exploited spontaneous phase separation during spin-casting of a mixed solution containing QDs and hole-conducting organic molecules, which allowed them to produce a well-defined EML/HTL bilayer. To complete the device, a hole-blocking layer (HBL) and an organic ETL were deposited by thermal evaporation. The use of an organic ETL between the QD EML and the cathode helped regulate the electron flow into the QDs, while incorporation of

DOI: 10.1021/acs.chemrev.6b00169
Chem. Rev. 2016, 116, 10513−10622

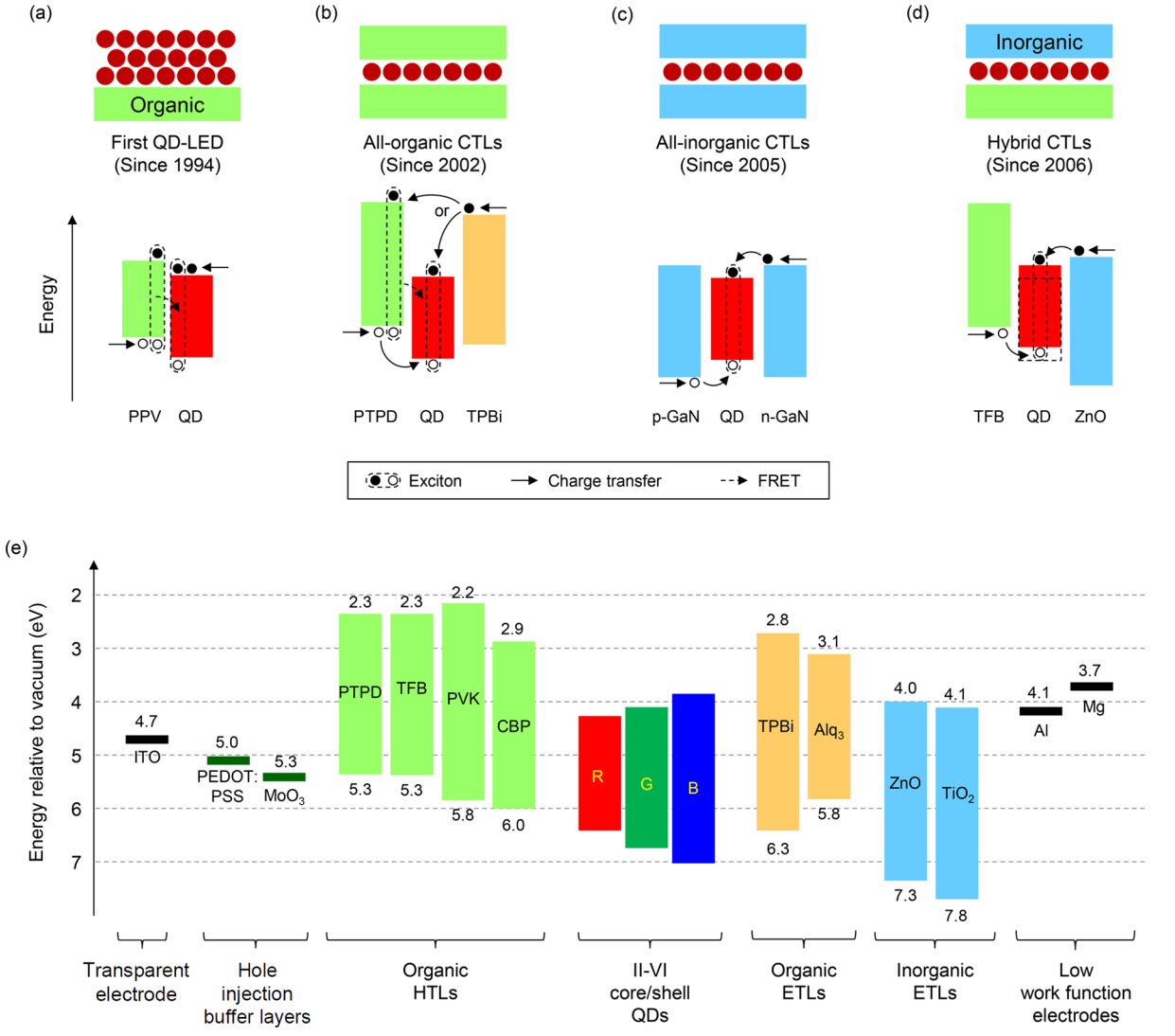

Figure 39. Simplified device structures of QD-LEDs (top) and their typical energy level diagrams (bottom). (a) A single organic (*e.g.*, PPV) charge transport layer (CTL) and a QD multilayer, which serves as both an emitting and a charge transport layer. (b) All-organic CTLs: a QD monolayer sandwiched between two organic CTLs (*e.g.*, TPD as a HTL and TPBi as an ETL). (c) All-inorganic CTLs: a QD monolayer sandwiched between two inorganic (*e.g.*, *p*- and *n*-GaN) CTLs. (d) Hybrid CTLs: an organic layer (*e.g.*, TFB) is usually used for hole injection into the VB of QDs, while an inorganic layer (*e.g.*, ZnO) for electron injection into CB of QDs. (e) Energy level positions for several typical metal electrodes (work function), hole injection buffer layers (modified work function in contact with ITO), organic CTLs (HOMO/LUMO states), inorganic CTLs (valence and conduction band edges), and II−VI QDs (band-edge electron and hole states). Abbreviations are explained at the bottom of the figure.

the HBL prevented hole leakage through the QD EML into the ETL. The resulting effect of these device modifications was the improvement of the charge balance within the QD EML, the suppression of EL from the ETL, and an increase in overall device efficiency. The first devices with "all-organic CTLs" demonstrated EQEs of ∼0.5%; subsequently, the EQE values were improved up to several percent.[400−407]

Despite the considerable progress in device performance achieved with all-organic CTLs, peak EQE was still far below the theoretical limit of ∼20%, determined by optical outcoupling (see Section 6.3). Imbalanced charge injection remained a significant factor: although the presence of organic CTLs between the EML and electrodes was shown to moderate charge injection, the band positions of traditionally used organic materials (Figure 39e) are not ideally suited for CdSe-based QDs. Specifically, the large offset from the LUMO of typical organic ETLs and the QD conduction band edge means that electron injection is strongly energetically favorable, even without an applied bias. At the same time, holes in the same all-organic device structure face an energetic barrier in transiting from the HTL to the QDs, requiring a significant overpotential.[317] The prevalence of the electron over hole injection current leads to an excess amount of electrons in the emitting layer. The resulting negatively charged dots are then susceptible

DOI: 10.1021/acs.chemrev.6b00169
Chem. Rev. 2016, 116, 10513−10622

to nonradiative Auger recombination (Section 4),[285,360] lowering the overall EQE.

In parallel with efforts on organic CTLs, all-inorganic CTLs were also explored, motivated by their inherent structural robustness and excellent electrical conductivity. The first QD-LED with all-inorganic CTLs comprised a CdSe/ZnS QD monolayer sandwiched between *p*- and *n*-doped GaN.[394] This structure offers an improvement over for typical organic CTL devices, in that both CdSe QD band-edge positions fall within the bandgap of GaN. This corresponds to a type-I alignment of electronic states, which enables direct injection of both electrons and holes into the QDs. Follow-up efforts on all-inorganic CTLs explored metal oxides for realizing both ETLs (*e.g.*, ZnO, SnO_2, ZnO:SnO_2, and ZnS)[408] and HTLs (*e.g.*, WO_3[408] and NiO[409]). QD-LEDs with inorganic CTLs exhibited enhanced long-term operational stability and could sustain considerably higher current densities (up to 4,000 mA cm^{-2})[408] compared to all-organic CTLs (maximum current density of ∼1,000 mA cm^{-2}).[405] However, the efficiencies achieved with all-inorganic CTLs (EQE < 0.01% for the *p*-GaN/QD/*n*-GaN structures[394] and < 0.1% for the NiO/QD/ZnO:SnO_2 structures[409]) were markedly lower than those of devices with all-organic injection layers; this has been attributed to the deterioration of the QD EML during the deposition of inorganic CTLs[394] as well as to exciton quenching via nonradiative energy transfer between the QDs and heavily doped inorganic films.[408]

Most recently, efforts in QD-LEDs have focused on "hybrid CTLs" (inorganic ETL and organic HTL) that combine the electrical/chemical robustness of inorganic materials with the relatively benign deposition of organic conducting layers. The first example of this structure was demonstrated by Caruge et al.,[410] who utilized NiO as the HTL and Alq_3 as ETL. The NiO HTL was expected to improve the charge balance within QDs due to the proximity of its valence band edge (∼6.7 eV) to that of QDs (∼6.8 eV); indeed, the increase in hole injection was so pronounced that the best performance was achieved using NiO with intentionally higher resistivity. Moreover, the insolubility of sputtered NiO toward organic solvents permitted direct deposition of the QD EML via conventional solution-based methods. This strategy is an example of so-called "orthogonal processing" in which deposition of each given device layer is accomplished without causing damage to the previous layer. It has been widely utilized for the fabrication of low-cost solution processed optoelectronic devices,[411] including QD-LEDs with all-organic CTLs[412−414] or sol−gel-processed TiO_2 ETLs.[322,323] Although promising, the first reported hybrid devices did not show a substantial improvement in performance: measured efficiencies (EQE of ∼0.2%) were comparable to those of QD-LEDs with all-inorganic or all-organic CTLs.

An important advance in QD-LEDs with hybrid CTLs was made by Stouwdam and co-workers.[415] They utilized solution-processable ZnO nanoparticles as the ETL, effectively recovering the benefits of an inorganic CTL without the deleterious consequences of harsh fabrication conditions (*e.g.*, metal−organic chemical vapor deposition or radio frequency sputtering). The band-edge positions in a ZnO nanoparticle film (Figure 39e) allow for injection of electrons from a cathode into QDs at a rate comparable to that of hole injection from typical organic HTLs, while at the same time preventing hole leakage from the QD EML, another step forward in improving charge balance in the QD layer. Subsequent optimization of materials and fabrication methods[317,416] has resulted in considerable progress in the performance of QD-LEDs with hybrid CTLs, and as a class such devices currently exhibit the highest EQEs and brightnesses (Figure 38).[395,285,318−320,391,396]

6.3. Performance-Limiting Factors: A Spectroscopic Perspective

LED performance is typically evaluated in terms of photometric quantities such as luminous flux measured in lumens (lm), luminance measured in candelas per m^2 (cd m^{-2}), and luminous efficacy measured in lumens per watt (lm W^{-1}). All of these quantities account for the nonuniform, roughly bell-shaped human eye sensitivity curve across the visible spectrum, which is centered at ∼2.23 eV (see Section 6.4.2). This nonuniform response results in a drastic color dependence of brightness. The same number of photons, for instance, of energy 2.3 eV (green) are 10-fold higher in brightness than if they were 2.7 eV (blue) or 2.0 eV (red). Two other useful and intuitive quantities, often used in research publications, are IQE (η_{IQE}) and EQE (η_{EQE}). These are related by the light extraction (or outcoupling) efficiency (η_{out}): $\eta_{EQE} = \eta_{out}\eta_{IQE}$. EQE can further be related to the emission QY of the QDs (η_{em}) and injection efficiency (η_{inj}; the number of excitons generated in the QDs relative to the number of injected e-h pairs) by the following relationship: $\eta_{EQE} = \eta_{inj}\eta_{em}\eta_{out.}$ Many of the advances described in the preceding section were the result of efforts to specifically improve η_{inj}, which in the earliest QD-LEDs with imperfect device structures (*e.g.*, carrier leakage to CTLs, possibly with parasitic emission) and large carrier injection barriers (Figure 39a-d) was quite far from ideal. In general, an increase in QD band gap reduces η_{inj} because it creates a larger injection barrier[317] for one or both carriers (Figure 39e); this is regarded as one of the main reasons peak EQE particularly of blue QD-LEDs is lower than that of green and red QD-LEDs. However, recent advances in device architecture and optimized device fabrication methods, particularly in the employment of ZnO nanoparticle ETLs, has improved η_{inj} to close to unity for red QD-LEDs.[318]

On the other hand, η_{out}, defined as the fraction of emitted light that actually escapes from the surface of a device, is determined largely by the optical properties of the materials of the LED, and imposes substantial limitations. In fact, in typical devices, a majority of the light generated in the EML will remain confined within the device due to the large refractive index constrast between the various inorganic and organic layers, ITO, glass, and air. The critical angle (relative to normal) for total internal reflection (θ_r) is given by Snell's law, and defines an "escape cone" for each interface, outside of which light will remain trapped. For instance, the organic semiconductors (n = 1.6−1.8) and ITO (n ∼ 1.8−2.2) interface results in $\theta_r \sim 55°-65°$, while the glass (n = 1.5) and air (n = 1) interface yields $\theta_r = 41.5°$. Light outside of the critical angle for each layer propagates within the plain of the device. A small fraction of such light can be outcoupled at the edge of the device, or escape through a scattering event that redirects it within the escape cone; a larger fraction is eventually lost to absorption by organic or QD layers, or attenuation by excitation of surface plasmon modes of the metal electrode.[417] In principle, η_{out} can be simply derived from the integration of light intensity over the escape cone. In real devices, however, the multiple reflection events in layered structure, the presence of a reflective electrode, the effects of dipole orientation, and optical interference effects can complicate precise prediction. In many cases, η_{out} can be simply expressed as $\xi\, n^{-2}$ for large n, where ξ is an empirical constant related to dipole alignment and device geometry, and n is the refractive index of surrounding layers. In case of a device with a reflective cathode,

DOI: 10.1021/acs.chemrev.6b00169
Chem. Rev. 2016, 116, 10513−10622

assuming an isotropic distribution of emitter dipole orientations yields $\xi \approx 0.5$,[418,419] which translates to a value of η_{out} of ~20% for typical devices. In Section 6.5.2, we overview methods for increasing outcoupling efficiency through advanced device engineering.

The final contribution to EQE reflects the QY of the emission process itself, η_{em}. Deviations from unity for this term are strongly material-dependent: in the case of QDs, primary factors include nonradiative recombination via defects, energy transfer within the QD EML (followed by nonradiative decay in an acceptor QD), and Auger recombination in charged dots. We analyze each of these factors in greater detail below.

Empirically, the emission QY of a QD is equal to the ratio of the radiative recombination rate (k_r) to the total recombination rate, which includes contributions from both radiative and nonradiative (k_{nr}) processes: $\eta_{em} = k_r/(k_r + k_{nr})$. Factors influencing k_r and typical radiative lifetimes for QDs are discussed in Section 2.5. For a singly excited QD, nonradiative losses are dominated by recombination at structural defects that are most often associated with the QD surface (Figure 40a). A typical strategy for eliminating surface defects is overcoating the emissive core with an inorganic semiconductor material of a wider bandgap to produce a type-I heterostructure (Section 3.4.1).[179,180] As discussed in Section 3.5, while a thicker shell should nominally be more effective at isolating core excitations from surface defects, other sources of defects (such as from strain) must be taken into consideration. Maximizing the stability and QY of core/shell heterostructured QDs by minimizing strain-induced defects results in positive impacts on LED performance.[319]

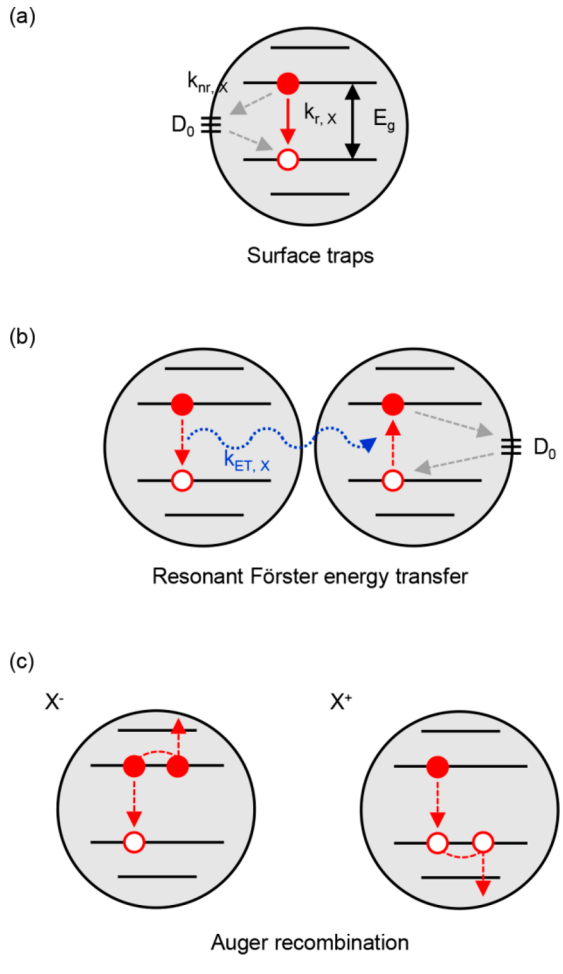

Figure 40. LED performance-limiting processes occurring in QDs. (a) Nonradiative recombination (rate $k_{nr,X}$) via surface defects (denoted as D_0) competing with the radiative band-edge transition (rate $k_{r,X}$). (b) Förster resonant energy transfer (rate $k_{ET,X}$) exacerbates nonradiative losses by allowing the exciton to sample defects not only in the oringally excited QD, but also in other QDs residing within the energy-transfer distance. (c) Nonradiative Auger recombination (see Section 4) in the presence of an extra electron (left) or a hole (right).

Exciton diffusion among QDs within EMLs can also be responsible for efficiency losses in QD-LEDs (Figure 40b). Typically, QD-LEDs utilize 1−4 monolayers of QDs in the EML. Because of the inherently small Stokes shifts of typical QDs (Section 2.4), there is significant overlap between their emission and absorption spectra. This means that excitons can diffuse in QD films by: (i) nonradiative Förster resonant energy transfer (ET), with an efficiency that varies with dot-to-dot distance, d, as $\sim d^{-6}$; or (ii) reabsorption of emitted photons by neighboring QDs, with a rate varying as $\sim d^{-2}$. Exciton diffusion intensifies the contribution to emission efficiency loss of fast nonradiative trapping, even if this occurs only in a minority of QDs, because it increases the number of QDs sampled by an exciton before it recombines radiatively. Since the ET rate depends on the energetic overlap between the emissive transition of the exciton "donor" QD and the absorbing transition of the exciton "acceptor" QD, resonant ET results in the directed migration of excitons in a close-packed ensemble from QDs with larger bandgaps to their counterparts of smaller bandgap. Thus, a telltale signature of ET is red-shifted ensemble emission (as compared to QDs dispersed in solution), and faster decay dynamics particularly on the high-energy side of the emission spectrum.[420,421]

Figure 41a demonstrates how these spectroscopic signatures of ET in QD films vary in CdSe/CdS core/shell QDs as a function of shell thickness.[422] The PL decay rate on the higher energy side of the PL spectrum (green) is faster in a film than in solutions of the same QDs (gray), but this difference gets smaller and eventually disappears in samples with progressively thicker CdS shells. This implies a considerable suppression of ET, which can be attributed to the increasing separation, d, between the nanocrystal cores even for adjacent QDs within the same film. QD-LEDs employing these CdSe/CdS QDs as EMLs have shown improved EQE with increasing shell thickness, which can be attributed to suppressed ET, but the extent of improvement is limited due to low PL QYs of thick-shell CdSe/CdS QDs and use of an unoptimized device structure.[422] With CdSe/CdZnS QDs with higher PL QYs, Lim et al. showed how increased shell thickness leads to improved retention of PL QYs of QDs in films (Figure 41b), due to substantial increase in ET time (Figure 41c); this manifested in a direct relationship between the shell thickness and IQE of the QD-LEDs[320] (Figure 41d). The ET rate, k_{ET}, can be extracted from the expression $Q_\infty = Q_0 k_r/[(k_r+k_{ET}(1-Q_0)]$, where Q_0 is PL QY of the noninteracting QD ensemble, Q_∞ is PL QY in the presence of ET processes, and k_r is the radiative rate.[360] ET times ($1/k_{ET}$) derived using this relationship clearly show the transition of ET mode from via Förster resonant ET (d^6 dependence) to an emission-reabsorption mechanism (d^2 dependence, Figure 41b-c).

In contrast to optical pumping, which creates carriers in the form of e-h pairs or excitons, in EL devices electrons and holes are injected into QDs independently of each other. When electron and hole injection currents are not perfectly balanced, individual QDs in the EML acquire a net charge. As was

DOI: 10.1021/acs.chemrev.6b00169
Chem. Rev. 2016, 116, 10513−10622

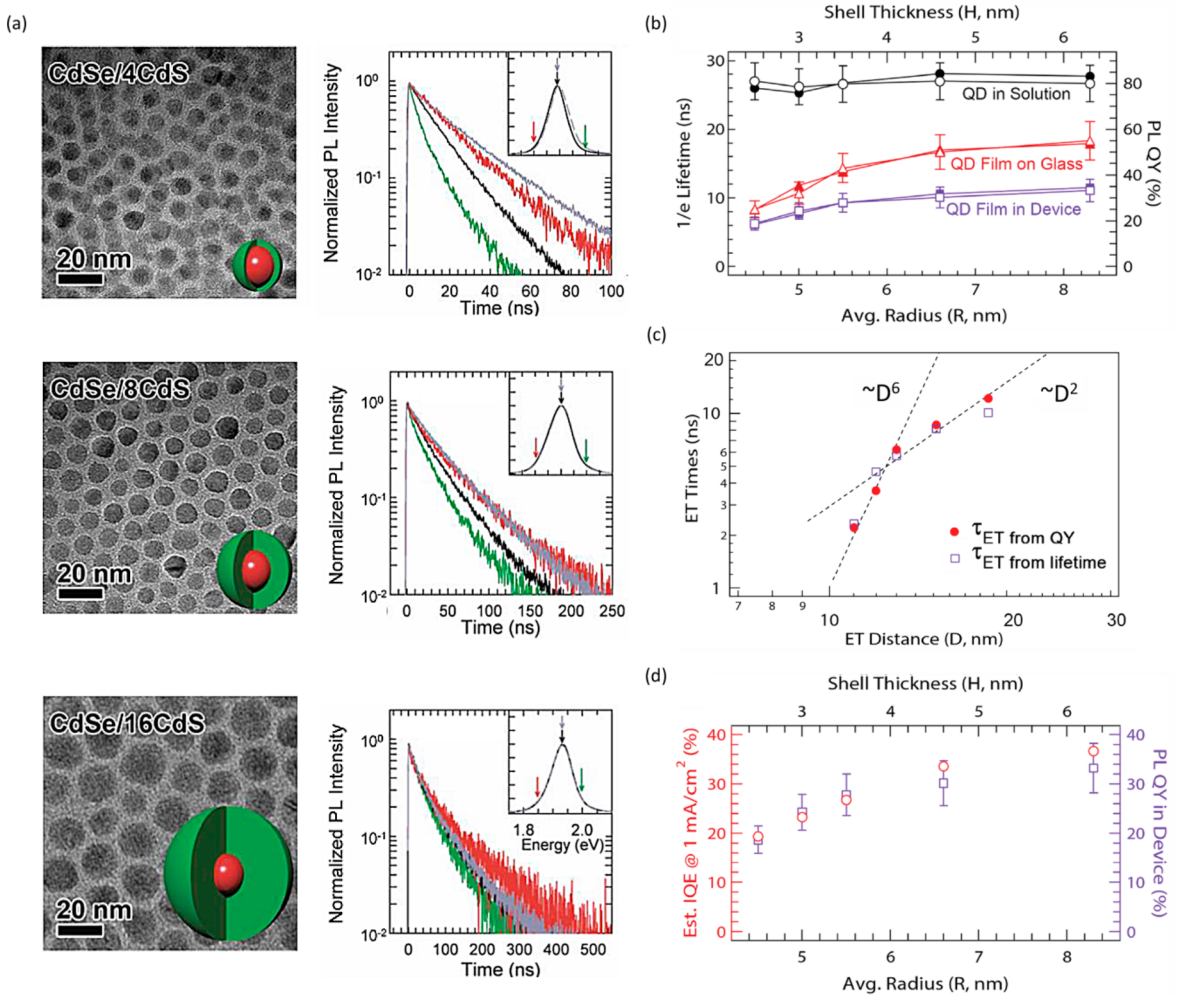

Figure 41. (a) Influence of core-to-core spacing on energy transfer in QD films. The increase in CdS shell thickness of CdSe/CdS QDs (shown in TEM images at the left, from top to bottom, H = 1.6, 3.2, and 6.4 nm) has a marked effect on the decay dynamics of dense QD films (right). The decay dynamics were collected at emission energies denoted by arrows in the insets, where the PL spectra of solution (dashed gray lines) and films (solid black lines) are displayed. Adapted with permission from ref 422. Copyright 2012 American Chemical Society. (b) PL QYs of a shell-thickness series of CdSe/CdZnS QDs in solution (black), on glass (red), and in QD-LEDs (purple). Energy transfer occurring in QD films can be suppressed by increasing core-to-core distance (proportional to average radius, R, when core size is held constant). The decrease in PL QYs of QD films in devices is attributed to spontaneous charging from ITO/ZnO. (c) Calculated energy transfer times from the PL QYs (filled circles) and the 1/e lifetime (open squares) of QD films as a function of dot-to-dot distance. (d) Estimated IQE at 1 mA cm^{-2} (left, circles) and PL QY of QD films (right, squares) in a device. Adapted with permission from ref 320. Copyright 2014 John Wiley & Sons, Inc.

discussed earlier (Section 6.2), this opens a new nonradiative decay channel via the Auger process (Figure 40c, and Section 4). In fact, studies of QD-LEDs with a ZnO ETL and an organic HTL reveal the propensity of QDs to acquire a net negative charge.[285] Under this circumstance, the PL lifetime of the QDs in a forward-biased device is dramatically reduced and approaches the Auger recombination lifetime of negatively charged trions (Figure 42a). This suggests that at least one of the factors limiting the performance of these structures is nonradiative Auger recombination. Since charge imbalance is expected to increase with increasing applied bias, the detrimental role of Auger decay should also increase. Thus, Auger recombination of charged QDs has been invoked to explain the so-called efficiency "droop" or "roll-off" phenomenon, that is, a decrease in the EQE at higher currents typically observed in QD-LED. These considerations suggest that optimization of QDs for applications in LEDs might involve not only improving their single-exciton PL QYs, but also the yields of charged and multiexciton states. The latter can be accomplished by developing approaches for reducing the rates of Auger recombination (see Section 4.3).

One strategy for suppressing Auger decay discussed in Section 4.3 involves "smoothing" the confinement potential by introducing an alloyed layer between the core and the shell, as was demonstrated by incorporating a thin layer of $CdSe_xS_{1-x}$ alloy at the interface between a small CdSe core and a thick CdS shell (Figure 42b–c).[86] The use of these QDs indeed improved device peak efficiency, and also led to a shift of the onset of EQE roll-off to a higher current (Figure 42d).[285] Improvements in device performance were directly correlated with a lengthening of charged-exciton and biexciton lifetimes (Figure 42c), confirming the assessment that Auger recombination is indeed one of the factors which limits the performance of QD-LEDs.

An additional approach to reducing Auger-related efficiency losses is to improve the balance between electron and hole injection. This is typically achieved by modifying the overall device architecture (Section 6.2); however, it can also be accomplished by modifying the QD emitters themselves. This

DOI: 10.1021/acs.chemrev.6b00169
Chem. Rev. 2016, 116, 10513–10622

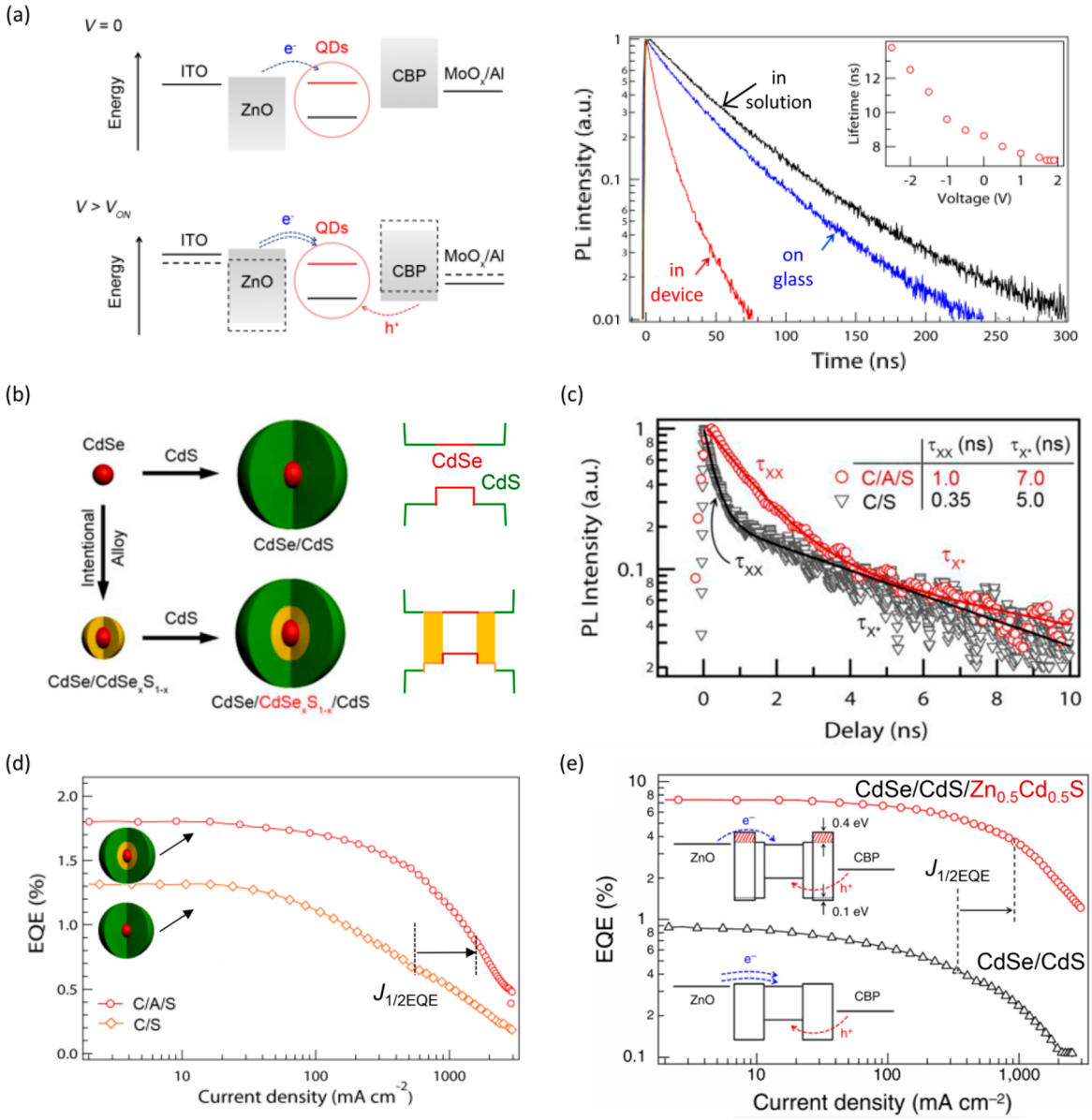

Figure 42. Mitigating the effects of QD charging in QD-LEDs. (a) Depiction of the charging of a QD by electron transfer from an adjacent ITO/ZnO ETL (left). PL decay dynamics of QDs in a solution, in a film on a glass substrate, and in an LED device (right). Inset: the PL lifetime as a function of applied bias before the EL turn-on; progressive shortening of the PL lifetime with increasing bias is a result of QD charging and concomitant Auger recombination. Adapted with permission from ref 285. Copyright 2013 Nature Publishing Group. (b) Schematic depiction of core/shell QDs with a "sharp" (top) versus "smooth" alloyed (bottom) interface along with corresponding band diagrams. (c) Initial fast component (<10 ns) of PL dynamics (after subtraction of single-exciton decay) measured for CdSe/CdS QDs with a sharp interface (C/S sample) and CdSe/CdSe$_x$S$_{1-x}$/CdS QDs with an intermediate alloy layer (C/A/S sample). The "smoothing" of the interfacial potential in the alloyed QDs leads to longer Auger lifetimes of both biexcitons (τ_{XX}) and charged excitons (τ_{X^*}). Adapted with permission from ref 86. Copyright 2013 American Chemical Society. (d) Incorporation of the alloy layer at the CdSe/CdS interface improves the LED EQE and increases the onset of the EQE droop (quantified in terms of the current, $J_{1/2EQE}$, at which EQE drops by half). These improvements in performance are a direct result of suppression of Auger recombination. (e) Suppression of QD charging is achieved by growing an outer shell of CdZnSe which creates a potential barrier limiting electron injection into the QDs. The resulting improvement in charge balance in the emitting layer leads to a considerable increase in the EQE and a delayed onset of the EQE droop. Adapted with permission from ref 285. Copyright 2013 Nature Publishing Group.

approach was explored in ref 285, in which a CdSe/CdS QD was overcoated with an additional shell of wider gap CdZnS that served as a mild barrier to electron injection from the ZnO ETL. Enhanced carrier balance in the resulting devices leads to a 5.8-fold enhancement in the peak efficiency, and a considerable increase (by a factor of 1.7) in the onset of the EQE droop (Figure 42e). These studies suggest even better performance may be achieved via a concerted approach to suppress Auger recombination and balance charge injection in the same device.

A number of other effects have also been implicated as possible sources for lost efficiency in QD-LEDs. For example, Joule heating elevates the temperature of operating devices, particularly at high current densities. It has been suggested that this can reduce emission efficiencies in a manner analogous to that of bulk semiconductor LEDs.[50,423] However, recent studies of PL of QDs at elevated temperatures suggest that the effect of heating may be related instead to increased surface trap-related recombination, which can be mediated and/or eliminated

DOI: 10.1021/acs.chemrev.6b00169
Chem. Rev. 2016, 116, 10513−10622

through inorganic passivation.[424,425] It has also been suggested that the electric field experienced by the QDs in an EML can pull the electron and hole within an exciton apart, either polarizing[426] or completely ionizing[427] it, which reduces the radiative recombination rate. An intriguing aspect of this argument is its contrasting prediction regarding the design of QDs for LEDs: while many models and studies find that thick-shell QDs should and/or do offer improved QD-LED performance (whether because of better charge balance and reduced Auger recombination,[285] reduced ET[320,422] or better resistance to heat-related surface trapping[424]), measurements of PL within a capacitive device structure suggest that thick-shell QDs should be more susceptible to field-induced polarization, decreasing device efficiency.[428] Further direct study of these disparate effects will be required to resolve their respective influence on QD-LED performance.

6.4. Applications of QD-LEDs

6.4.1. Full-Color QD Displays. To achieve the full range of color in a typical display, sources of single red, green and blue (RGB) colors are mixed in controlled proportions. Given fixed wavelengths and line widths for the sources of these three primary colors, it is possible to define an absolute color space, relative to a reference color space [*e.g.*, the Commission International de l'Eclairage XYZ (CIE XYZ) space], that encompasses all colors that can be generated. Examples of absolute color spaces that have become industry standards are displayed in the reference chromaticity diagram in Figure 43, and they include sRGB (widely used in general high-definition televisions), Adobe RGB (for printing), and Rec. 2020 (recommendation for ultrahigh-definition 4K and 8K televisions; Figure 43). Choosing primary colors to make the largest possible color triangle results in the greatest possible color variance to the human eye.

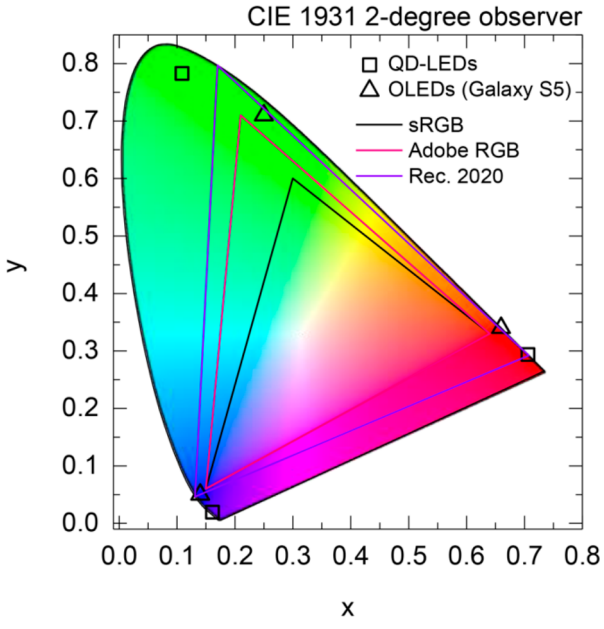

Figure 43. Representative RGB color spaces (solid lines) and chromaticity points of RGB QD-LEDs (squares) and cutting-edge OLEDs product (triangles) relative to the CIE 1931 chromaticity diagram. Chromaticity points of QD-LEDs are calculated from the PL spectra in Figure 37b. While the state-of-the-art OLEDs can only cover sRGB or Adobe RGB color space with the help of optical engineering (*e.g.*, optical cavity structure), QD-LEDs easily meet the current standards and satisfy Rec. 2020, which is to be the new standard for 4K or 8K ultra-high-definition TV.

Figure 43 also depicts the chromaticity points of the RGB spectra of QDs shown in Figure 37b (open squares) and those of state-of-the-art OLEDs used in mobile display (open circles). Conventional OLEDs (fwhm of 40−60 nm) do not reach the edges of spectral locus without elaborate engineering of the EL line width (*e.g.*, optical cavity structure) to meet the requirements of the display industry. By contrast, QD-LEDs offer around 20−30 nm fwhm that is tunable over the entire visible region[381,384,385] (Figure 37b). Because the emissions of these QDs are located close to the perimeter in the chromaticity diagram, they offer a wider color gamut that satisfies the current standard for displays as well as the recommendation for next generation displays, such as Rec. 2020.

For displays, three primary colored QD-LEDs need to be made in microsized pixel arrays. A large number of distinct pixel sets that consist of the RGB subpixels create the image. Finer pixel sizes allow for more natural images in displays. As an example of the demands of current and near-future technologies, in the case of 40-in. flat panel displays, pixel pitch needs to be 150 μm for full-HD, 1920 × 1080 pixel displays, but will need to be reduced to 35 μm for 8K UHD (7680 × 4320 pixels).[429] Further, increasing demands on mobile displays and computer monitors require defect-free fabrication at even higher pixel densities of over 300 PPI, because decreased viewing distance makes dead pixels much more noticeable. For example, the Retina LCD display on the iPhone 6plus (Apple, Inc.) offers 401 pixels per square inch[430] (PPI) with pixel pitch = 78 μm), while the Galaxy S6 edge (Samsung) offers 577 PPI with pixel pitch = 44 μm.[431] Accordingly, to compete with these conventional display technologies, QD-LEDs need to be pixelated on a scale approaching tens of micrometers.

The fabrication of QD EMLs in prototype devices usually uses spin-casting, which nonspecifically covers the entire substrate with QDs. Therefore, additional processes are required to pixelate red, green and blue QD emissive layers for realization of full-color displays. The microcontact printing method, a multistep approach that realizes patterning using an elastomer [*e.g.*, poly(dimethylsiloxane)] stamp, is the most widely used to fabricate QD pixel arrays.[321,429−431] In this method, QD patterns are formed by direct spin-casting of QD dispersions on the stamp[433,434] or by indirect transfer of QD patterns from QD-coated substrates[435] and then stamped onto a desired substrate. The stamp is molded using a silicon master engraved by photolithography, which, in principle, defines the ultimate pattern size limits. After the conceptual work for patterning of red, green, and blue QD EMLs was demonstrated,[433] Kim et al., demonstrated a full-color QD-LED display in 2011.[323] They placed red, green, and blue QD pixels (46 μm x 96 μm) on a metal oxide TFT array and realized 4-in. full-color displays with 320 × 240 pixel resolution (Figure 44a−c). Continuous optimization of the printing processes has reduced pattern sizes down to 6 μm, comparable to commercial LCD displays.[429]

In addition to the microcontact printing, mist printing[436] or inkjet printing[432,438−440] has been suggested as an option for QD patterning. Inkjet printing has received particular attention because of liberal design of patterns without prepatterns prepared by photo- or e-beam lithography that requires expensive and time-consuming processing. Recent advances in inkjet printing (so-called electrodynamic jet printing,[432] Figure 44d−g) have succeeded in fabricating minute QD pattern arrays (~5 μm) satisfying the basic requirements of pixel pitch for

DOI: 10.1021/acs.chemrev.6b00169
Chem. Rev. 2016, 116, 10513−10622

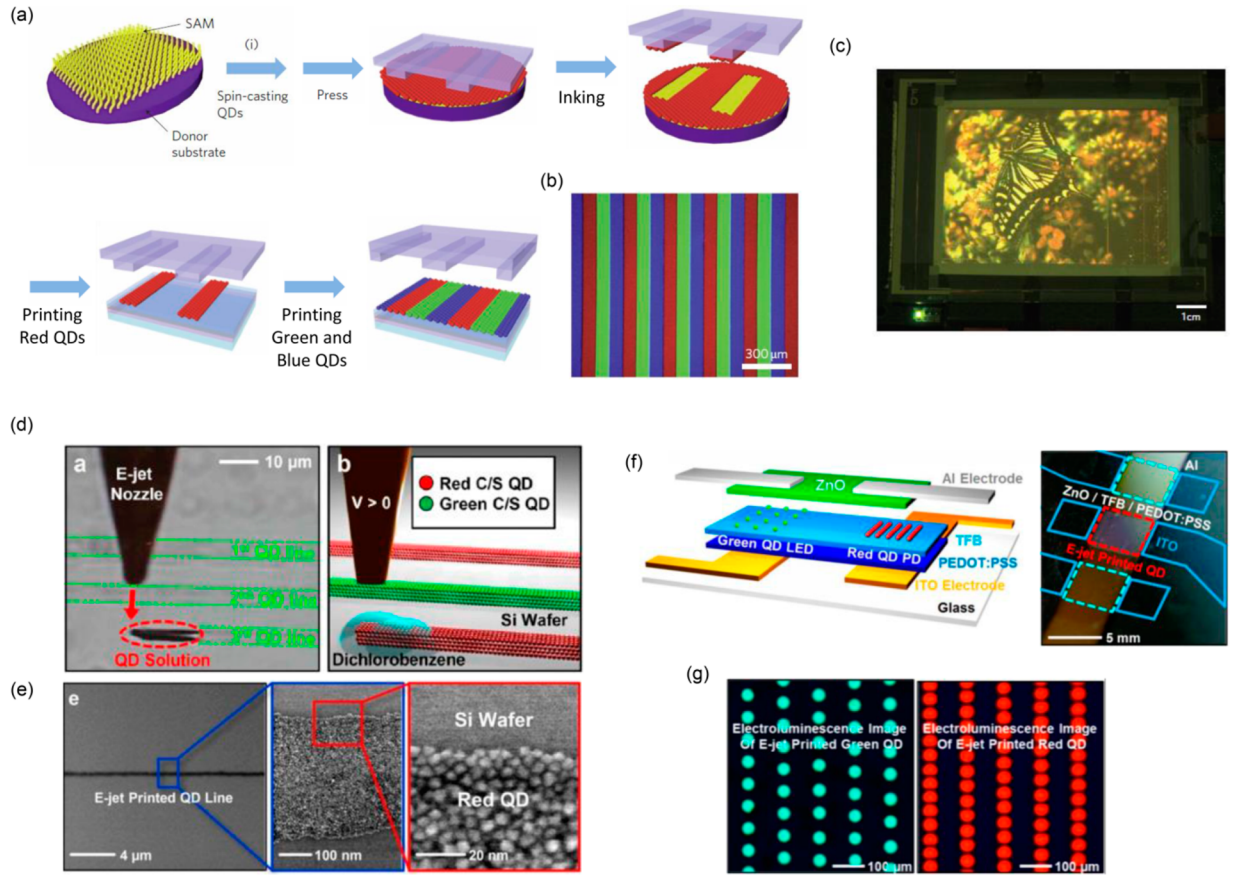

Figure 44. Fabrication of full-color QD-based display. (a) Patterning sequence of red, green, and blue QD stripes and (b) their optical microscopy image. (c) A 4-in. full-color QD display with a 320 × 240 resolution. Adapted with permission from ref 323. Copyright 2011 Nature Publishing Group. (d) A picture of an electrodynamic-jet (E-jet) nozzle (left) and a 3-dimensional schematic (right). A voltage applied between the substrate and nozzle triggers rapid ink flow through the fine opening (diameter ~5 μm). (e) A 400 nm-wide stripe pattern printed by an E-jet nozzle. (f) Device structure (left) and photograph of QD-LEDs (right). (g) Green (left) and red (right) EL from QD-LEDs. Adapted with permission from ref 432. Copyright 2015 American Chemical Society.

commercial displays, and have demonstrated pixel arrays of QD-LEDs containing various colors.

6.4.2. QD-Based White-Light LEDs. Solid-state lighting is one of the most important technologies for reducing future energy consumption. The best white LEDs (WLEDs) currently offer superior efficiency (100−150 lm W^{-1}) and operational lifetime (>50,000 h) over incandescent bulbs (5−15 lm W^{-1} and 1,000 h) and fluorescent lamps (50−100 lm W^{-1} and 10,000−20,000 h),[441] although there is considerable room for further improvement. Beyond serving as drop-in replacements for current illumination applications, enhanced controllability and new functionality/form-factors potentially available with solid-state lighting could potentially open new markets in the future. For instance, adaptive lighting, visible light communication, or urban farming have been suggested as possible applications based on the fast response and potentially tunable emission profiles of WLEDs.[437] However, for such potential to be realized, high adoption cost and long payback time (1−2 years), and limits to the size of the emitting area are stumbling blocks that have to be resolved. QDs may well emerge as the new class of materials that both reduces the production cost and offers entry into unprecedented functionalities, such as large-area, lightweight, low-glare, and flexible WLEDs.

The tunable emission of QDs is a useful feature to maximize the brightness (lm) and luminous efficacy (lm W^{-1}) of WLEDs. Conventional light sources, including state-of-the-art WLEDs, have a meaningful fraction of their emission spectrum either at wavelengths shorter than 440 nm or longer than 650 nm,[442] which reduces the luminous efficacy due to weak eye perception at this region (Figure 45a). If one can concentrate the emission spectrum within the 450−650 nm region, one can use electricity solely for generating light visible to the eye and thereby maximize the luminous efficacy. To achieve high color rendering index (CRI, a metric describing the ability of illuminating light to render the color of objects) in white emission, precise tuning of emitters is required.[443] Figure 45c-e display the spectra that are produced by dichromatic, trichromatic and tetrachromatic WLEDs based on QDs, along with their associated CRI of white emission spectra. Mixing of blue (453 nm) and yellow QDs (562 nm) with narrow line width resulted in poor CRI around 14, because it leaves a wide spectral gap between the two peaks. As the visible spectrum is more completely filled with three [blue (453 nm), green (545 nm), and red (624 nm)] and four colors [blue (453 nm), cyan (513 nm), yellow (562 nm), and red (624 nm)], the CRIs are improved to 68 and 93.[395] Interestingly, the increase in color constituents actually decreases luminous efficacy from 2.1 (for dichromatic) to 1.3 lm W^{-1} because this metric is most strongly influenced by the intensity within the most eye-sensitive region of the spectrum (peak at 555 nm); nonetheless, the narrow emission features of QDs helps to mitigate this reduction by minimizing emission outside the 450−650 nm window.

DOI: 10.1021/acs.chemrev.6b00169
Chem. Rev. 2016, 116, 10513−10622

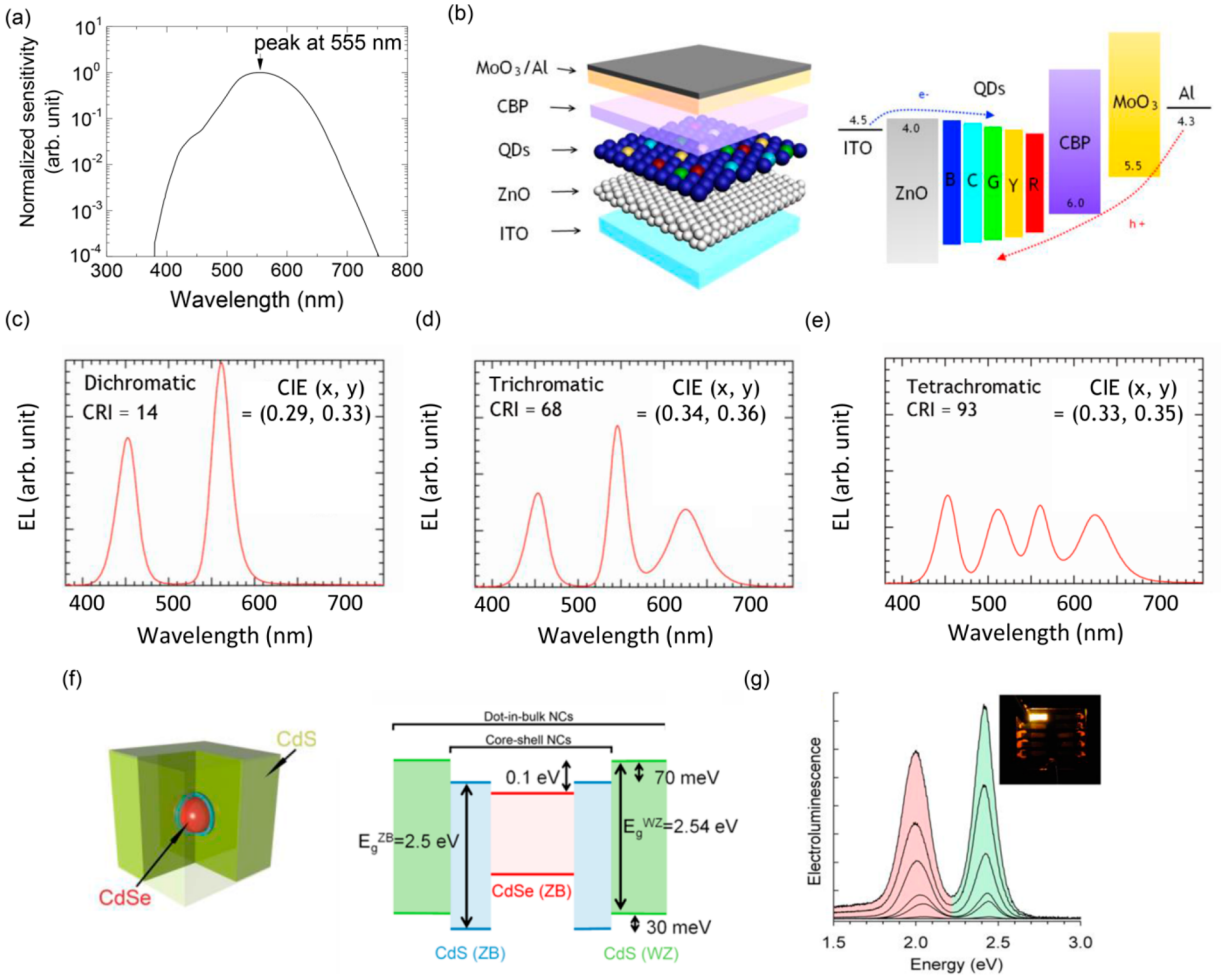

Figure 45. (a) CIE photopic sensitivity function normalized at 555 nm as unity. The eye sensitivity to colors rapidly drops off at wavelengths <450 nm and >650 nm, meaning that emission at these wavelengths barely contributes to the luminous efficacy of a device. (b) Schematic of white QD-LEDs with a mixed QD active layer (left) and their energy level diagram (right). EL spectra of (c) dichromatic (blue + yellow), (d) trichromatic (blue + green + red), and (e) tetrachromatic (blue + cyan + yellow + red) white QD-LEDs and their CRI values. Chromaticity coordinates of four fundamental colors and resulting white emission are provided as an inset. Reproduced with permission from ref 395. Copyright 2014 John Wiley & Sons, Inc. (f) Schematic (left) and electronic structure (right) of CdSe/CdS dot-in-bulk QDs and (g) their dual-color EL in a QD-LED. Adapted with permission from ref 439. Copyright 2014 American Chemical Society.

Conventional organic or inorganic WLEDs are constructed with multiple or separated EMLs that inevitably complicate the fabrication process and increase cost. By contrast, QD-based WLEDs can be realized with a single EML containing a mixture of QD emitters (Figure 45a). Since the first conceptual work by Li,[444] QD-based WLEDs with mixed QD EMLs have been incorporated into various types of device structures, such as RGB QD-HTL composites,[444] all-organic CTLs,[445] and hybrid CTLs.[395,446,447] Recent trichromatic WLEDs with hybrid CTL structures achieved a peak EQE of 10.9% and brightness over 20,000 cd m^{-2},[447] which already exceeds requirements for use in displays.[448] However, variation in white-emission spectra and the correlated color temperature (CCT, a metric capturing the perceived "warmness" of white light) with current density remains as an unresolved issue in QD-based WLEDs.[395] In devices with mixed EMLs, this can be attributed to the different carrier injection characteristics of QDs of different color. While abandoning the mixed EML approach in favor of pixellation (at increased cost and complexity) is always an option,[323,429] an alternative approach might be to use single nanocrystals that exhibit multicolor emission. For example, dual emission, associated with distinct parts of the heterostructure, has been observed in CdSe/CdS dot-in-bulk nanocrystals (Figure 45f,g),[439] CdSe/CdS tetrapods,[449] and various QD/quantum well systems,[190,450−452] including within actual EL devices.

6.5. Future Directions in QD-LEDs

6.5.1. Heavy Metal-Free QD-LEDs. Most QD-LEDs employ CdSe-based QDs within the EML because the chemistry to engineer these structures is well established and their photophysical properties are the most thoroughly understood. Regardless of the substantial technological progress in QD-LEDs, growing concern over the environmental and health consequences of the widespread use of heavy metals [as embodied, *e.g.*, by the regulations on Cd, Hg, and Pb use in electronics imposed by the Restrictions of Hazardous Substances (RoHS)[453] directive adopted by the European Union in 2003 and reenacted in 2011] raises serious questions regarding the use of CdSe-based QDs in lighting and displays. To continue the advance of QD-LEDs, alternative QDs that meet the safety regulations may be required.

Figure 46a displays the emission ranges of heavy metal-based (top) and heavy metal-free QDs (bottom). So far, Cd-based QDs

DOI: 10.1021/acs.chemrev.6b00169
Chem. Rev. 2016, 116, 10513−10622

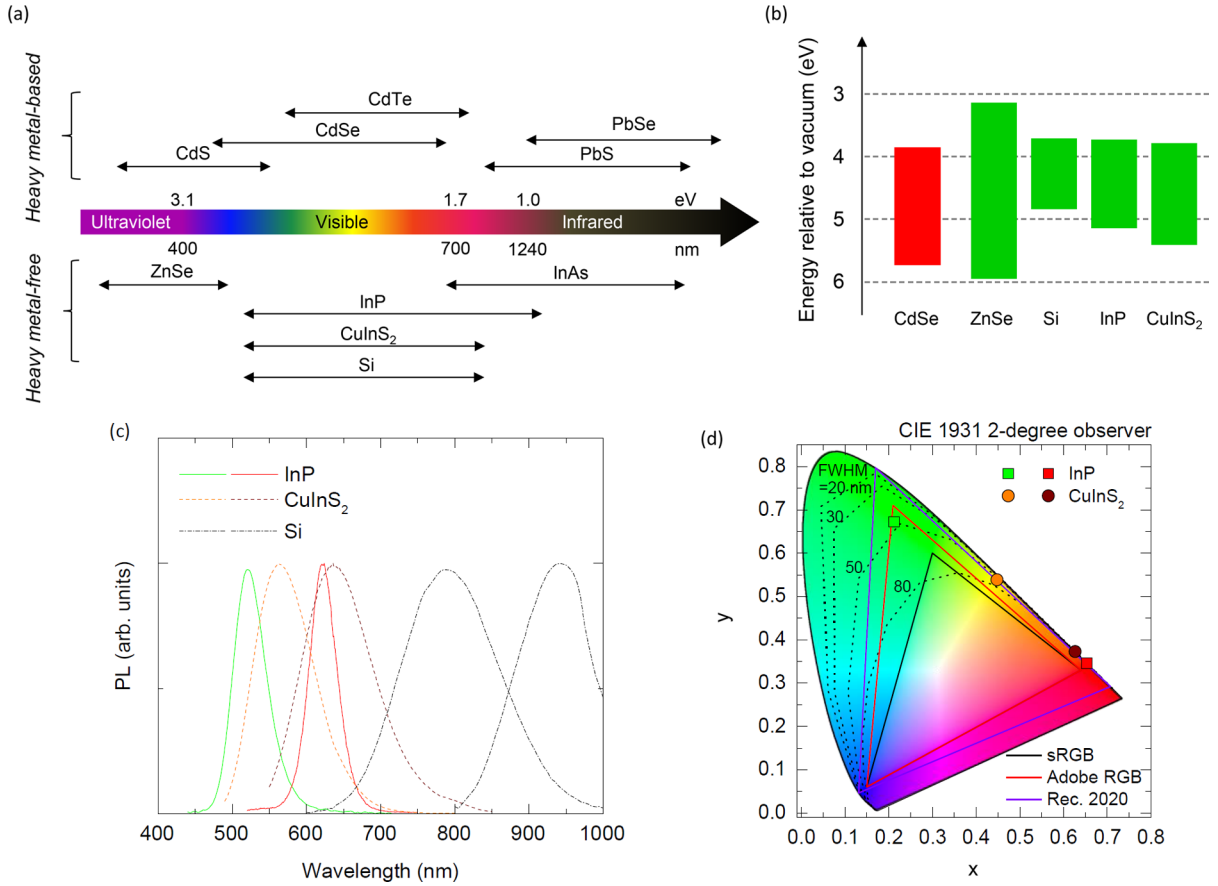

Figure 46. (a) Previous heavy metal-based QDs covering the ultraviolet (CdS), visible (CdSe and CdTe), and infrared (PbSe and PbS) regions have heavy metal-free alternatives: ZnSe for ultraviolet; InP, $CuInS_2$, and Si for visible; InAs for infrared. (b) Band-edge energies of bulk CdSe, ZnSe, Si, InP,[454,455] and $CuInS_2$[456] relative to vacuum. (c) Representative PL spectra of InP (solid), $CuInS_2$ (dotted), and Si QDs (dash−dot). (d) Positions of Gaussian luminescence spectra with various fwhm (20, 30, 50, and 80 nm) in the CIE chromaticity diagram. Chromaticity points of luminescent spectra in (c) are also included. InP-based QDs with ∼50 nm fwhm satisfy sRGB, and Adobe RGB as an example, but $CuInS_2$-based QDs with ∼100 nm fwhm fall well within the sRGB color space. Si QDs located outside the visible range are not included.

have been used to cover the ultraviolet and visible ranges, and Pb-based QDs are used for infrared applications. Cd- and Pb-free alternatives include InP, $CuInS_2$, and Si QDs for the visible and near-infrared range, and InAs QDs extend further into the mid-infrared region. For ultraviolet and blue light, it is already proven that ZnSe QDs exhibit reasonable PL QY as well as device performance in QD-LEDs.[457] Importantly, these alternatives have energy level positions that are similar to those of CdSe (Figure 46b), which implies that they may operate within the framework of previous QD-LED architectures optimized for CdSe-based QDs.

The drive for "greener" QDs has motivated ongoing efforts to improve PL QYs as well as photochemical stability of heavy metal-free QDs. Core/shell QDs based on InP[241,458] and $CuInS_2$[163] have recently exhibited over 70% PL QY; Si QDs have shown over 60% PL QY with only organic ligand passivation.[459] Based on these advances, the performance of heavy metal-free QD-LEDs has also rapidly improved; full-color InP QD-LEDs were demonstrated by Yang and co-workers[460] and the recent InP-based QD-LEDs by Lim et al. exhibited peak EQEs of 3.46% and maximum brightness of 3,900 cd m^{-2}.[458] $CuInS_2$ QD-LEDs have reached peak EQEs as high as 2.19% and 2,785 cd m^{-2} of maximum brightness.[461] Finally, near-infrared Si QD-LEDs have demonstrated peak EQEs up to 8.6%,[462] which is comparable with recent PbS/CdS QD-LEDs (8.3%).[463]

Despite the great interest in heavy metal-free QD-LEDs, their benefits have been offset, to date, by their poorer color purity than CdSe-based QDs. Figure 46c shows representative PL spectra of InP/ZnS, $CuInS_2$/ZnS, and Si QDs, and Figure 46d shows the corresponding points on the chromaticity diagram. As drawn with dotted lines, wider luminescence peaks shift chromaticity points closer to the white point, as also shown with the area of their color space. The PL fwhm of the brightest InP-based QDs ranges from 40 to 60 nm, rendering them barely able to satisfy Adobe RGB as well as sRGB color space. Worse, the fwhm of the best $CuInS_2$- and Si-based QDs exceeds 80 nm, placing their points well inside the sRGB color space. In order to displace conventional competitors in display applications in paticular, the emission line widths of these alternatives need to approach those of CdSe QDs.

6.5.2. Outcoupling Efficiency Improvement. As we pointed out in Section 6.3, a major portion of the light generated in an EML remains confined within the device trapped in waveguide modes. The outcoupling efficiency, η_{out}, depends on the CTL layer thicknesses, the refractive indices of the constituent materials, and the location of the EML relative to the electrodes; typically, it is around 20%. In OLEDs, η_{out} has been improved by perturbing the natural waveguide modes in the substrate by adding an external microlens array[464,465] or scattering nanostructures,[466] or intensifying constructive interference with so-called microcavities.[467] The concept of engineer-

DOI: 10.1021/acs.chemrev.6b00169
Chem. Rev. 2016, 116, 10513−10622

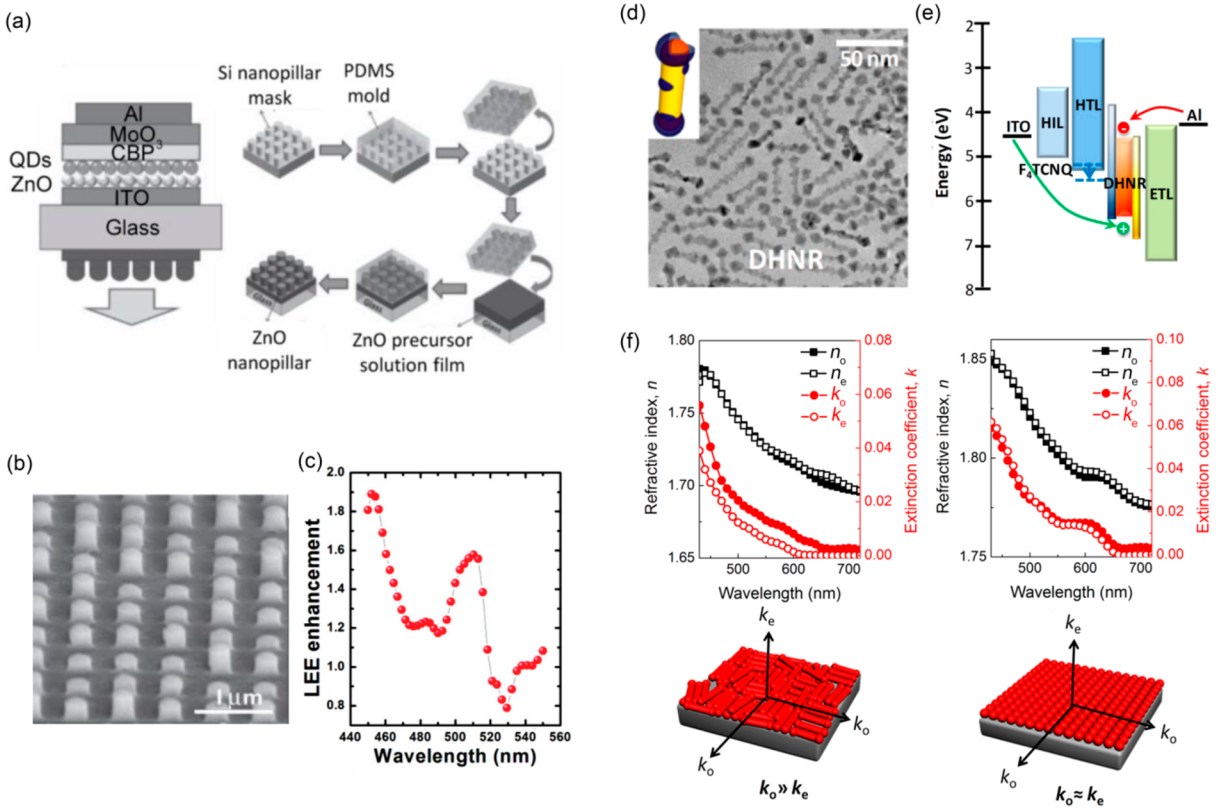

Figure 47. (a) Fabrication of ZnO nanopillars on the backside of QD-LEDs. The ZnO nanopillars are formed inside the poly(dimethylsiloxane) mold that is prepared from the Si nanopillar master. (b) Scanning electron microscopy image of ZnO nanopillars. (c) Light extraction enhancement compared to the control device (without nanopillars). The periodic nature of ZnO nanopillars brings about Bragg diffraction of light penetrating into the nanopillars and results in wavelength-dependent enhancement of the outcoupling efficiency. Adapted with permission from ref 469. Copyright 2014 John Wiley & Sons, Inc. (d) Transmission electron microscopy image of dual-heterojunction nanorods (DHNRs) comprising CdS nanorod (yellow)−CdSe tips (orange) covered with ZnSe (blue). (e) Energy level diagram of DHNR-LEDs. Due to similar valence band positions of ZnSe (blue) and CdSe (orange), the ZnSe shell passivates the CdSe emission centers without inhibiting hole injection. (f) Ordinary (in-plane) real (n_0) and imaginary parts (k_0) of the refractive index, and extraordinary (out-of-plane) components, n_e and k_e, obtained from DHNR (left) and CdSe/CdS core/shell QD (right) films. The k_0 of DHNR films is significantly larger than k_e, implying the parallel orientation of the dipole. Adapted with permission from ref 471. Copyright 2015 American Chemical Society.

ing the orientation of emitter dipoles[419,468] has also been explored as a means to decrease the fraction of vertically polarized light that easily couples to waveguiding modes parallel to the substrates as well as to plasmonic modes of the electrode.

Due to the structural similarity of QD-LEDs and OLEDs, the origin of low η_{out} and the possible solutions are similar for these two types of devices. For instance, ZnO nanopillar arrays on the glass improved η_{out} by a factor of ∼1.9 (Figure 47a−c)[469] by reducing the amount of trapped light propagating in the glass substrate. Nanoscopic patterns located at the glass−ITO interface can scatter light, enhancing η_{out} by a factor of ∼1.3.[470] In addition, improved light extraction by in-plane oriented nanorods has been demonstrated by Nam et al.[471] (Figure 47d−f). Previously, Hikmet et al.[472] and Rizzo et al.[473] reported polarized EL from ordered CdSe/CdS nanorod assemblies, but they did not study the potential effect of dipole orientation on the light outcoupling efficiency. In their study, EMLs comprising nanorods showed anisotropy between emission along the in-plane and out-of-plane directions (Figure 47f), a signature of large-scale orientation of dipoles. The EQE of nanorod-based LEDs was reported to be 12%. This was higher than the expected value of ∼8% obtained assuming $\eta_{inj} = 1$ and using the measured emission efficiency $\eta_{em} = 0.4$, implying that the η_{out} was improved to 0.3 by the in-plane orientation of the dipoles of nanorod emitters.

The examples mentioned above demonstrate that light extraction from QD-LEDs can be improved by exploiting general engineering concepts established for OLEDs. In particular, in-plane dipole orientation, which is easy to realize, seems to be a viable approach to improving η_{out} without the need for complex photonic structures. Whereas polymeric or molecular emitters require delicate control of molecular structure to produce and spatially orient dipoles, nanorods can adopt in-plane orientation spontaneously during spin-coating.

6.5.3. Long-Term Stability. To date, the majority of QD-LED efforts have focused on aspects of performance such as EQE, brightness and color purity. For future real-world applications, stable and reliable device operation over tens of thousands of hours is essential. The lifetime of QD-LEDs has improved as their efficiency has gone up. State-of-the-art QD-LEDs exhibit highly extended half-life (*e.g.*, the time over which the brightness fades to 50% of the original value) of over 300,000 h for red, and 90,000 h for green starting at 100 cd m^{-2} (extrapolated from accelerated aging conditions).[319] These already are acceptable levels of stability for display applications.[397] Although longer lifetimes seem to correlate with performance improvements, there is still a lack of detailed

DOI: 10.1021/acs.chemrev.6b00169
Chem. Rev. 2016, 116, 10513−10622

understanding of degradation mechanism in QD-LEDs. So far, factors such as electro- or photochemical reactions involving the emitters, thermal degradation, migration of ionic species, cathode delamination, impurities contained in device constituents, and incompatible encapsulation have been identified as contributing to degradation of OLEDs.[397,474] Further studies of these and other potential sources of degradation are essential to developing strategies for further enhancing the stability of QD-LEDs.

7. CARRIER MULTIPLICATION

7.1. Principles of Carrier Multiplication and Theoretical Considerations

7.1.1. CM Fundamentals. In the typical photoexcitation scenario, absorption of a photon with energy in excess of the band gap promotes an electron from within the valence band to a state within the conduction band, creating a single electron−hole pair. The photon energy in excess of the energy gap is very quickly dissipated as heat by exciting lattice vibrations (phonons) as the excited carriers relax to the band edge.[475] Strong carrier−carrier interactions can, in principle, open a competing carrier relaxation channel, in which the excess energy of a hot conduction band electron or a valence-band hole does not dissipate via electron−phonon scattering, but is instead transferred to a valence-band electron exciting it across the energy gap in a collision-like impact-ionization event (Figure 48a). As a result, the absorption of a photon in this case produces not one but two or more e-h pairs: accordingly, this process is referred to as carrier multiplication (CM) or multiple exciton generation (MEG). This process can be thought of as the inverse of Auger recombination (Section 4) of a trion (Figure 18b), whereby a three-particle state (*e.g.*, two electrons and hole) recombines leaving behind a hot carrier. While Auger recombination has been usually considered as a detrimental effect, which leads to "nonproductive" nonradiative losses of carriers, CM can, in principle, lead to substantial improvements in the efficiency of photoconversion that could benefit a range of technologies, and especially, photovoltaics and photocatalysis. In particular, calculations show that a material with CM can increase the power conversion efficiency of a single-junction photovoltaic from 33.7% to 44.4%.[476]

CM was first observed in bulk semiconductors in the 1950s,[477] and since then has been studied extensively both experimentally and theoretically. A typical photon-energy dependence of quantum efficiency (QE) of photon to e-h pair conversion observed for bulk semiconductors is schematically depicted in Figure 48b (red line).[477] It exhibits a turn on of CM at a certain threshold energy ($\hbar\omega_{th}$), which is followed by a near linear growth of QE to efficiencies greater than unity. The overall efficiency of the CM process can be expressed using $\hbar\omega_{th}$ and the inverse slope of a plot of QE (q) vs photon energy above the $\hbar\omega_{th}$, which represents the e-h pair creation energy, $\varepsilon_{eh} = [dq/d(\hbar\omega)]^{-1}$. Specifically, at energies above $\hbar\omega_{th}$, QE can be expressed as $q = 1 + \hbar(\omega - \omega_{th})/\varepsilon_{eh}$. The quantity of ε_{eh} can be thought of as the additional photon energy required to generate a new e-h pair at spectral energies above $\hbar\omega_{th}$. A large body of experimental data suggests that the spectral threshold of CM and the e-h pair creation energy are intrinsically linked by the relationship $\hbar\omega_{th} = \varepsilon_{eh} + E_g$.[478] Formally, this connection between the threshold and the e−h pair creation energy can be understood by treating the CM efficiency as arising from the competition between carrier cooling and impact ionization.[479]

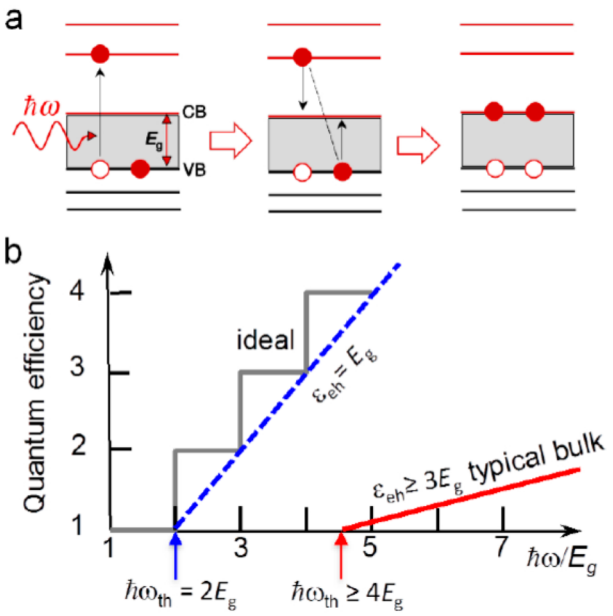

Figure 48. (a) Following the absorption of a high-energy photon (first panel), an electron with a kinetic energy greater than the band gap of the material may excite an additional e-h pair through a Columbic interaction (second panel). The net result of this process, known as carrier multiplication (CM), is two e-h pairs produced by a single photon (third panel). (b) The quantum efficiency (QE) of photon to e-h pair conversion for CM materials is plotted as a function of the photon energy divided by the band gap of the material ($\hbar\omega/E_g$). This representation allows the CM efficiencies of materials with different band gaps to be directly compared in one plot. The energy conservation limit for CM (gray line) corresponds to a step-like increase in the QE for every unit increase in $\hbar\omega/E_g$. Also shown is the semi-ideal linear dependence (dashed blue line, $\varepsilon_{eh} = E_g$, $\hbar\omega_{th} = 2E_g$) along with the approximate dependence observed in bulk semiconductors (solid red line, $\varepsilon_{eh} \geq 3E_g$, $\hbar\omega_{th} \geq 4E_g$). Adapted with permission from ref 265. Copyright 2014 Annual Reviews.

The ideal CM yield is described by a staircase function in which each increment of the incident photon energy ($\hbar\omega$) divided by the band gap (E_g) results in a new e-h pair, corresponding to an increase of QE of photon-to-exciton conversion by one (or 100%, Figure 48b; gray line). In the CM case, QE is greater than unity and the value of $\eta = (q - 1)$ defines the multiexciton yield. In Figure 48b, we also display a semi-ideal linear dependence of QE on ($\hbar\omega/E_g$), which is characterized by the CM onset of $2E_g$ and the e-h pair creation energy of E_g (blue dashed line in Figure 48b). In this case, both $\hbar\omega_{th}$ and ε_{eh} correspond to the minimal values as defined by energy conservation. In bulk materials, however, in addition to energy conservation, the CM process is also controlled by translation momentum conservation, which pushes $\hbar\omega_{th}$ and ε_{eh} to values that are higher than those in the semi-ideal case.[480,481] Specifically, the requirement of translation momentum conservation leads to an additional *kinetic* contribution (E_K) to ε_{eh}, which in the free-carrier approximation can be expressed as $E_K \approx 1.8E_g$. Phonon losses (E_{ph}) lead to a further increase in ε_{eh} by *ca.* 0.5−1.0 eV. Summarizing the above considerations, the e-h pair creation energy can be calculated from $\varepsilon_{eh} = E_g + E_K + E_{ph}$. This implies that in bulk materials ε_{eh} is at least $\sim 3E_g$, instead of the ideal value of E_g, and that the CM threshold is at least $\sim 4E_g$, versus the energy-conservation-defined limit of $2E_g$ (red solid line in Figure 48b). For traditional PV materials such as Si, GaAs, or CdTe with near ideal band gaps of 1.1−1.4 eV, the spectral

DOI: 10.1021/acs.chemrev.6b00169
Chem. Rev. 2016, 116, 10513−10622

onset of CM, therefore, is above 4 eV. Since only a very small fraction of solar radiation is available at these energies, the benefits from CM in conventional PVs are negligible, regardless of the chemical composition and detailed band structure.

As was suggested by Nozik, CM could be enhanced by using quantum-confined QDs.[53] A wide separation between electronic states has been expected to suppress phonon losses leading to a reduced contribution from E_{ph} to the e-h pair creation energy. Furthermore, several studies have highlighted how Auger processes, which govern the impact ionization, are strongly modified in nanocrystalline materials due to the relaxation of the translation momentum conservation.[260,274] As discussed in Section 4.2, a survey of Auger lifetimes in QDs of direct- and indirect-gap semiconductors reveals their conversion to values that are strongly dependent on QD sizes but almost insensitive to QD composition (Figure 20b).[274] This is in striking contrast to the 4 orders of magnitude variation found for their bulk counterparts.[482] The convergence of Auger rates strongly suggests that in nanomaterials, translational momentum is *not* conserved, at least in carrier−carrier collision processes. This further implies that in the case of the QD materials a kinetic contribution (E_k) to ε_{eh} is reduced compared to the bulk or, perhaps even completely eliminated. These considerations have motivated recent renewed interest in CM with a focus on quantum-confined nanostructures.

The first experimental evidence for efficient CM in QDs was provided by spectroscopic studies of PbSe QDs reported by Schaller and Klimov in 2004.[59] An especially important result of this work was the observation of a considerable reduction of the CM threshold compared to bulk PbSe (to less than $3E_g$) confirming the beneficial effect of quantum confinement on the CM process. Later, spectroscopic signatures of CM were observed for QDs of other compositions[141,483−489] including the important PV material Si.[490]

7.1.2. Theoretical Models. Following the initial observations, there has been much progress in understanding the theoretical underpinnings of the enhancement CM efficiency in QDs. Modeling the CM yield requires a theory that self-consistently describes both the relaxation of the high-energy states along with the coupling between the single-exciton and multiexciton states. Due to the difficulty of accurately modeling the large density of electronic states at energies much past the bandgap, theoretical models must make some assumptions to render the problem more tractable.

Several models have been proposed that yield results that are consistent with the measured CM yields. First, in strong-coupling models, the Coulomb interaction between carriers induces mixing between the single- and multicarrier states.[491−494] Following photoexcitation, the system oscillates between these states and the multiexciton yield is ultimately determined by the strength of the Coulomb coupling and the difference in the dephasing rates of single-exciton and multiexciton states. The enhancement of CM yield in nanomaterials then principally arises from the increased mixing between states facilitated by the relaxation of momentum conservation that "uncouples" single- from multiexciton states of similar energy in bulk materials. The principle experimental prediction of this model would be the coherent buildup of the multiexciton population (*e.g.*, in the form of coherent oscillations), which may be inhibited due to the large density of states where CM occurs efficiently; sample inhomogeneity could also obscure coherent dynamics due to ensemble dephasing.[492]

The potential of confinement-enhanced carrier−carrier interactions additionally allows for the direct photogeneration of multiexcitons via virtual single-exciton and biexciton states.[495,496] Within this model, strong coupling mediates the direct photoexcitation of multicarrier states via a virtual single-exciton or biexciton state, which is similar to phonon-assisted transitions in indirect semiconductors and Raman processes mediated by virtual electronic states.[497] The larger CM yields are then rationalized as arising from an enhancement in the coupling between biexcitons and excitons in nanoscale materials and a large number of intermediate states that can mediate the process. While there is no direct experimental data confirming the enhancement of exciton-to-biexciton coupling, the binding energy of biexcitons, which measures excition-exciton interactions, have been experimentally shown to be larger in QDs than in bulk materials,[272] suggesting an increase in other types of carrier−carrier interactions in strongly confined QDs. This model differs from the previous strong-coupling model in that the dephasing rate is assumed to dominate over the Coulomb interaction, whereas the coherent superposition model requires the opposite regime.

Incoherent weak-coupling models, in which the Coulomb interaction is treated perturbatively within Fermi's golden rule and treating a carrier cooling rate as an adjustable parameter have also been explored.[498−501] Within these models, the absolute value of the CM yield and its spectral dependence are controlled by the relationship between the densities of multiexciton and single-exciton states and the interplay between the rate of intraband cooling and the strength of Coulomb coupling. Results from the incoherent models are consistent with the experimental observations without the need to invoke any changes in the bulk impact ionization mechanism or strength of carrier−carrier interactions. Instead of a change of the mechanism increasing the efficiency of CM, the incoherent models suggest that the changes in the CM yield can be ascribed to subtle changes in the density of states near the band gap induced by confinement.[498]

As previously discussed in Section 5.1, carrier cooling was initially expected to be strongly inhibited in QDs due to discrete electronic structure near the band gap leading to a so-called phonon bottleneck. However, femtosecond optical measurements have consistently revealed increasing rates of carrier cooling in QDs with greater confinement.[15,349,503] These experiments reveal that while phonon emission may be suppressed, fast carrier cooling is maintained through alternative energy-dissipation mechanisms. For example, in CdSe the electron may additionally cool through an Auger-mediated energy transfer to the hole, thereby coupling to the larger density of hole states that are less strongly affected by the phonon-bottleneck phenomenon.[15] Meanwhile, in PbSe, where the effective masses of electron and holes are similar, nonadiabatic electron−phonon interactions can mediate efficient multi-phonon emission.[349] Additionally, the dynamics and cooling of high-energy carriers are consistent with the notion of being effectively bulk like, albeit with an increased scattering due to interactions with the nanocrystal surface and/or surface-bound species (*e.g.*, ligands).[504] These results indicate that the modification of carrier cooling does not likely lead to the enhancement of the CM yield.

With a lack of experimental measurements of the relevant theoretical parameters governing CM, *i.e.*, the dephasing rate of high-energy excitons, coupling strength between single-exciton and multiexciton states, and carrier cooling dynamics of high-energy single-exciton and multiexciton states, it is difficult to

DOI: 10.1021/acs.chemrev.6b00169
Chem. Rev. 2016, 116, 10513−10622

evaluate the validity of one model over the others. However, all calculations point to strong Coulomb coupling along with slow carrier cooling to being paramount to obtaining more efficient CM. Furthermore, all the models are consistent with the experimental observation of an enhancement in the energy efficiency of CM in QDs, although with different physical origins. While QDs consistently exhibit more efficient CM then their bulk counterparts in terms of the energy output,[265,500] the established yields in QDs of all known binary semiconductors to date are insufficient to appreciably increase the power conversion efficiency of a photovoltaic device. Importantly, though, unlike in bulk semiconductors the above considerations indicate that there are no fundamental physical constraints that limit the potential CM yields in nanoscale materials, opening the potential for engineering materials with further enhanced CM.

7.1.3. Implications for Photovoltaics. As originally suggested by Nozik, a CM-enabled photovoltaic could offer substantial gains in the power conversion efficiency.[53] Indeed, calculations within the detailed balance limit show that the power conversion efficiency for a single-junction photovoltaic under AM1.5 illumination can be increased to over 44%.[476,505] However, the obtainable power conversion efficiencies are strongly dependent on the efficiency of the CM process in the material. Shown in Figure 49a are several CM scenarios that were explored by Hanna and Nozik.[506] The energy conservation limit is given by M_{max}, where the linear semi-ideal limit is shown as L_2. The case of L_3 corresponds to the CM efficiencies experimentally observed for PbSe QDs, while L_4 corresponds to the efficiencies typical of bulk materials. Finally, the case labeled SQ refers to the Shockley-Queisser limit of single-junction photovoltaics without CM.[507] Calculations of the band gap dependence of the power conversion efficiency (PCE) of a solar cell for the above CM scenarios are shown in Figure 49b. Here we see that 1) for the measured CM yields in PbSe QDs, there is no appreciable increase in the maximum power conversion efficiency; and 2) the CM efficiencies must approach the energy conservation limit (M_{max} or L_2) in order to have appreciable gains over the SQ case. Interestingly, while the current CM yields cannot appreciable increase the efficiency of a solar cell in ambient light, calculations show a dramatic effect under concentrated sunlight, even with existing CM characteristics.[506] In fact, in the limit of maximum possible solar concentration, the PCE for a material with QE characterized by L3 reaches ~50%, over the 38% achievable with a conventional material. For a perfect CM material, the PCE can reach values over 80% at high concentration. These results highlight the need for CM to be as close as possible to the energy conservation limit in order to obtain substantial gains over conventional photovoltaics under unconcentrated light.

7.2. Carrier Multiplication Probed by Transient Optical Spectroscopies

7.2.1. CM Signatures in TA and Time-Resolved PL. In the first report on experimental observation of CM in QDs published 2004,[59] biexcitons produced by this process were detected by their distinct Auger decay signature in carrier population dynamics measured by TA. In these studies, a TA method was used to monitor the temporal evolution of the band-edge bleach produced by photogenerated carriers via the state-filling effect. Most of the follow-up experimental studies of CM have used a similar methodology implemented with a variety of time-resolved spectroscopic techniques including TA probing intraband transitions[493] and interband transitions,[508] time-resolved terahertz spectroscopy,[509] and time-resolved PL.[354,510]

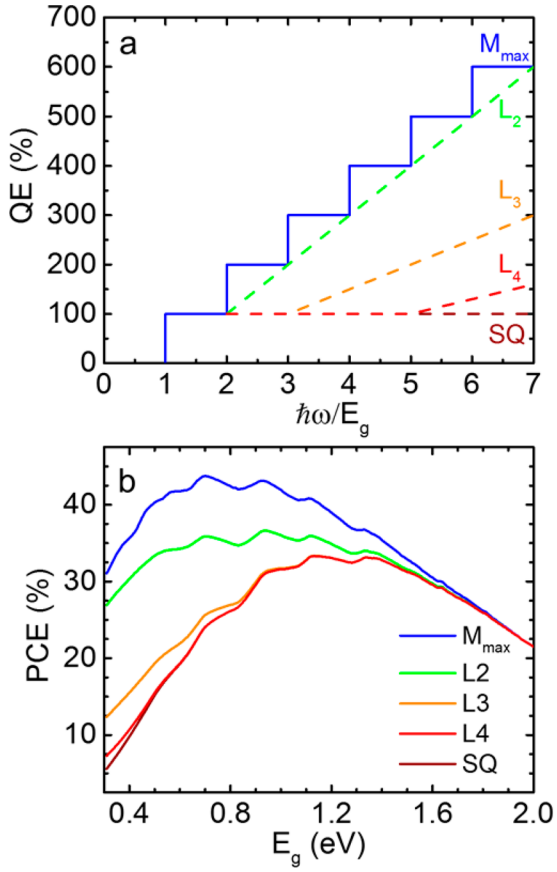

Figure 49. (a) Spectral dependence of QE of photon-to-e-h-pair conversion for different CM scenarios: the energy conservation limit (M_{Max}), a semi-ideal linear limit (L_2), an approximate behavior of the QE observed for PbSe QDs (L_3), a typical bulk semiconductor (L_4), and the no-CM case (SQ). (b) Band gap dependence of the power conversion efficiency (PCE) calculated in the detailed balance limit for the CM scenarios shown in (a). Adapted with permission from ref 506. Copyright 2012 American Chemical Society.

In these experiments, multiexcitons can clearly be distinguished from single excitons due to the large difference in the recombination time scales. For example, in lead chalcogenides QDs, the single-exciton lifetimes are typically characterized by microsecond time scales[503] defined by the combination of radiative recombination and nonradiative processes that are fairly slow in well-passivated QDs. The lifetimes of multicarrier states, on the other hand, are extremely short (ten-to-hundreds of picoseconds) because of very efficient nonradiative Auger recombination.[34] (Section 4). Thus, at early time after short-pulse excitation (several nanoscale time scales), the population of single-exciton states will remain nearly constant and the recombination of multicarrier states can be clearly distinguished, allowing for a quantitative measure of the relative fraction of photogenerated multiexcitons versus single excitons (see Figure 50 discussed below).

In TA measurements, the carrier population is typically monitored with the probe beam tuned to the lowest energy absorption feature. The amplitude of the bleach signal, $\Delta\alpha_{1S}$, measured in this way is proportional to the filling factor of the band-edge 1S state.[71] For the case of the lead chalcogenides, the high 8-fold degeneracy of the band-edge levels ensures that $\Delta\alpha_{1S}$ is also proportional to the total number of excitons residing in the QD for most of the experimental conditions used in literature

DOI: 10.1021/acs.chemrev.6b00169
Chem. Rev. 2016, 116, 10513−10622

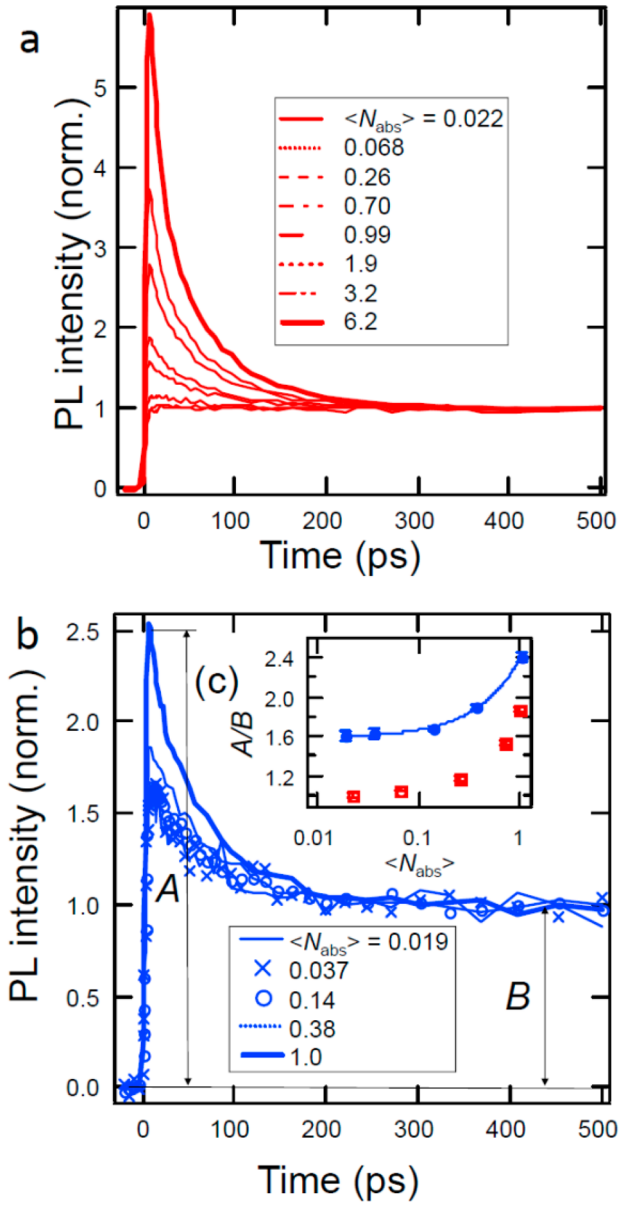

Figure 50. (a) Long-time normalized, time-resolved PL transients as a function of fluence for PbSe QDs with E_g = 0.80 eV excited at 1.54 eV. (b) Same as in (a), but with 3.08 eV excitation. The inset shows the ratio of the early time to late-time signal for excitation with 1.54 eV (red) and 3.08 eV (blue) photons. The blue line is a fit to Poisson photon absorption statistics. Adapted with permission from ref 354. Copyright 2008 American Chemical Society.

studies. Hence, the peak amplitude of the 1S bleach measured after all carriers cool to the band edge reports on the average number of excitons generated per dot across the ensemble. In principle, this can allow one to directly measure the CM yield through the magnitude of the peak signal in TA measurements. Specifically, when CM is active, the 1S bleach signal is expected to be larger than that estimated based on the absorption cross section at the pump wavelength. However, this direct method is prone to errors due, *e.g.*, to nonuniformity of the excitation power across the probed volume of the sample and inaccuracies in the determination of the absorption cross sections. Therefore, in the original report on the observation of CM in QDs[59] as well as in the most of the follow-up studies, the CM yield was evaluated based on the relative amplitudes of the multiexciton versus single-exciton signals in TA or time-resolved PL traces.

For example, in the case of TA measurements, the early time signal measured immediately following carrier cooling to the band edge (signal amplitude a) is proportional to the total number of e-h pairs generated by the pump pulse within the volume sampled by the probe beam. Because of fast Auger recombination, all multiexcitons will quickly decay to a single-exciton state. Hence, the signal measured directly following Auger recombination (signal amplitude b) is proportional the total number of photoexcited QDs. The ratio between a and b, then, yields the average number of excitons generated by the pump pulse per a photoexcited QDs. This quantity is known as the exciton multiplicity ($\langle N_X \rangle$) and based on the above considerations it can be directly obtained from the experimental TA traces by taking the ratio of the early time peak signal to the height of the slow single-excitonic background: $\langle N_X \rangle = a/b$. In the limit of low pump fluences ($j \to 0$), where predominantly only one photon is absorbed by a QD, the QE of photon-to-exciton conversion can then be determined from the experimental transients: $q = \lim_{j \to 0} \langle N_X \rangle$.

In the absence of CM events, the distribution of carriers generated by a laser pulse across the ensemble following photoexcitation at high spectral energies can be described by Poisson statistics (see Section 5.2).[71] In this case, the fraction of photoexcited QDs can be expressed as $p_{exc} = 1 - p_0 = 1 - e^{-\langle N \rangle}$, where p_0 is the fraction of unexcited QDs and $\langle N \rangle$ is the average QD excitonic occupancy, which is directly linked to the average number of photons absorbed per QD per pulse on average ($\langle N_{abs} \rangle$), $\langle N \rangle = \langle N_{abs} \rangle = j\sigma$; here, the pump fluence j is expressed in terms of the number of photons per unity area. The exciton multiplicity can then be directly related to the absorption cross section by $\langle N_X \rangle = \langle N \rangle / p_{exc} = \langle N \rangle / (1 - p_0) = j\sigma / (1 - e^{-j\sigma})$. In the limit of low fluence, $\langle N_X \rangle$ approaches unity, as expected in the absence of CM.

When CM is active, the average number of photons absorbed per QD per pulse remains Poissonian; however, the resulting carrier distribution will not follow Poisson statistics due to the additional e-h pairs generated through CM.[511] In the case when QE is limited by 200% ($q \leq 2$), the exciton multiplicity can be related to q and $\langle N_{abs} \rangle$ by[265]

$$\langle N_X \rangle = q\langle N_{abs} \rangle [1 - \exp(-\langle N_{abs} \rangle)]^{-1} = qj\sigma[1 - \exp(-j\sigma)]^{-1} \quad (22)$$

As expected, the low-fluence limit of eq 22 yields the QE. In a typical experiment, a/b values for a series of fluence are measured and the data fit either directly to eq 22 or to its simplified version obtained by taking into account only the first two terms of its Taylor expansion: $\langle N_x \rangle \approx q(1 + \langle N_{abs} \rangle / 2)$.

In time-resolved PL measurements, CM also manifests as a fast Auger decay component, which persists in the limit of zero fluences when $\langle N_{abs} \rangle$ is much less than unity. However, the quantitative relationship between the QE and the ratio of the early- and late-time PL signals (A and B, respectively) in this case is different from that in TA measurements. The instantaneous PL intensity is defined by the emission rate, which in the QDs scales as the product of the occupancies of the band-edge electron (N_e) and hole (N_h) states.[264,354,510,512,513] Hence, the emission rate of biexcitons (r_2) is expected to be four times that of a single exciton (r_1), which is in agreement with estimations from experimental results.[264,510,513] If we assume that a single photon may only

DOI: 10.1021/acs.chemrev.6b00169
Chem. Rev. 2016, 116, 10513−10622

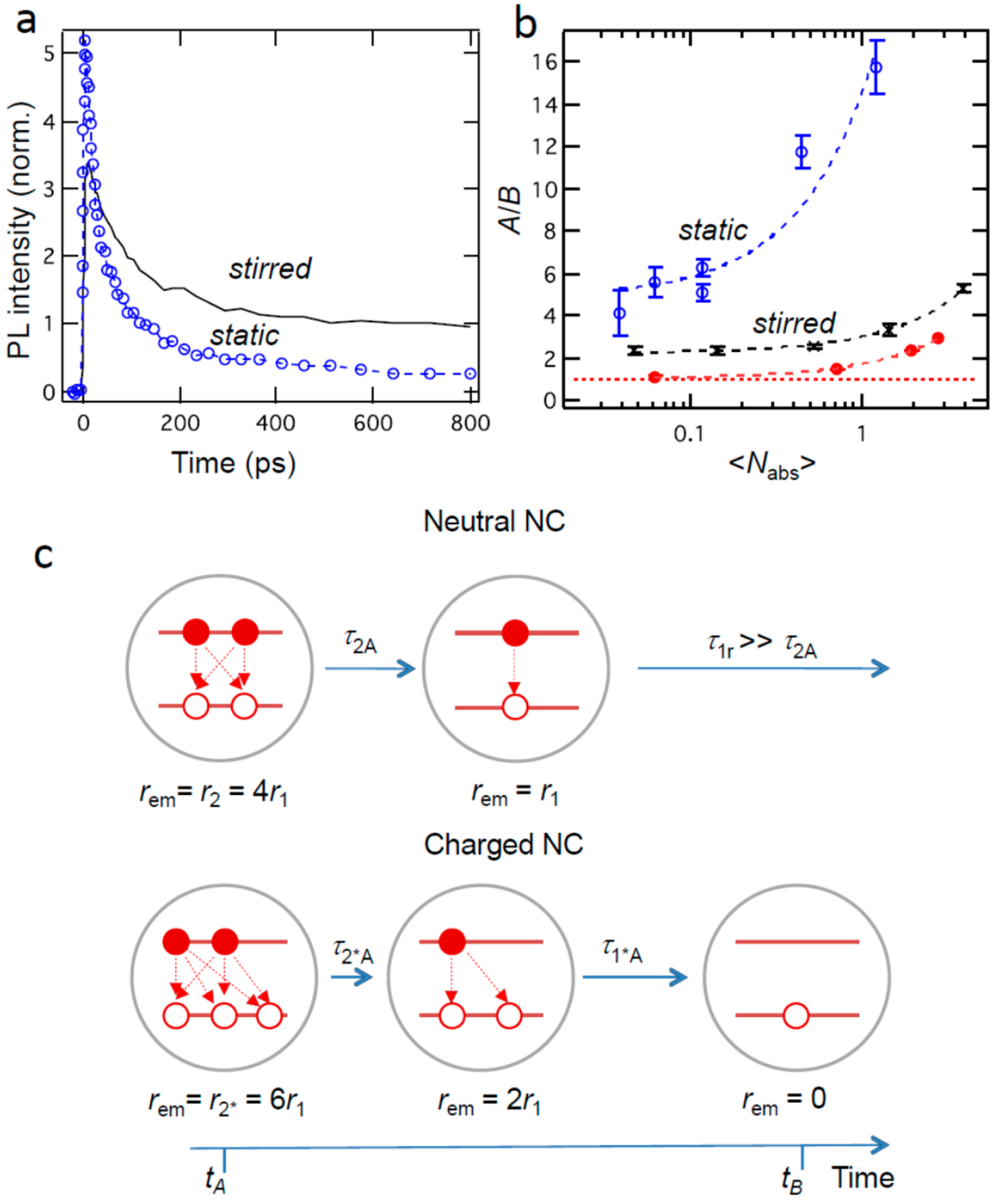

Figure 51. (a) Time-resolved PL transients for static (blue open circles) and stirred (black solid line) solutions of PbSe QDs with E_g = 0.63 eV excited at 3.08 eV, at a fluence corresponding to $\langle N_{eh} \rangle$ = 1.4. (b) Ratio of the early to late time PL intensities (A/B) as a function of pump fluence for the static (blue open circles) and the stirred (black crosses) samples (3.08 eV excitation); red circles are similar measurements for the stirred sample excited at 1.54 eV. (c) The sequence of recombination events for the neutral QD (top row) and the charged QD (bottom row). Adapted with permission from ref 264. Copyright 2010 American Chemical Society.

generate an exciton [probability $(1-\eta)$] or a biexciton (probability η), the early time peak of the PL signal is given by $A = (1-\eta)r_1 + \eta r_2 = (1+3\eta)r_1$, while the long-lived single-exciton signal will be given by $B = r_1$. The ratio of the early to late time signals can again be directly related to the CM efficiency: $A/B = 1 + 3\eta$. This yields

$$\eta = (A/B - 1)/3. \tag{23}$$

It should be noted that time-resolved PL is in principle a more sensitive probe of CM, as the CM yield derived from PL measurements is amplified by a factor of 3 ($A/B - 1 = 3\eta$) when compared to TA measurements ($a/b - 1 = \eta$). This is a direct consequence of a superlinear scaling of the PL signal with exciton multiplicity, which is in contrast to the linear scaling of the TA signal.[264,510,512]

Figure 50 shows a representative example of pump-intensity-dependent time-resolved PL data obtained for PbSe QDs for excitation below (panel a) and above (panel b) the CM threshold.[354] Below the CM threshold, a fast decay due to Auger recombination of multiexcitons can be clearly observed at high fluence, but it is absent in the lower fluence transients (Figure 50a). On the other hand, above the CM threshold, a fast picosecond signal persists even at $\langle N_{abs} \rangle$ as low as ~0.02 (Figure 50b). The inset of Figure 50b shows the A/B values as a function

DOI: 10.1021/acs.chemrev.6b00169
Chem. Rev. 2016, 116, 10513−10622

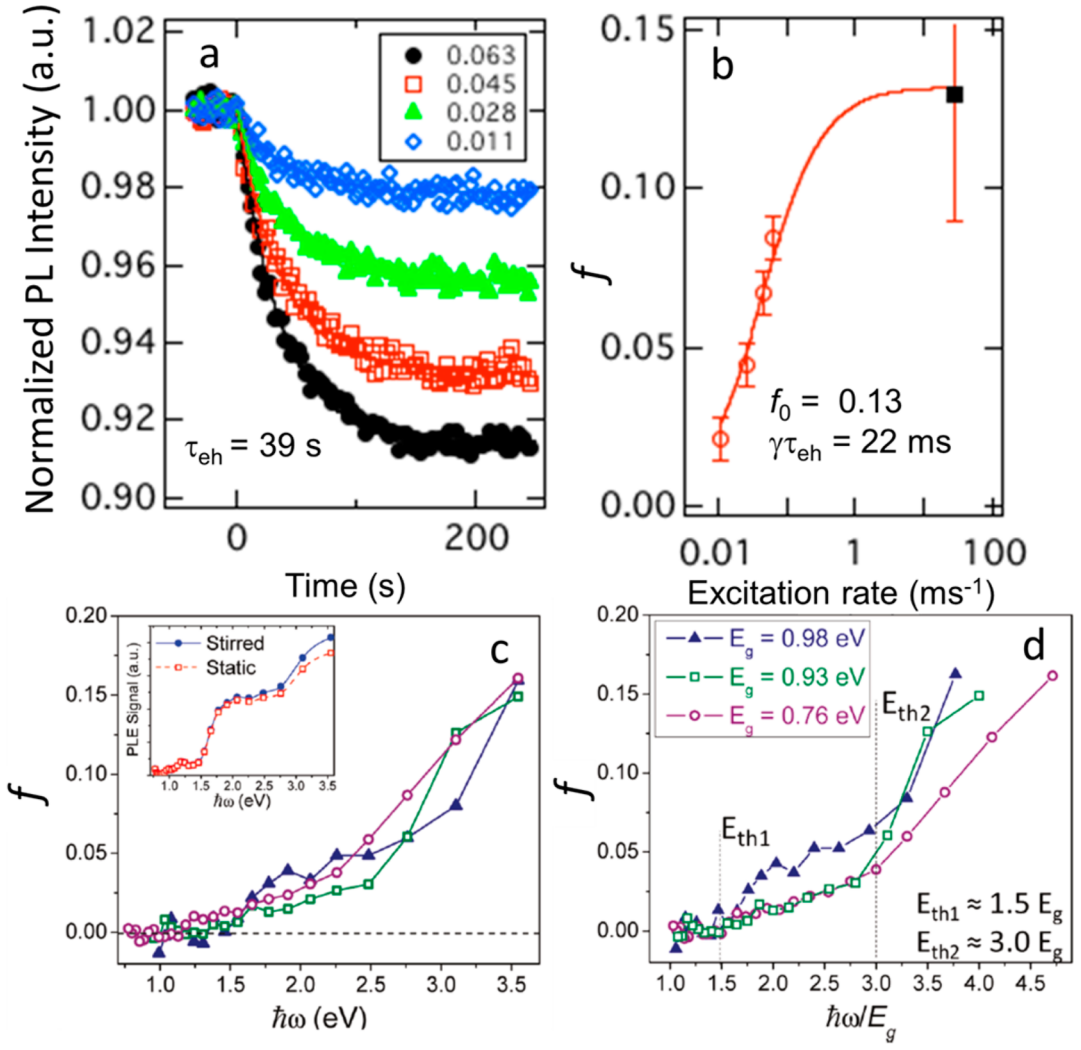

Figure 52. (a) Change in the PL intensity when stirring of a solution of PbSe QDs is suddenly stopped; different color traces are different excitation rates, given in ms^{-1}. The decay time relates to the lifetime of the charge-separated state. (b) The fraction of photocharged QDs of PbSe as a function of the excitation rate. The red line is a fit to eq 25. (c) Spectral dependence of the fraction of photocharged PbSe quantum dots with a bandgap of 0.98 eV (blue triangles), 0.93 eV (green squares), and 0.76 eV (purple circles). The inset shows photoluminescence excitation spectra for static and stirred samples, from which the data is derived. (d) Same as in (c) but plotted as a function of photon energy normalized by the QD bandgap. Adapted with permission from refs 518 and 523. Copyright 2010, 2011 American Chemical Society.

of fluence for excitation both above and below the CM threshold. Extrapolation to low fluence for the signal displaying signatures of CM yields $A/B \approx 1.6$, which correspond to $\eta \approx 0.2$.

7.2.2. Photocharging Artifacts in CM Measurements. One problem uncovered by early studies of CM in QDs was a large variation in the CM efficiencies reported for nominally identical materials.[484,485,493,510,512,514−516] These discrepancies in experimental observations were later found to be mostly due to the effects of uncontrolled QD photocharging,[264,354,517] which produced long-lived charge-separated states in which one charge (*e.g.*, an electron) remains confined in the QD core while the other (*e.g.*, a hole) was expelled from the QD and resides in a surface-related state.[518] In measurements on colloidal suspensions, the effects of photocharging can be mitigated by refreshing the probed sample volume through either stirring[264,354,510,512] or flowing[519] the QD sample. Greater care must be taken in measurements on solid-state samples, such as QD films, for which refreshing the sample volume is more difficult to implement. It is important to note that extensive experiments from different groups that ensure refreshing of the sample volume or account for effects of photocharging by appropriate corrections to the measured results show consistent values of CM yields across multiple experimental techniques.[264,265,354,489,514,519−522]

The effects of photocharging are especially pronounced in time-resolved PL experiments, as seen in Figure 51a,b. When the sample is not refreshed between incident laser pulses (so-called "static" sample), a population of QDs (f) in a charge-separated state may build up and contribute significantly to the overall signal which manifests in the apparent increase of the multiexcitonic decay component (blue open circles in Figure 51a) versus the stirred sample (black line in Figure 51a) due to contributions from Auger recombination of charged excitons (trions) and charge beixcitons. The difference between the amplitudes of the fast PL component in the static and stirred cases persists in the limit of low pump fluences (Figure 51b) which might lead to the overestimation of the CM yield if the effects of photocharging are not accounted for.

McGuire et al.[472] proposed a quantitative model for relating apparent CM yields in the presence of photocharging to true CM

DOI: 10.1021/acs.chemrev.6b00169
Chem. Rev. 2016, 116, 10513−10622

efficiencies. This model, depicted in Figure 51c, considers the situation when the QE is limited to 200%, i.e., the absorbed photon can produce only a single exciton or a biexciton, which is analogous to the assumptions discussed in the previous subsection in the context of the derivation of CM yields from PL measurements. It is further assumed that the fraction $f \leq 1$ of the QDs in the measured samples contains a single charge (a hole in Figure 51c), while the rest of the QDs [fraction $(1 - f)$] remains neutral.

As was discussed earlier, in the case of PL measurements, the early- and late-time signals in the case of neutral dots is given by $A = (1 + 3\eta)r_1$ and $B = r_1$, respectively. Both of these expressions, however, are modified in the case of charged QDs. The presence of an extra charge increases the emission rate of both a single exciton and a biexciton (they become, respectively, a trion and a charged biexciton). Specifically, assuming the N_eN_h scaling of the radiative rate, we find that the emission rate of a charged exciton or a trion (r_1^*) is twice that of a neutral exciton $r_1^* = 2r_1$, and it is 6 times greater than r_1 for a charged biexciton, $r_2^* = 6r_1$. Given these values, the peak PL signal for a partially charged QD ensemble is given by $A^* = r_1[1 + 3\eta + f(1 + \eta)]$, *i.e.*, is increased by $\Delta A = r_1 f(1 + \eta)$ compared to the case of all-nuetral QDs. On the other hand, photocharging leads to the reduction of the late-time PL amplitude, as following Auger recombination, both charged biexcitons and trion end up in a nonemissive single-carrier state (Figure 51c; bottom row). As a result, in a partially charged QD sample, the PL intensity after the completion of Auger decay is expressed as $B^* = r_1(1 - f)$. The net effect of photocharging is an enhancement in the early to-late-time PL signal ratio, which can be interpreted as the increase in the "apparent" CM yield (η^*). Using the above considerations, η^* can be related to a "true" CM yield (η) by the following expression:

$$\eta^* = (A^*/B^* - 1)/3 = [\eta + f(2 + \eta)/3](1 - f)^{-1} \quad (24)$$

In addition to changing PL signal amplitudes, photocharging leads to the emergence of new fast-decay components that are not present in samples of all-neutral QDs. These components are due to Auger recombination of various charged species (*e.g.*, trions and charged biexcitons), which are characterized by lifetimes that are distinct from those of neutral biexcitons.[264,354]

The studies of ref 264 demonstrated that if the degree of photocharging is determined from independent measurements, then true CM efficiencies could be accurately derived from the apparent CM values. The fraction of photocharged QDs can be evaluated, for example, from quenching of steady-state PL, bleaching of the band absorption, or a comparison of the long-lived transient PL signals in static versus stirred samples.[264] Using either method for obtaining fraction f in static samples along with eq 24 produces the mulitexciton yields that are consistent with those measured under stirred conditions.[264] This indicates the validity of the quantitative analysis of the effects of photocharging of ref 264 and also suggests that the presence of extra charges in the QDs does not appreciably influence the CM process. The latter might be expected as CM involves scattering of carriers in higher-energy electronic states, while pre-existing charges occupy the lowest-energy band-edge states.

Further studies of the physics of photocharging clarified its dependence on photon energy and excitation intensity which helped understand why spectroscopic artifacts due to photocharging can closely mimic CM signatures.[518,523] The experimental results on the pump fluence dependence of photocharging can be consistently described if one assume that only a certain fraction of the QDs (f_0) within any sample is susceptible to photocharging.[518] The equilibrium population of photocharged QDs will then depend on the excitation rate (g_{abs}, defined as the average number of photons absorbed per QD per unity time), the lifetime of the charge-separated states (τ_{eh}), and the probability of photoionization following the absorption of a photon (γ):

$$f = f_0 g_{abs}[g_{abs} + (\gamma\tau_{eh})^{-1}]^{-1} \quad (25)$$

Experiments monitoring the change in PL intensity when stirring is abruptly stopped provide a direct measure of the lifetime of the charge-separated species (Figure 52a), while excitation rate-dependent studies provide a measure of f_0 along with $\gamma\tau_{eh}$ through fitting to eq 25 (Figure 52b).[518]

Experimental studies of PbSe and PbS QDs indicate that the lifetimes of the charge-separated state range from 20−85 s, while the probability of photoionization is from 10^{-4} to 10^{-1}.[518,523] Despite the small values of γ, a large population of charged QDs may still build up at low pump fluences due to the long lifetime of the charge-separated states. This model helps rationalize the large variations in the apparent CM yields as occurring due to large variations in both the ionization probability and the fraction of "chargeable" QDs which varies from a few to over 20 percent.

The spectrally dependent measurements of photocharging indicate that the ionization probability strongly varies with photon energy, exhibiting two pronounced thresholds, which were tentatively assigned to the 1P and 2P electronic states (Figure 52c−d).[523] As the energies of these states scale with the band gap, the threshold for photoionization also scales with E_g, and coincidentally, the onset for strong ionization (occurs around the $2P_e$−$2P_h$ transition) is located near the CM threshold.

The above considerations indicate that great caution must be taken when measuring the CM yield of QDs. To ensure accurate measurements, it is best to refresh the sample to avoid the buildup of photoionized species. Furthermore, careful analysis of the decay dynamics, verifying that the same lifetime for the short-lived multiexciton states are measured both above and below the CM threshold, can also help avoid spurious effects.[524] We note that this experimental check will not be valid in the presence of significant photocharging at energies below the CM threshold. Great care must also be taken for samples which do not exhibit (at least nearly) "flat" single-exciton dynamics on a few nanosecond time scale as additional decay channels with fast time constants comparable to those of Auger decay may also alter the measured CM values.[525]

7.3. Carrier Multiplication in QDs versus Bulk Semiconductors

An important motivation for studies of QDs in the context of CM has been the expectation that this effect is enhanced by strong 3D confinement. Given a large of body of experimental data available for bulk and QD forms of lead chalcogenides (*e.g.*, PbSe and PbS), these materials have been often used for evaluating the effect of nanostructuring on CM efficiencies. In Figure 53a, the CM results for PbSe QDs[60,479,522] are compared with the efficiencies in bulk PbSe, obtained through ultrafast terahertz measurements.[526] In this plot, the QE of photon to e-h pair conversion is shown versus photon energy normalized by E_g. Based on these data, the CM threshold ($\hbar\omega_{th}$) can be determined from the onset of the QE growth above unity, while the e-h pair creation energy (ε_{eh}) can be found from the inverse slope of the

DOI: 10.1021/acs.chemrev.6b00169
Chem. Rev. 2016, 116, 10513−10622

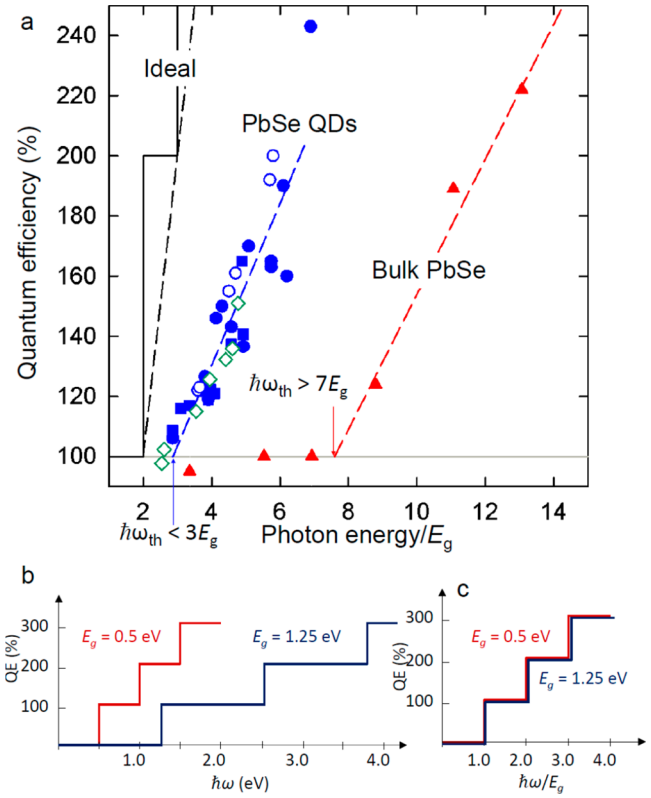

Figure 53. (a) Comparison between bulk values of the QE for photon to e-h pair conversion (red triangles, ref 526) and valued of the PbSe QDs measured with TA (blue solid and open circles, data from refs 479 and 522), time-resolved PL (blue solid squares[522]), and photocurrent measurements[60] (green open diamonds). The CM threshold is greatly reduced in QDs compared to bulk. QEs for the energy-conservation-defined limit (black line) and a semi-ideal linear limit (dashed black line) are shown for reference. (b,c) QEs for two ideal CM materials with different band gaps of 0.5 and 1.25 eV plotted as a function of photon energy $\hbar\omega$ (panel b) and normalized photon energy $\hbar\omega/E_g$ (panel c). Adapted with permission from ref 265. Copyright 2014 Annual Reviews.

QE dependence on $\hbar\omega/E_g$ at energies above $\hbar\omega_{th}$. Based on this approach, the CM threshold in the QDs is ~2.6E_g, which is substantially lower than ~7.6 E_g for bulk PbSe, and significantly smaller even than the ~4E_g theoretical minimum for bulk semiconductors (see Section 7.1.1).[480,481] This dramatic reduction in $\hbar\omega_{th}$ is likely a direct result of translation momentum conservation in the QDs (see discussion in Section 4.1), as the difference between the practical bulk limit for $\hbar\omega_{th}$ (~4E_g) and the energy-conservation-defined limit (2E_g) arises primarily from the requirement of the momentum conservation. The e-h pair creation energy also shows a modest reduction in the QDs over bulk values, decreasing to ~4E_g for QDs from a bulk value of ~4.3E_g. These improvements indicate that strongly confined QDs indeed show enhanced CM performance compared to extended bulk solids.

While the enhancement of the CM efficiency is readily apparent when accounting for confinement induced increase in the band gap, the bulk values for the multiexciton yields can appear larger than for the QDs if analyzed in terms of the absolute photon energies, particularly for very strongly confined QDs.[264,500,510] This observation has led to a discussion of the validity of using a band gap normalized representation for comparing the CM performance of QDs to bulk semiconductors or between two different materials in general.[500,510,527]

A convincing argument in favor of the $\hbar\omega/E_g$ scale for evaluating CM comes from a comparison of CM efficiencies for two materials with different band gaps but the same ideal staircase-like spectral dependence of the QE. In the absolute $\hbar\omega$ representation, the material with a smaller band gap appears to exhibit enhanced CM compared to a larger-gap semiconductor (Figure 53b). This assessment, however, is obviously not accurate as both materials show perfect CM performance limited only by energy conservation. On the other hand, on a normalized energy scale (Figure 53c), both semiconductors exhibit the same QEs, which immediately leads to the correct conclusion that they are identical with regard to their CM performance. This highlights the importance of taking into account the difference in band gaps when evaluating one material versus the other.

The significance of the energy-gap factor in comparing CM efficiencies between different materials is also apparent from the point of view of practical applications where the parameter of ultimate importance is an output power. From this perspective, a more relevant quantity than the CM QE is the product of the QE and the band gap that can be considered as proxies for a photocurrent and a photovoltage, respectively. The value of qE_g, then, can serve as a proxy for the output power. As was shown in ref 264, when evaluated in terms of qE_g, PbSe QDs show an appreciable improvement over bulk PbSe, because while showing comparable CM efficiencies they have a considerably larger band gap.

A rigorous thermodynamic analysis of the PV performance of CM materials also suggest that the enhancement in the PCE due multiexciton generation is controlled not by the absolute values of CM yields, but by the proportionality factors that relate the CM threshold and the e-h creation energy to the band gap energy (see Section 7.1.3).[476,505] Specifically, the closer $\hbar\omega_{th}$ and ε_{eh} to the energy-conservation defined limits (2E_g and E_g, respectively) the larger the enhancement in the PCE. The fact that in QDs the normalized values of these parameters ($\hbar\omega_{th}/E_g$ and ε_{eh}/E_g) are lower than in bulk semiconductors (see Figure 53a) points toward greater practical utility of CM in QDs versus bulk materials.

7.4. Effects of Quantum-Dot Size and Composition in Carrier Multiplication

7.4.1. Effect of QD Size. While being enhanced compared to bulk semiconductors, the CM performance observed in standard QDs is still not sufficiently high to meaningfully increase the PCE of a PV device.[476,500] To further improve the CM yields of nanocrystal materials, a greater understanding of the underlying factors that govern the CM efficiency is needed. In this section we will discuss the insights into these factors provided by experiments that probe the size and composition dependence of CM in nanocrystalline materials.

The data shown in Figure 53a represents PbSe QDs with radii ranging from *ca.* 1−3 nm. Interestingly, even though QDs exhibit enhanced CM over bulk PbSe, the close correspondence between CM yields for differently sized QDs when compared for the same normalized photon energy ($\hbar\omega/E_g$) suggests that the CM performance is essentially independent of nanocrystal dimensions, at least in this range of sizes. The similarity in the CM behaviors between QDs of different sizes shown in Figure 53a becomes apparent if the CM performance is evaluated in terms of a ratio of E_g and the e-h pair creation energy, which we will call a CM figure of merit $\chi_{CM} = E_g/\varepsilon_{eh}$ (in some references, such as, *e.g.*, ref 479, it is also called "CM efficiency"). This quantity defines the slope of the QE versus ($\hbar\omega/E_g$) dependence

DOI: 10.1021/acs.chemrev.6b00169
Chem. Rev. 2016, 116, 10513−10622

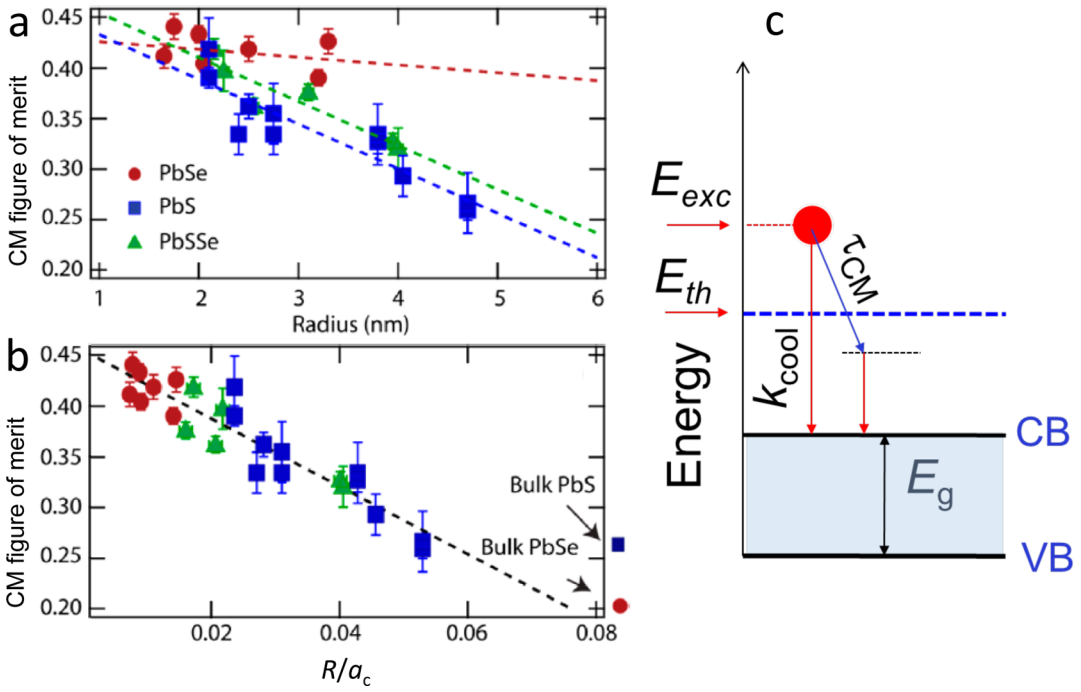

Figure 54. (a) Plot of the CM figure of merit for PbSe (red circles), PbS (blue squares), and $PbSe_xS_{1-x}$ (green triangles) QD as a function of QD radius. (b) Same data as in (a) plotted as a function of R/a_c. Adapted with permission from ref 521. Copyright 2013 American Chemical Society. (c) Main features of the "Window-of-opportunity" model, where the overall CM yield is determined by the competition between non-CM carrier cooling (k_{cool}) and the intrinsic time scale of CM (τ_{CM}). CM processes may occur within the time window when the energy of the carrier remains above the energetic threshold for CM (E_{th}), which is determined by the excess energy of the excitation (E_{exc}) and the rate of non-CM relaxation (k_{cool}). Adapted with permission from ref 275. Copyright 2013 American Chemical Society.

above $\hbar\omega_{th}$ and in the semi-ideal limit when $\varepsilon_{eh} = E_g$, $\chi_{CM} = 1$. Based on the data in Figure 53a, the CM figure of merit for PbSe QDs is ~0.25, almost independent of the QD size.

In contrast, size-dependent values of χ_{CM} are observed for PbS and PbS_xSe_{1-x} QDs.[489,521] Specifically, larger QDs exhibit near bulk CM yields, while the CM figure of merit steadily increases with decreasing QD size (Figure 54a), suggesting that the process is enhanced by spatial confinement. Importantly, the Bohr radius (a_B) in PbSe (~46 nm) is significantly larger than that in PbS (~18 nm). This implies that, for a given QD size, PbSe nanoparticles correspond to the regime of stronger confinement than PbS nanocrystals, which might be responsible for the apparent difference in the observed size-dependent trends between the two materials.

To elucidate the role of spatial confinement in the CM process, ref 521 introduced a "smallness" parameter, which was given by the ratio of the QD radius to a critical radius (a_c), which corresponded to the QD size at which the Coulomb e-h interaction energy was equal to the confinement energy. Based on this definition, $a_c = \pi^2\hbar^2\varepsilon_\infty/2m_{eh}e^2$, where ε_∞ is the bulk high-frequency dielectric constant, and m_{eh} is the reduced e-h mass introduced in Section 2.1. For the alloyed QDs, a_c was taken as a weighted reciprocal average of the PbS and PbSe values. Plotting χ_{CM} versus the ratio of the QD radius to the critical radius (R/a_c) reveals that the values for PbSe, PbSe, and PbS_xSe_{1-x} alloy QDs all fall on the same line, which indicates a "universal" inverse scaling with (R/a_c) (Figure 54b), that is, the increase in the CM figure of merit with increasing spatial confinement.

The observed size dependence of χ_{CM} likely arises from the interplay of the size-dependent trends that govern impact-ionization-like scattering events that lead to CM (characteristic time τ_{CM}) and the rate of competing intraband cooling, which can be characterized in terms of the energy lost per unity time (r_{cool}).[275,521,522] In fact, using a so-called "window-of-opportunity" model introduced in ref 275, it is possible to directly link ε_{eh} and χ_{CM} to τ_{CM} and k_{cool}. This model considers the situation where the excitation energy is just above the CM threshold $\hbar\omega_{th}$. In this case, the relaxation time (T_i; $i = e$ or h for the electron and the hole, respectively) of a hot carrier from its original state (energy E_i) to the state which constitutes the CM threshold (energy $E_{i,th}$) can be found from $T_i = (E_i - E_{i,th})/k_{i,cool}$ (Figure 54c). If T_i is short compared to τ_{CM} (which is ensured by exciting the sample sufficiently close to $\hbar\omega_{th}$), the multiexciton yield, which is defined by the probability to generate an additional e-h pair by the CM event, can be found from the ratio of T_i and τ_{CM}. The total CM yield is the sum of e-h pair producing events initiated by both a hot electron and a hot hole: $\eta = \eta_e + \eta_h = T_h/\tau_{CM} + T_h/\tau_{CM} = \sum_{i=e,h}(E_i - E_{i,th})/(k_{i,cool}\tau_{i,CM})$. For lead chalcogenides that have mirror-symmetric conduction and valence bands, τ_{CM}, k_{cool}, and $E_{i,th}$ are expected to be similar for electrons and holes. This allows one to easily add up the electron and hole terms in the expression for η, which yields $\eta = (\hbar\omega - \hbar\omega_{th})/(k_{cool}\tau_{CM})$ and further produces the following expressions for the e-h pair creation energy and the CM figure of merit: $\varepsilon_{eh} = d(\hbar\omega)/d\eta = k_{cool}\tau_{CM}$ and $\chi_{CM} = E_g/(k_{cool}\tau_{CM})$. These expressions indicate that both quantities, as it might be intuitively expected, are directly defined by the competition between CM and non-CM relaxation processes.

One can use the above analysis to rationalize the experimentally observed size-dependent trends in the CM process (Figure 54b) in terms of the size dependences of two individual constants (τ_{CM} and k_{cool}) that define CM yields. Since it is difficult to measure τ_{CM} experimentally, its size dependence is often assumed to be the same as for a related process of Auger

DOI: 10.1021/acs.chemrev.6b00169
Chem. Rev. 2016, 116, 10513−10622

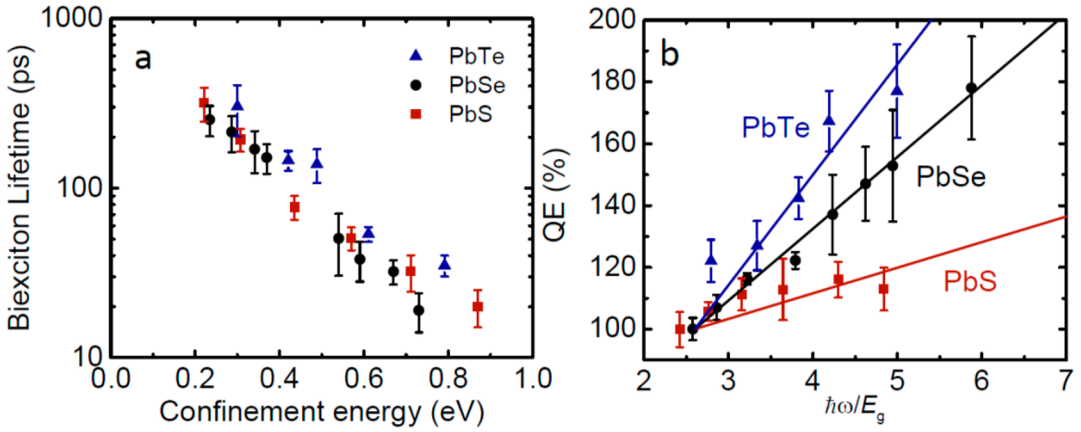

Figure 55. (a) Biexciton lifetimes for PbTe (blue triangles), PbSe (black circles), and PbS (red squares) QDs as a function of confinement energy (the difference between the QD and bulk band gaps). The close correspondence between the biexciton lifetimes suggests that carrier−carrier interactions, and hence the rates of CM, are similar in these materials. (b) Quantum efficiency of photon to e-h pair conversion for PbTe (blue triangles), PbSe (black circles), and PS (red squares) QDs of different sizes with excitation at 3.1 eV. A clear trend in the CM yields is observed: similar CM thresholds and clear differences in the e-h pair creation energies. Adapted with permission from ref 275. Copyright 2013 American Chemical Society.

recombination, which is controlled by the same type of carrier−carrier interactions. Based on numerous experimental studies, Auger lifetimes exhibit the R^3 size dependence (see Section 4.2),[34,274] suggesting that a similar scaling also applies to τ_{CM}. In fact, theoretical studies of size-dependent trends in CM agree with this assessment based on experimental observations.[528,529] Based on these considerations, the characteristic time τ_{CM} is expected to quickly shorten with decreasing the QD size, which should favor the CM processes by reducing ε_{eh}, *i.e.*, increasing χ_{CM}. On the other hand, according to many experiments,[15,349] the rate of intraband carrier cooling increases with decreasing QD size which, in principle, should increase ε_{eh} (decrease χ_{CM}) and thus hamper the CM effect. As a result, the overall effect of decreasing QD size on the CM efficiency is defined by the interplay between two size-dependent trends controlling the changes in the rates of e-h pair producing events and "nonproductive" intraband energy losses.

In the case of more strongly confined QDs (the PbSe case), these two trends likely compensate each other (*i.e.*, τ_{CM} and $1/k_{cool}$ scale approximately in a similar way with the QD size), and as a result, the CM performance evaluated in terms of ε_{eh} or χ_{CM} appears to be size-independent.[522] The situation, however, is different in the regime of weaker confinement realized in PbS and mixed $PbSe_xS_{1-x}$ QDs. In this case, the scaling of $1/k_{cool}$ with size is likely slower than that for τ_{CM}, and as a result χ_{CM} progressively increases (as a_c/R) with decreasing QD dimensions until it eventually reaches the maximum values realized in strongly confined PbSe QDs.

7.4.2. Effect of Composition (Pb-Chalcogenide Family). The analysis of competition between e-h-pair-producing events and non-CM energy losses also helped rationalize the effect of composition on CM yields observed for QDs of PbS, PbSe, and PbTe.[275,489] Interestingly, for all three materials, the rate of Auger recombination is nearly identical when considered as a function of confinement energy (Figure 55a), indicating that carrier−carrier interactions responsible for CM are also likely similar in these materials. However, measurements of CM reveal clear differences, indicating the following relationship between the multiexciton yields measured for the same E_g-normalized photon energy: $\eta_{PbTe} > \eta_{PbSe} > \eta_{PbS}$ (Figure 55b). These results can be explained by expected differences in the rate of phonon-mediated carrier cooling competing with CM. The energy-loss rate can be estimated by the product of the polar carrier-phonon coupling (α_{pol}) and the LO phonon energy ($\hbar\omega_{LO}$): $k_{cool} \propto \alpha_{pol}\hbar\omega_{LO}$.[475] Based on bulk values of these parameters: $k_{cool}(PbTe):k_{cool}(PbSe):k_{cool}(PbS) \approx 1.0:2.9:7.4$.[489] In ref 275, the rate of carrier cooling was also inferred from TA measurements of intraband relaxation between the 1P and 1S near-band-edge states. Specifically, the energy loss rate for this process (k_{1P1S}) was calculated as the 1S-1P energy difference divided by the time constant of the 1S bleach build-up. Studies monitoring the intraband bleach found a clear trend in the 1P-1S energy loss rate, $k_{1S1P}(PbTe):k_{1S1P}(PbSe):k_{1S1P}(PbS) \approx 1.0:2.0:4.2$, which was in qualitative agreement with estimations based on parameters of bulk materials. Assuming that a similar relationship also applies to cooling rates at high CM-relevant energies and taking into account that τ_{CM} does not considerably change between the three materials, one might expect that the relative changes in the e-h pair creation energy will follow those in the measured k_{1P1S} rates. This direct correspondence was indeed observed in experiments that indicated that the values of ε_{eh}/E_g scaled between PbTe, PbSe, and PbS QDs as 1.0:1.8:4.5. These results suggest a progressive increase in the CM figure of merit from 0.1 for PbS QDs to 0.25 for PbSe QDs, and finally 0.375 for PbTe QDs.

7.4.3. Other Compositions. Just as impact ionization is a general effect expected to occur in all bulk semiconductors, CM is similarly expected to occur in all types of the QDs, albeit with different efficiencies. Therefore, a survey of variations in the measured CM yields for different compositions can in principles provide valuable insights into the relevant physics governing the CM process.

Measurements on close-packed solids of Si nanocrystals in SiO_2 matrix have indicated signatures of nearly 100% efficient CM, through an unusual increase in the emission efficiency at higher-energy excitation[530,531] and an enhanced amplitude of the peak TA signal.[490] These measurements further suggested that the enhanced CM arises from strong interactions between the QDs, resulting in a "quantum cutting" process whereby multiple single excitons are generated in neighboring QDs following the absorption of a single photon,[530,532] as evident from the enhancement of the emission efficiency with nanocrystal packing density[531] and the absence of Auger recombination in low fluence measurements above the CM threshold.[490] It is not clear

DOI: 10.1021/acs.chemrev.6b00169
Chem. Rev. 2016, 116, 10513−10622

what the efficiency of CM in noninteracting nanocrystals is, as the only report measuring CM in isolated colloidal Si QDs[533] predated the discovery of photocharging in artifacts, while another report showed no signatures of CM in either isolated QDs or more densely packed QD solids.[534] Recent studies have also found very efficient CM in solid samples of Ge QDs dispersed in SiO_2 based on the analysis of multiexciton populations monitored with TA experiments.[487] As a whole, the origin(s) of the reported enhanced CM efficiencies in QDs of Group IV materials over QDs of other compositions currently remains unclear, and additional experiments are required to verify these observations.

Measurements of CM efficiencies in InP and $CuInSe_2$ QDs have found more modest yields, with both materials exhibiting ε_{eh} of $\sim 3E_g$.[486,488] Interestingly, the CM threshold is these QDs is reduced to $\sim 2.4E_g$ and $\sim 2.1E_g$ for $CuInSe_2$ and InP, respectively, which is an improvement over $\sim 2.7E_g$ in lead chalcogenide QDs. This may reflect the advantage of materials possessing a large difference between the effective masses of electrons and holes, which leads to unequal partitioning of the photon energy between the conduction and the valence band.

Indeed, for CM to occur, either an electron or a hole must have excess energy greater than the band gap to undergo a CM process, since Auger is a three particle process. Based on optical selection rules, the energy of a photon in excess of E_g is partitioned between the electron (E_e) and the hole (E_h) according to

$$E_e = \frac{m_h}{m_e + m_h}(\hbar\omega - E_g), \qquad E_h = \frac{m_e}{m_e + m_h}(\hbar\omega - E_g) \tag{26}$$

The onset of CM is defined by the condition $\mathrm{Max}(E_e,E_h) = E_g$. If for example, the electron is lighter than the hole or both have the same masses, the CM threshold is given by[484]

$$\hbar\omega_{th} = (2 + m_e/m_h)E_g \tag{27}$$

Thus, for the lead chalcogenides, where $m_e \approx m_h$, one expects $\hbar\omega_{th} \approx 3E_g$, which is in a reasonable agreement with the observed thresholds of $2.6-2.8E_g$.[59,489,493,514,521,524] On the other hand, in II–VI, III–V, and I–III–VI_2 materials, where m_e is smaller than m_h, the threshold becomes lower than $i3E_g$, and in the case when $m_e \ll m_h$, it can approach the ultimate $2E_g$ limit.

7.5. Carrier Multiplication in Engineered Nanostructrues

The above analysis of size- and composition-dependent trends in CM demonstrates the practicality of the approach wherein this process is treated in terms of the competition of CM-producing scattering events and non-CM energy losses. In fact, a simple relationship between ε_{eh} (or χ_{CM}) and τ_{CM} and k_{cool} obtained in the window-of-opportunity model allows for an accurate quantitative prediction of the CM performance based on the measurements of Auger lifetimes (used as a proxy for τ_{CM}) and near-band-edge intraband relaxation rates (used as a proxy for k_{cool}). In this section, we illustrate how the use of engineered nanostructrures (nanorods, nanosheets, and core/shell QDs) allows one to boost CM performance by either enhancing carrier–carrier interactions or reducing the rate of non-CM cooling.

7.5.1. Shape Effects in CM. A well-known result from the physics of quantum wells is the enhancement of carrier–carrier interactions in 2D nanostructures relative to their 3D counterparts.[535] As was discussed by Keldysh, carrier–carrier interactions in nanoscale materials deviate from those in the bulk through both dimensionality and dielectric effects.[536] In fact, in the case of 1D confinement the binding e-h energy diverges to infinity, due to the singularity of the Coulomb interaction in the limit of zero separation between charges.[537,538] These results suggest that nanocrystal morphology could provide an experimental route to strengthen the carrier–carrier interactions. Indeed, theoretical calculations of the electronic structure of *quasi*-one-dimensional PbSe nanorods find an enhancement of carrier–carrier interactions over spherical QDs.[539]

The synthesis of elongated nanorods of infrared-active materials such as PbSe and PbS is more challenging due to the centrosymmetric crystal structure, which precludes using the same synthetic strategy demonstrated for CdSe nanorods, where kinetic control of the growth rate for different crystal facets can lead to asymmetric 1D growth of a nanostructure.[26] Instead, an oriented attachment methodology can be utilized, whereby the elimination of high-energy surfaces through the fusion of nanocrystals can offer access to elongated particles, including nanorods and nanowires.[250−252,540,541] This synthetic strategy allows for spectroscopic-quality nanorods of varied radius and length to be studied in detail.[251,520,524]

Spectroscopic investigations of PbSe nanorods reveal that the optical properties are modified when compared to 0D QDs. Measurements of absorption cross sections show an enhancement in the local field strength, suggesting an enhancement of carrier–carrier interactions due to reduced dielectric screening.[524] The rate of Auger recombination is reduced, as expected based on the increase in the volume in elongated nanorods. Specifically, Auger lifetimes exhibit a linear dependence on the length of the nanorod for a fixed diameter.[524,542,543] Interestingly, the scaling of multiexciton lifetimes for elongated nanorods shows a bimolecular dependence on exciton multiplicity characteristic of bound excitons;[542,543] this is in contrast to QDs that follow statistical scaling, which reduces to the cubic dependence in the limit of large multiplicities (see Section 4.1).[268] These results confirm that the interactions between carriers are modified in *quasi*-1D nanorods compared to spherical (or near-spherical) QDs.

Shown in Figure 56a are the measured CM yields for PbSe nanorods with different diameters and lengths, along with the results for PbSe QDs.[524] The general trend of increasing QE with $\hbar\omega/E_g$ is again observed; however, there is significant spread in the data, indicating that besides E_g there are additional parameters which influence the CM efficiency. Indeed, when one plots the relative enhancement factor, β_{CM} (the ratio of CM yield for a given nanorod sample to the CM yield of QDs of the same band gap), against the nanorod aspect ratio (Figure 56b) a clear trend emerges; the aspect ratio is defined as L/D, where L is the nanorod length and D is its diameter. The data show a nonmonotonic dependence of the CM-enhancement on L/D, with an optimal aspect ratio of ~7, where the e-h pair creation energy is found to be reduced to $\sim 2.7E_g$ from $\sim 4E_g$ in the QDs, indicating the improvement in the CM figure of merit to ~0.37 from ~0.25. The CM threshold is at $\sim 2.6E_g$, without any appreciable dependence on the aspect ratio; this value is close to one for the QDs, suggesting that the observed improvement in the CM performance is mainly derived from the reduced ε_{eh}.

According to the window-of-opportunity model, the e-h pair creation energy can be reduced due to either reduced carrier cooling rate or the increased rate of CM scattering events. Studies monitoring the rate of carrier-cooling in nanorods reveal relaxation time scales that are similar to those in the QDs,

DOI: 10.1021/acs.chemrev.6b00169
Chem. Rev. 2016, 116, 10513−10622

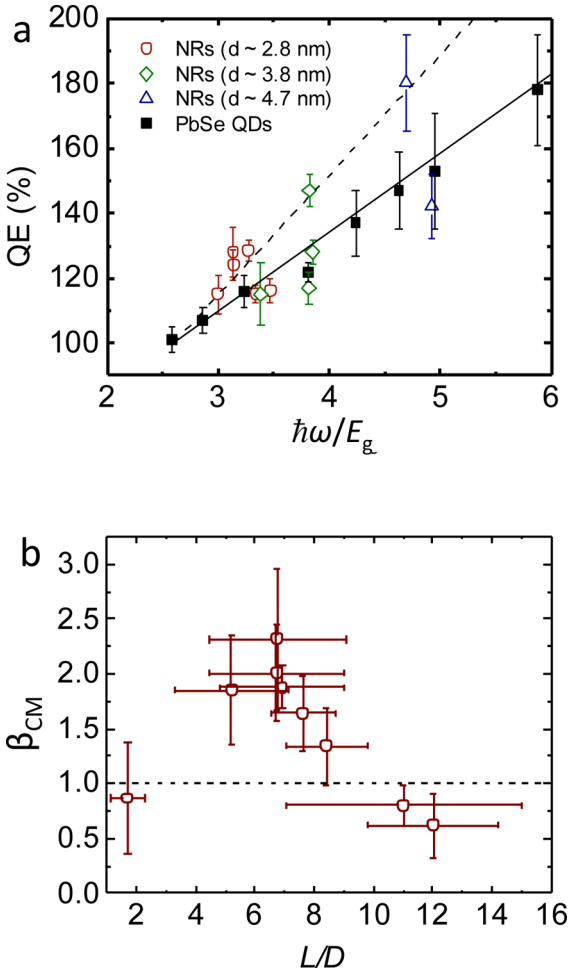

Figure 56. (a) Comparison of the quantum efficiency of photon to e-h pair conversion between PbSe nanorods and QDs as a function of $\hbar\omega/E_g$. (b) Relative enhancement factor, β_{CM}, as a function of the aspect ratio of the nanorods. CM yield was measured with 3.1 eV excitation. Adapted with permission from ref 524. Copyright 2013 American Chemical Society.

suggesting that carrier cooling is not strongly modified by the quasi-1D confinement.[542,543] This suggests that the enhancement of the multiexciton yields in nanorods must then arise from a shortening of the intrinsic time scale for CM. This would seem to suggest that the Auger recombination rates should also exhibit a similar enhancement in elongated nanorods. However, measurements of multiexciton dynamics indicate that Auger lifetimes are consistently longer in nanorods than those for QDs of a similar volume or band gap.[524,542,543] This discrepancy has been rationalized by invoking the difference in the character of high- and low-energy excitations in the nanorods.[524] As discussed above, the enhancement in carrier−carrier interactions leads to a stronger binding of e-h pairs near the band edge.[539,544] As a result, Auger recombination becomes less efficient than in QDs, as it occurs via the collision of charge neutral excitons,[544] as evident from a weaker scaling of Auger lifetimes with exciton multiplicity.[327,543]

The role of excitonic effects is less significant in the case of CM, as this process involves hot unrelaxed charges before they form bound states. First, this implies that in the case of the nanorods, the trends inferred from Auger recombination cannot be directly applied to the CM process. Second, this suggests that in the nanorods, CM is likely similar to that in the QDs but it occurs via stronger Coulomb interactions, enhanced by reduced dielectric screening and the 1D character of electronic states. This enhancement likely drives the increase in the CM efficiency at moderate aspect ratios (up to *ca.* 6−7). The decrease in the multiexciton yield at larger aspect ratios likely results from restoration of translation symmetry along the longer nanorod axis, which imposes additional restrictions on CM scattering events due to requirements of the momentum conservation.

A considerable effect of the nanostructure shape on the CM process is also indicated by recent studies of PbS nanosheets that exhibit confinement in only one dimension.[545] Here, the authors found larger values for the CM threshold of $\sim 4E_g - 5.5E_g$, most likely due to the strict requirements of momentum conservation discussed above. Interestingly, both the e-h pair creation energy along with the threshold exhibited an improvement as the thickness of the nanosheets decreased, with ε_{eh} values approaching the energy conservation limited value at small thicknesses. These studies of nanosheets and nanorods clearly demonstrate that the particle morphology can be utilized for enhancing carrier−carrier interactions, and thereby CM.

7.5.2. Cooling-Rate Engineering in Core/Shell QDs. The results described in Section 7.5.1 strongly indicate that rapid carrier cooling directly impacts the CM performance by competing with CM-producing carrier−carrier scattering events. This suggests that one approach to enhancing CM yields is through the development of nanostructures with reduced cooling rates. As described in numerous places in the previous sections, carrier cooling in nanocrystals may occur through a variety of mechanisms, such as Auger-mediated relaxation,[15,502] nonadiabatic multiphoton emission,[349] coupling to ligand vibrations,[347] and bulk-like emission of phonons dominated by polar coupling to longitudinal Optical (LO) phonons.[504] Previous experiments have realized the suppression of carrier cooling in heterostructured CdSe-based QDs,[350] suggesting potential methods for controlling intraband relaxation rates.

The first example of engineered infrared hetero-QDs with slowed intraband cooling was reported in refs 211 and 546. These structures comprise a PbSe core overcoated with a thick shell of CdSe (Figure 57). They are synthesized through a controlled cation exchange of large PbSe QDs, where moderate reaction temperatures (130 °C) ensure the formation of a thick shell while avoiding the formation of pure CdSe QDs.[209,211] This synthesis maintains the overall diameter of the QD and allows for facile tuning of the aspect ratio (ρ), defined as the ratio of the shell thickness (H) to the total radius (R): $\rho = H/R$.

Due to the small offset between the conduction bands of CdSe and PbSe, the electron is expected to be delocalized across the entire volume of the QD, while the hole will remain confined to the core due to the relatively large offset between valence band edges (Figure 57a).

Theoretical modeling of these structures indicates that a large valence and a significant disparity between hole masses in CdSe and PbSe lead to strong backscattering of hole wave functions at the core/shell interface. Therefore, at large shell thicknesses, the higher-energy hole states are almost entirely shell localized, while the lower-energy states remain confined to the core. As a result, these two types of states become electronically decoupled, which is further emphasized by a large gap separating core- and shell-based electronic levels (Figure 57a). These effects are expected to slow down cooling of a hot shell-localized hole, which should favor the CM events associated with scattering of the long-lived energetic hole with a pre-existing electron in the band-edge core-localized states

DOI: 10.1021/acs.chemrev.6b00169
Chem. Rev. 2016, 116, 10513−10622

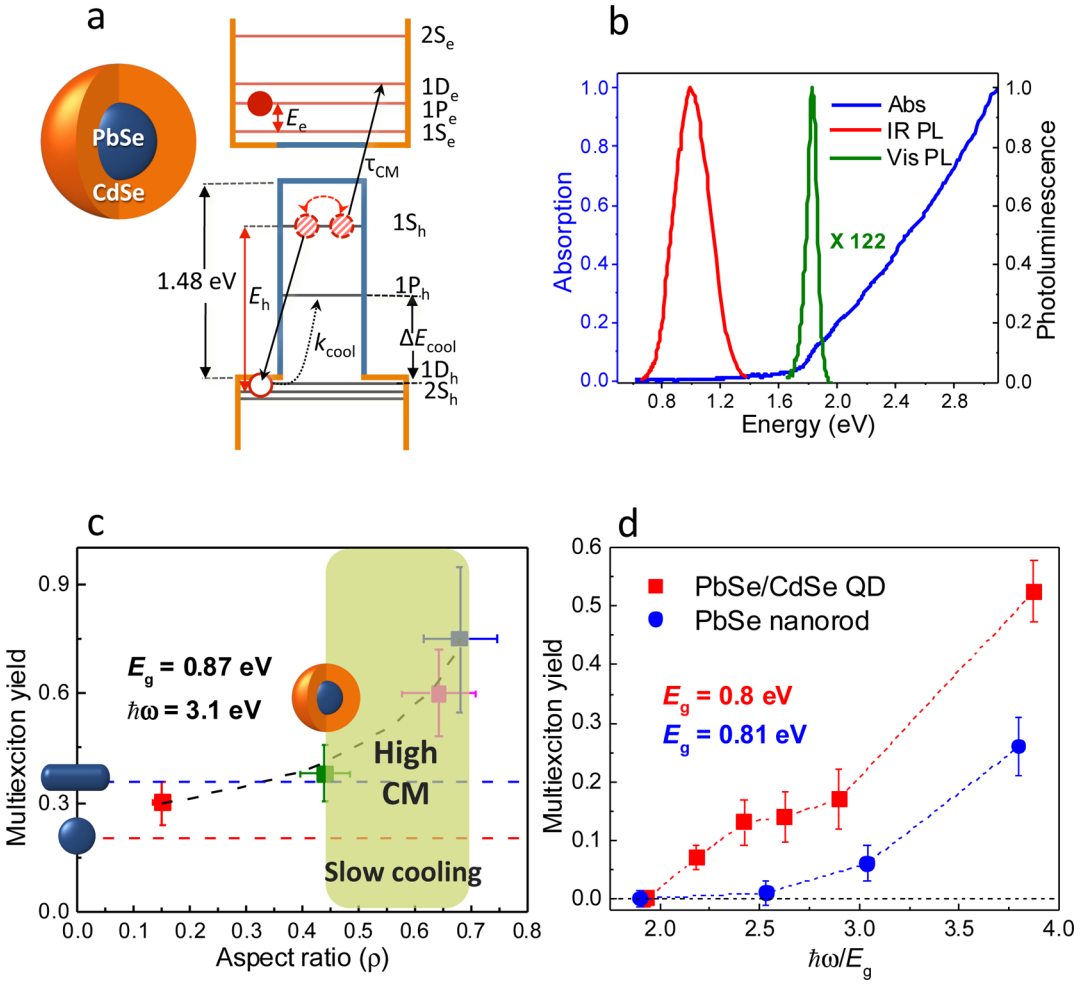

Figure 57. (a) Approximate electronic structure of a PbSe/CdSe core/shell QD with a 2 nm core radius and 2 nm shell thickness. Optical excitation into the shell results in an asymmetric distribution of energy between the two carriers (E_e and E_h; red arrows) which allows for a reduction in the CM threshold. Hot hole relaxation may occur through either a CM process (solid black lines) or thermalization (dotted black lines). (b) Absorption (blue) and emission (red and green lines) spectra of PbSe/CdSe QDs with $\rho = 0.64$. Emission results from thermalized e-h pairs in the core, along with shell-based emission resulting from the recombination of a hot hole with a band-edge electron. (c) Aspect ratio dependence of the CM yield in PbSe/CdSe QDs with the ~0.87-eV band gap. The shaded region is where energy conservation and slow cooling are both realized. The dashed red and the dashed blue lines correspond to CM yields in, respectively, QDs and nanorods with the similar band gap. (d) CM threshold measurements of PbSe/CdSe QDs with $E_g = 0.8$ eV, and PbSe nanorods with $E_g = 0.81$ eV. Adapted with permission from ref 546. Copyright 2014 Nature Publishing Group.

A prominent signature of slowed hole cooling is the emergence of the second emission band in the visible at large shell thicknesses, which is observed together with the infrared PL from the core (Figure 57b). The onset of the development of the visible band corresponds to the aspect ratios of 0.4−0.5. With further increasing shell thickness, the visible band red-shifts toward (but remains above) the bulk band gap of CdSe, while its quantum efficiency continuously increases. These results support the assignment of the visible emission to recombination between an electron in the lowest conduction-band state and a hot valence-band hole residing in the shell. In most semiconductor nanocrystals, such hot emission is suppressed due to rapid cooling of carriers to the band edge. Thus, the emergence of hot emission suggests that cooling of shell-localized holes into core states has indeed been strongly inhibited in these QDs.

In addition to demonstrating reduced cooling rates, the structures designed for efficient CM must also satisfy a certain "energetic" requirement. Specifically, in order for CM to occur the energy released during relaxation of a hot hole (given by the difference in energies of the visible and infrared PL) must be greater or at least equal to the band gap energy (given by the energy of the infrared PL). An example of a structure, which is at the border for meeting the energetic requirement is shown in Figure 57b. The shell thickness in this case is already sufficiently large for realizing the regime of slow hole cooling as indicated by the development of visible emission peaked at ~1.8 eV. The infrared emission in these QDs is at ~0.9 eV, indicating that the energy separation between the shell- and core-localized holes is also ~0.9 eV, *i.e.*, right at the onset of the hot-hole-driven CM pathway.

Measurements of the CM efficiency as a function of ρ for the fixed excitation energy and for structures with similar E_g indeed show an enhancement for large shell thicknesses (Figure 57c). For the thinnest-shell sample ($\rho = 0.15$), the CM yield is modestly enhanced above the core-only value, but still lower than the yields in PbSe nanorods. As the aspect ratio increases, the CM yield rapidly increases, following a trend qualitatively similar to that of the quantum efficiency of visible emission. For the largest aspect ratio ($\rho = 0.68$), the multiexciton yield reaches 0.75, which is nearly 4 times greater than that in core-only QDs.

DOI: 10.1021/acs.chemrev.6b00169
Chem. Rev. 2016, 116, 10513−10622

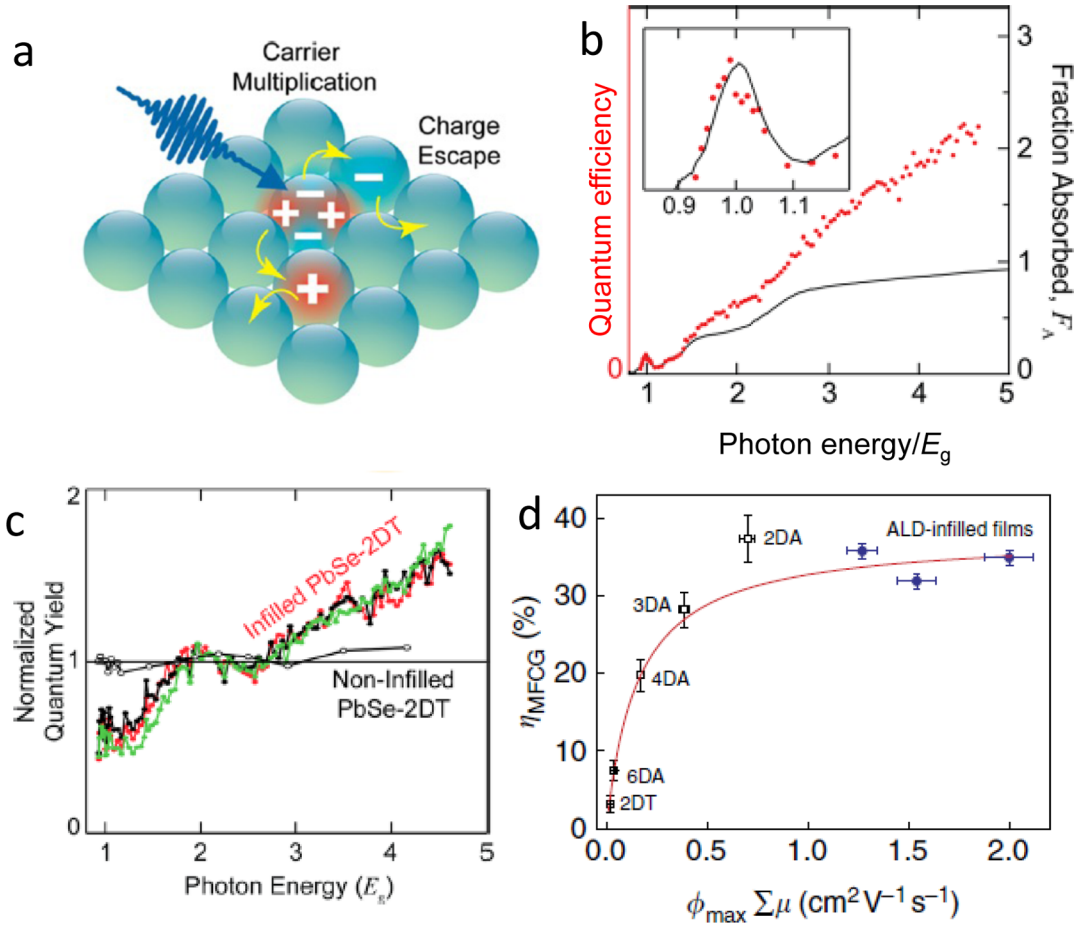

Figure 58. (a) Multiple e-h pairs generated in a close packed film of PbSe QDs must dissociate to neighboring QDs to be detected in microwave conductivity measurements. (b) Absorptance spectra (black line) and photon energy dependence of the photoconductivity (red dots). The inset shows that the photoconductivity closely follows the absorptance at low photon energies. (c) CM efficiency derived from the measurements in (b) for three ALD-coated samples (solid symbols), and for an EDT-treated film (open circles). (d) Detected multiexciton yields as a function of mobility. The red line is a fit to eq 30. Adapted with permission from ref 549. Copyright 2015 American Chemical Society.

This suggest that in thick-shell PbSe/CdSe QD, the dominant contribution to the overall CM yield is provided by hot holes. The energy conservation requirement discussed above provides a limit to the maximum aspect ratio before the excess energy of the hole becomes less than the band gap, effectively shutting down this CM pathway. It is estimated that for QDs with the total radius R = 4 nm, the critical aspect ratio is ~0.7, suggesting an optimal range of the aspect ratio where both slow cooling and energy conservation are maintained between approximately 0.45−0.7 (shaded region in Figure 57c).

In addition to the increase in CM yield, the asymmetry between the conduction and the valence band leads to a reduction of the CM threshold. Excitation-dependence measurements of the CM yield for the PbSe/CdSe and PbSe nanorods are compared in Figure 57d. For the nanorods, the efficiency drops to zero near 2.5−2.6E_g, consistent with the previous results conducted on nanorods of differing aspect ratios (Section 7.5.1). For the core−shell structure, a measurable CM yield is still present under excitation at 1.75 eV, which corresponds to $\hbar\omega/E_g$ of 2.18, very near the energy conservation limit of 2. Further improvements may be realized through additionally enhancing the carrier−carrier interactions, for example through the type of shape control described above, to potentially approach even closer the energy conservation limit in the CM performance.

7.6. Carrier Multiplication in Device-Grade Nanocrystal Films Evaluated by Electro-Optical Techniques

While the optical experiments above clearly demonstrate the promise of nanostructures for enhanced CM, the vast majority of experiments have been conducted on colloidal suspensions of isolated QDs, whereas devices utilize films of electronically coupled nanocrystals. The experimental challenges due to long-lived charge-separated states complicate traditional optical experiments on films, where it is more difficult to ensure accurate artifact-free measurements of the CM yield. Moreover, the introduction of coupling between nanocrystals may complicate the previously used analysis strategies as they do not consider additional relaxation and recombination pathways introduced with interdot coupling. This suggests alternatives to optical experimental methodologies are required to assess the CM performance of device-grade films of electronically coupled QDs.

An additional consideration is that, in order for devices to benefit from the additional carriers generated through CM, charge extraction must occur faster than the rate of Auger recombination of multiexcitons. While in standard solar cells, Auger recombination is only active under concentrated solar radiation, it will always be present in CM-based devices independent of incident flux, and in principle can eliminate the additional carriers generated by CM if charge extraction is

DOI: 10.1021/acs.chemrev.6b00169
Chem. Rev. 2016, 116, 10513−10622

insufficiently fast. Since optical probes of CM rely on the signature of Auger recombination, device needs and experimental needs are seemingly at odds, even before considering that the strong coupling between dots to facilitate rapid charge separation can result in changes to the electronic structure, potentially modifying the CM yield. In fact, early experiments conducted on PbSe films utilizing standard spectroscopic CM analysis methods found large variations in the apparent CM yield,[547] presumably due to the above-mentioned effects of coupling. However, the discovery of photocharging artifacts in later studies suggests that at least some of the observed variations might have resulted from uncontrolled photoionization. Finally, as described in Section 7.4.3, experiments on close-packed films of Si QDs have suggested that a new mechanism for CM may be active in strongly coupled films, whereby additional charges are generated in NCs adjacent to the photoexcited NCs due to a quantum-cutting effect.[490]

7.6.1. Time-Resolved Microwave Conductivity Measurements. To explore the influence of coupling on CM, Siebbeles and co-workers employed time-resolved microwave conductivity (TRMC) experiments to study QD films as a function of intradot coupling controlled through various ligand treatments.[547−549] In these experiments, films of QDs mounted in a microwave waveguide cell are photoexcited with a nanosecond optical pulse, and the change in microwave power reflected from the film is then measured as a function of time following photoexcitation (Figure 58a).

The change in microwave power (ΔP) can be related to the change in the conductance (ΔG) due to photoinjected carriers by the following expression:

$$\frac{\Delta P(t)}{P(t)} = -K\Delta G(t) \tag{28}$$

where P is the incident microwave power and K is an instrument-dependent sensitivity factor. The mobility of the photogenerated carriers can then be determined from the peak of the photoconductivity:

$$\Delta G|_{t=0} = q\Phi\left(e\beta I_0 F_a \sum \mu\right) \tag{29}$$

where β is the parameter related to dimensions of the microwave waveguide cell, I_0 is the incident photon fluence, F_a is the fraction of light absorbed by the sample, Φ is the yield of free (mobile) e-h pairs per photogenerated exciton, $\sum\mu$ is the sum of the electron and hole mobilities, and q, as before, is the QE of photon-to-exciton conversion.

To characterize the CM yield of films of PbSe QDs, the photoconductivity is measured for excitation with various photon energies. Following photoexcitation, carriers quickly thermalize to the band edge on a picosecond time scale, much faster than the nanosecond temporal resolution of the TRMC measurements. Thus, one might expect that carrier mobilities measured by this technique should be independent of the excitation energy. Experiments measuring the photoconductivity as a function of ligand length, along with time-resolved THz experiments, suggest that below the CM threshold Φ is near unity for PbSe QD films,[550] presumably due to the high dielectric constant that effectively screens the e-h interaction and facilitates charge separation. The changes in the photoconductivity should then reflect changes in the fraction of absorbed photons, along with any contributions from CM above the CM threshold.

The schematic of these measurements along with results obtained for PbSe QD films in ref 548 are displayed in Figure 58. Panel (b) of this figure shows plots of the absorption spectrum along with the photoconductivity divided by the fluence for a film infilled with Al_2O_3 via atomic layer deposition (ALD). As expected, for low photon energies, the photoconductivity closely follows the absorption spectrum, while at higher energies an increasing enhancement in the photoconductivity is observed. Utilizing eq 29, the QE of photon to e-h pair conversion can be calculated, and it is shown in Figure 58c, assuming that $q = 1$ for excitation below the CM threshold. For most of the studied films, the obtained CM yields follow the trend, which is similar to that from previous spectroscopic measurements on QD solutions (colored traces in Figure 58c).). However, the sample with a lower mobility shows a greatly reduced CM efficiency (black line in Figure 58c).

To explain these observations, the authors of ref 551 proposed that chemical treatments applied to change interdot coupling do not modify the intrinsic multiexciton yield (η) but do affect the rate of extraction of extra carriers produced by CM from the QD. If the extraction is slow compared to the Auger lifetime of a multicarrier state, the extra carrier decays without being detected by the TRMC experiment because of its limited time resolution. Thus, the apparent CM yield revealed by these measurements (η_{TRMC}) depends not only on η but also on carrier mobilites.

By accounting for the competition between Auger recombination (rate r_A) and charge extraction (r_{ext}), one can relate the apparent TRMC CM yield to the true one by the following relationship:[551]

$$\eta_{TRMC} = \eta\frac{r_{ext}}{r_A + r_{ext}} \tag{30}$$

Using the Miller−Abrahams approach for calculating r_{ext},[552] the authors of ref 551 calculated the apparent TRMC yield of free carriers as a function of QD film mobility (red line in Figure 58d) and found a good agreement with the experimentally measured values. Their results further indicated that the values of intrinsic CM yields derived from the TRMC measurements of QD films were comparable to the yields measured spectroscopically for QD solutions, suggesting that the CM process was not considerably modified by interdot coupling. Finally, they made a conclusion that for devices to efficiently collect additional charges generated through CM, the mobility of the QD solid must be at least ~1 $cm^2 V^{-1} s^{-1}$ to ensure that charge extraction outcompetes Auger recombination. It should be noted that for more efficient CM materials with the potential to generate three or more e-h pairs per photon, even higher mobilites would be required due to a fast scaling of Auger lifetimes with the number of carriers per QD (Section 4.1).

7.6.2. Ultrafast Photocurrent Spectroscopy of QD Films. A new high-temporal-resolution technique for studies of CM in device-grade QD films and transient photoconductivity in general was recently introduced in ref 525. This technique is based on measurements of a transient photocurrent excited in a photoconductor incorporated into a gap of a 50 Ohm transmission line by a short laser pulse. The time resolution demonstrated in ref 525 was 50 ps, but it more recent implementations it was improved to ~10 ps.

This devices used in these studies are similar to a so-called Auston switch applied in ultrafast electro-optical sampling.[553] The structures studied in ref 525 comprised a 200-nm-thick film of QDs deposited on a glass substrate (Figure 59a). The film either was treated with 1,2-ethanedithiol (EDT) or was exposed to a sequential treatment with EDT and hydrazine using standard procedures.[60] The device was completed by thermally

DOI: 10.1021/acs.chemrev.6b00169
Chem. Rev. 2016, 116, 10513−10622

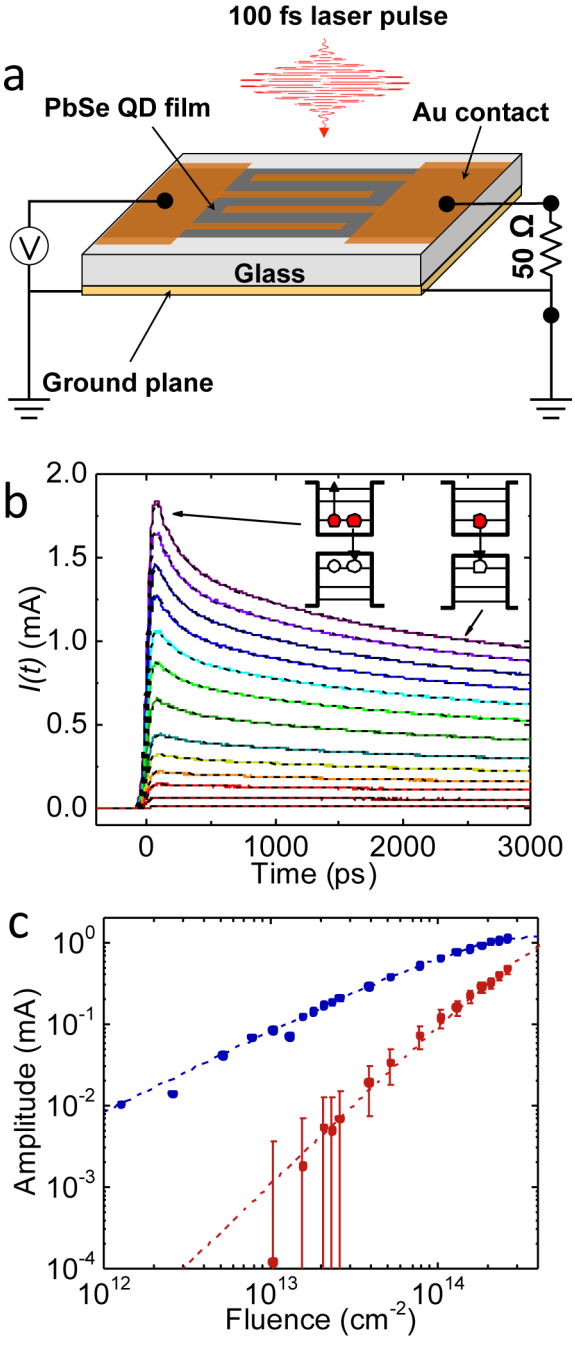

Figure 59. (a) Schematic of a photoconductive Auston switch with PbSe QDs utilized as the photoactive material. One side of the device is biased with a DC voltage, and photocurrent is monitored on the other terminal using a 20 GHz oscilloscope. (b) Fluence-dependent photocurrent transients, with $\langle N_{abs}\rangle$ from 0.003 to 0.68, measured for PbSe QDs with E_g = 0.69 eV and excitation at 1.55 eV. (c) The fluence dependence of the biexciton (red) and single-exciton (blue) populations obtained from the analysis of traces in (b) is well described by Poissonian statistics (lines). Adapted with permission from ref 525. Copyright 2015 Nature Publishing Group.

evaporating 100-nm-thick interdigitated gold contacts and a ground plane, forming a coplanar microstrip transmission line with 50 Ohm impedance. One of the top contacts was biased with an adjustable DC voltage, while the current was monitored on the other terminal with a 20 GHz sampling oscilloscope. The devices were excited with femtosecond pulses at 1.55 or 3.1 eV, and resulting photocurrent transients were detected with a temporal resolution of ~50 ps, which was sufficiently fast to follow Auger recombination of multiexcitons.

The temporal evolution of the photocurrent detected in these measurements can be described by the following expression:

$$j(h\nu, t) = 2q(h\nu)e\mu(t)En_{QD}\langle N(t)\rangle \quad (31)$$

where $j(h\nu,t)$ is the current density, which is proportional to the experimentally measured photocurrent, $I(t)$, e is the electron charge, E is the applied electric field, μ is the mobility of charge carriers (it is assumed that electron and hole mobilities are similar to each other), $q(h\nu)$ is the photon-energy-dependent quantum efficiency of photon to e-h pair conversion, n_{QD} is the density of the QDs, and $\langle N(t)\rangle$ is the average number of e-h pairs per QD. Equation 31 reveals that the temporal evolution of the photocurrent is governed by changes in the average occupancy from recombination processes, along with changes in the mobility arising, *e.g.*, from trapping of charges into lower-mobility localized states. However, if the charge trapping process is slow compared to recombination time scales, the photocurrent directly reports on population dynamics, suggesting that the early time dynamics will be analogous to those measured in TA experiments where the probe pulse monitors the population of the band-edge bleach.

Figure 59b displays photocurrent transients for EDT-treated films with a band gap of 0.69 eV, an electrical bias of 60 V, and excitation at 1.55 eV, which is below the CM threshold for these QDs. At low fluences, the photocurrent exhibits a slow decay on the nanosecond time scale, and the dynamics are virtually independent of excitation fluence, consistent with expectations for the situation when QDs are excited with only single excitons. With increasing pump fluence, an additional short-lived component develops, which is a typical signature of Auger recombination of multiexcitons. The lifetime of the short component is found to be 170 ± 10 ps, which is close to the expected Auger lifetime of 180 ps. Further, the quantitative analysis of the fast (biexciton) and the slow (single-exciton) signal components confirms that their amplitudes follow the expected pump intensity dependence (evaluated in terms of $\langle N_{abs}\rangle$) calculated based on Poisson statistics of photon absorption events (Figure 59c). These results validate expectations that the measured photocurrent transients directly report on carrier population decay in the QDs, and thus allow one to quantify CM yields via a usual analysis of exciton multiplicities.

Figure 60a displays similar measurements but conducted with 3.1 eV excitation when CM is possible ($\hbar\omega/E_g$ = 4.5). These measurements reveal that a fast Auger component persists in the limit of extremely low excitation intensities (down to $\langle N_{abs}\rangle$ of 0.007; inset of Figure 60b), at which the likelihood of multiple photon absorption is negligibly small (<1%). Importantly, the low-pump-intensity 3.1 eV transients can be replicated using 1.55 eV excitation, albeit with much higher pump fluences (Figure 60a inset). These results are clear signatures of CM. The low-pump intensity limit of exciton multiplicities derived from these measurements (Figure 60b) indicates *QE* of 144%, which corresponds to the multiexciton yield of 44%.

Importantly, for all studied QD sizes, multiexciton yields obtained by the transient photocurrent method are in close agreement with previous ultrafast optical studies of PbSe QD solutions (Figure 60b), indicating a negligible effect of interdot coupling on the CM process and suggesting that the CM yields observed for QD colloidal suspensions can in principle be reproduced in practical devices, at least at early stages after

DOI: 10.1021/acs.chemrev.6b00169
Chem. Rev. 2016, 116, 10513−10622

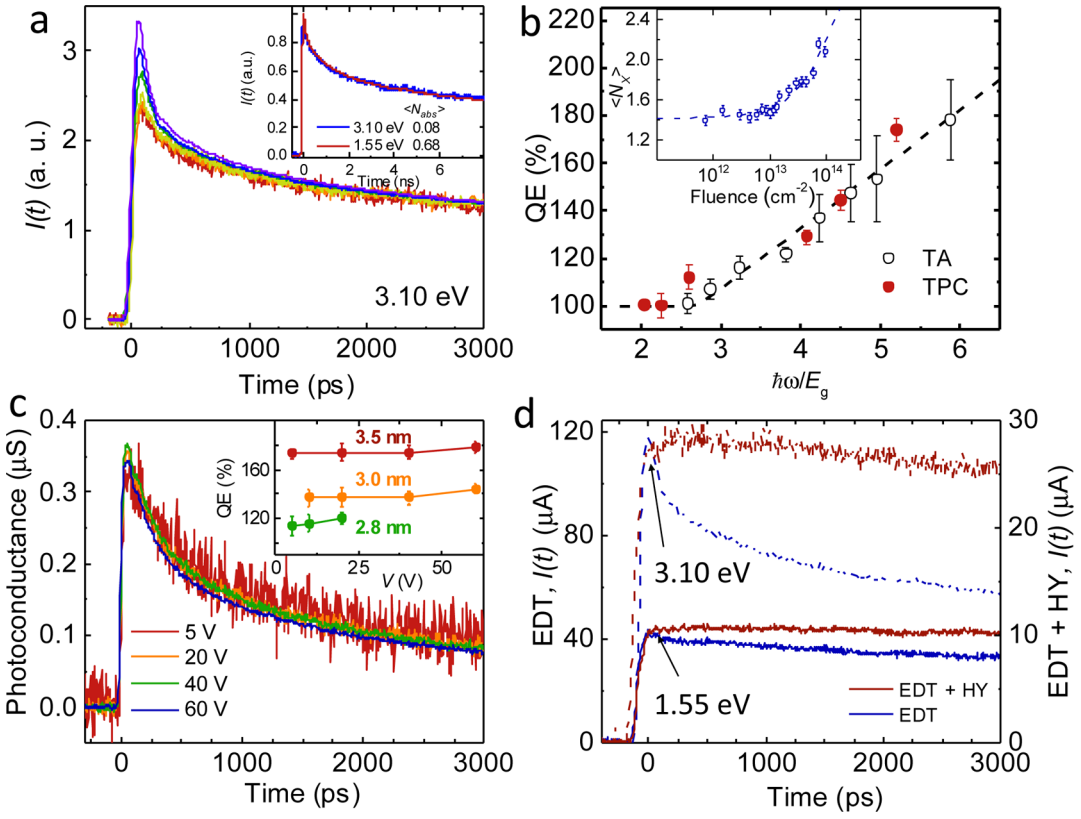

Figure 60. Long-time normalized photocurrent transients for the same sample as in Figure 59, but with 3.1 eV photon energies. Pump fluences correspond to $\langle N_{abs} \rangle$ from 0.04 to 1.3 (from bottom to top).The inset shows that the dynamics recorded with 1.55 and 3.1 eV excitation are identical. (b) Comparison of the CM yields measured for QD solutions via TA (black open circles) and by the transient photocurrent method for QD films (solid red circls). The inset shows the fluence dependence of the exciton multiplicity from the data in (a). (c) The voltage dependence of the transients exhibits Ohmic behavior, with no change in the CM yield. The inset shows the voltage dependence of the QE for QDs of three sizes. (d) The QD films treated with EDT and hydrazine (red) maintain the same increase in the early time amplitude as the EDT-treated film (blue) when comparing 3.1 eV (dashed) and 1.55 eV (solid) excitation. The lack of Auger decay at the low fluence observed together with the same signal amplitude is evidence of complete charge separation prior to Auger recombination. Adapted with permission from ref 525. Copyright 2015 Nature Publishing Group.

photoexcitation before any significant carrier losses due to recombination occur. These results are also in good agreement with the conclusions of the TRMC measurements, with the advantage of being obtained in a more direct way without the need for extraction from apparent efficiencies distorted by incomplete charge extraction.

It is known that impact ionization, which underlies CM in extended bulk solids, is enhanced by an electric field,[554,555] modifying both the threshold and e-h pair creation energy.[556] The photocurrent methodology easily allows for an evaluation of the influence an electric field on the CM process in QDs. Control experiments conducted below the CM threshold indicate that the photoconductance is constant for all fluences measured, revealing the expected Ohmic behavior. At excitation above the CM threshold, no dependence of the measured dynamics on the applied voltage is observed either (Figure 60c). This behavior indicates that the CM yield is independent of an electric field, at least for field strengths up to ~24 kV/cm. Further, since the applied fields are of the same order of magnitude as those existing in the depletion region of a *p-n* junction QD solar cell one can conclude that the presence of built-in electric fields in practical PV structures will not affect the CM performance of the QDs.

The transient photocurrent technique is also well suited for direct evaluation of the competition between Auger recombination and charge extraction, the importance of which was indicated by previous TRMC studies (see previous subsection). The above measurements on EDT-treated films (Figure 60a and blue traces in Figure 60d) indicate that biexcitons produced by CM quickly decay prior to extraction from the QDs. However, if films are exposed to sequential treatment with EDT and hydrazine, which is known to enhance inter-QD coupling,[42] the signatures of Auger decay disappear from the transient measured with 3.1 eV excitation while the photocurrent amplitude still shows a CM-related enhancement. Based on the signal amplitudes measured with 1.55 and 3.1 eV excitation, the QE in the film treated with EDT/hydrazine is 148%, which is in agreement with the QE of 144% found for the EDT-treated films. This result once again indicates that the additional film treatment can enhance charge separation without modifying the CM yield and confirm the practicality of extracting the additional charges generated from CM.

7.6.3. Carrier Multiplication in Solar Cells and Photodetectors. Since the initial discovery of CM, great strides have also been made in the development of QD solar cells that exhibit signatures of CM in the collected current. The physics and design considerations of QD solar cells have been recently been reviewed in ref 557, and we restrict ourselves to devices exhibiting enhanced efficiency due to CM. Signatures of CM can be observed in QD solar cells by examining the dependence of the external and internal quantum efficiencies (EQE and IQE, respectively) as a function of photon energy. Studies of devices comprising PbSe QDs exhibited an enhancement of the EQE at

DOI: 10.1021/acs.chemrev.6b00169
Chem. Rev. 2016, 116, 10513−10622

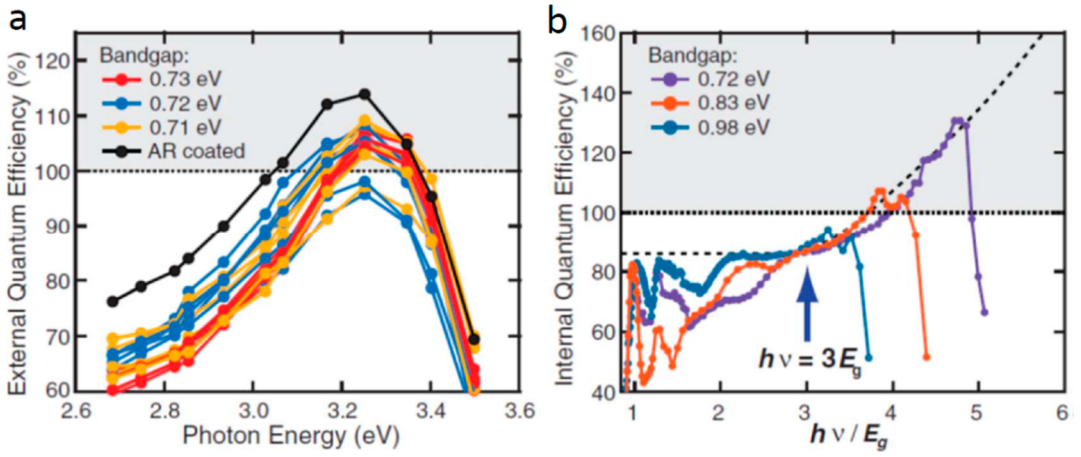

Figure 61. (a) Photon energy dependence of the EQE for 18 independent PV devices with PbSe QDs of band gaps 0.71 eV (yellow), 0.72 eV (blue), and 0.73 eV (red), and a device with an antireflective coating (black). (b) EQE curves as a function of $\hbar\omega/E_g$, exhibiting similar behavior to colloidal suspension measurements. The dashed black line is the average result for PbSe QDs in solution, with the base value offset to account for intrinsic losses in the device. Adapted with permission from ref 60. Copyright 2011 AAAS.

large photon energies that reached peak values of up to 114%, directly indicating the generation and collection of multiple e-h pairs produced by single photons (Figure 61a).[60] A plot of the IQE versus E_g-normalized photon energy shows spectral trends that are similar to those observed for colloidal suspensions via optical spectroscopies and more recently via TRMC and ultrafast photocurrent measurements on device-grade films discussed above. In fact, after a correction by a factor of ∼1.18, which accounts for recombination and transport losses, the CM quantum yields extracted from solar cell measurements show also a good quantitative agreements with results of spectroscopic studies.

EQEs of greater than 120% have also been demonstrated in QD solar cells of $CuInSe_2$ and PbTe.[61,558] These results further support the expectation that CM efficiencies observed in QD solutions can be realized in practical devices. Experiments on QD-sensitized solar cells also revealed enhancement in the collected photocurrent at high photon energies, suggesting that alternative solar cell designs besides a traditional p−n junction can benefit from CM active materials.[559]

As was discussed earlier, high carrier mobilities are required to foster efficient charge separation that could outcompete Auger recombination.[525,551] However, in a solar cell the quantum efficiency of collected charges relates more to the charge carrier lifetime, which is largely determined by the density of trap sites, as opposed to the mobility of a QD film.[560] Hence, it is possible to have efficient QD solar cells exhibiting long carrier lifetimes but low mobilities that would not, then, exhibit signatures of CM due to efficient Auger recombination. QD solar cells that aim to exploit CM will require both high mobility and long carrier lifetimes, which will in turn require a significant decrease in the trap state density over what is realized in currently available QD films. Additional improvements in device design, along with further improvements in the CM efficiencies (using, *e.g.*, engineered nanocrystals), will also be needed to realize CM-enhanced solar cells with PCEs that would become of commercial significance.

In addition to be observable in solar cells, CM enhancements have also been shown in photoconductive detectors comprising PbS QDs.[561] In these detectors, large photocurrent gain is achieved through the efficient trapping of one type of charge carriers (an electron or a hole), allowing for the other type of carriers to be recirculated multiple times during the lifetime of the trapped charge. In this way, the additional "uncompensated" carriers generated through either Auger ionization following CM or direct photoionization will lead to an enhancement of the detector sensitivity at high photon energies. Indeed, experiments showed a sharp enhancement in the gain of these detectors at high photon energies.[561] However, it is difficult to evaluate the relative contribution from direct photoionization versus the CM process. The data do show trends expected for CM when plotted versus $\hbar\omega/E_g$, however, as was discussed in 7.2.2 direct photoionization can also exhibit a similar behavior.[523] Nonetheless, these results are interesting and suggest the practicality of using CM not only in solar cells but also high-sensitivity photodetectors.

8. QUANTUM DOT LUMINESCENT SOLAR CONCENTRATORS

8.1. Introduction to Luminescent Solar Concentrators

For lasing and LED applications (see Sections 5 and 6, respectively) the properties and performance of QDs are often compared to those of currently used organic fluorophores. Similarly, QDs are rapidly emerging as valuable alternatives to organic dyes for next generation luminescent solar concentrators (LSCs). In their simplest use, LSCs are photon management devices that are cost-effective alternatives to optics-based solar concentration systems.[562−564] In addition to potentially enhancing the performance of stand-alone solar cells, LSCs offer completely new possibilities for integrating PV devices into existing or newly constructed buildings,[563,565] in the form of, for example, semitransparent PV windows that would transform nominally energy-passive building façades into large-area energy generation units. PV-active windows and other architectural elements can be combined with existing solar technologies for the realization of future net zero-energy consumption buildings.[64,563,566−569]

A typical LSC consists of an optical waveguide (usually a flat plastic or glass slab) doped or coated with fluorophores.[570,571] Both direct and diffuse sunlight can penetrate the plastic or glass matrix, where it is absorbed by the fluorophores and re-emitted at a longer wavelength. The luminescence, guided by total internal reflection, propagates to the waveguide edges, where it is

DOI: 10.1021/acs.chemrev.6b00169
Chem. Rev. 2016, 116, 10513−10622

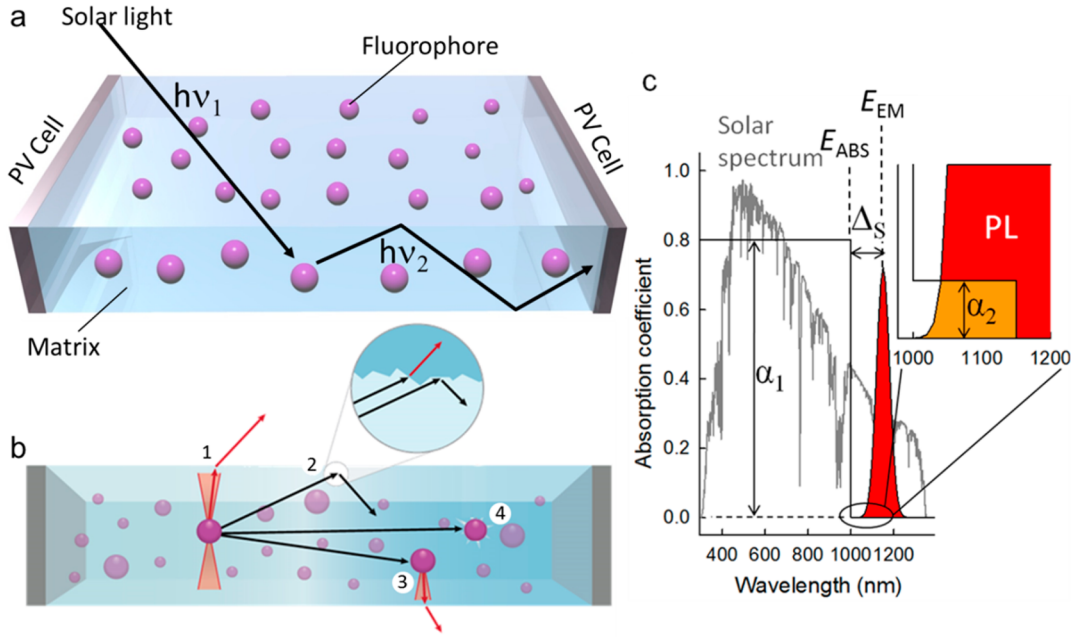

Figure 62. (a) Schematic representation of an LSC made of a transparent matrix doped with fluorophores. (b) Depiction of possible optical losses: (1) geometric loss due to isotropic emission into the escape cone defined by the refractive index contrast between the matrix and the surrounding medium; (2) scattering at surface or bulk defects, followed by propagation through the interface; (3) reabsorption followed by emission into the escape cone; and (4) reabsorption followed by nonradiative recombination. (c) Schematic depiction of the optical properties of an idealized LSC emitter featuring a step-like optical absorption (black line) covering the majority of the solar spectrum (gray line), and a substantial effective Stokes shift (Δ_S) with $\alpha_1 \gg \alpha_2$.

converted into electricity by PV cells installed along the slab perimeter (Figure 62a).[562−564] There are several sources for performance versus cost gains in this scenario. LSCs are much less expensive to produce than PV devices on a per unit area basis, so like a conventional optical concentrator (*e.g.*, a Fresnel lens), they represent a cost-effective means for effectively increasing the collection area for a smaller solar cell. In addition to increasing the flux of radiation incident onto the PV device and thus boosting the photocurrent,[563,570] this minimizes concerns regarding the cost of the PV material itself, allowing one to use higher efficiency devices that would be prohibitively expensive to produce in large-area forms. Importantly, unlike a lens, the collection efficiency of an LSC is not strongly dependent on the angle of incidence of the light, making them uniquely effective at capturing diffuse and reflected light. Finally, an additional increase in the power output can be realized because LSCs convert the incident solar spectrum into spectrally narrow light. For a typical solar cell, the quantum efficiency of the photon-to-charge-carrier conversion process (expressed as the EQE; Section 7.6.3) varies with photon energy, and usually falls dramatically in the UV part of the spectrum. An LSC can be matched to a PV device such that all absorbed photons are down-converted to a wavelength at which conversion is most efficient (the spectral peak of the EQE for a given device).

Based on these potential advantages, the LSC concept was originally introduced in the 1970s in an attempt to mitigate the high costs associated with crystalline silicon (c-Si) PVs.[570,572−574] Despite a great flurry of experimental and theoretical studies,[564,566,568,571,575−579] low oil prices over the past four decades, together with technical bottlenecks associated with the limitations of dyes that prevented the realization of real world LSCs, have led to near abandonment of the field. More recently, however, QDs with optical properties nearly ideal for LSC applications[64,325,567,580] have instigated a renaissance that might lead to commercialization of QD-LSCs for building integrated PV applications in the near future.

In this Section, we will discuss the basic operating principles of LSCs and review the most promising QD-based approaches for the realization of efficient, large-area devices. Particular emphasis will be placed on the fundamental physical mechanisms, and consequent advantages and limitations of so-called "Stokes-shift engineering" strategies that are being pursued for achieving "reabsorption-free" QDs for large-area LSCs. We will also review and examine strategies for controlled incorporation of QDs into polymer matrices to serve as LSC waveguides, as well as colorimetric evaluations of the aesthetic and functional impact of building-integrated PV-windows based on QD-LSCs, in comparison to those based on organic dyes.

8.2. Operating Principles and Main Characteristics of Luminescent Solar Concentrators

As mentioned above, the basic LSC design consists of a plastic or glass waveguide doped or coated with fluorophores, and coupled to PV cells along the perimeter edges (Figure 62a). The efficiency with which light incident upon the surface of the LSC can be guided to the PV cells is subject to a number of potential loss processes along the path (Figure 62b), all of which combine to reduce the overall efficiency of the device. Upon irradiation of the LSC with sunlight, a fraction of the incident flux is reflected from the top surface of the matrix, as determined by the reflectivity (R) of the waveguide material, which is a function of the contrast between its refractive index (n) and that of its optical surroundings ($n = 1$ for air). For an LSC with refractive index $n = 1.5$ (typical for silica glass and common transparent plastic matrixes across the UV and visible portions of the solar spectrum), at normal incidence, the optical transmittance (T) of the top surface of the waveguide is $T = (1 - R) = 1 - [(n - 1)/(n + 1)]^2 = 0.96$. Of this transmitted light, a fraction is then absorbed by the fluorophores within the waveguide, as

DOI: 10.1021/acs.chemrev.6b00169
Chem. Rev. 2016, 116, 10513−10622

determined by the total optical density. This can be expressed as the product of the wavelength-dependent absorption coefficient, $\alpha(\lambda)$, which is in turn a function of fluorophore absorption cross section and concentration and device thickness, d. Light is then re-emitted isotropically at a longer wavelength according to the PL QY, η_{PL}. The portion of this luminescence that gets trapped and guided inside the waveguide is, again, determined by the refractive index of the matrix material, which, according to the Snell's law, defines the critical angle for total internal reflection $\theta_c = \sin^{-1}(1/n)$ (Figure 62b). Only the luminescence approaching the waveguide/air interface with an incidence angle $\theta \geq \theta_c$ is trapped inside the matrix; the remainder falls within the so-called "escape cone" and is lost through the top or bottom surface of the waveguide. This effect is commonly expressed in terms of the trapping efficiency of light at the emission wavelength, $\eta_{TR}(\lambda_{em}) = \cos\theta_c = (1 - 1/n^2)^{1/2} = 0.745$ (for $n = 1.5$), which represents the maximum achievable optical efficiency for a defect free waveguide with perfect emitters, without special reflective coatings (*e.g.*, engineered "selective reflectors") on the top and bottom surfaces of the device. Light emitted outside the escape cone is then subject to scattering at surface or bulk defects; the probability that such a scattering event occurs and results in the scattered photon being directed into the escape cone can be denoted $\eta_S(\lambda_{em})$. Finally, as long as the fluorophores have a nonzero absorption cross section at the wavelength of emission, emitted photons are subject to reabsorption by other fluorophores. When this occurs, the isotropic emission process is repeated, raising again the possibility of η_{PL}-related and escape-cone losses; the fraction of light lost to reabsorption-related events can be expressed as $\eta_{RA}(\lambda_{em})$.

To quantify the external optical efficiency of an LSC, we first introduce a "monochromatic", single-wavelength external efficiency $\eta_{LSC}(\lambda)$, which is defined as $\eta_{LSC}(\lambda) = \Phi_{OUT}(\lambda_{em})/\Phi_{IN}(\lambda)$, where $\Phi_{IN}(\lambda)$ is the photon flux at the wavelength λ incident onto the LSC surface and $\Phi_{OUT}(\lambda_{em})$ is the output photon flux at the fluorophore emission wavelength λ_{em} at the waveguide edges attached to the PV cells (strictly speaking, the quantity Φ is the spectral density of the photon flux measured in units of time^{-1} × wavelength^{-1}). An expression for η_{LSC} that captures the role of the parameters of the matrix and the fluorophores described above can be presented as

$$\eta_{LSC}(\lambda) = [1 - R(\lambda)](1 - e^{-\alpha(\lambda)\cdot d})\eta_{TR}(\lambda_{em})\eta_{PL} \times [1 - \eta_{RA}(\lambda_{em})][1 - \eta_S(\lambda_{em})] \quad (32)$$

Using eq 32, we can calculate an overall external quantum efficiency ($\eta_{LSC,QE}$) and a power conversion efficiency ($\eta_{LSC,PE}$) of an LSC:

$$\eta_{LSC,QE} = [\int \eta_{LSC}(\lambda)S(\lambda)d\lambda][\int S(\lambda)d\lambda]^{-1},$$
$$\eta_{LSC,PE} = [(\lambda_{em}^{-1})\int \eta_{LSC}(\lambda)S(\lambda)d\lambda][\int \lambda^{-1}S(\lambda)d\lambda]^{-1} \quad (33)$$

These quantities account for the spectral distributions of solar radiation, which is described in terms of the spectral density of the solar photon flux $S(\lambda)$.

An important parameter for maximizing the overall output of the LSC is the coverage of the solar spectrum achievable with a given fluorophore, as it determines the fraction of the solar spectrum that can be harvested and eventually converted into electricity. A common intrinsic limitation of organic emitters is their relatively large band gaps, falling within the visible region of the spectrum, as shifting into the near-IR is difficult to realize via straightforward extension of the length of a conjugated system, and it is typically accompanied by a progressive weakening of the dipole moment, reducing both absorption and emission efficiencies. Finally, efficient intersystem crossing and coupling to C−H vibration overtones further reduce emission efficiency. As a result, near-IR absorbing organic fluorophores are intrinsically inefficient emitters, which directly impacts the optical efficiency of LSCs based on such dyes.

From eq 32 it is evident that a scattering-free optical waveguide and near-unity η_{PL} for the fluorophore are necessary but insufficient for achieving highly efficient LSCs. An important parameter which has so far stymied LSCs as a viable technology is the η_{RA} (reabsorption loss) term. The significant overlap between the absorption and emission spectra of organic fluorophores leads to a considerable probability that guided light will be reabsorbed, potentially even more than once. This becomes an especially serious problem in the case of the long optical pathways expected in large-area LSCs,[581] and it ultimately results in a strong device-size dependence of the LSC optical efficiency.[575,582,583] For this reason, ideal LSC emitters should exhibit no overlap between their absorption and emission spectra. In the example schematically depicted in Figure 62c, the optical absorption of an idealized fluorophore extends across the whole visible spectrum at a high average value denoted α_1, while emission occurs in the near-IR, centered around energy E_{EM}. In the inset, an expanded view shows that absorption in the spectral region of the emission peak, α_2, is much smaller than α_1.

The separation between E_{EM} and the onset of strong absorption, E_{ABS}, is often discussed in terms of an effective Stokes shift $\Delta_S = E_{ABS} - E_{EM}$. The optimal value of Δ_S is determined by a balance of factors. Typically, the less abrupt shape of the absorption profile of real fluorophores, combined with the finite emission peak width, imposes a minimum value of Δ_S necessary for achieving $\alpha_2 \ll \alpha_1$. Minimizing α_2 is essential, particularly in large LSCs: for $\alpha_2 = 10^{-1}$ cm^{-1}, ∼99% of the guided photons generated at the center of an LSC with lateral dimensions of 1 m would experience at least one reabsorption event. On the other hand, an excessively large Δ_S can be detrimental to LSC efficiency, as it introduces a transparency window within which solar photons are not harvested, reducing both $\eta_{LSC,QE}$ and $\eta_{LSC,PE}$.

One further important parameter describing the performance of an LSC is the optical concentration factor $C = \phi_{OUT}/\phi_{IN}$, which is the ratio between the output and incident photon flux densities or irradiences. These quantities are defined as $\phi_{IN} = \Phi_{IN}/A_{IN}$ and $\phi_{OUT} = \Phi_{OUT}/A_{OUT}$ (where A_{IN} and A_{OUT} are the areas of the illuminated and output surfaces of the LSC, respectively), and are measured in units of time^{-1} × area^{-1} × wavelength^{-1}. The concentration factor depends directly on both the optical efficiency of the device and its dimensions according to the expression $C = G\eta_{LSC}$, where G is the so-called geometric gain factor $G = A_{IN}/A_{OUT}$. C defines the effective increase (or decrease) in the area of a PV cell coupled to an LSC compared to its actual area. If C is greater than unity, then its value directly translates into increased photocurrent, and thereby increased power output of the LSC−PV system. Importantly, while increasing the photocurrent, light concentration using an LSC does not lead to an increase in either open-circuit voltage (V_{oc}) or PCE, at least in ideal solar cells with low nonradiative losses. This is in contrast to traditional geometric concentration with lenses and mirrors, which boosts both V_{oc} and PCE. A detailed

DOI: 10.1021/acs.chemrev.6b00169
Chem. Rev. 2016, 116, 10513−10622

discussion of the PV aspects of the LSC technology can be found in refs 572 and 584.

In a planar LSC depicted in Figure 62a, the increase in the device length (L), or its geometric gain factor, leads at first to a linear increase in the optical concentration factor ($C \propto L \propto G$); however, at a certain critical length (L_c), defined by the abosrption coefficient at the wavelegth of guided light ($L_c \propto 1/\alpha_2$), it saturates at the value $C = C_{sat}$. As demonstrated in ref 583, in the case of a stepwise absorption coefficient shown in Figure 62c, the saturated value of C can be expressed as

$$C_{sat} = \frac{(1-R)}{2\beta(\eta_{PL}^{-1}\eta_{TR}^{-1}-1)}\frac{(1-e^{-\alpha_1 d})}{\alpha_2 d}$$

where α_1 and α_2 are the absorption coefficients for light incident onto the LSC and re-emitted radiation, respectively; $\beta = 1.4$ is a constant obtained by fitting the exact expression for the L-dependent efficiency of a planar LSC from ref 574 to the analytical model of ref 583. The maximum of C_{sat} is realized when $\alpha_1 d$ approaches 0, which defines an ultimate concentration limit (C_0) attainable with a given fluorophore for the device configuration shown in Figure 62a:

$$C_0 = \frac{(1-R)}{2\beta(\eta_{PL}^{-1}\eta_{TR}^{-1}-1)}\frac{\alpha_1}{\alpha_2} = FQ_{LSC}$$

here $F = (1-R)[2\beta(\eta_{PL}^{-1}\eta_{TR}^{-1}-1)]^{-1}$ and $Q_{LSC} = \alpha_1/\alpha_2$ is the so-called LSC quality factor introduced in ref 583. In the case of an ideal emitter with $\eta_{PL} = 1$ and the glass/air interface ($\eta_{TR} = 0.75$ and R = 0.04 for the normal incidence), $F = 1.45/\beta$ or $F \approx 1$, if $\beta = 1.4$. This indicates that the maximum concentration factor achievable with a given fluorophore is directly proportional to Q_{LSC}, and furthermore, in the case of the ideal quantum yield, it is approximately equal to the LSC quality factor, *i.e*, $C_0 \approx Q_{LSC}$.

8.3. Quantum Dots as an Alternative to Organic Dyes for Applications in Luminescent Solar Concentrators

To date, the realization of LSC devices for real world application has been hindered by the nonideal properties of typical organic emitters, which do not offer the requisite combination of broadband optical absorption across the whole visible spectrum, efficient fluorescence, and suitably large Δ_S. Even the best conjugated organic and organometallic candidate fluorophores fulfill only some of the above requirements, generally exhibiting only limited coverage of the solar spectrum and/or significant reabsorption losses.[581,585] In Figure 63, we overlay the absorption (black line) and emission (red line) spectra of some representative organic dyes that have been used in experimental LSCs with the spectrum of solar radiation at sea-level (gray) to evaluate their light-harvesting capability. For example, 4-dicyanomethyl-6-dimethylaminostiryl-4H-pyran (DCM; Figure 63a) is a red-emitting dye with an absorption onset at ~470 nm;[586] while this means it offers a relatively large Δ_S, its coverage of the solar spectrum is very limited. Yellow-emitting CrS040 dye (Figure 63b) is even worse, as its LSC performance is further undermined by a very small Δ_S. Some organometallic dyes illustrate how excessive Δ_S ultimately hurts efficiency: the lanthanide complexes shown in Figure 63c and d offer essentially zero self-absorption, but they are transparent to large portions of the solar spectrum. The IR-emitting ytterbium chelate in Figure 63d is further hampered by low luminescence efficiency, as it is strongly quenched by coupling to C−H vibration overtones. To date, the top-performing organic dyes include BASF Lumogen red (Figure 63e) and various perylene

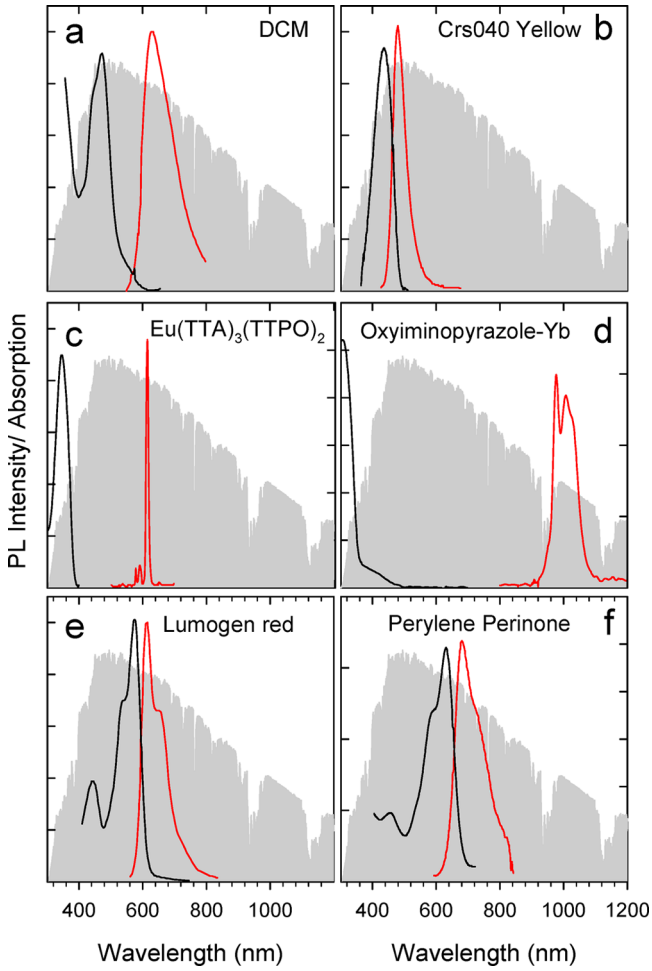

Figure 63. Optical absorption (black lines) and PL spectra (red lines) of some organic LSC dyes: (a) 4-dicyanomethyl-6-dimethylaminostyryl-4H-pyran (DCM[572]); (b) yellow-emitting CrS040 Dye from Radiant Color;[569] (c) europium tris(2-thenoyl trifluoro acetonate)-di-(triphenylphosphine oxide) ($Eu(TTA)_3(TPPO)_2$);[587] (d) a near-IR-emitting oxyiminopyrazole-based ytterbium chelate;[588] (e) BASF Lumogen red; and (f) a perylene perinone dye.[589,590] The spectrum of solar radiation at sea level is shown as gray shading to highlight the different solar harvesting abilities of the chromophores.

perinone derivatives (Figure 63f). They offer excellent absorption over the most intense portion of the solar spectrum, and they are highly fluorescent. Nonetheless, the significant overlap between their absorption and emission spectra leads to dramatic losses to reabsorption even over relatively short optical distances.[64,585] In addition, these organic dyes also tend to produce strongly colored devices, which limits their use in architecture, as will be discussed in detail in Section 8.7.

Colloidal QDs are a promising alternative to organic/organometallic dyes as LSC materials.[64,563,566,567,591,592] They feature high, sometimes near-unity PL quantum yields, large absorption coefficients over broad spectral windows, and a tunable emission wavelength controlled by the QD size and/or composition. Furthermore, colloidal QDs show enhanced photostability over organic chromophores,[62,592−594] and can be incorporated into various organic and inorganic matrices via solution-based procedures.[594−597] Finally, tuning the emission of QDs into the IR does not come at a cost of the luminescence QY η_{PL}. For QDs, the phonon energies are small (typically <50 meV); as a result, the effects of intersystem crossing are

DOI: 10.1021/acs.chemrev.6b00169
Chem. Rev. 2016, 116, 10513−10622

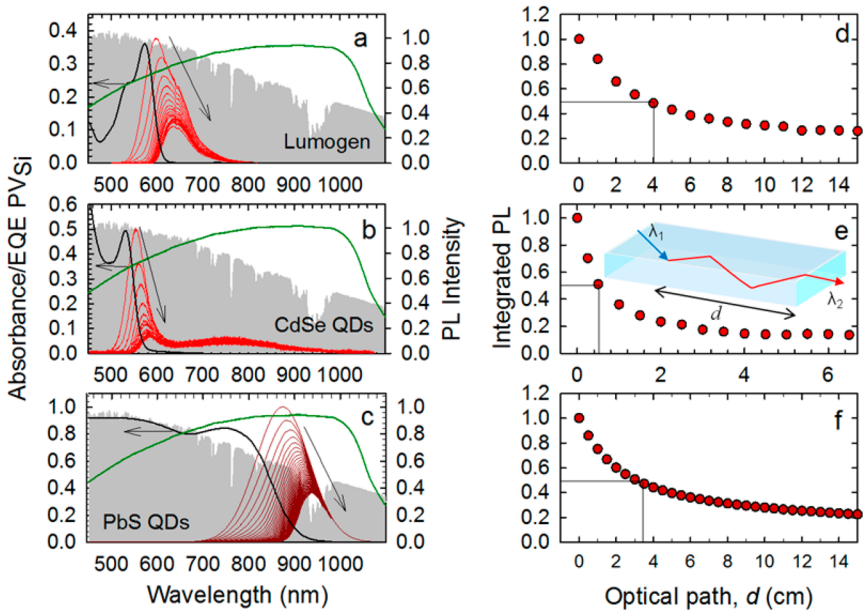

Figure 64. (a) Optical absorption (black line) and PL spectra (red lines, excitation at 473 nm) collected at the edge of an LSC based on BASF Lumogen R305, as the distance, *d*, between the excitation spot and the slab edge gets progressively larger. The shape of the PL spectrum changes dramatically with *d* as a result of strong reabsorption of emitted light. (b) Same for an LSC based on CdSe QDs (excitation at 405 nm). As a result of strong reabsorption, after 20 mm, the PL spectrum is dominated by a weak trap emission, which is not affected by reabsorption. (c) Same for an LSC based on PbS QDs. In (a)−(c), the green line is a representative EQE spectrum of a c-Si PV device, and the spectrum of solar radiation at sea level is shown as gray shading. It is apparent that, out of the three fluorophores, PbS QDs provide the best coverage of the solar spectrum and the most optimal position of the PL band for coupling to the Si PV. (d, e, f) Spectrally integrated PL intensity as a function of the *d* extracted from the PL spectra in a, b, and c, respectively.

insignificant and exciton coupling with the environment is strongly inhibited, especially in the presence of passivating shells. As a result, there are numerous examples of QDs with efficient IR-emission, including hetrostructured QDs based on ternary I−III−VI_2 semiconductors (*e.g.*, $CuInS_2$, $CuInSe_2$ and their alloys) with emission efficiencies >85% for PL at around 800 nm,[163] and lead chalcogenide QDs exhibiting fluorescence QY of 50−90% at even considerably longer wavelengths.[255,598]

One challenge associated with conventional QDs for use in LSCs is their fairly small apparent Stokes shift, Δ_S, which is in fact comparable to those of organic dyes (Figure 64a−c). In colloidal QDs, Δ_S arises from a combination of the effects of band-edge fine-structure splitting (due, *e.g.*, to shape anisotropy, electron−hole exchange interactions, and the crystal field;[67] see Section 2.4), phonon replicas, and size polydispersity.[597] In standard core-only or type-I heterostructured QDs based on CdSe, it is typically on the order of a few tens of millielectronvolts, which is comparable to the width of the QD emission peak.[62,64,577,581,599−601] As a result, the optical losses to reabsorption in an LSC based on such QDs are even more severe than those suffered by LSCs based on Lumogen red dye.[64] This can be demonstrated and quantified by examining the evolution of the emission spectra collected at the edge of representative LSCs based on each fluorophore as the excitation spot is moved a progressively larger distance (*d*) away from the edge (Figure 64). In Figure 64a and d, we see that increasing *d* to 4 cm for a Lumogen-based LSC results in a decrease in the intensity of edge-collected light of *ca.* 50%; a similar loss is observed for a CdSe-based LSC over a propagation length approximately ten times shorter (*ca.* 0.5 cm; Figure 64b and e). The situation becomes slightly better when using small PbS QDs that exhibit modestly larger Δ_S (Figure 64c and f); in this case, optical losses due to reabsorption become comparable to those of Lumogen red.[593,602] Importantly, PbS QDs also feature a much narrower energy gap with respect to both Lumogen and CdSe QDs and, as a result, their optical absorption spectrum extends to over 850 nm, a significant improvement in solar harvesting capability. Despite such an improvement, even PbS QDs are still unsuitable for real-world LSCs, which would require propagation lengths of at least tens of cm.

8.4. Approaches to Stokes-Shift Engineering with QDs

8.4.1. QD Heterostructures. A possible approach to tackling the reabsorption problem in QD-LSCs is the use of specifically designed heterostructures wherein the absorption and emission functions are separated between distinct structural domains of a nanocrystal.[64,581,601] The examples of this class of heterostructures are so-called giant thick-shell CdSe/CdS (or g-QDs;[601,603] Section 3.5) or "dot-in-bulk" CdSe/CdS nanocrystals featuring even thicker shells.[439,604−606] In these *quasi*-type-II systems, the small energy offset between the conduction band edges of CdSe and CdS allows for the electron wave function to delocalize over the entire nanocrystal volume, while the hole is confined to the CdSe core due to a much larger offset between valence band edges (Figure 65a).[600] In these structures, light absorption is dominated by the thick CdS shell due to its very large volume and consequently larger absorption cross- section. On the other hand, due to a very fast (<1 ps[605]) transfer of holes from the CdS shell to the CdSe core the emission originates from recombination of CdSe-core localized excitons. As a result of a large difference between CdSe and CdS band gaps (~0.67 eV), these structures exhibit a very large apparent Stokes shift (>0.4−0.5 eV; Figure 65b).

The combination of CdSe and CdS has been used to induce large Δ_S in a variety of structures, including spherical core/shell QDs,[605,607] dot-in-plate,[608] dot-in-rod[609] and rod-in-rod[610,611] nanoparticles, tetrapods,[612] octapods[613] and nanoplatelets.[614−616] In addition to the large Δ_S, the core/thick-shell

DOI: 10.1021/acs.chemrev.6b00169
Chem. Rev. 2016, 116, 10513−10622

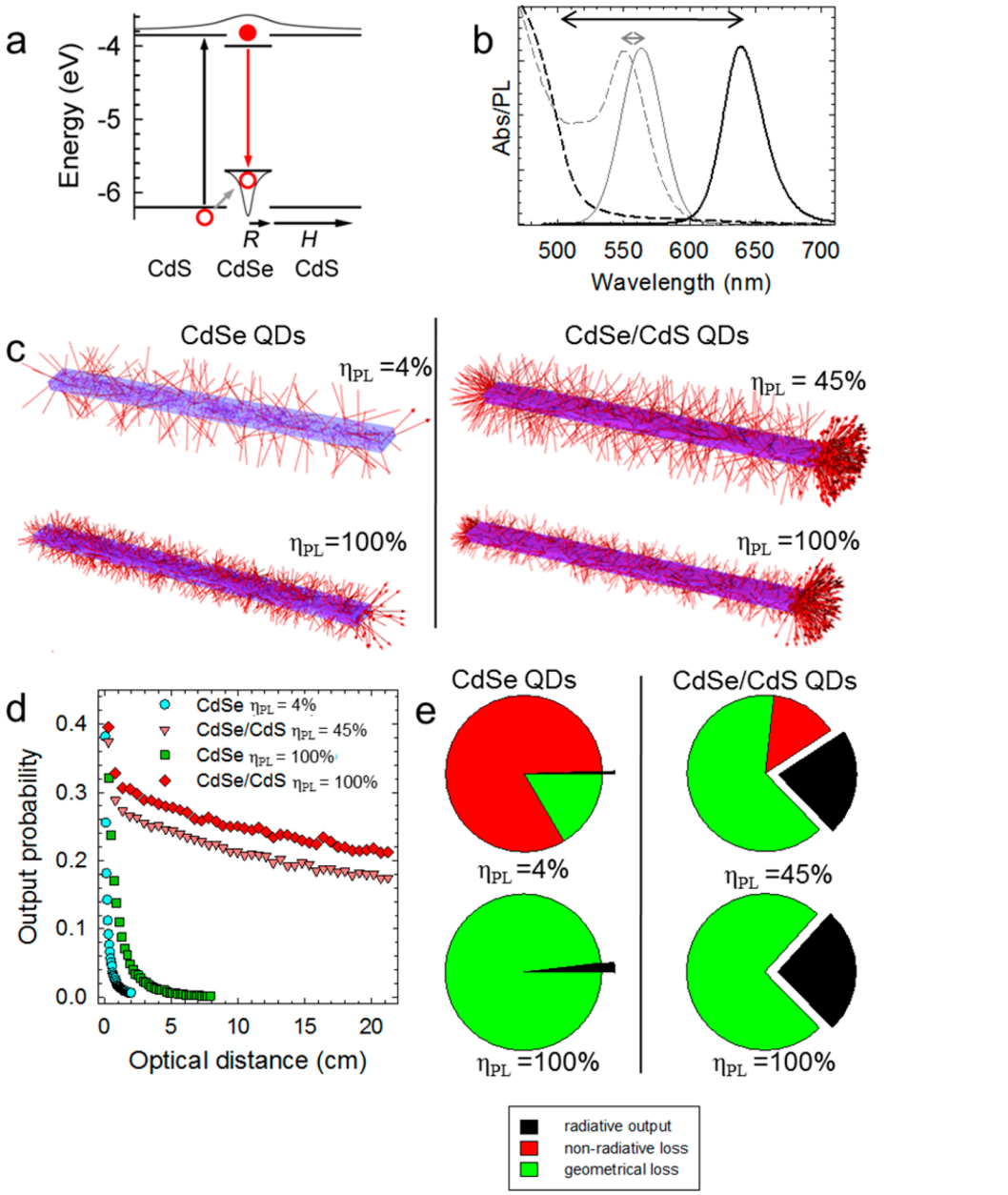

Figure 65. (a) Approximate band diagram of CdSe/CdS QDs. Following photon absorption in the shell (black arrow), photogenerated holes undergo rapid transfer to the core (gray arrow). The red arrow shows radiative recombination of a core-localized exciton. (b) Optical absorption (dashed lines) and PL (solid lines) spectra of reference core-only CdSe QDs with radius R = 1.5 nm (gray lines) and core/shell CdSe/CdS QDs with the same core radius and the shell thickness H = 4.2 nm (black lines). (c) Visualization of Monte Carlo ray-tracing simulations for LSC devices comprising reference core-only CdSe QDs and core/shell CdSe/CdS QDs; emission quantum yields are 4% and 45%, respectively. The LSCs are uniformly illuminated from the top, perpendicular to the slab surface (lateral dimensions 1.3 cm × 21.5 cm). Photons emerging from the device face coupled to a PV cell (not included in the figure) are shown by red arrows. The lower panels show the ray-tracing simulation for the same QDs but for the ideal emission efficiency of 100%; these calculations illustrate the role of losses due to re-emission into the escape cone. Despite identical emission quantum yields, core/shell structures show a considerably stronger performance compared to core-only QDs because of the reduced number of reabsorption events on the same propagation path. (d) Probability of a photon emitted at a certain distance (d) from the slab edge reaching the PV cell as a function of d for the LSCs shown in panel c. (e) Chart plots illustrating a breakdown of the total number of the originally emitted photons into three categories: photons reaching the PV cell (black area), photons lost to nonradiative recombination (red area), and photons escaped from the waveguide through the side walls and the opposite edge (green area). Figure adapted with permission from ref 64. Copyright 2014 Nature Publishing Group.

motif offers several other important advantages for LSC applications over conventional core-only QDs. One is a nearly complete isolation of the emitting core from the potentially harmful effects of environment by the thick outer shell. This reduces carrier losses due to nonradiative recombination via surface defects[617] and greatly improves the stability of QDs toward harsh thermal and/or chemical conditions that can arise during incorporation of QDs into sol−gel[595] or polymer matrices[64] (see Section 8.6).

A further advantage of thick-shell CdSe/CdS QDs is a reduction in the strength of inter-QD dipole−dipole coupling (due to increased core-to-core separation), which has been shown to suppress energy transfer in arrays of QDs used, *e.g.*, in QD-LEDs (see Section 6).[320] This can be important in the case

DOI: 10.1021/acs.chemrev.6b00169
Chem. Rev. 2016, 116, 10513−10622

of QD-LSCs, as incorporation of QDs into matrices often results in some degree of aggregation, opening the possibility of the same type of energy-transfer-related reduction in emission efficiency observed in QD films (Section 6.3).

Furthermore, thick-shell QDs (as well as dot-in-rod and rod-in-rod structures) can also offer reduced rates of nonradiative Auger recombination (see Section 4.3).[218,617] While multi-excitons should be rare under solar illumination, photocharging can still occur even at very low incident light intensities as was discussed Section 7.3. This would lead to long-lived charged QDs in which subsequent photoexcitation will produce trions susceptible to nonradiative Auger recombination, reducing the overall PL efficiency. In addition, carriers expelled from the QDs during Auger ionization can induce damaging chemical reactions in polymeric matrices, possibly producing absorptive color centers active in the ultraviolet and/or visible spectral regions. Reduced rates of Auger decay in thick-shell QDs (Section 4) lead to higher emission efficiencies for charged exictons[86,282] and also decrease the likelihood of Auger ionization and subsequent photochemical reactions, thus, partially alleviating harmful effects associated with photoionization.[523]

An important milestone in the field of QD-LSCs was the first practical demonstration of high-performance, large-area devices (tens of centimeters dimensions) utilizing Stokes-shift engineered thick-shell CdSe/CdS QDs.[64] The advantage of these QDs for LSC applications are apparent when their properties are compared to those of standard core-only CdSe (see Figure 65b–e). Figure 65b shows the absorption and PL spectra of CdSe QDs of radius 1.5 nm (gray lines) together with those of CdSe/CdS QDs with the same core size and the 4.2 nm thick CdS shell (black lines). The core-only CdSe QDs show a typical global Stokes shift of ~70 meV (gray double arrow). On the other hand, since in the CdSe/CdS QDs the CdS shell volume is ~80 times larger than that of the CdSe core (~1150 nm^3 vs. ~ 15 nm^3), the absorption spectrum is dominated by the CdS shell, which leads to an apparent absorption onset at ~510 nm.[218,314,600] At the same time, delocalization of the electron wave function into the CdS shell shifts the luminescence spectrum of the core/shell QDs to ~640 nm. As a result, CdSe/CdS QDs show a very large apparent Stokes shift of more than 400 meV (black double arrow in Figure 65b), which approaches the value defined by the difference in the band gaps of bulk CdSe and CdS.

A large effective Stokes shift in thick-shell CdSe/CdS QDs leads to a dramatic improvement of their LSC performance with respect to conventional core-only CdSe QDs. This is evident from Figure 65c, where we compare Monte Carlo ray-tracing simulations of light propagation in LSCs based on core-only and core/shell QDs. In order to disentangle the effects of suppressed reabsorption from those of the enhanced QD efficiency resulting from better surface passivation in thick-shell QDs, we show simulations performed using both actual experimental emission efficiencies (4% for core-only CdSe QDs and 45% for core/shell CdSe/CdS QDs) and the idealized case of 100% emission efficiencies. In the core-only QD LSC, only 0.2% of the originally emitted photons reach the PV cell due to strong reabsorption and low emission efficiency (Figure 65c, top left panel). In contrast, in the case of core/shell QDs, because of greatly reduced reabsorption and the increased emission efficiency, the number of outgoing photons is increased more than 100-fold (to 22% of the original number of emitted photons; Figure 65c, top right panel).

In Figure 65d, we show the dependence of the probability (P_c) for an emitted photon to be collected by the PV device on the distance from its origin from the edge. These data allow us to estimate the effective photon-collection length (L_c), defined as the distance at which P_c drops by 50%. For the core-only QDs, L_c is extremely short (1.3 cm), which severely limits the useful working area of LSCs. In contrast, the use of core/shell QDs allows for a considerable increase of L_c (up to *ca.* 20 cm), which indicates that this type of QDs is indeed suitable for the realization of large-area concentrators. Finally, the calculations assuming emission efficiency of 100% indicate that even in this ideal case, the effects of reabsorption still have a very significant effect on the LSC performance. In the case of core-only QDs, despite the absence of nonradiative losses, only 2% of the initially emitted photons reach the photovoltaic cell, while 98% escape from the waveguide due to reabsorption followed by re-emission into the escape cone. On the other hand, in the case of the core/shell QD-LSC, 26% of all emitted photons reach the PV cell. This indicates a more than 10-fold improvement in the optical efficiency obtained using QDs with a large engineered Stokes shift, which reduces the number of reabsorption events.

In a proof-of-principle demonstration of utility of Stokes-shift engineered QDs in LSCs, large-area prototype devices with dimensions 21.5 × 1.35 × 0.5 cm^3 were fabricated by incorporating CdSe/CdS QDs (1.5 nm core radius, 5 nm shell thickness) into a poly(methyl methacrylate) (PMMA) matrix.[64] A photo of one of these devices taken under ultraviolet illumination is displayed in Figure 66a; it highlights how luminescence generated across the device is collected and guided toward its edge. The effect of reduced reabsorption losses in these LSCs is illustrated in Figure 66b, which shows the absorption spectrum of the QD-doped polymer slab together with a set of edge-collected emission spectra for different distances (d) of the excitation spot from the edge. The data show that the shape of the emission band remains unchanged up to d = 20 cm, confirming the absence of noticeable reabsorption losses that otherwise would lead to a pronounced red-shift of the PL band (see an example of this effect in Figure 64a–c). Scattering losses were evaluated in a control experiment using 835 nm light that cannot be absorbed by the QDs and used to correct the PL output for losses to scattering. The corrected data (black open squares in Figure 66c) show a virtually d-independent PL signal, further confirming the negligible role of reabsorption.

Measurements using 1.5 AM Global illumination from a solar concentrator yield the overall quantum efficiency $\eta_{LSC,QE}$ of ~1%. This is equivalent to the effective (or "internal") quantum efficiency of 10% per absorbed photon, if one accounts that the studied devices absorb only 10% of incident radiation. The concentration factor can be calculated by multiplying $\eta_{LSC,QE}$ by the geometric gain factor (G = 21.5/0.5 = 43), which yields C = 0.43, or 4.3 per absorbed photon. A follow-up study utilizing the same type of core/shell CdSe/CdS QDs reported the optical efficiency of *ca.* 48% at 400 nm.[321] The primary factors contributing to this improvement were a higher luminescence quantum yield (86%), smaller device dimensions (2 × 2 cm), and increased absorptance (~85% at 400 nm).

At first glance, it would appear that the benefits of using thick-shell heterostructured QDs should continue to increase as that thickness is further increased; however, because of the large dielectric contrast between the QDs and typical matrices, at very large QD sizes, scattering (which scales with QD volume) becomes an important factor. In a recent study,[325] Nuzzo and co-workers investigated the optimal QD geometry by synthesizing CdSe/CdS QDs with a constant 2.5 nm core diameter and increasing shell thicknesses that were compared on the basis of

DOI: 10.1021/acs.chemrev.6b00169
Chem. Rev. 2016, 116, 10513–10622

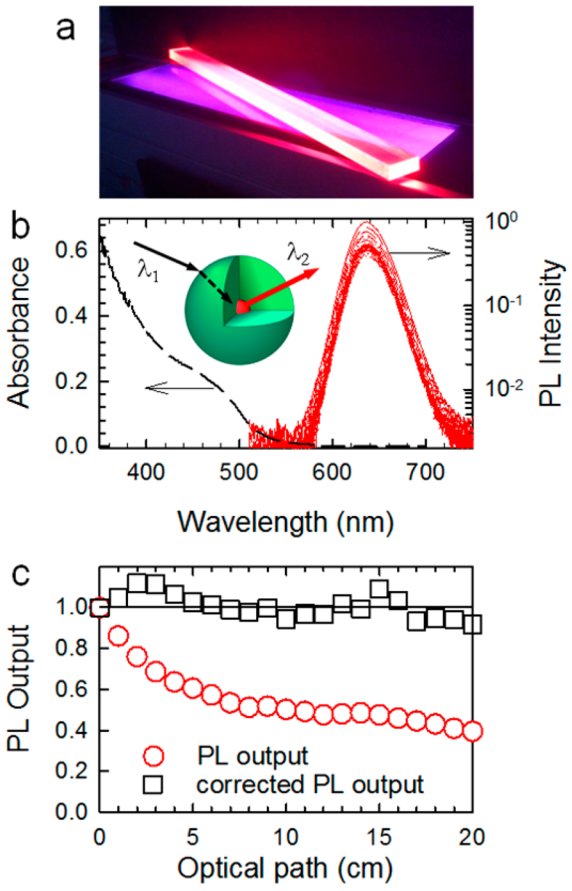

Figure 66. (a) Photograph of an LSC (dimensions: 21.5 × 1.35 × 0.5 cm^3) comprising CdSe/CdS QDs (R = 1.5 and H = 5 nm) in a poly(methyl methacrylate) (PMMA) matrix, illuminated by a 365 nm lamp. (b) Optical absorption spectra of the QD−PMMA composite (same as in a; black line), and PL spectra (red lines, excitation at 473 nm, logarithmic scale) collected at the edge of the LSC as a function of d (0−20 cm). Inset: schematic depiction of a giant shell CdSe/CdS QD showing optical absorption in the shell (λ_1) followed by emission at a longer wavelength form the CdSe core (λ_2). (c) Spectrally integrated QD intensity as a function of d (red circles; derived from data in part b) and the PL intensity corrected for scattering losses (black squares) showing no appreciable variation with d. Figure adapted with permission from ref 64. Copyright 2014 Nature Publishing Group.

the ratio of extinction coefficient at 450 nm and at the peak luminescence wavelength (Figure 67a). The authors found that for small shell thicknesses, the extinction of emitted light is dominated by reabsorption, whereas for QDs with shell thickness exceeding 8 nm, the extinction is dominated by scattering. Analysis of these experimental results based on an electrostatic dipole model for CdSe core sizes ranging between 2 and 5 nm, revealed that the ratio between extinction at higher energies (shell-based absorption) and at the energy of emission reaches a maximum at a QD diameter between 15 and 20 nm, representing the best compromise between suppressed reabsorption capability and limited light scattering.[325]

A similar balance of considerations applies to CdSe/CdS dot-in-rod nanoparticles, in which a small spherical CdSe core is embedded into an elongated CdS rod;[65] this was examined by the same authors by combining light propagation experiments with Monte Carlo ray-tracing simulations on LSC devices integrated with microsilicon PV cells. These studies showed that in the regime of ideal light trapping, the concentration factor scales linearly with the nanorod volume due to progressively reduced reabsorption of the large nanorods. However, in the limit of excessively large particles, scattering in the polymer matrix becomes progressively more important, which leads to saturation of the propagation distance, and therefore, the concentration factor.[65]

The trade-off between reabsorption and scattering losses imposes a maximum shell/core volume ratio that, in turn, determines an upper limit to the LSC device size that can be achieved with this type of fluorophores. Considering, for example, spherical CdSe cores with 3 nm diameter, light scattering imposes a limit on the maximum particle size of ∼20 nm, which yields a maximum shell/core volume ratio ∼300:1, beyond which extinction by the shell becomes dominated by light scattering.[325] While such a volume ratio is sufficient to ensure negligible losses to reabsorption for propagation lengths of the scale shown in Figure 66, it is still inadequate for larger LSCs.

This effect has been recently investigated by Gamelin and co-workers,[580] who used solution-based waveguides to study reabsorption losses of spherical core/shell and dot-in-rod CdSe/CdS QDs. Figure 67b shows the absorption and emission spectra of CdSe/CdS core/thick-shell QDs and dot-in-rod particles with the same core size (2.7 nm diameter) and similar core/shell (rod) volume ratio (114:1 and 110:1, respectively), together with those from impurity-doped QDs (Section 8.4.2.). All spectra are collected for QDs in solution with concentrations adjusted to reach optical density *ca.* 1 at the first intense absorption feature in a 1 mm path length cuvette.[580] Under these conditions, all samples appear to have minimal overlap between absorption and luminescence spectra (not shown), as desired for LSC applications. Using thicker cuvettes (optical path of 1 cm; Figure 67b) reveals, however, a significant overlap between the absorption spectrum and the emission peak in both types of CdSe/CdS heterostructures. As a result, the intensity of the luminescence collected at the edge of the linear liquid waveguide under UV excitation at increasing distance from the excitation spot drops considerably for optical paths of tens of centimeters, approaching zero at approximately 120 cm for core/shell CdSe/CdS QDs (Figure 67c).

The high emission quantum yields and well-developed syntheses have motivated the use of CdSe-based QDs as a model materials system in these initial efforts at applying structural engineering to the specific needs of LSCs. However, other options involving materials with smaller bandgaps should allow for improved spectral coverage. One example may be thick-shell PbSe/CdSe QDs (Sections 3.4.3 and 7.5) that feature an absorption onset near the bulk CdSe bandgap of 1.75 eV, and near-IR luminescence, resulting in a large apparent Δ_S.[211,546] As other core/shell systems, PbSe/CdSe QDs (and related nanocrystals) will still be subject to the limits imposed by the maximum core/shell volume ratio, and consequent limits to the ultimate size of the LSC devices.

8.4.2. Doped QDs for LSC Applications. Also featured in Figure 67 is a different class of Stokes-shift engineered QDs of potential interest for LSCs: QDs doped with luminescent metal impurities (Figure 67b−d).[580] In these systems, the incorporation of transition metal ion impurities into the QD lattice during crystal growth or via controlled cation exchange procedures after growth[253,254,618−620] introduces localized states that can be optically active. This typically results in highly red-shifted and very long-lived emission.[254,621,622] The most investigated class of doped QDs are based on II−VI semi-

DOI: 10.1021/acs.chemrev.6b00169
Chem. Rev. 2016, 116, 10513−10622

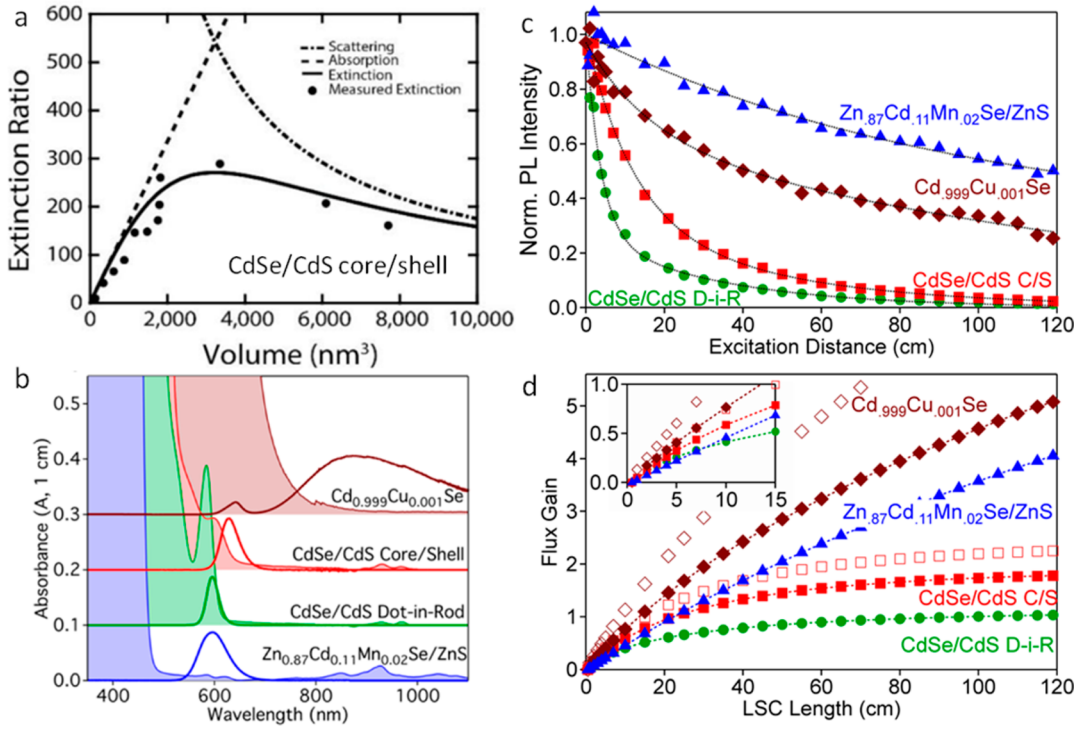

Figure 67. (a) Data and simulation of the relationship between shell volume and the ratio of extinction at 450 nm to extinction at 600 nm for CdSe/CdS core/shell QDs with a 2.5 nm core diameter. The dashed lines represent the ratio of extinction at 450 nm to the absorption at 600 nm and scattering at 600 nm, as calculated by the electrostatic dipole approximation. The solid line is the ratio of the extinction at 450 nm to the sum of absorption and scattering at 600 nm. Adapted with permission from ref 325. Copyright 2015 American Chemical Society. (b) Absorption (shaded areas) and PL (lines) spectra of various types of Stokes-shift engineered QDs, illustrating the overlap between absorption and emission spectra. Note that the absorption features at longer wavelength observed for Mn:ZnCdSe/ZnS QDs are due to the capping agents. (c) Spectrally integrated PL intensity plotted as a function of distance from the excitation spot for the same QDs as in part b in a solution-based LSC. Intensities are corrected for waveguide losses. (d) Flux gains of the same QDs as in part b under AM1.5 solar irradiation plotted as a function of LSC length. Solid symbols use as-measured luminescence QYs, and open symbols were calculated using best-reported luminescence QYs. Inset shows the expanded view of the short-length region. Adapted with permission from ref 325. Copyright 2015 American Chemical Society.

conductors combined with Mn^{2+} ions. Because of the magnetic activity of Mn^{2+}, many such studies have been motivated by potential applications in magnetic memory and spin-based electronics.[253,254,618,621−624] In II−VI QDs, such as the ZnCdSe QDs shown in Figure 67b, substitutional Mn^{2+} impurity ions possess a $^6A_1$ ground state, and exhibit luminescence associated with an internal $^4T_1 \rightarrow {}^6A_1$ d-d transition at approximately 590 nm (2.1 eV),[253,618,622,625] which is efficiently sensitized by energy transfer from the host QD. Importantly for LSC applications, the corresponding absorbing transition ($^6A_1 \rightarrow {}^4T_1$) is nominally spin-forbidden, and therefore exhibits a maximum extinction coefficient of only ∼1 M^{-1} cm^{-1}, which is ∼5 orders of magnitude smaller than that of the band-edge transition in 3−5-nm-diameter ZnSe QDs.[622] It should be noted that this ratio exceeds by over 100 times the maximum ratio achievable in the thick-shell heterostructured QDs described in Section 8.4.1. Moreover, the size-tunable absorption of the II−VI host can be significantly higher in energy than the essentially fixed energy of the Mn-based emission, allowing apparent Δ_S values as high as 1 eV (Figure 67b). Accordingly, Mn-doped ZnSe (Mn:ZnSe) QDs with an absorption onset at 400 nm and Mn-emission at 590 nm can be used to realize virtually reabsorption-free LSCs.[253]

The same benefit of a large apparent Δ_S can also be obtained with the Mn:ZnCdSe QDs shown in Figure 67b−d, where the light collection efficiency measured for QDs dispersed in toluene is reduced by less than 50% for an optical path as long as 120 cm, outperforming heterostructured QDs. The solar harvesting ability of LSCs based on Mn-doped QDs is, however, limited by the fact that the Mn-related emission is essentially untunable, which prevents the use of QD hosts with absorption edge at wavelengths longer than ∼560 nm. This limits the light-harvesting ability of these QDs and also results in strong coloring of the devices.

Better spectral coverage is possible using QDs doped with transition metal ions that introduce an intragap state, which participates in the recombination processes with a band-edge electron or hole photogenerated in the host QD. This is the case of dopants such as Cu or Ag in II−VI QDs; these systems exhibit red-shifted emission that is responsive to typical methods for controlling the host material's electronic states, such as by manipulation of size, composition or internal structure.[621,626−634] For example, by doping ZnSe/CdSe QDs with Cu ions, Viswanatha et al. reported ultrabroad tunability of the emission peak position from 1.2−2.7 eV, with a large apparent Stokes shift of *ca.* 650 meV.[635] More recently, a reverse cation exchange reaction was applied to synthesize Ag:CdSe and Ag:CdSeS QDs emitting at ∼650 nm with $\Delta_S \approx 350$ meV.[619]

Cu-doping of II−VI QDs has been the subject of numerous reports.[620,627,630,632,635−640] According to studies on bulk semiconductors doped with Cu,[641−643] the dopant-related emission can be attributed to transition that couples the conduction band-edge state to a level associated with the Cu impurity. Magneto-optical studies of Cu:ZnSe/CdSe QDs find evidence of paramagnetism, suggesting the presence of some

DOI: 10.1021/acs.chemrev.6b00169
Chem. Rev. 2016, 116, 10513−10622

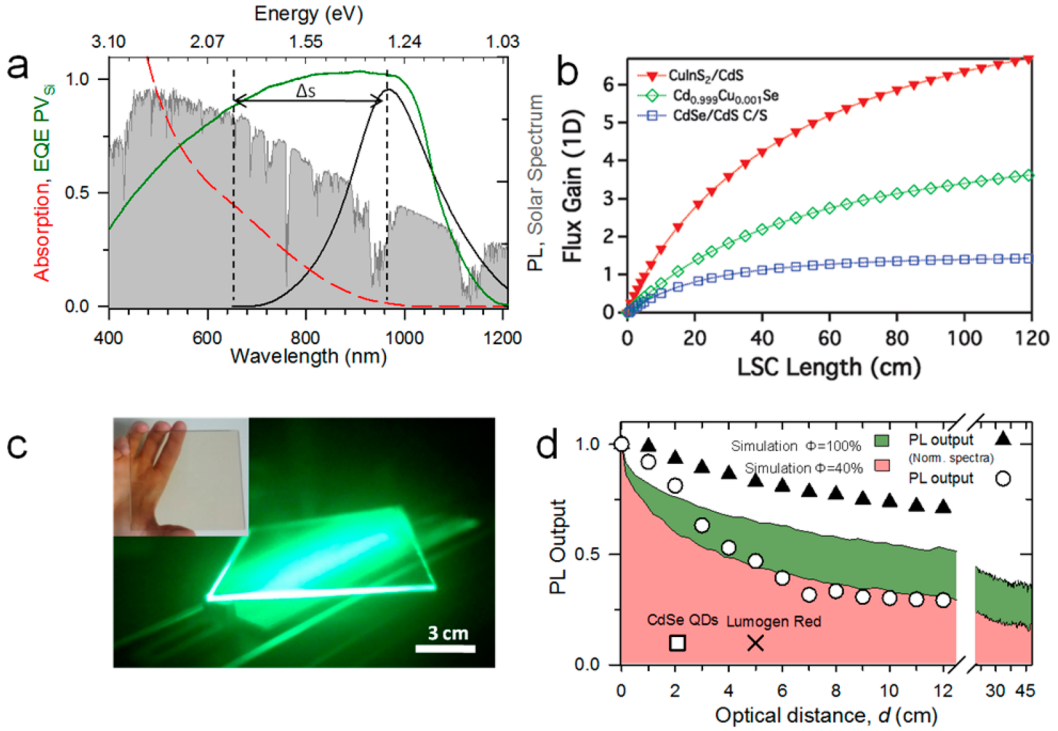

Figure 68. (a) Absorption (red dashed line) and emission (solid black line) spectra of ZnS-coated CISeS QDs. PL was measured using *c.w.* excitation at 405 nm; $\Delta_S = 0.53$ eV. The spectrum of solar radiation at sea level is shown by gray shading, and the green line is a representative EQE spectrum of a c-Si solar cell. (b) Optical concentration factor or the flux gain as a function of the length of a one-dimensional LSC incorporating $CuInS_2$/CdS QDs coupled to c-Si PVs and illuminated with AM 1.5 simulated solar radiation. Results for the same Cu:CdSe QDs and CdSe/CdS core−shell QDs as in Figure 67b are included for direct comparison. (c) Photograph of an LSC comprising 0.3 wt % ZnS-coated CISeS QDs (LSC dimensions: $12 \times 12 \times 0.3$ cm^3) taken with an ultraviolet-filtered near-IR camera. The LSC is illuminated at 365 nm. (d) QD output collected at the edge of the LSC as the excitation spot is moved an increasing distance (d from 0 to 12 cm) away from the edge (circles), compared with the probability of a photon reaching the LSC edge computed using Monte Carlo ray-tracing (shaded in pink and green for PL quantum yields of 40% and 100%, respectively). The PL output obtained by integrating normalized QD spectra is shown as black triangles. Panel b is adapted with permission from ref 591. Copyright 2015 Royal Society of Chemistry. All other panels are adapted with permission from ref 567. Copyright 2015 Nature Publishing Group.

Cu^{2+}.[635] With a d^9 electronic configuration, a Cu^{2+} cation can be considered as a combination of a closed shell (d^{10}) Cd^+ cation and a surplus hole.[635] While such a hole is not associated with an absorbing transition, it can participate in radiative recombination with a photoexcited electron in the conduction band of the QD host, resulting in emission with an effective Stokes shift of several hundreds of meV (determined by the difference between the impurity hole state and the valence band-edge energy of the host semiconductor).[635,644] In addition, since the intragap dopant state is of essentially fixed energy, the Cu-related emission is spectrally tunable via manipulation of the host conduction band-edge level, while retaining large values of Δ_S.[635,644] As a result, through suitable choice of the host semiconductor, it is in principle possible to realize Cu-doped QDs that absorb across the visible spectrum and emit at IR wavelengths, and are thus immune to reabsorption.

The spectra in Figure 67b show, however, a partial overlap between the long wavelength tail of the absorption spectrum and the emission profile of Cu:QDs simply due to the very broad line width of the Cu-related luminescence band, which results from the combination of the energetic dispersity of the Cu^{2+} dopant level (which can vary with the precise chemical environment of the impurity ion) and the typical sources of broadening (*e.g.*, size dispersity) of the QD conduction band. Fluorescence line narrowing studies reveal that, while the band-edge emission of Cu:ZnSe QDs shows the typical vibronic structure under resonant excitation at cryogenic temperature,[640,644] spectroscopic selection does not affect the spectral profile of the Cu emission, which remains 350−400 meV wide for all excitation energies;[640] this is consistent with the attribution of broadening of the Cu impurity level to local structural inhomogeneity.

As a result of the partial overlap between the absorption and emission spectra, the propagation of guided luminescence in LSCs based on Cu:QDs suffers from relatively large reabsorption losses as compared to devices incorporating Mn-doped QDs (Figure 67c). Nevertheless, their extended coverage of the solar spectrum with respect to both CdSe/CdS heterostructures and Mn:ZnCdSe/ZnS QDs still makes Cu:CdSe QDs the best LSC emitter among these materials. This is highlighted in Figure 67d, which compares the concentration factors (expressed here in terms of a "flux gain"[580]) of one-dimensional liquid waveguides incorporating the three types of emitters under AM 1.5 irradiation. Clearly, the detrimental effect of reabsorption due to partial absorption/emission overlap in Cu:CdSe QDs is compensated by the broader absorption spectrum that enables harvesting of solar photons of wavelengths up to 650 nm, and thus ultimately results in higher concentration factors than for other QD systems.

One limitation of Cu-doped CdSe QDs is that their spectral coverage cannot be extended beyond the red portion of the visible spectral region due to the fairly large energy gap of the host material. In principle, this obstacle could be surmounted by using a host of a smaller band gap. However, such a system would have to meet the full series of other requirements (the impurity-

DOI: 10.1021/acs.chemrev.6b00169
Chem. Rev. 2016, 116, 10513−10622

associated energy level must fall within the band gap, nonradiative recombination processes must not favorably compete with dopant-based emission, *etc.*) in order to be effective as an LSC fluorophore.

8.4.3. Heavy-Metal-Free QDs for Highly Efficient LSCs. With the exception of the Mn:ZnSe QDs, all nanocrystalline systems described so far contain hazardous heavy metal ions such as Cd or Pb, and thus require expensive disposal/recycling protocols and are potentially subject to restrictions due to health and environmental risks.[453] A recently demonstrated approach for avoiding these issues involves the use of QDs of ternary I–III–VI_2 semiconductors such as $CuInS_2$ (CIS), $CuInSe_2$ (CISe), and their alloys ($CuInSe_xS_{2-x}$; CISeS).[567,591,645] These QDs do not contain heavy metals[646] and can be fabricated in large quantities via high-throughput, noninjection techniques using inexpensive precursors.[567] Importantly for LSC applications, they exhibit Δ_S > 100 meV without heterostructuring or doping (Figure 68a).[163,647−649] Furthermore, their large absorption cross sections and spectrally tunable, near-IR absorption onset are well-suited to harvesting solar radiation,[650] including in QD-sensitized solar cells.[207,651] They are also highly efficient, tunable emitters, with PL QYs reaching above 80% with appropriate inorganic passivation.[652,653] Their versatility and lack of toxic heavy metals makes I–III–VI_2 QDs very attractive for a range of applications including PVs,[488,650,651,654] bioimaging,[648,655] LEDs,[646,647,656] and as recently demonstrated, LSCs.[567,591,645]

CISeS QDs with a thin ZnS capping layer were used in the first large-area QD-LSCs free of toxic elements (such as cadmium or lead) with both reduced reabsorption losses and extended coverage of the solar spectrum.[567] Thanks to limited absorption/emission overlap and high luminescence efficiencies of the QDs [which were preserved upon their incorporation into a poly(laurylmethacrylate) matrix], an optical power efficiency of 3.27% was achieved. This is the highest value reported to date for large-area LSCs (lateral dimension >10 cm) using any type of chromophore without the assistance of back-reflectors. The suitability of ternary I–III–VI_2 QDs for the realization of large-area LSCs was confirmed by theory[645] and a proof-of-concept study[591] that combined Monte Carlo ray-tracing simulations with optical measurements on a one-dimensional liquid waveguide. Figure 68b demonstrates, for example, that, in terms of the achievable concentration factors or flux gains, LSCs made of $CuInS_2$/CdS QDs outperform those based on either CdSe/CdS heterostructures or Cu-doped CdSe QDs.[591]

The high potential of CISeS QDs for LSC applications is evident upon inspection of their optical absorption and emission spectra of the QDs themselves (Figure 68a; red and black lines, respectively).[567] In Figure 68a, these spectra are overlaid with the sea-level spectrum of solar radiation (gray shading) and a typical EQE spectrum of a crystalline-Si (c-Si) solar cell (green line). As is typical of QDs of this materials family, the absorption spectrum is almost featureless,[645] and in this case it extends over the entire range of visible wavelengths to approximately 900 nm. This allows for efficient capture of solar radiation over a broad spectral range, which is *ca.* 200 nm wider than that of the Cu:CdSe QDs in Figure 67b.[591,650] Importantly, the emission spectrum is energetically matched to the low-energy onset of the EQE spectrum of a c-Si PV device, optimal for converting emitted photons into electrical current with minimal energetic losses. The absorption spectrum exhibits a weak shoulder at approximately 640 nm (1.85 eV), which marks the position of the QD band edge. It is displaced from the emission band by >250 nm (550 meV), which indicates a very large Δ_S, greatly exceeding that of core-only CdSe,[64,218] PbS[489] or PbSe[598] QDs (Figure 64) and even CdSe/CdS heterostructures and many types of doped QDs.

A large apparent Stokes shift observed for both pure (*i.e.*, CIS and CISe) and alloyed (CISeS) I–III–VI_2 QDs[598,657,658] has been the focus of several recent studies. Transient absorption spectra of CIS QDs[488567] reveal a prominent bleach feature located exactly at the position of the absorption shoulder in the steady-state spectrum, corroborating its association with the QD band edge. The magnitude of the Δ_S represented by the difference in energy from this bleach feature and the emission peak indicates that emission does not arise from the radiative decay of purely band-edge excitons, but is due to recombination involving an electron in the conduction band and a hole residing in an intragap acceptor state, as suggested by Li et al.[163] Importantly, across numerous reports, the position of the emission band is remarkably consistent among I–III–VI_2 QD samples prepared by different chemical approaches,[648,657−659] which suggests that the defect responsible for the shifted emission is likely intrinsic to the "bulk" material of the QD, rather than being associated with the much more chemically variable QD surface. An important insight into the possible nature of the defect state has been suggested by Rice et al.,[660] who used magnetic circularly dichroism and magneto-luminescence measurements to demonstrate a surprising similarity between the magneto-optics of CIS QDs and that of Cu:doped II–VI QDs,[635,660,661] which (as described in the previous Section) arise from Cu-dopants in the +2 oxidation state. In structural terms, I–III–VI_2 semiconductors are analogs of II–VI materials: their unit cell can be pictured as comprising two zinc-blende II–VI unit cells joined together and distorted along the *c*-axis, in which the Group II ions are alternately replaced by Group I and Group III ions. In this scenario, substitutional Cu^{2+} impurities should be just as feasible in I–III–VI_2 QDs as in II–VI QDs, where they are commonly observed. Such a "defect" might occur in a number of ways, including defect pairs in which two Cu^{2+} ions replace Cu^{1+} and In^{3+} in adjacent subcells, or as (Cu^{2+} + Cu^{1+}-vacancy) pairs, which are well-known in bulk I–III–VI_2 materials.[662]

The advantageous properties of CISeS QDs were successfully exploited to realize the first example of a full-spectrum LSC with Stokes-shifted near-IR emission.[567] A photograph of this device taken with a UV-filtered IR camera (Figure 68c) shows how the QD luminescence excited by radiation incident upon the top face of the LSC is guided toward the slab edges. Light propagation experiments (Figure 68d) indicate that due to the large Δ_S, only 25% of emitted photons are lost to reabsorption for optical distances as long as 12 cm. Monte Carlo ray-tracing simulations further confirm that in this LSC, the optical losses are mostly due to scattering of the guided light at optical imperfections in the polymer matrix and on the device surfaces, while reabsorption plays only a minor role. The simulation further indicates that for idealized QDs with 100% emission efficiency, and in the absence of scattering, the propagation length required for 50% optical loss is as long as 1 m, which is comparable to the dimensions of real windows. A 12 cm × 12 cm LSC containing 0.5 wt % of CISeS/ZnS QDs coupled to c-Si PV cells along its perimeter reached an unprecedented power efficiency of 3.27% under AM 1.5 solar illumination. This result is particularly remarkable as it was achieved with a device exhibiting 80% transmittance across the visible spectral region, and without the assistance of back reflectors, which is the configuration used in PV windows.[567]

DOI: 10.1021/acs.chemrev.6b00169
Chem. Rev. 2016, 116, 10513−10622

8.5. QD-Polymer Waveguides: The Importance of the Nanocomposite Matrix

A critical aspect for the realization of efficient QD-LSCs is the ability to fabricate optical-grade waveguides doped with highly emissive QDs. In this regard, the choice of the matrix material is as important as the optimization of the emitters, as any incompatibility between the host and the QDs can result in the formation of structural defects or phase-segregated domains that would lead to dramatic optical losses due to scattering of the guided light. Furthermore, the matrix material has to be completely transparent in the spectral window of the QD emission, so as not to absorb the QD luminescence. This requirement is particularly stringent for LSCs intended for building-integrated applications that need to reach lateral dimensions of hundreds of centimeters in order to be used as PV windows. In addition to polymers, a number of other host materials have been proposed for the encapsulation of QDs including sol–gel matrices,[576,656] epoxy resins[663] and macrocrystals.[597]

A material suitable for the fabrication of highly transparent LSC waveguides is PMMA prepared by mass polymerization of a dispersion of QDs in liquid methyl methacrylate (MMA) monomer. PMMA features a reasonably high refractive index n = 1.5, and an absorption coefficient in the visible spectral region of ~0.02 cm^{-1}, which is over ten times smaller than polystyrene or polycarbonate.[664] The most common fabrication protocol for PMMA-based LSCs derives directly from the industrial cell-casting procedure commonly used for the fabrication of optical-grade PMMA windows.[665] Specifically, the QDs are added to the MMA monomer along with a thermally activated radical initiator (such as a peroxide or azo-compound; see Figure 69a for the chemical structures of typical examples azobis(isobutyronitrile) and lauroyl peroxide). The mixture is then poured into a mold and heated to the activation temperature of the initiator to trigger radical polymerization. The final PMMA:QD nanocomposite is obtained in 48–72 h, depending on the decomposition time of the initiator.

The quality of QD-LSCs made by this method can be reduced by two major detrimental phenomena. The first is substantial aggregation and formation of phase-separated domains can occur over the course of the slow polymerization process because of the relatively limited miscibility of QDs capped with native fatty organic ligands in polar liquid MMA. This will result in opaque, highly scattering slabs. Second, because of the long polymerization time, the QDs can react with mobile radical initiators, leading to surface damage that can create recombination centers that diminish the QD luminescence efficiency (see Table 1). Recently, an optimized version of the industrial cell-casting procedure was introduced to mitigate these problems and allow one to produce high-optical-quality PMMA nanocomposites without considerable PL quenching. This "soft polymerization" route is a two step process: (1) a fast prepolymerization at high temperature yields viscous PMMA/MMA "syrup", into which the QDs are added; and (2) a slow reaction at lower temperature completes the polymerization process into solid PMMA.[666] The PMMA matrices fabricated through this soft polymerization procedure feature high molecular weight ($M_w > 10^6$ g/mol) and a high glass-transition temperature (T_g = 117 °C) similar to that of industrial grade PMMA.

The above approach has three main advantages for applications in QD-LSCs: (1) it requires a very limited amount of radical initiator (a few hundreds of ppm, w/w); (2) the prepolymerization step reduces the formation of heterogeneities in PMMA itself, thus increasing the optical transparency of the final composite;[667] and (3) the high viscosity of the prepolymerized MMA intermediate medium reduces the mobility of all chemical species, thereby hampering QD aggregation and limiting the interaction between the QDs and the radical initiators. The effectiveness of this approach was proven for PMMA slabs incorporating CdSe/CdS QDs.[64] Importantly, thanks to the soft polymerization approach and the protective role of the thick shell, the optical properties of the QDs were perfectly retained.

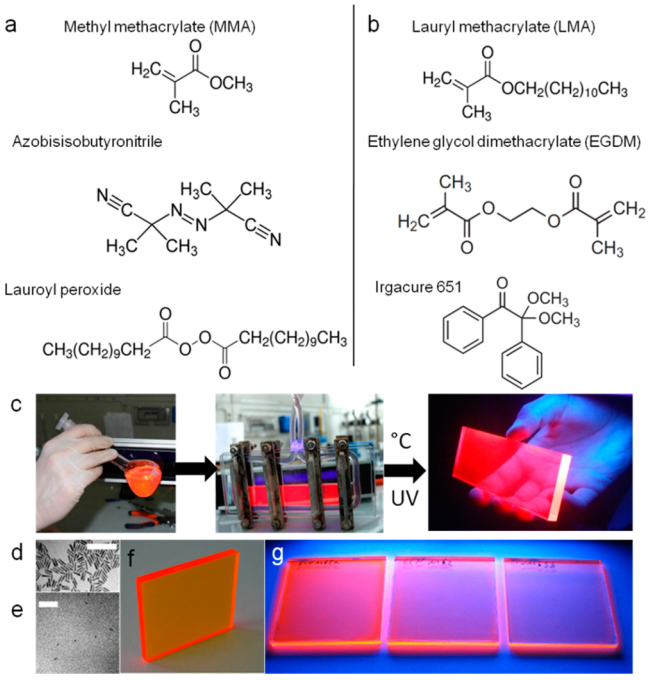

Figure 69. Chemical structure of organic precursors and radical photoinitiators or thermal-initiators used for the fabrication of (a) PMMA- and (b) PLMAbased QD-LSCs. (c) Cell-casting procedure used for the fabrication of QD-LSCs starting from a dispersion of QDs in the liquid monomer. The solution is poured into a mold and successively polymerized by thermal or ultraviolet photoactivation of the radical initiator. A photograph of a representative PMMA-LSC comprising 0.5 wt % CdSe/CdS QDs is shown in the rightmost panel. (d) TEM image of CdSe/CdS dot-in-rods (e) in the poly(LMA-*co*-EGDM) composite. (f) Photograph of the nanocomposite in (e) (0.05 wt % dot-in-rod particles) showing bright luminescence in daylight illumination. (g) Photograph of cellulose triacetate nanocomposite layers on glass substrates containing the same CdSe/CdS dot-in-rods (from left to right: 2 wt %, 1 wt %, 0.5 wt %). Adapted with permission from ref 599. Copyright 2010 Beilstein-Institut.

Another acrylate polymer that is commonly used for QD-LSCs is cross-linked polylauryl methacrylate (PLMA). PLMA uses the same functional group as PMMA, but each monomer unit features a long alkyl side chain that dramatically improves the dispersibility of QDs in the liquid monomer and almost completely prevents aggregation of the QDs.[62,65,324,599,668] Moreover, PLMA has a glass transition temperature of −65 °C, and at room temperature represents a rubber-like material with long alkyl side chains that display dynamics resembling those of liquids. Since the polar methacrylate backbone and the nonpolar alkyl side chains are immiscible, the polymer bulk exhibits a form of ordering at the nanoscopic level,[669] in which the QDs find a local environment very similar to that of 1-

DOI: 10.1021/acs.chemrev.6b00169
Chem. Rev. 2016, 116, 10513–10622

Table 1. Published PL Efficiencies of Nanocrystal Solution Samples and Nanocrystals Embedded in Different Polymer Matrixes along with the Corresponding PL Quenching Factor

Nanocrystal type: QDs (*R*/*H* = Core radius/Shell thickness); Nanorods (*L*/*D* = Length/Diameter)	PL quantum yield (Solution)	PL quantum yield (Polymer)	Quenching %	Polymer matrix type	ref
Core-only or Thin-shell QDs					
CdSe/ZnS core/shell	0.3 (Hexane)	0.24	~20%	P(LMA-*co*-EGDM)	263
(R = 2.3 nm, H < 1 nm)					
CdSe/ZnS core/shell	0.5 (toluene)	0.22	~56%	PMMA/HMITFSI	672
	0.63 (HMITFSI)		~65%		
(R = 1.3 nm, H ≪ 1 nm)					
			~97%	Urethane	578
			~56%	OLEO- polysol	
			~40%	MMA	
CdSe/ZnS core/shell	n.d	n.d	~78%	Urethane	
(R = 1.25 nm, H < 1 nm)			~89%	Urethane	
			~78%	Urethane	
			~32%	Epoxy	
CdSe/CdS/CdZnS/ZnS core/multishell	0.6	0.45	~25%	P(LMA-*co*-EGDM)	62
	0.51 (TOPO capped)	0.18 (TOPO capped)	~64%		
CdSe/ZnS/CdS/ZnS core/multishell	0.59 (OT capped)	0.15 (OT capped)	~75%	PMMA (secondary dispersion)	671
	0.28 (TP capped)	0.05 (TP capped)	~82%		
PbS (R = 1.1 nm, core only)	0.3	0.09	~70%	PMMA (secondary dispersion)	593,673
PbS (R = 1.1 nm, core only)	0.3	0.19	~35%	PMMA	
CuInSeS	0.4 (toluene)	0.2	~50%	P(LMA-*co*-EGDM)	567
CuInSeS/ZnS	0.4 (toluene)	0.4	~0%	P(LMA-*co*-EGDM)	
Giant QDs					
CdSe/CdS core/shell	(hexane)				
(R = 1.5 nm, core only)	0.17	0.04	~77%		
(R = 1.5 nm, H = 0.7 nm)	0.18	0.08	~56%		
(R = 1.5 nm, H = 1.75 nm)	0.20	0.15	~27%	PMMA	64
(R = 1.5 nm, H = 3.15 nm)	0.30	0.22	~26%		
(R = 1.5 nm, H = 4.9 nm)	0.47	0.44	~6%		
CdSe/CdS core/giant shell (R = 1.25 nm, H = 6.45 nm)	0.68	0.6	~12%	P(LMA-*co*-EGDM)	325
CdSe/CdS core/giant-shell (R = 1.9 nm, H = 5 nm)	0.86 (Hexane)	0.82	5%	P(LMA-*co*-EGDM)	324
Dot-in-rod nanocrystals					
CdSe/CdS dot-in-rods (R = 1.15 nm, *D* = 2.4 nm, L = 32 nm)	0.7 ($CHCl_3$)	0.7	~0%	P(LMA-*co*-EGDM)	599
CdSe/CdS dot-in-rods (R = 1.15 nm, *D* = 2.4 nm, L = 32 nm)	0.7 ($CHCl_3$)	0.52	~26%	Cellulose triacetate	599
CdSe/CdS dot-in-rods (R = 1.25 nm, *D* = 0.8 nm, L = 8.8 nm)	0.7	0.7	~0%	P(LMA-*co*-EGDM)	65
(R = 1. nm, *D* = 3.4 nm, L = 78 nm)25	0.38	0.38	~0%		
Nanoplatelets					
CdSe Nanoplatelets (Plate thickness = 2 nm, Side = 58 nm, Side = 38 nm)	0.2	0.2	~0%	PMMA	674

octadecene or other analogous solvents[670] used in the QD synthesis.

The chemical structures of the organic precursors employed in the fabrication of cross-linked PLMA slabs are shown in Figure 69b. The fabrication procedure consists of initial wetting of the QDs in a small volume of lauryl methacrylate (LMA) monomer for 3 h to ensure fine dispersion of the individual particles. The monomer-QD mixture is then added to a larger volume of monomer, together with ethylene glycol dimethacrylate (EGDM), which is a cross-linking agent. It is important that the EGDM molecules, which bridge the main chains and impart mechanical stability to the slabs, are located outside the hydrophobic domains of the nanocomposite, and thus are spatially separated from the QDs and unlikely to react with them and alter their electronic properties. The LSCs are then fabricated following a cell-casting procedure similar to that used for PMMA (Figure 69c).[64,599] In contrast to the thermal polymerization of PMMA, PLMA is polymerized using a photoinitiated radical catalyst (*i.e.*, IRGACURE 651). The main advantage of this approach is that the polymerization reaction occurs in a strong kinetic overdrive regime, leading to solidification of the matrix in a matter of minutes, instead of days as with PMMA. This fast reaction time further inihibits phase segregation of the QDs. Using this approach, several examples of QD-LSCs have been fabricated incorporating various types of QDs.[65,325,567,592,599]

Importantly, while the optical quality of the matrix is mainly determined by the choice of monomer and polymerization procedure, the preservation of the luminescence efficiency of the QDs upon their incorporation into the polymer is mostly

DOI: 10.1021/acs.chemrev.6b00169
Chem. Rev. 2016, 116, 10513−10622

Table 2. Published LSC Efficiencies, Specifying the Type of the LSC Fluorophore, Device Dimensions, Structure and Presence/Absence of Back-Reflectors[a]

	LSC fluorophore	LSC size (cm)	Back-reflector	Device color	PV cell	Semitransparent	Reported efficiency	ref
Large-area LSC ($\geq$100 cm^2)	CISeS/ZnS QDs	12 × 12	No	Colorless	c-Si	Yes	3.27% Overall Power	567
	CdSe/ZnS QDs	11.5 × 11.5	Perspex	Red	Si	No	1.5% Overall power (Electrical)	577
	CdSe/CdS QDs	22 × 1.5	No	Red	c-Si	Yes	1% Overall Quantum	577
	Lumogen	10 × 10	TiO_2	Red	c-Si	No	1.8% Overall Quantum	62
	perylene perinone + Lumogen[b]	10 × 10	TiO_2	Dark Red	c-Si	No	2.5% Overall Quantum	590
	DCM	120 × 100	No	Red	c-Si	Yes	1.3% Overall power (Electrical)	572
	Coumarin, Rhodamine	120 × 100	No	Red	c-Si	Yes	1.3% Overall power (Electrical)	572
Small-area LSC (<100 cm^2)	CdSe/CdS/CdZnS/ZnS core/multishell QD	5 × 5	PTFE	Red	mc-Si	No	2.8% Overall Quantum	62
	PbS QDs (toluene solution)	4.5 × 1.2	No	Colorless	c-Si	Yes	3.2% Internal power	593
	CdSe/ZnS (toluene solution)	4.5 × 1.2	No	Red	c-Si	Yes	1.2% Internal power	593
	Rhodamine	4.5 × 1.2	No	Red	c-Si	Yes	1.3% Internal power	593
	Lumogen F Red 300	5 × 5	Perspex	Red	Si	No	3% Overall power (Electrical)	577
	CdSe/CdS QDs	5 × 5	Perspex	Red	Si	No	2% Overall power (Electrical)	577
	CdSe/ZnS QDs	5 × 5	Perspex	Red	Si	No	1.75% Overall power (Electrical)	577
	Lumogen	5 × 5	No	Red	c-Si	Yes	2.3% Overall Quantum	62
	Lumogen	5 × 5	MCPET	Red	c-Si	No	2.8% Overall Quantum	62
	perylene perinone + Lumogen[b]	5 × 5	No	Dark red	c-Si	Yes	3.4% Overall Quantum	590
	perylene perinone + Lumogen[b]	5 × 5	MCPET	Dark Red	c-Si	No	4.2% Overall Quantum	590
	Lumogen + CRS040	5 × 5	Yes (97% reflection)	Red	GaAs	No	6.7−7.1% Overall power	593
	Lumogen + CRS040	5 × 5	No	Red	GaAs	Yes	5.3% Overall power	593
	Lumogen	5 × 5	No	Red	mc-Si	Yes	2.4% Overall power	564
	Lumogen + CRS040	5 × 5	No	Red	mc-Si	Yes	2.7% Overall power	564
	BA241	2 × 2	$BaSO_4$-coated aluminum	Red	GaInP	No	5.1% Overall power	675
	BA241, BA856[b]	2 × 2	$BaSO_4$-coated aluminum	Dark red	GaInP	No	6.7% Overall power	675
	BA241	5 × 10	$BaSO_4$-coated aluminum	Red	GaInP	No	2.6% Overall power	675

[a]Unless otherwise specified, all LSCs are planar bulk waveguides with fluorophes uniformly dispersed within the waveguide interior. [b]Double-layer devices.

controlled by the passivation of the QD surfaces. Table 1 reports a literature survey of the luminescence quenching suffered by different QD systems incorporated into various polymer matrixes. The general trend that emerges from these data is the critical role of a large energy gap inorganic shell in protecting the emissive QD core. Specifically, core-only or core/shell QDs with thin shells undergo the most severe luminescence quenching due to surface degradation upon incorporation in mass-polymerized matrices, while QDs with a thick passivating shell preserve their luminescence efficiency almost completely. It should be noted that emission quenching is not only a result of exposure to radical polymerization initiators, but can also affect QDs incorporated into polymers by solution-casting from a codispersion in a common solvent.[671]

8.6. Assessing the State-of-the-Art in LSC Technologies: QDs versus Organic Dyes

The efficiency of LSCs depends on multiple factors including the device size, the level of transparency, the optical quality of the LSC waveguide, and finally details of the device architecture (*e.g.*, single versus multiple LSC layers, embedded fluorophores versus fluorophores prepared as coating(s), the use of back reflectors, *etc.*). Here we limit our analysis to single- and double-layer devices that are categorized according to their size in two groups: large-area (dimensions equal to or larger than 10 cm × 10 cm) and small area (dimensions equal to or smaller than 5 × 5 cm) LSCs; see Table 2.

To date, the record optical power efficiency for large-area LSCs ($\eta_{opt,PE}$ of 3.27%) has been obtained using I−III−VI_2 QDs incorporated into PLMA waveguides.[567] The reported devices had 80% transmission across the visible spectrum, did not utilize back reflectors, and were characterized using c-Si PVs. Using organic dyes, Debije and co-workers[590] fabricated 10 cm × 10 cm double-layer stacked LSCs with one layer containing Lumogen Red and the other blue-emitting perylene-perinone. In addition to double-layer architecture, these devices also utilized TiO_2 diffuse back-reflectors to maximize the amount of harvested light.

DOI: 10.1021/acs.chemrev.6b00169
Chem. Rev. 2016, 116, 10513−10622

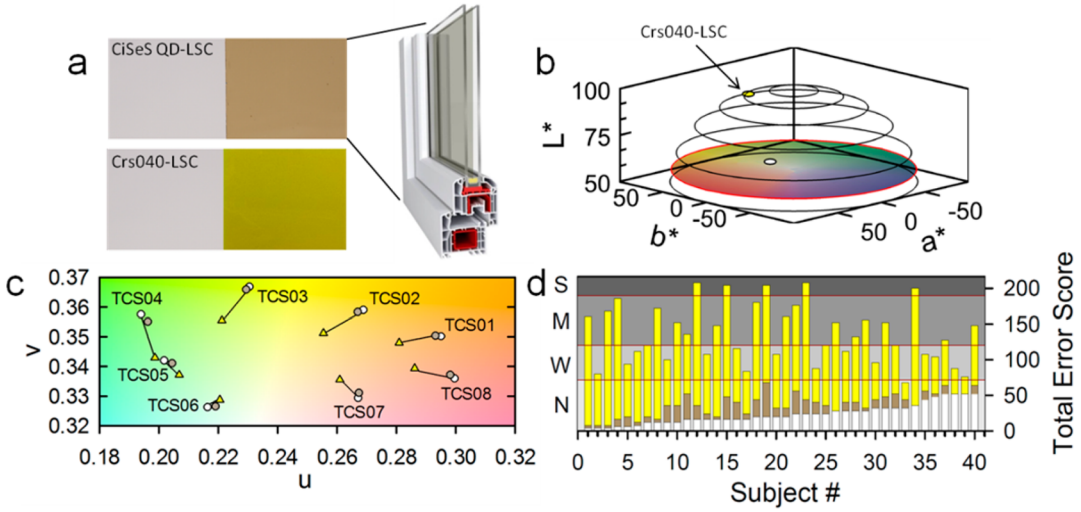

Figure 70. (a) Photographs of a reflecting white background taken with a Canon EOS 400D camera, with half of each field of view filtered by an LSC incorporating 0.5 wt % of CISeS/ZnS QDs (top) or Crs040 dye (bottom). To the right is a depiction of a PV-window utilizing a colorless QD-LSC. (b) Color coordinates in the CIE L*a*b* color space of the QD-LSC (white circle, color coordinates L* = 56.6, a* = 5.1, and b* = 32.1), compared to a device based on Crs040 yellow organic dye (yellow circle, L* = 90.7, a* = 3.3, and b* = 55.3). (c) Color coordinates (CIE 1960 Uniform Color Space) of original Munsell test color samples (TCS) under D65 reference illumination, either unfiltered (white dots) or with spectral filtering provided by a QD-LSC (brown dots) or a Crs040-LSC (yellow triangles). (d) Histogram of Farnsworth−Munsell 100 hue color vision test performed on 40 normal subjects. The test was performed without color filtering (white) and by filtering the subject's vision with the QD-LSC (brown) and with Crs040 LSC (yellow). Total error score, TES < 70, corresponds to normal chromatic vision (N), indicating no artificially induced color blindness. Higher TES values correspond to strong alteration of the perceived colors, leading to weak (W), moderate (M), or severe (S) artificial color blindness. Figure adapted with permission from ref 567. Copyright 2015 Nature Publishing Group.

Despite a sophisticated device design, the achieved efficiency was limited by 2.5% (evaluated in terms of $\eta_{LSC,QE}$), *i.e.*, was lower than for much simpler QD-based structures reported in ref 567. The poorer performance was likely a direct consequence of considerable efficiency losses due to reabsorption, a typical problem of dye-based LSCs. Indeed using smaller devices (5 cm × 5 cm) supplemented by microcellular-formed polyethylene terephthalate (MCPET) back reflectors, the authors of the same publication observed the improvement in the performance to $\eta_{LSC,QE}$ = 4.2%. Even higher efficiency has been achieved by Sloof et al.[579] also using a small-area (5 cm × 5 cm) LSCs based on a mixture of Lumogen red and a coumarine dye. These devices showed the overall optical power efficiency of 5.3% without a back reflector and 6.7−7% with the reflector.

Table 2 provides a more complete survey of reported LSC efficiencies along with the type of fluorophores used in the devices, the resulting device coloring, and the type of the PV cell(s) used in the measurements. In this table, we also specify the type of the published efficiency. Most commonly reported quantities are overall power or quantum optical efficiencies (*i.e.*, efficiencies for broad-band incident radiation with a solar-like spectrum as defined by eq 33), internal power optical efficiency calculated not per incident but absorbed power, and finally overall power electrical efficiency measured as the ratio between the electrical power generated by PV cells coupled to an LSC and the power of light incident onto the device.

8.7. Colorless QD LSCs for Building-Integrated PVs

One important and often unaddressed issue concerning LSCs designed for building-integrated applications is the effect of an LSC window on the color of transmitted light. The color of an LSC is not just relevant because of potential aesthetic considerations (*i.e.*, the building appearance to an outside observer), but also as it determines the alteration of color perception imparted upon individuals within buildings with LSC-based windows. It should be pointed out that fluorophores providing partial absorption of the visible region of incident solar radiation modify the chromatic coordinates of transmitted sunlight, with potentially detrimental effects on color rendering within the indoor setting.

In order to address this important point, a recent study[567] compared the color appearance and the effects on color perception of two LSCs, both exhibiting ∼20% absorptance across the whole solar spectrum. One was based on an organic dye (Crs040 Yellow)[675] and the other on CISeS/ZnS QDs. To provide a simple qualitative indication of the respective color of the two LSCs, Figure 70a contains two photographs taken with fixed exposure time and aperture of a white-scattering background. In each photograph, half of the field of view is filtered by one of the two devices. Clearly, the organic dye-based LSC imparts an intense yellow coloring, due to the absorption edge of Crs040 at ∼480 nm (see Figure 63), while the QD-LSC image appears neutral in color. For the QD-LSCs, colorimetric characterization using the CIE-L*a*b* (Commission Internationale de le Éclairage) color space yields CIE L*a*b* coordinates of L* = 56.6, a* = 5.1 and b* = 32.1, which correspond to the dark brownish range of Munsell's color atlas. This is the typical coloring of neutral sunglass lenses. On the other hand, the LSC containing Crs040 dye has L* = 90.7, a* = 3.3 and b* = 55.3, corresponding to Munsell brilliant yellow color (Figure 70b).[676]

These effects were further quantified by measuring both the CIE chromaticity coordinates and the color rendering index of sunlight [D65 (noon daylight) reference illumination] after it has been passed through LSCs containing CISeS QDs or Crs040 dye (Figure 70). In the QD-LSC case, the CIE coordinates (x = 0.45, y = 0.44) are close to the 2650 K blackbody radiation of incandescent lightbulbs and to the color rendering index R_a = 91, corresponding to CIE color rendering group 1A, which fulfills the

DOI: 10.1021/acs.chemrev.6b00169
Chem. Rev. 2016, 116, 10513−10622

highest requirements for indoor illumination (typical applications: galleries, medical examinations, color mixing). On the other hand, the coordinates after filtering through the Crs040-LSC ($x = 0.47, y = 0.51$) correspond to yellow light; moreover, R_a = 57 corresponds to CIE group 3, suitable at best for industrial illumination. This level of modification of the incoming light spectrum can alter the indoor-to-outdoor chromatic perception of individuals residing in buildings with LSC windows, with an effect comparable to artificially induced color blindness. This was verified by a Farnsworth−Munsell 100 hue color vision test, performed on 40 individuals by filtering each subject's vision with each respective LSC. While the QD-LSCs filtration resulted in normal vision with no sign of artificial color blindness, Crs040-LSCs filtration produced significant color distortion, leading to various degrees of induced color blindness (Figure 70d).[567] Experimental and theoretical data[567,591,645] indicate the great promise of I−II−VI_2 QDs for the realization of real-world LSCs, particularly for building-integrated PVs that would take advantage of their unmatched architectural integrability.

8.8. Addressing Remaining Challenges for QD-LSCs

Despite being a fairly new application for QDs, QD-LSCs have already shown considerable promise, especially in the case of Stokes-shift-engineered nanostructures (*e.g.*, thick-shell CdSe/CdS QDs[64,325] and Mn- and Cu-doped II−VI QDs[63,580]) as well as I−III−VI_2 nanocrystals[567,591,645] with a large "intrinsic" Stokes shift. The demonstrated efficiencies have exceeded those of devices based on organic dyes (Table 2), and QD-LSC dimensions are already in the tens of centimeters range, *i.e.*, approaching the sizes required for practical applications as PV windows. There are, however, still a few remaining challenges. While the devices based on Stokes-shift-engineered QDs do exhibit high internal optical efficiencies (as a result of reduced losses to reabsorption), in most of the reported cases, the QD absorption onset is too high in energy; therefore, the total fraction of solar photons absorbed by the devices is low, limiting the overall external optical efficiencies.

Promising structures for overcoming this problem are CISeS QDs whose absorption onset can be tuned into the near-IR by selecting an appropriate Se/S ratio and the QD size. This improves the coverage of the solar spectrum and, hence, the overall device absorptance. In this respect, it is not surprising that the current record of ∼3.3% in the overall optical power efficiency has been demonstrated with CISeS QDs.[567] Further improvements in this type of device can come from improved PL efficiencies. As was shown in ref 583, in the range of moderate and high PL QYs (η_{PL} > 40%), the LSC efficiency scales approximately as a square of η_{PL}. Therefore, an increase in PL QY from 40% (exhibited by CISeS QD/polymer composites in ref 567) to, for example, ∼70−80%[163] (demonstrated for the best solution samples of CISeS QDs), can help triple or even quadruple the overall efficiency, bringing it to >10% values. According to a QD-LSC cost analysis,[677] for such efficiencies, the LSC-PV system becomes cost-competitive with standalone PV modules.

There is also considerable room for improvement in the area of QD LSC matrices/waveguides. Most of the literature devices are based on QD/polymer composites fabricated by bulk polymerization. Independent of the specific choice of material, the long-term stability of polymers and especially the robustness of their optical properties under solar irradiation are still poorly addressed issues. Furthermore, unavoidable fluctuations in the refractive index of a polymer matrix with material density can lead to considerable losses due to scattering.[64] A possible approach to mitigating this problem is by replacing an all-polymer LSC waveguide with a thin QD coating on top of a high-optical-quality glass slab. The loss to optical scattering in such structures due to imperfections in the QD/polymer composite is expected to be reduced in direct proportion to the ratio between the overall device thickness and the thickness of the polymer layer. Such layered structures fabricated using a doctor-blade approach have been recently demonstrated.[677] This method is well suited for producing very large-area devices and, further, is considerably less time- and material-consuming than bulk polymerization. Using the doctor-blade QD/polymer deposition, the authors of ref 677 were able to fabricate LSCs with sizes up to *ca.* 90 × 30 cm^2, comparable to a standard window. Importantly, due to the very small thickness of the polymer layer (∼50 μm), the losses due to scattering at imperfections within the QD matrix were almost completely eliminated, which allowed for high internal efficiencies of more than 25% in 10 cm long devices and ∼5% in extra-large ∼90 cm structures.

Over the past few years, the area of QD-LSCs has seen considerable progress on multiple fronts, including the synthesis of specially designed QD-fluorophores, the development of new approaches for incorporating QDs into LSC waveguides, the demonstration of high-efficiency devices, and the development of effective theoretical approaches for guiding work on both new types of QD emitters as well as the overall device design. All of these new developments suggest that it is very likely that in the near future QD LSCs may become a commercial reality, as has recently happened with QD-based displays, which are now currently under development by all major display manufacturers.

9. NANOCRYSTAL QUANTUM DOTS: PRESENT STATUS AND OUTLOOK FOR THE FUTURE

Despite its more than 30-year history, the science of colloidal nanocrystals still represents an exciting area of research that appeals to scientists with a range of backgrounds, including inorganic and colloidal chemistry, condensed matter physics, materials and optical sciences, as well as biological and medical sciences. The allure of nanocrystals has been further increased by recent demonstrations of their applicability in technologies ranging from bioimaging and biolabeling[48,678] to high-efficiency, multicolor LEDs, lasers, and LSCs. Such advances prove that nanocrystals are no longer just the subject of scientific curiosity, but are materials with a proven potential for applications, rapidly garnering the attention of engineering and entrepreneurial communities.

While nanocrystal-based technologies are at various stages of development, some applications, such as QD-based down-converting displays,[273,283] have already become a commercial reality. This has been enabled by the development of methods for producing high-optical quality composites that maintain the efficient tunable emission and photostability of QDs. Based on this, a logical direction for the next big expansion in nanocrystal application will be their use in LSCs, devices that present many of the same requirements as displays. While nanocrystal-based LSCs at present are still far from being fully optimized, their performance is already superior to those based on organic dyes, even those specifically tailored for LSC applications (Section 8). One promising direction in this area is the development of semitransparent LSCs for the realization of "solar windows" that provide a desired degree of shading and/or coloring while also serving as power-generation units. In this vein, the ability to finely tune both the absorption and fluorescence properties of

DOI: 10.1021/acs.chemrev.6b00169
Chem. Rev. 2016, 116, 10513−10622

engineered nanocrystals, potentially even independently in suitably designed heterostructured or doped nanocrystals, will allow this dynamic class of materials to achieve performance levels completely inaccessible using any other class of fluorophore.

Also in part inspired by the successes of QD displays, the area of QD-LEDs has considerably advanced over the past several years, via improvements both in the properties of the QDs and in the device architecture. Recently demonstrated LEDs show EQEs of around 20%,[416] very near the limit defined by the light extraction coefficient of high-index QD media (Section 6.2). Furthermore, parallel engineering efforts have demonstrated full-color active-matrix-driven QD displays with patterned red, green, and blue QD light-emitting layers. Outstanding challenges in this field are efficiency roll-off at high driving currents (also known as "droop") that limit the achievable brightness of QD-LEDs, and device long-term stability that is still below that required for real-world applications. Recent studies of the mechanisms underlying these behaviors indicate that, rather than being a matter of continuing to refine device architectures, larger gains can be achieved through optimization of the nanocrystals themselves. Specifically, efficiency losses associated with charged excitons or multiexcitons can be minimized through use of advanced heterostructures engineered to reduce the efficiency of non-radiative Auger recombination (Section 4.3). Stability issues related to degradation of the organic ligands of QDs, on the other hand, might be mitigated by using more stable "all-inorganic" passivation, such as has been used in QD PV.[679]

Practical, high-performance, solution-processed, nanocrystal-based, optical-gain media are an inherently attractive class of materials that remain very challenging to attain. They will ultimately require advances on all of the above fronts, including control over the absorbance and emission of the nanocrystals, development of highly stable nanocrystal solids and composites, and suppression of Auger recombination. While a certain degree of control of Auger decay has been demonstrated in the literature, it is not yet sufficient for demonstrating QD lasing under *cw* excitation. An even bigger challenge is the realization of lasing using direct electrical excitation, which would require essentially "droop-free" devices with long-term stable operation at high injection currents sufficient for achieving the population inversion in the active QD layer. An additional complication arises from the thickness requirements for the emitting layer: while the most successful QD-LEDs are built upon only a few monolayers of nanocrystals (*ca.* 10−50 nm total thickness), for a laser, the active layer should ideally be sufficiently large to maintain a wave-guided mode. This condition requires that high emission quantum yield be maintained in a nanocrystal layer that at the same time presents suitably high carrier mobilities for efficient charge transport throughout its entire thickness. At present, there have been no demonstrations of LEDs that would satisfy either of these conditions; solving both issues simultaneously will require advances in Auger-engineered nanocrystals and, likely, new concepts in nanocrystal passivation that will alleviate the formation of surface traps without restricting the QD−QD coupling needed for efficient charge transport.

Efficient CM is one of the most truly unique phenomena found in QDs, and it too has made great strides along the path from the laboratory to real application. The most important recent advances in this area include the demonstrations of *p-n* junction QD solar cells with more than 100% quantum efficiency,[60] as well as novel nanostructures with a considerable enhancement in the CM yield achieved via "cooling-rate engineering".[546] Nonetheless, a true impact on the power output of PV devices due to CM will require additional improvements in the CM performance of the nanocrystals and, specifically, a further reduction in the e-h pair creation energy to near the energy-conservation-defined limit of E_g. A phenomenological model (Section 7.2) suggests the key is to shift the balance between CM and competing relaxation mechanisms, by making CM more efficient (*i.e.*, faster) and/or slowing processes such as phonon-mediated cooling. This, in turn, indicates that future focus should be placed on engineered nanostructures with enhanced intercarrier Coulomb interactions but weak carrier-phonon coupling and/or sparse phonon band structures. Recent advances in nanostructured thermoelectric materials that possess at least some of these characteristics may offer insights that could lead to a breakthrough in this direction. At the same time, even CM at the thermodynamic efficiency limit is not, on its own, enough to enable generation-III devices that surpass the Shockley−Queisser limit.[507] Such an achievement will also require a considerable improvement in the performance of QD solar cells from the current PCE record of ∼10%.[680]

Finally, in the rush to identify and develop the next QD-based gadget, it remains important to remember that in addition to being of significant technological interest, semiconductor nanocrystals are also a deeply fertile materials platform for exploring novel nanoscale phenomena in both individual quantum-confined particles and small (molecule-like) and extended (solid-like) interacting ensembles. Such exploration is greatly benefited by the matchless adaptability of these materials, which offer myriad possibilities for fine-tuning of their individual and collective electronic properties through modification of their composition, size, shape, surface structure, and method of assembly into clusters and arrays. Because of this, the use of QDs as model systems in studies of individual quantum emitters and quantum-confined Auger recombination and CM continues to produce key fundamental insights. Similarly, they are a versatile "building block" for analysis of the complex structure of band-edge electronic states arising from long- and short-range exchange interactions, and of the effects of material shape on electronic energies within or near the quantum-confinement regime. In addition, colloidal nanocrystals (particularly complex heterostructured, alloyed, and/or doped QDs) are ideally suited for testing the principles of "wave-function engineering" as a means for controlling spectral and dynamical behaviors of electronic excitations and carrier−carrier interactions. Chemically synthesized nanocrystals have also been widely used in studies of charge and energy transport in ordered and disordered assemblies, as well as within hybrid structures combining QDs with other types of semiconductor-, metal-, or molecular-based systems. Based on the history of this dynamic field, the contributions of engineering and commercialization efforts notwithstanding, further progress in the technologies reviewed above, as well as toward completely new uses for colloidal QDs, critically relies on continued fundamental advances and discoveries in the physics and chemistry of these fascinating materials.

AUTHOR INFORMATION

Corresponding Author

*E-mail: klimov@lanl.gov.

Notes

The authors declare no competing financial interest.

DOI: 10.1021/acs.chemrev.6b00169
Chem. Rev. 2016, 116, 10513−10622

Biographies

Jeffrey M. Pietryga is Deputy Group Leader for the Physical Chemistry and Applied Spectroscopy Group at Los Alamos National Laboratory. He received a B.S. in Chemistry from the University of Michigan—Flint (1997) and a Ph.D. in Inorganic Chemistry from the University of Texas, Austin (2002). His current research centers on the synthesis of novel nanocrystals and their use in detection and solar energy conversion.

Young-Shin Park is an Assistant Research Professor within the Center for High Technology Materials at the University of New Mexico, and a guest scientist at Los Alamos National Laboratory. He earned a B.S. in Physics Education (1996), an M.S. in Physics (1998) from Seoul National University, and a Ph.D. in Physics from the University of Oregon (2009). His research focuses on single-particle spectroscopy of nanocrystal quantum dots and their optoelectronic applications, particularly in lasers and LEDs.

Jaehoon Lim is a postdoctoral associate at Los Alamos National Laboratory. He received his B.S. (2007) and Ph.D. (2013) in Chemical Engineering from Seoul National University in 2013. Thereafter, he held a postdoctoral position at Interuniversity Semiconductor Research Center in Seoul National University. His current research interests are the band gap engineering of core−shell heterostructured quantum dots and their applications toward light-emitting diodes, luminescent solar concentrators, and lasers.

Andrew F. Fidler is a Director's Postdoctoral Fellow at Los Alamos National Laboratory. He received his B.S. in Physics and Chemistry from Albion College (2008) and his Ph.D. in Chemistry from the University of Chicago (2013). His research interest is in spectroscopic and electrical measurements of materials for energy-related applications.

Wan Ki Bae is a senior research scientist at Korea Institute of Science and Technology. He received his B.S. (2003), M.S. (2005), and Ph.D. degrees (2009) in Chemical Engineering from Seoul National University. He conducted postdoctoral research work within the Department of Electrical Engineering and Computer Science at Seoul National University (2009−2010) and within the Chemistry Division of Los Alamos National Laboratory (2010−2013). His research interests include synthesis and characterization of QDs and their optoelectronic applications.

Sergio Brovelli is Professor of Physics and Nanotechnology at the Department of Materials Science of the University of Milano Bicocca (Italy). He graduated (2003) and earned his Ph.D. (2006) in Materials Science at the University of Milano Bicocca. He has been a Marie Curie Postdoctoral Fellow at the London Centre for Nanotechnology and a Director's Postdoctoral Fellow at the Los Alamos National Laboratory. His research revolves around the design and physical investigation of colloidal nanomaterials and related devices for applications in solar energy conversion, optoelectronics, sensing, and bioimaging.

Victor I. Klimov is a LANL Fellow and the director of the Center for Advanced Solar Photophysics of the U.S. Department of Energy. He received his M.S. (1978), Ph.D. (1981), and D.Sc. (1993) degrees from Moscow State University, Russia. His research interests include optical spectroscopy of semiconductor nanocrystals, carrier relaxation processes, strongly confined multiexcitons, energy and charge transfer, and fundamental aspects of lasing, light-emitting diodes, and photovoltaics.

ACKNOWLEDGMENTS

For the topical discussions of carrier multiplication (Section 7) and luminescent solar concentrators (Section 8), we gratefully acknowledge the support of the Center for Advanced Solar Photophysics (CASP), an Energy Frontier Research Center funded by the U.S. Department of Energy (DOE), Office of Science (OS), Office of Basic Energy Sciences (BES). Preparation of the topical discussions of quantum dot electronic states (Sections 2, 3), Auger recombination (Section 4), lasing (Section 5), and light emitting diodes (Section 6) was supported by the Chemical Sciences, Biosciences and Geosciences Division of BES, OS, U.S. DOE.

REFERENCES

(1) Ekimov, A. I.; Onushchenko, A. A. Quantum Size Effect in Three Dimensional Microscopic Semiconductor Crystals. *JETP Lett.* **1981**, *34*, 345.
(2) Ekimov, A. I.; Onushchenko, A. A.; A.Tzehomski, V. Excitonic Absorption by CuCl Microcrystals in a Glass Matrices. *Sov. Phys. Chem. of Glass* **1980**, *6*, 511.
(3) Golubkov, V. V.; Ekimov, A. I.; Onushchenko, A. A.; Tzehomski, V. A. Growth Kinetics of CuCl Microcrystals in Glassy Matrix. *Sov. Phys. Chem. of Glass* **1982**, *7*, 265.
(4) Borrelli, N. F.; Hall, D. W.; Holland, H. J.; Smith, D. W. Quantum Confinement Effects of Semiconducting Microcrystallites in Glass. *J. Appl. Phys.* **1987**, *61*, 5399−5409.
(5) Henglein, A. Photo-Degradation and Fluorescence of Colloidal-Cadmium Sulfide in Aqueous Solution. *Ber. Bunsen. Phys. Chem.* **1982**, *86*, 301−305.
(6) Henglein, A. Catalysis of Photochemical Reactions by Colloidal Semiconductors. *Pure Appl. Chem.* **1984**, *56*, 1215.
(7) Rossetti, R.; Ellison, J.; Gibson, J.; Brus, L. Size Effects in the Excited Electronic States of Small Colloidal CdS Crystallites. *J. Chem. Phys.* **1984**, *80*, 4464−4469.
(8) Vandyshev, Y. V.; Dneprovskii, V. S.; Klimov, V. I. Manifestation of Dimensional Quantization Levels in the Nonlinear Transmission Spectra of Semiconductor Microcrystals. *JETP Lett.* **1991**, *53*, 314−318.
(9) Ekimov, A. I.; Hache, F.; Schanne-Klein, M. C.; Ricard, D.; Flytzanis, C.; Kudryavtsev, I. A.; Yazeva, T. V.; Rodina, A. V.; Efros, A. L. Absorption and Intensity-Dependent Photoluminescence Measurements On CdSe Quantum Dots: Assignment of the First Electronic Transitions. *J. Opt. Soc. Am. B* **1993**, *10*, 100−107.
(10) Klein, M. C.; Hache, F.; Ricard, D.; Flytzanis, C. Size Dependence of Electron-Phonon Coupling in Semiconductor Nanospheres: the Case of CdSe. *Phys. Rev. B: Condens. Matter Mater. Phys.* **1990**, *42*, 11123−11132.
(11) Nomura, S.; Kobayashi, T. Exciton-LO-Phonon Couplings in Spherical Semiconductor Microcrystallites. *Phys. Rev. B: Condens. Matter Mater. Phys.* **1992**, *45*, 1305−1316.
(12) Machol, J. L.; Wise, F. W.; Patel, R. C.; Tanner, D. B. Vibronic Quantum Beats in PbS Microcrystallites. *Phys. Rev. B: Condens. Matter Mater. Phys.* **1993**, *48*, 2819−2822.
(13) Trallero-Giner, C.; Debernardi, A.; Cardona, M.; Menéndez-Proupín, E.; Ekimov, A. I. Optical Vibrons in CdSe Dots and Dispersion Relation of the Bulk Material. *Phys. Rev. B: Condens. Matter Mater. Phys.* **1998**, *57*, 4664−4669.
(14) Woggon, U.; Giessen, H.; Gindele, F.; Wind, O.; Fluegel, B.; Peyghambarian, N. Ultrafast Energy Relaxation in Quantum Dots. *Phys. Rev. B: Condens. Matter Mater. Phys.* **1996**, *54*, 17681−17690.
(15) Klimov, V. I.; Mcbranch, D. W. Femtosecond 1P-To-1S Electron Relaxation in Strongly-Confined Semiconductor Nanocrystals. *Phys. Rev. Lett.* **1998**, *80*, 4028−4031.
(16) Olbright, G. R.; Peyghambarian, N.; Koch, S. W.; Banyai, L. Optical Nonlinearities of Glasses Doped With Semiconductor Microcrystallites. *Opt. Lett.* **1987**, *12*, 413−415.
(17) Roussignol, P.; Kull, M.; Ricard, D.; De Rougemont, F.; Frey, R.; Flytzanis, C. Time-Resolved Direct Observation of Auger Recombination in Semiconductor-Doped Glasses. *Appl. Phys. Lett.* **1987**, *51*, 1882−1884.
(18) Dneprovskii, V. S.; Efros, A. L.; Ekimov, A. I.; Klimov, V. I.; Kudriavtsev, I. A.; Novikov, M. G. Time-Resolved Luminescence of CdSe Microcrystals. *Solid State Commun.* **1990**, *74*, 555−557.

DOI: 10.1021/acs.chemrev.6b00169
Chem. Rev. 2016, 116, 10513−10622

(19) Klimov, V. I.; Mcbranch, D. W. Auger-Process-induced Charge Separation in Semiconductor Nanocrystals. *Phys. Rev. B: Condens. Matter Mater. Phys.* **1997**, *55*, 13173−13179.
(20) Vandyshev, Y. V.; Dneprovskii, V. S.; Klimov, V. I.; Okorokov, D. K. Lasing on a Transition Between Quantum-Well Levels in a Quantum Dot. *JETP Lett.* **1991**, *54*, 442−445.
(21) Murray, C. B.; Norris, D. J.; Bawendi, M. G. Synthesis and Characterization of Nearly Monodisperse CdE (E = S, Se, Te) Semiconductor Nanocrystallites. *J. Am. Chem. Soc.* **1993**, *115*, 8706−8715.
(22) Hines, M. A.; Guyot-Sionnest, P. Synthesis and Characterization of Strongly Luminescing ZnS-Capped CdSe Nanocrystals. *J. Phys. Chem.* **1996**, *100*, 468−471.
(23) Kim, S.; Fisher, B.; Eisler, H.-J.; Bawendi, M. G. Type-II Quantum Dots: CdTe/CdSe(Core/Shell) and CdSe/ZnTe(Core/Shell) Heterostructures. *J. Am. Chem. Soc.* **2003**, *125*, 11466−11467.
(24) Balet, L. P.; Ivanov, S. A.; Piryatinski, A.; Achermann, M.; Klimov, V. I. Inverted Core/Shell Nanocrystals Continuously Tunable Between Type-I and Type-II Localization Regimes. *Nano Lett.* **2004**, *4*, 1485−1488.
(25) Ivanov, S. A.; Nanda, J.; Piryatinski, A.; Achermann, M.; Balet, L. P.; Bezel, I. V.; Anikeeva, P. O.; Tretiak, S.; Klimov, V. I. Light Amplification Using inverted Core/Shell Nanocrystals: Towards Lasing in the Single-Exciton Regime. *J. Phys. Chem. B* **2004**, *108*, 10625−10630.
(26) Peng, X. G.; Manna, L.; Yang, W. D.; Wickham, J.; Scher, E.; Kadavanich, A.; Alivisatos, A. P. Shape Control of CdSe Nanocrystals. *Nature* **2000**, *404*, 59−61.
(27) Manna, L.; Scher, E. C.; Alivisatos, A. P. Synthesis of Soluble and Processable Rod-, Arrow-, Teardrop-, and Tetrapod-Shaped CdSe Nanocrystals. *J. Am. Chem. Soc.* **2000**, *122*, 12700−12706.
(28) Nirmal, M.; Norris, D. J.; Kuno, M.; Bawendi, M. G.; Efros, A. L.; Rosen, M. Observation of the Dark Excitons in CdSe Quantum Dots. *Phys. Rev. Lett.* **1995**, *75*, 3728−3731.
(29) Norris, D. J.; Efros, A. L.; Rosen, M.; Bawendi, M. G. Size Dependence of Exciton Fine Structure in CdSe Quantum Dots. *Phys. Rev. B: Condens. Matter Mater. Phys.* **1996**, *53*, 16347−16354.
(30) Efros, A. L.; Kharchenko, V. A.; Rosen, M. Breaking the Phonon Bottleneck in Nanometer Quantum Dots: Role of Auger- Like Processes. *Solid State Commun.* **1995**, *93*, 281−284.
(31) Guyot-Sionnest, P.; Shim, M.; Matranga, C.; Hines, M. Intraband Relaxation in CdSe Quantum Dots. *Phys. Rev. B: Condens. Matter Mater. Phys.* **1999**, *60*, 2181−2184.
(32) Cooney, R. R.; Sewall, S. L.; Dias, E. A.; Sagar, D. M.; Anderson, K. E. H.; Kambhampati, P. Unified Picture of Electron and Hole Relaxation Pathways in Semiconductor Quantum Dots. *Phys. Rev. B: Condens. Matter Mater. Phys.* **2007**, *75*, 245311−245314.
(33) Crooker, S. A.; Barrick, T.; Hollingsworth, J. A.; Klimov, V. I. Multiple Temperature Regimes of Radiative Decay in CdSe Nanocrystal Quantum Dots: Intrinsic Limits to the Dark-Exciton Lifetime. *Appl. Phys. Lett.* **2003**, *82*, 2793−2795.
(34) Klimov, V. I.; Mikhailovsky, A. A.; Mcbranch, D. W.; Leatherdale, C. A.; Bawendi, M. G. Quantization of Multiparticle Auger Rates in Semiconductor Quantum Dots. *Science* **2000**, *287*, 1011−1013.
(35) Fisher, B.; Caruge, J.-M.; Chan, Y.-T.; Halpert, J.; Bawendi, M. G. Multiexciton Fluorescence from Semiconductor Nanocrystals. *Chem. Phys.* **2005**, *318*, 71−81.
(36) Pandey, A.; Guyot-Sionnest, P. Multicarrier Recombination in Colloidal Quantum Dots. *J. Chem. Phys.* **2007**, *127*, 111104.
(37) Nirmal, M.; Dabbousi, B. O.; Bawendi, M. G.; Macklin, J. J.; Trautman, J. K.; Harris, T. D.; Brus, L. E. Fluorescence Intermittency in Single Cadmium Selenide Nanocrystals. *Nature* **1996**, *383*, 802−804.
(38) Empedocles, S. A.; Norris, D. J.; Bawendi, M. G. Photoluminescence Spectroscopy of Single CdSe Nanocrystallite Quantum Dots. *Phys. Rev. Lett.* **1996**, *77*, 3873−3876.
(39) Blanton, S. A.; Hines, M. A.; Guyot-Sionnest, P. Photoluminescence Wandering in Single CdSe Nanocrystals. *Appl. Phys. Lett.* **1996**, *69*, 3905−3907.
(40) Kuno, M.; Fromm, D. P.; Hamann, H. F.; Gallagher, A.; Nesbitt, D. J. Nonexponential "Blinking" Kinetics of Single CdSe Quantum Dots: A Universal Power Law Behavior. *J. Chem. Phys.* **2000**, *112*, 3117−3120.
(41) Yu, D.; Wang, C. J.; Wehrenberg, B. L.; Guyot-Sionnest, P. Variable Range Hopping Conduction in Semiconductor Nanocrystal Solids. *Phys. Rev. Lett.* **2004**, *92*, 216802−216804.
(42) Talapin, D. V.; Murray, C. B. PbSe Nanocrystal Solids For n- and p-Channel Thin Film Field-Effect Transistors. *Science* **2005**, *310*, 86−89.
(43) Leatherdale, C. A.; Kagan, C. R.; Morgan, N. Y.; Empedocles, S. A.; Kastner, M. A.; Bawendi, M. G. Photoconductivity in CdSe Quantum Dot Solids. *Phys. Rev. B: Condens. Matter Mater. Phys.* **2000**, *62*, 2669−2680.
(44) Choi, J.-H.; Fafarman, A. T.; Oh, S. J.; Ko, D.-K.; Kim, D. K.; Diroll, B. T.; Muramoto, S.; Gillen, J. G.; Murray, C. B.; Kagan, C. R. Bandlike Transport in Strongly Coupled and Doped Quantum Dot Solids: A Route to High-Performance Thin-Film Electronics. *Nano Lett.* **2012**, *12*, 2631−2638.
(45) Zarghami, M. H.; Liu, Y.; Gibbs, M.; Gebremichael, E.; Webster, C.; Law, M. p-Type PbSe and PbS Quantum Dot Solids Prepared With Short-Chain Acids and Diacids. *ACS Nano* **2010**, *4*, 2475−2485.
(46) Bruchez, M.; Moronne, M.; Gin, P.; Weiss, S.; Alivisatos, A. P. Semiconductor Nanocrystals as Fluorescent Biological Labels. *Science* **1998**, *281*, 2013−2016.
(47) Chan, W. C. W.; Nie, S. Quantum Dot Bioconjugates for Ultrasensitive Nonisotopic Detection. *Science* **1998**, *281*, 2016.
(48) Medintz, I. L.; Uyeda, H. T.; Goldman, E. R.; Mattoussi, H. Quantum Dot Bioconjugates for Imaging, Labelling and Sensing. *Nat. Mater.* **2005**, *4*, 435−446.
(49) Jang, E.; Jun, S.; Jang, H.; Lim, J.; Kim, B.; Kim, Y. White-Light-Emitting Diodes with Quantum Dot Color Converters For Display Backlights. *Adv. Mater.* **2010**, *22*, 3076−3080.
(50) Colvin, V. L.; Schlamp, M. C.; Alivisatos, A. P. Light-Emitting Diodes Made from Cadmium Selenide Nanocrystals and a Semiconducting Polymer. *Nature* **1994**, *370*, 354−357.
(51) Mattoussi, H.; Radzilowski, L. H.; Dabbousi, B. O.; Thomas, E. L.; Bawendi, M. G.; Rubner, M. F. Electroluminescence from Heterostructures of Poly(Phenylene Vinylene) and Inorganic CdSe Nanocrystals. *J. Appl. Phys.* **1998**, *83*, 7965−7974.
(52) Greenham, N. C.; Peng, X. G.; Alivisatos, A. P. Charge Separation and Transport in Conjugated-Polymer/Semiconductor-Nanocrystal Composites Studied By Photoluminescence Quenching and Photoconductivity. *Phys. Rev. B: Condens. Matter Mater. Phys.* **1996**, *54*, 17628−17637.
(53) Nozik, A. J. Quantum Dot Solar Cells. *Phys. E* **2002**, *14*, 115−120.
(54) Sargent, E. H. Colloidal Quantum Dot Solar Cells. *Nat. Photonics* **2012**, *6*, 133−135.
(55) Wang, X.; Koleilat, G. I.; Tang, J.; Liu, H.; Kramer, I. J.; Debnath, R.; Brzozowski, L.; Barkhouse, D. A. R.; Levina, L.; Hoogland, S.; et al. Tandem Colloidal Quantum Dot Solar Cells Employing A Graded Recombination Layer. *Nat. Photonics* **2011**, *5*, 480−484.
(56) Luther, J. M.; Gao, J.; Lloyd, M. T.; Semonin, O. E.; Beard, M. C.; Nozik, A. J. Stability Assessment on a 3% Bilayer PbS/ZnO Quantum Dot Heterojunction Solar Cell. *Adv. Mater.* **2010**, *22*, 3704−3707.
(57) Kim, G.-H.; García De Arquer, F. P.; Yoon, Y. J.; Lan, X.; Liu, M.; Voznyy, O.; Yang, Z.; Fan, F.; Ip, A. H.; Kanjanaboos, P.; et al. High-Efficiency Colloidal Quantum Dot Photovoltaics Via Robust Self-Assembled Monolayers. *Nano Lett.* **2015**, *15*, 7691.
(58) Lan, X.; Voznyy, O.; García De Arquer, F. P.; Liu, M.; Xu, J.; Proppe, A. H.; Walters, G.; Fan, F.; Tan, H.; Liu, M.; et al. 10.6% Certified Colloidal Quantum Dot Solar Cells Via Solvent-Polarity-Engineered Halide Passivation. *Nano Lett.* **2016**, *16*, 4630.
(59) Schaller, R. D.; Klimov, V. I. High Efficiency Carrier Multiplication in PbSe Nanocrystals: Implications For Solar-Energy Conversion. *Phys. Rev. Lett.* **2004**, *92*, 186601−186604.
(60) Semonin, O. E.; Luther, J. M.; Choi, S.; Chen, H. Y.; Gao, J. B.; Nozik, A. J.; Beard, M. C. Peak External Photocurrent Quantum Efficiency Exceeding 100% Via MEG in A Quantum Dot Solar Cell. *Science* **2011**, *334*, 1530−1533.

DOI: 10.1021/acs.chemrev.6b00169
Chem. Rev. 2016, 116, 10513−10622

(61) Böhm, M. L.; Jellicoe, T. C.; Tabachnyk, M.; Davis, N. J.; Wisnivesky Rocca Rivarola, F.; Ducati, C.; Ehrler, B.; Bakulin, A. A.; Greenham, N. C. Lead Telluride Quantum Dot Solar Cells Displaying External Quantum Efficiencies Exceeding 120%. *Nano Lett.* **2015**, *15*, 7987.
(62) Bomm, J.; Büchtemann, A.; Chatten, A. J.; Bose, R.; Farrell, D. J.; Chan, N. L. A.; Xiao, Y.; Slooff, L. H.; Meyer, T.; Meyer, A.; et al. Fabrication and Full Characterization of State-Of-The-Art Quantum Dot Luminescent Solar Concentrators. *Sol. Energy Mater. Sol. Cells* **2011**, *95*, 2087−2094.
(63) Erickson, C. S.; Bradshaw, L. R.; Mcdowall, S.; Gilbertson, J. D.; Gamelin, D. R.; Patrick, D. L. Zero-Reabsorption Doped-Nanocrystal Luminescent Solar Concentrators. *ACS Nano* **2014**, *8*, 3461−3467.
(64) Meinardi, F.; Colombo, A.; Velizhanin, K. A.; Simonutti, R.; Lorenzon, M.; Beverina, L.; Viswanatha, R.; Klimov, V. I.; Brovelli, S. Large-Area Luminescent Solar Concentrators Based on "Stokes-Shift-Engineered" Nanocrystals in a Mass-Polymerized PMMA Matrix. *Nat. Photonics* **2014**, *8*, 392−399.
(65) Bronstein, N. D.; Li, L.; Xu, L.; Yao, Y.; Ferry, V. E.; Alivisatos, A. P.; Nuzzo, R. G. Luminescent Solar Concentration With Semiconductor Nanorods and Transfer-Printed Micro-Silicon Solar Cells. *ACS Nano* **2014**, *8*, 44−53.
(66) Efros, A. L.; Efros, A. L. Interband Absorption of Light in a Semiconductor Sphere. *Sov. Phys. Sem.* **1982**, *16*, 772−775.
(67) *Nanocrystal Quantum Dots*, 2nd ed.; Klimov, V. I., Ed.; Taylor & Francis: 2009.
(68) Brus, L. E. A Simple Model For the Ionization Potential, Electron Affinity, and Aqueous Redox Potentials of Small Semiconductor Crystallites. *J. Chem. Phys.* **1983**, *79*, 5566−5571.
(69) Grigoryan, G. B.; Rodina, A. V.; Efros, A. L. Excitons and Biexcitons in Quantum-Well Semiconductor Microcrystals in An insulating Glassy Matrix. *Sov. Phys. Solid. State* **1990**, *32*, 2037−2042.
(70) Klimov, V. I. In *Handbook On Nanostructured Materials and Nanotechnology*; Nalwa, H. S., Ed.; Academic Press: San Diego, 2000; Vol. *4*.
(71) Klimov, V. I. Optical Nonlinearities and Ultrafast Carrier Dynamics in Semiconductor Nanocrystals. *J. Phys. Chem. B* **2000**, *104*, 6112−6123.
(72) Leatherdale, C. A.; Woo, W. K.; Mikulec, F. V.; Bawendi, M. G. On the Absorption Cross Section of CdSe Nanocrystal Quantum Dots. *J. Phys. Chem. B* **2002**, *106*, 7619−7622.
(73) Yu, W. W.; Qu, L. H.; Guo, W. Z.; Peng, X. G. Experimental Determination of the Extinction Coefficient of CdTe, CdSe, and CdS Nanocrystals. *Chem. Mater.* **2003**, *15*, 2854−2860.
(74) Moreels, I.; Lambert, K.; De Muynck, D.; Vanhaecke, F.; Poelman, D.; Martins, J. C.; Allan, G.; Hens, Z. Composition and Size-Dependent Extinction Coefficient of Colloidal PbSe Quantum Dots. *Chem. Mater.* **2007**, *19*, 6101−6106.
(75) Koch, S. W.; Hu, Y. Z.; Fluegel, B.; Peyghambarian, N. Coulomb Effects and Optical-Properties of Semiconductor Quantum Dots. *J. Cryst. Growth* **1992**, *117*, 592−597.
(76) Xia, J. B. Electronic-Structures of Zero-Dimensional Quantum Wells. *Phys. Rev. B: Condens. Matter Mater. Phys.* **1989**, *40*, 8500−8507.
(77) Norris, D. J.; Bawendi, M. G. Measurement and Assignment of the Size-Dependent Optical Spectrum in CdSe Quantum Dots. *Phys. Rev. B: Condens. Matter Mater. Phys.* **1996**, *53*, 16338−16346.
(78) Efros, A. L.; Rosen, M.; Kuno, M.; Nirmal, M.; Norris, D. J.; Bawendi, M. Band-Edge Exciton in Quantum Dots of Semiconductors with a Degenerate Valence Band: Dark and Bright Exciton States. *Phys. Rev. B: Condens. Matter Mater. Phys.* **1996**, *54*, 4843−4856.
(79) Kuno, M.; Lee, J. K.; Dabbousi, B. O.; Mikulec, F. V.; Bawendi, M. G. the Band Edge Luminescence of Surface Modified CdSe Nanocrystallites: Probing the Luminescing State. *J. Chem. Phys.* **1997**, *106*, 9869−9882.
(80) Htoon, H.; Cox, P. J.; Klimov, V. I. the Structure of Excited-State Transitions in individual Semiconductor Nanocrystals Probed by Photoluminescence Excitation Spectroscopy. *Phys. Rev. Lett.* **2004**, *93*, 187402−187404.
(81) De Mello Donegá, C.; Bode, M.; Meijerink, A. Size- and Temperature-Dependence of Exciton Lifetimes in CdSe Quantum Dots. *Phys. Rev. B: Condens. Matter Mater. Phys.* **2006**, *74*, 085320.
(82) Wuister, S. F.; Van Houselt, A.; Donega, C. D. M.; Vanmaekelbergh, D.; Meijerink, A. Temperature Antiquenching of the Luminescence from Capped CdSe Quantum Dots. *Angew. Chem., Int. Ed.* **2004**, *43*, 3029−3033.
(83) Oron, D.; Aharoni, A.; Donega, C. D.; Van Rijssel, J.; Meijerink, A.; Banin, U. Universal Role of Discrete Acoustic Phonons in the Low-Temperature Optical Emission of Colloidal Quantum Dots. *Phys. Rev. Lett.* **2009**, *102*, 177402.
(84) Labeau, O.; Tamarat, P.; Lounis, B. Temperature Dependence of the Luminescence Lifetime of Single CdSe/ZnS Quantum Dots. *Phys. Rev. Lett.* **2003**, *90*, 257404 DOI: 10.1103/PhysRevLett.90.257404.
(85) Kortan, A.; Hull, R.; Opila, R.; Bawendi, M.; Steigerwald, M.; Carroll, P.; Brus, L. E. Nucleation and Growth of Cadmium Selendie On Zinc Sulfide Quantum Crystallite Seeds, and Vice Versa, in Inverse Micelle Media. *J. Am. Chem. Soc.* **1990**, *112*, 1327−1332.
(86) Bae, W. K.; Padilha, L. A.; Park, Y.-S.; Mcdaniel, H.; Robel, I.; Pietryga, J. M.; Klimov, V. I. Controlled Alloying of the Core−Shell Interface in CdSe/CdS Quantum Dots for Suppression of Auger Recombination. *ACS Nano* **2013**, *7*, 3411−3419.
(87) Freund, T.; Gomes, W. Electrochemical Methods for Investigating Catalysis by Semiconductors. *Catal. Rev.: Sci. Eng.* **1970**, *3*, 1−36.
(88) Fujishima, A.; Honda, K. Electrochemical Photolysis of Water at a Semiconductor Electrode. *Nature* **1972**, *238*, 37−38.
(89) Kraeutler, B.; Bard, A. J. Heterogeneous Photocatalytic Synthesis of Methane from Acetic Acid-New Kolbe Reaction Pathway. *J. Am. Chem. Soc.* **1978**, *100*, 2239−2240.
(90) Kraeutler, B.; Bard, A. J. Heterogeneous Photocatalytic Preparation of Supported Catalysts. Photodeposition of Platinum on Titanium Dioxide Powder and Other Substrates. *J. Am. Chem. Soc.* **1978**, *100*, 4317−4318.
(91) Gerischer, H. Electrochemical Photo and Solar Cells Principles and Some Experiments. *J. Electroanal. Chem. Interfacial Electrochem.* **1975**, *58*, 263−274.
(92) Ellis, A. B.; Kaiser, S. W.; Bolts, J. M.; Wrighton, M. S. Study of n-Type Semiconducting Cadmium Chalcogenide-Based Photoelectrochemical Cells Employing Polychalcogenide Electrolytes. *J. Am. Chem. Soc.* **1977**, *99*, 2839−2848.
(93) Kohl, P.; Bard, A. Semiconductor Electrodes. 13. Characterization and Behavior of n-Type Zinc Oxide, Cadmium Sulfide, and Gallium Phosphide Electrodes in Acetonitrile Solutions. *J. Am. Chem. Soc.* **1977**, *99*, 7531−7539.
(94) Harbour, J. R.; Hair, M. L. Superoxide Generation in the Photolysis of Aqueous Cadmium Sulfide Dispersions. Detection By Spin Trapping. *J. Phys. Chem.* **1977**, *81*, 1791−1793.
(95) Saeva, F. D.; Olin, G. R.; Harbour, J. R. Mechanism of the Cadmium Sulphide Sensitized Photo-Oxidation of Leuco Crystal Violet in Nonaqueous Solution. *J. Chem. Soc., Chem. Commun.* **1978**, 417−418.
(96) Kalyanasundaram, K.; Borgarello, E.; Duonghong, D.; Grätzel, M. Cleavage of Water by Visible-Light Irradiation of Colloidal CdS Solutions; Inhibition of Photocorrosion by Ruo2. *Angew. Chem., Int. Ed. Engl.* **1981**, *20*, 987−988.
(97) Kuczynski, J.; Thomas, J. Photochemistry at the Surface of Colloidal Cadmium Sulfide. *Chem. Phys. Lett.* **1982**, *88*, 445−447.
(98) Mokrushin, S.; Tkachev, Y. D. Experimental Investigation of Laminar Systems 27. Formation of Ultrathin Cadmium Sulfide Layers at Solution Solid Interface. *Colloid. J. USSR* **1961**, *23*, 438.
(99) Miller, B.; Heller, A. Semiconductor Liquid Junction Solar Cells Based on Anodic Sulphide Films. *Nature* **1976**, *262*, 680−681.
(100) Minoura, H.; Nakamura, T.; Ueno, Y.; Tsuiki, M. Electrochemical Photocell Using Sprayed CdS Film Electrode. *Chem. Lett.* **1977**, 913−916.
(101) Dung, D.; Ramsden, J.; Graetzel, M. Dynamics of Interfacial Electron-Transfer Processes in Colloidal Semiconductor Systems. *J. Am. Chem. Soc.* **1982**, *104*, 2977−2985.

DOI: 10.1021/acs.chemrev.6b00169
Chem. Rev. 2016, 116, 10513−10622

(102) Rossetti, R.; Brus, L. Electron-Hole Recombination Emission as a Probe of Surface Chemistry in Aqueous Cadmium Sulfide Colloids. *J. Phys. Chem.* **1982**, *86*, 4470−4472.
(103) Rossetti, R.; Nakahara, S.; Brus, L. E. Quantum Size Effects in the Redox Potentials, Resonance Raman-Spectra, and Electronic-Spectra of CdS Crystallites in Aqueous-Solution. *J. Chem. Phys.* **1983**, *79*, 1086−1088.
(104) Brus, L. E. Electron-Electron and Electron-Hole Interactions in Small Semiconductor Crystallites: The Size Dependence of the Lowest Excited Electronic State. *J. Chem. Phys.* **1984**, *80*, 4403−4409.
(105) Fojtik, A.; Weller, H.; Koch, U.; Henglein, A. Photo-Chemistry of Colloidal Metal Sulfides 8. Photo-Physics of Extremely Small CdS Particles - Q-State CdS and Magic Agglomeration Numbers. *Ber. Bunsen. Phys. Chem.* **1984**, *88*, 969−977.
(106) Weller, H.; Schmidt, H.; Koch, U.; Fojtik, A.; Baral, S.; Henglein, A.; Kunath, W.; Weiss, K.; Dieman, E. Photochemistry of Colloidal Semiconductors. Onset of Light Absorption as a Function of Size of Extremely Small CdS Particles. *Chem. Phys. Lett.* **1986**, *124*, 557−560.
(107) Brus, L. Electronic Wave Functions in Semiconductor Clusters: Experiment and Theory. *J. Phys. Chem.* **1986**, *90*, 2555−2560.
(108) Dannhauser, T.; O'neil, M.; Johansson, K.; Whitten, D.; Mclendon, G. Photophysics of Quantized Colloidal Semiconductors. Dramatic Luminescence Enhancement by Binding of Simple Amines. *J. Phys. Chem.* **1986**, *90*, 6074−6076.
(109) Mokrushin, S. G. Thomas Graham and the Definition of Colloid. *Nature* **1962**, *195*, 861.
(110) Reed, M.; Bate, R.; Bradshaw, K.; Duncan, W.; Frensley, W.; Lee, J.; Shih, H. Spatial Quantization in Gaas−Algaas Multiple Quantum Dots. *J. Vac. Sci. Technol., B: Microelectron. Process. Phenom.* **1986**, *4*, 358−360.
(111) Ekimov, A. I.; Efros, A. L.; Onushchenko, A. A. Quantum Size Effect in Semiconductor Microcrystals. *Solid State Commun.* **1985**, *56*, 921−924.
(112) Henglein, A.; Gutierrez, M. Photochemistry of Colloidal Metal Sulfides 5. Fluorescence and Chemical Reactions of ZnS and ZnS/CdS Co-Colloids. *Ber. Bunsen. Phys. Chem.* **1983**, *87*, 852−858.
(113) Nenadovic, M.; Rajh, T.; Micic, O. Size Quantization in Small Semiconductor Particles. *J. Phys. Chem.* **1985**, *89*, 397−399.
(114) Weller, H.; Fojtik, A.; Henglein, A. Photochemistry of Semiconductor Colloids: Properties of Extremely Small Particles of Cd3P2 and Zn3P2. *Chem. Phys. Lett.* **1985**, *117*, 485−488.
(115) Fojtik, A.; Weller, H.; Henglein, A. Photochemistry of Semiconductor Colloids. Size Quantization Effects in Q-Cadmium Arsenide. *Chem. Phys. Lett.* **1985**, *120*, 552−554.
(116) Nedeljkovic, J.; Nenadovic, M.; Micic, O.; Nozik, A. Enhanced Photoredox Chemistry in Quantized Semiconductor Colloids. *J. Phys. Chem.* **1986**, *90*, 12−13.
(117) Fojtik, A.; Weller, H.; Fiechter, S.; Henglein, A. Preparation of Colloidal Silicon and Preliminary Photochemical Experiments. *Chem. Phys. Lett.* **1987**, *134*, 477−479.
(118) Eicke, H.-F. Aggregation in Surfactant Solutions: Formation and Properties of Micelles and Microemulsions. *Pure Appl. Chem.* **1980**, *52*, 1349−1357.
(119) Lianos, P.; Thomas, J. K. Cadmium Sulfide of Small Dimensions Produced in Inverted Micelles. *Chem. Phys. Lett.* **1986**, *125*, 299−302.
(120) Steigerwald, M.; Alivisatos, A.; Gibson, J.; Harris, T.; Kortan, R.; Muller, A.; Thayer, A.; Duncan, T.; Douglass, D.; Brus, L. Surface Derivatization and Isolation of Semiconductor Cluster Molecules. *J. Am. Chem. Soc.* **1988**, *110*, 3046−3050.
(121) Steigerwald, M. L.; Brus, L. E. Synthesis, Stabilization, and Electronic-Structure of Quantum Semiconductor Nanoclusters. *Annu. Rev. Mater. Sci.* **1989**, *19*, 471−495.
(122) Chemseddine, A.; Weller, H. Highly Monodisperse Quantum Sized CdS Particles by Size Selective Precipitation. *Ber. Bunsen. Phys. Chem.* **1993**, *97*, 636−638.
(123) Brennan, J.; Siegrist, T.; Carroll, P.; Stuczynski, S.; Reynders, P.; Brus, L.; Steigerwald, M. Bulk and Nanostructure Group II-VI Compounds from Molecular Organometallic Precursors. *Chem. Mater.* **1990**, *2*, 403−409.
(124) Brennan, J. G.; Siegrist, T.; Carroll, P.; Stuczynski, S.; Brus, L.; Steigerwald, M. The Preparation of Large Semiconductor Clusters Via the Pyrolysis of a Molecular Precursor. *J. Am. Chem. Soc.* **1989**, *111*, 4141−4143.
(125) Douglas, T.; Theopold, K. H. Molecular Precursors for Indium Phosphide and Synthesis of Small III-V Semiconductor Clusters in Solution. *Inorg. Chem.* **1991**, *30*, 594−596.
(126) LaMer, V. K.; Dinegar, R. H. Theory, Production and Mechanism of Formation of Monodispersed Hydrosols. *J. Am. Chem. Soc.* **1950**, *72*, 4847−4854.
(127) Norris, D.; Sacra, A.; Murray, C.; Bawendi, M. Measurement of the Size Dependent Hole Spectrum in CdSe Quantum Dots. *Phys. Rev. Lett.* **1994**, *72*, 2612.
(128) Norris, D.; Bawendi, M. Structure in the Lowest Absorption Feature of CdSe Quantum Dots. *J. Chem. Phys.* **1995**, *103*, 5260−5268.
(129) Hines, M. A.; Guyot-Sionnest, P. Bright UV-Blue Luminescent Colloidal ZnSe Nanocrystals. *J. Phys. Chem. B* **1998**, *102*, 3655−3657.
(130) Malik, M. A.; Revaprasadu, N.; O'Brien, P. Air-Stable Single-Source Precursors for the Synthesis of Chalcogenide Semiconductor Nanoparticles. *Chem. Mater.* **2001**, *13*, 913−920.
(131) Li, L. S.; Pradhan, N.; Wang, Y.; Peng, X. High Quality ZnSe and ZnS Nanocrystals Formed by Activating Zinc Carboxylate Precursors. *Nano Lett.* **2004**, *4*, 2261−2264.
(132) Zhang, J.; Sun, K.; Kumbhar, A.; Fang, J. Shape-Control of ZnTe Nanocrystal Growth in Organic Solution. *J. Phys. Chem. C* **2008**, *112*, 5454−5458.
(133) Green, M.; O'Brien, P. A Novel Synthesis of Cadmium Phosphide Nanoparticles Using the Single-Source Precursor [MeCdP-(t-Bu)2]3. *Adv. Mater.* **1998**, *10*, 527−528.
(134) Green, M.; O'Brien, P. A Novel Metalorganic Route To Nanocrystallites of Zinc Phosphide. *Chem. Mater.* **2001**, *13*, 4500−4505.
(135) Harris, D. K.; Allen, P. M.; Han, H.-S.; Walker, B. J.; Lee, J.; Bawendi, M. G. Synthesis of Cadmium Arsenide Quantum Dots Luminescent in the Infrared. *J. Am. Chem. Soc.* **2011**, *133*, 4676−4679.
(136) Malik, M. A.; O'Brien, P.; Revaprasadu, N. A Novel Route for the Preparation of CuSe and CuInSe2 Nanoparticles. *Adv. Mater.* **1999**, *11*, 1441−1444.
(137) Allen, P. M.; Bawendi, M. G. Ternary I− III− VI Quantum Dots Luminescent in the Red to Near-infrared. *J. Am. Chem. Soc.* **2008**, *130*, 9240−9241.
(138) Murray, C. B.; Sun, S.; Gaschler, W.; Doyle, H.; Betley, T. A.; Kagan, C. R. Colloidal Synthesis of Nanocrystals and Nanocrystal Superlattices. *IBM J. Res. Dev.* **2001**, *45*, 47−56.
(139) Hines, M. A.; Scholes, G. D. Colloidal PbS Nanocrystals With Size-Tunable Near-infrared Emission: Observation of Post-Synthesis Self-Narrowing of the Particle Size Distribution. *Adv. Mater.* **2003**, *15*, 1844−1849.
(140) Lu, W.; Fang, J.; Stokes, K. L.; Lin, J. Shape Evolution and Self Assembly of Monodisperse PbTe Nanocrystals. *J. Am. Chem. Soc.* **2004**, *126*, 11798−11799.
(141) Murphy, J. E.; Beard, M. C.; Norman, A. G.; Ahrenkiel, S. P.; Johnson, J. C.; Yu, P.; Micic, O. I.; Ellingson, R. J.; Nozik, A. J. PbTe Colloidal Nanocrystals: Synthesis, Characterization, and Multiple Exciton Generation. *J. Am. Chem. Soc.* **2006**, *128*, 3241−3247.
(142) Peng, Z. A.; Peng, X. Formation of High-Quality CdTe, CdSe, and CdS Nanocrystals Using CdO As Precursor. *J. Am. Chem. Soc.* **2001**, *123*, 183−184.
(143) Yu, W. W.; Wang, Y. A.; Peng, X. Formation and Stability of Size-, Shape-, and Structure-Controlled CdTe Nanocrystals: Ligand Effects On Monomers and Nanocrystals. *Chem. Mater.* **2003**, *15*, 4300−4308.
(144) Olshavsky, M.; Goldstein, A.; Alivisatos, A. Organometallic Synthesis of Gallium-Arsenide Crystallites, Exhibiting Quantum Confinement. *J. Am. Chem. Soc.* **1990**, *112*, 9438−9439.
(145) Uchida, H.; Matsunaga, T.; Yoneyama, H.; Sakata, T.; Mori, H.; Sasaki, T. Preparation and Optical Nonlinearity of Quantized Indium Arsenide Nanocrystals. *Chem. Mater.* **1993**, *5*, 716−719.

DOI: 10.1021/acs.chemrev.6b00169
Chem. Rev. 2016, 116, 10513−10622

(146) Micic, O. I.; Curtis, C. J.; Jones, K. M.; Sprague, J. R.; Nozik, A. J. Synthesis and Characterization of InP Quantum Dots. *J. Phys. Chem.* **1994**, *98*, 4966−4969.
(147) Micic, O.; Sprague, J.; Curtis, C.; Jones, K.; Machol, J.; Nozik, A.; Giessen, H.; Fluegel, B.; Mohs, G.; Peyghambarian, N. Synthesis and Characterization of InP, GaP, and GaInP2 Quantum Dots. *J. Phys. Chem.* **1995**, *99*, 7754−7759.
(148) Heath, J. R. A Liquid-Solution-Phase Synthesis of Crystalline Silicon. *Science* **1992**, *258*, 1131−1133.
(149) Taylor, B. R.; Kauzlarich, S. M.; Lee, H. W.; Delgado, G. R. Solution Synthesis of Germanium Nanocrystals Demonstrating Quantum Confinement. *Chem. Mater.* **1998**, *10*, 22−24.
(150) Yang, C.-S.; Bley, R. A.; Kauzlarich, S. M.; Lee, H. W.; Delgado, G. R. Synthesis of Alkyl-Terminated Silicon Nanoclusters by a Solution Route. *J. Am. Chem. Soc.* **1999**, *121*, 5191−5195.
(151) Yang, C.-S.; Liu, Q.; Kauzlarich, S. M.; Phillips, B. Synthesis and Characterization of Sn/R, Sn/Si-R, and Sn/SiO2 Core/Shell Nanoparticles. *Chem. Mater.* **2000**, *12*, 983−988.
(152) Lu, X.; Korgel, B. A.; Johnston, K. P. High Yield of Germanium Nanocrystals Synthesized From Germanium Diiodide in Solution. *Chem. Mater.* **2005**, *17*, 6479−6485.
(153) Lee, D. C.; Pietryga, J. M.; Robel, I.; Werder, D. J.; Schaller, R. D.; Klimov, V. I. Colloidal Synthesis of Infrared-Emitting Germanium Nanocrystals. *J. Am. Chem. Soc.* **2009**, *131*, 3436−3437.
(154) Green, M.; Wakefield, G.; Dobson, P. J. A Simple Metalorganic Route To Organically Passivated Mercury Telluride Nanocrystals. *J. Mater. Chem.* **2003**, *13*, 1076−1078.
(155) Jeong, K. S.; Deng, Z.; Keuleyan, S.; Liu, H.; Guyot-Sionnest, P. Air-Stable n-Doped Colloidal HgS Quantum Dots. *J. Phys. Chem. Lett.* **2014**, *5*, 1139−1143.
(156) Deng, Z.; Jeong, K. S.; Guyot-Sionnest, P. Colloidal Quantum Dots Intraband Photodetectors. *ACS Nano* **2014**, *8*, 11707−11714.
(157) Cao, Y. C.; Wang, J. One-Pot Synthesis of High-Quality Zinc-Blende CdS Nanocrystals. *J. Am. Chem. Soc.* **2004**, *126*, 14336−14337.
(158) Yang, Y. A.; Wu, H.; Williams, K. R.; Cao, Y. C. Synthesis of CdSe and CdTe Nanocrystals Without Precursor Injection. *Angew. Chem.* **2005**, *117*, 6870−6873.
(159) Talapin, D. V.; Haubold, S.; Rogach, A. L.; Kornowski, A.; Haase, M.; Weller, H. A Novel Organometallic Synthesis of Highly Luminescent CdTe Nanocrystals. *J. Phys. Chem. B* **2001**, *105*, 2260−2263.
(160) Mohamed, M. B.; Tonti, D.; Al-Salman, A.; Chemseddine, A.; Chergui, M. Synthesis of High Quality Zinc Blende CdSe Nanocrystals. *J. Phys. Chem. B* **2005**, *109*, 10533−10537.
(161) Cademartiri, L.; Bertolotti, J.; Sapienza, R.; Wiersma, D. S.; Von Freymann, G.; Ozin, G. A. Multigram Scale, Solventless, and Diffusion-Controlled Route to Highly Monodisperse PbS Nanocrystals. *J. Phys. Chem. B* **2006**, *110*, 671−673.
(162) Zhong, H.; Lo, S. S.; Mirkovic, T.; Li, Y.; Ding, Y.; Li, Y.; Scholes, G. D. Noninjection Gram-Scale Synthesis of Monodisperse Pyramidal CuInS2 Nanocrystals and Their Size-Dependent Properties. *ACS Nano* **2010**, *4*, 5253−5262.
(163) Li, L.; Pandey, A.; Werder, D. J.; Khanal, B. P.; Pietryga, J. M.; Klimov, V. I. Efficient Synthesis of Highly Luminescent Copper Indium Sulfide-Based Core/Shell Nanocrystals With Surprisingly Long-Lived Emission. *J. Am. Chem. Soc.* **2011**, *133*, 1176−1179.
(164) Van Embden, J.; Chesman, A. S.; Jasieniak, J. J. The Heat-Up Synthesis of Colloidal Nanocrystals. *Chem. Mater.* **2015**, *27*, 2246−2285.
(165) Zhong, X.; Han, M.; Dong, Z.; White, T. J.; Knoll, W. Composition-Tunable ZnXCd1-XSe Nanocrystals With High Luminescence and Stability. *J. Am. Chem. Soc.* **2003**, *125*, 8589−8594.
(166) Jang, E.; Jun, S.; Pu, L. High Quality CdSes Nanocrystals Synthesized By Facile Single injection Process and Their Electroluminescence. *Chem. Commun.* **2003**, 2964−2965.
(167) Bailey, R. E.; Nie, S. Alloyed Semiconductor Quantum Dots: Tuning the Optical Properties Without Changing the Particle Size. *J. Am. Chem. Soc.* **2003**, *125*, 7100−7106.
(168) Ueno, A.; Kakuta, N.; Park, K.; Finlayson, M.; Bard, A.; Campion, A.; Fox, M.; Webber, S.; White, J. Silica-Supported ZnS-CdS Mixed Semiconductor Catalysts for Photogeneration of Hydrogen. *J. Phys. Chem.* **1985**, *89*, 3828−3833.
(169) Youn, H. C.; Baral, S.; Fendler, J. H. Dihexadecyl Phosphate, Vesicle-Stabilized and in Situ Generated Mixed Cadmium Sulfide and Zinc Sulfide Semiconductor Particles: Preparation and Utilization for Photosensitized Charge Separation and Hydrogen Generation. *J. Phys. Chem.* **1988**, *92*, 6320−6327.
(170) Spanhel, L.; Haase, M.; Weller, H.; Henglein, A. Photochemistry of Colloidal Semiconductors 20. Surface Modification and Stability of Strong Luminescing CdS Particles. *J. Am. Chem. Soc.* **1987**, *109*, 5649−5655.
(171) Henglein, A.; Gutierrez, M.; Weller, K.; Fojtik, A.; Jirkovský, J. Photochemistry of Colloidal Semiconductors 30. Reactions and Fluorescence of AgI and AgI—Ag2S Colloids. *Ber. Bunsen. Phys. Chem.* **1989**, *93*, 593−600.
(172) Zhou, H.; Honma, I.; Komiyama, H.; Haus, J. W. Coated Semiconductor Nanoparticles; the Cadmium Sulfide/Lead Sulfide System's Synthesis and Properties. *J. Phys. Chem.* **1993**, *97*, 895−901.
(173) Hässelbarth, A.; Eychmüller, A.; Eichberger, R.; Giersig, M.; Mews, A.; Weller, H. Chemistry and Photophysics of Mixed Cadmium Sulfide/Mercury Sulfide Colloids. *J. Phys. Chem.* **1993**, *97*, 5333−5340.
(174) Eychmüller, A.; Mews, A.; Weller, H. A Quantum Dot Quantum Well: CdS/HgS/CdS. *Chem. Phys. Lett.* **1993**, *208*, 59−62.
(175) Mews, A.; Eychmüller, A.; Giersig, M.; Schooss, D.; Weller, H. Preparation, Characterization, and Photophysics of the Quantum Dot Quantum Well System Cadmium Sulfide/Mercury Sulfide/Cadmium Sulfide. *J. Phys. Chem.* **1994**, *98*, 934−941.
(176) Hoener, C. F.; Allan, K. A.; Bard, A. J.; Campion, A.; Fox, M. A.; Mallouk, T. E.; Webber, S. E.; White, J. M. Demonstration of a Shell-Core Structure in Layered Cadmium Selenide-Zinc Selenide Small Particles by X-Ray Photoelectron and Auger Spectroscopies. *J. Phys. Chem.* **1992**, *96*, 3812−3817.
(177) Hirai, T.; Shiojiri, S.; Komasawa, I. Preparation of Metal Sulfide Composite Ultrafine Particles in Reverse Micellar Systems and Their Photocatalytic Property. *J. Chem. Eng. Jpn.* **1994**, *27*, 590−597.
(178) Danek, M.; Jensen, K. F.; Murray, C. B.; Bawendi, M. G. Synthesis of Luminescent Thin-Film CdSe/ZnSe Quantum Dot Composites Using CdSe Quantum Dots Passivated with an Overlayer of ZnSe. *Chem. Mater.* **1996**, *8*, 173−180.
(179) Dabbousi, B. O.; Rodriguez-Viejo, J.; Mikulec, F. V.; Heine, J. R.; Mattoussi, H.; Ober, R.; Jensen, K. F.; Bawendi, M. G. (CdSe)ZnS Core-Shell Quantum Dots: Synthesis and Characterization of a Size Series of Highly Luminescent Nanocrystallites. *J. Phys. Chem. B* **1997**, *101*, 9463−9475.
(180) Peng, X.; Schlamp, M. C.; Kadavanich, A. V.; Alivisatos, A. P. Epitaxial Growth of Highly Luminescent CdSe/CdS Core/Shell Nanocrystals With Photostability and Electronic Accessibility. *J. Am. Chem. Soc.* **1997**, *119*, 7019−7029.
(181) Li, J. J.; Wang, Y. A.; Guo, W.; Keay, J. C.; Mishima, T. D.; Johnson, M. B.; Peng, X. Large-Scale Synthesis of Nearly Monodisperse CdSe/CdS Core/Shell Nanocrystals Using Air-Stable Reagents Via Successive Ion Layer Adsorption and Reaction. *J. Am. Chem. Soc.* **2003**, *125*, 12567−12575.
(182) Xie, R.; Zhong, X.; Basché, T. Synthesis, Characterization, and Spectroscopy of Type-II Core/Shell Semiconductor Nanocrystals With ZnTe Cores. *Adv. Mater.* **2005**, *17*, 2741−2745.
(183) Lincheneau, C.; Amelia, M.; Oszajca, M.; Boccia, A.; D'Orazi, F.; Madrigale, M.; Zanoni, R.; Mazzaro, R.; Ortolani, L.; Morandi, V. Synthesis and Properties of ZnTe and ZnTe/ZnS Core/Shell Semiconductor Nanocrystals. *J. Mater. Chem. C* **2014**, *2*, 2877−2886.
(184) Sahu, A.; Qi, L.; Kang, M. S.; Deng, D.; Norris, D. J. Facile Synthesis of Silver Chalcogenide (Ag2E; E= Se, S, Te) Semiconductor Nanocrystals. *J. Am. Chem. Soc.* **2011**, *133*, 6509−6512.
(185) Cao, Y.; Banin, U. Growth and Properties of Semiconductor Core/Shell Nanocrystals with InAs Cores. *J. Am. Chem. Soc.* **2000**, *122*, 9692−9702.

DOI: 10.1021/acs.chemrev.6b00169
Chem. Rev. 2016, 116, 10513−10622

(186) Cao, Y. W.; Banin, U. Synthesis and Characterization of InAs/InP and InAs/CdSe Core/Shell Nanocrystals. *Angew. Chem., Int. Ed.* **1999**, *38*, 3692−3694.
(187) Li, L.; Daou, T. J.; Texier, I.; Kim Chi, T. T.; Liem, N. Q.; Reiss, P. Highly Luminescent CuIns2/ZnS Core/Shell Nanocrystals: Cadmium-Free Quantum Dots For in Vivo Imaging. *Chem. Mater.* **2009**, *21*, 2422−2429.
(188) Xie, R.; Rutherford, M.; Peng, X. Formation of High-Quality I−III− VI Semiconductor Nanocrystals By Tuning Relative Reactivity of Cationic Precursors. *J. Am. Chem. Soc.* **2009**, *131*, 5691−5697.
(189) Talapin, D. V.; Mekis, I.; Götzinger, S.; Kornowski, A.; Benson, O.; Weller, H. CdSe/CdS/ZnS and CdSe/ZnSe/ZnS Core-Shell-Shell Nanocrystals. *J. Phys. Chem. B* **2004**, *108*, 18826−18831.
(190) Battaglia, D.; Blackman, B.; Peng, X. Coupled and Decoupled Dual Quantum Systems in One Semiconductor Nanocrystal. *J. Am. Chem. Soc.* **2005**, *127*, 10889−10897.
(191) Aharoni, A.; Mokari, T.; Popov, I.; Banin, U. Synthesis of InAs/CdSe/ZnSe Core/Shell1/Shell2 Structures With Bright and Stable Near-infrared Fluorescence. *J. Am. Chem. Soc.* **2006**, *128*, 257−264.
(192) Xie, R.; Kolb, U.; Li, J.; Basché, T.; Mews, A. Synthesis and Characterization of Highly Luminescent CdSe-Core CdS/Zn0.5Cd0.5S/ZnS Multishell Nanocrystals. *J. Am. Chem. Soc.* **2005**, *127*, 7480−7488.
(193) Kim, S.-W.; Zimmer, J. P.; Ohnishi, S.; Tracy, J. B.; Frangioni, J. V.; Bawendi, M. G. Engineering InAsXP1-X/InP/ZnSe III-V Alloyed Core/Shell Quantum Dots for the Near-Infrared. *J. Am. Chem. Soc.* **2005**, *127*, 10526−10532.
(194) Bae, W. K.; Char, K.; Hur, H.; Lee, S. Single-Step Synthesis of Quantum Dots with Chemical Composition Gradients. *Chem. Mater.* **2008**, *20*, 531−539.
(195) Li, H.; Zanella, M.; Genovese, A.; Povia, M.; Falqui, A.; Giannini, C.; Manna, L. Sequential Cation Exchange in Nanocrystals: Preservation of Crystal Phase and Formation of Metastable Phases. *Nano Lett.* **2011**, *11*, 4964−4970.
(196) Son, D. H.; Hughes, S. M.; Yin, Y.; Alivisatos, A. P. Cation Exchange Reactions in Ionic Nanocrystals. *Science* **2004**, *306*, 1009−1012.
(197) Zhang, J.; Gao, J.; Church, C. P.; Miller, E. M.; Luther, J. M.; Klimov, V. I.; Beard, M. C. PbSe Quantum Dot Solar Cells With More Than 6% Efficiency Fabricated in Ambient Atmosphere. *Nano Lett.* **2014**, *14*, 6010−6015.
(198) Kim, S.; Marshall, A. R.; Kroupa, D. M.; Miller, E. M.; Luther, J. M.; Jeong, S.; Beard, M. C. Air-Stable and Efficient PbSe Quantum-Dot Solar Cells Based Upon ZnSe to PbSe Cation-Exchanged Quantum Dots. *ACS Nano* **2015**, *9*, 8157−8164.
(199) Smith, A. M.; Nie, S. Bright and Compact Alloyed Quantum Dots with Broadly Tunable Near-Infrared Absorption and Fluorescence Spectra Through Mercury Cation Exchange. *J. Am. Chem. Soc.* **2011**, *133*, 24−26.
(200) Robinson, R. D.; Sadtler, B.; Demchenko, D. O.; Erdonmez, C. K.; Wang, L.-W.; Alivisatos, A. P. Spontaneous Superlattice Formation in Nanorods Through Partial Cation Exchange. *Science* **2007**, *317*, 355−358.
(201) Sadtler, B.; Demchenko, D. O.; Zheng, H.; Hughes, S. M.; Merkle, M. G.; Dahmen, U.; Wang, L.-W.; Alivisatos, A. P. Selective Facet Reactivity During Cation Exchange in Cadmium Sulfide Nanorods. *J. Am. Chem. Soc.* **2009**, *131*, 5285−5293.
(202) Luther, J. M.; Zheng, H.; Sadtler, B.; Alivisatos, A. P. Synthesis of PbS Nanorods and Other Ionic Nanocrystals of Complex Morphology By Sequential Cation Exchange Reactions. *J. Am. Chem. Soc.* **2009**, *131*, 16851−16857.
(203) Miszta, K.; Dorfs, D.; Genovese, A.; Kim, M. R.; Manna, L. Cation Exchange Reactions in Colloidal Branched Nanocrystals. *ACS Nano* **2011**, *5*, 7176−7183.
(204) Zhang, J.; Chernomordik, B. D.; Crisp, R. W.; Kroupa, D. M.; Luther, J. M.; Miller, E. M.; Gao, J.; Beard, M. C. Preparation of Cd/Pb Chalcogenide Heterostructured Janus Particles Via Controllable Cation Exchange. *ACS Nano* **2015**, *9*, 7151−7163.
(205) Lee, D.; Kim, W. D.; Lee, S.; Bae, W. K.; Lee, S.; Lee, D. C. Direct Cd-To-Pb Exchange of CdSe Nanorods into PbSe/CdSe Axial Heterojunction Nanorods. *Chem. Mater.* **2015**, *27*, 5295−5304.
(206) Park, J.; Kim, S.-W. CuIns2/Zns Core/Shell Quantum Dots by Cation Exchange and Their Blue-Shifted Photoluminescence. *J. Mater. Chem.* **2011**, *21*, 3745−3750.
(207) Mcdaniel, H.; Fuke, N.; Makarov, N. S.; Pietryga, J. M.; Klimov, V. I. An Integrated Approach to Realizing High-Performance Liquid-Junction Quantum Dot Sensitized Solar Cells. *Nat. Commun.* **2013**, *4*, 2887.
(208) Mcdaniel, H.; Koposov, A. Y.; Draguta, S.; Makarov, N. S.; Pietryga, J. M.; Klimov, V. I. Simple Yet Versatile Synthesis of CuInseXS2−X Quantum Dots for Sunlight Harvesting. *J. Phys. Chem. C* **2014**, *118*, 16987−16994.
(209) Pietryga, J. M.; Werder, D. J.; Williams, D. J.; Casson, J. L.; Schaller, R. D.; Klimov, V. I.; Hollingsworth, J. A. Utilizing the Lability of Lead Selenide to Produce Heterostructured Nanocrystals with Bright, Stable Infrared Emission. *J. Am. Chem. Soc.* **2008**, *130*, 4879−4885.
(210) Lambert, K.; Geyter, B. D.; Moreels, I.; Hens, Z. PbTe|CdTe Core|Shell Particles By Cation Exchange, a HR-TEM Study. *Chem. Mater.* **2009**, *21*, 778−780.
(211) Lin, Q.; Makarov, N. S.; Koh, W.-K.; Velizhanin, K. A.; Cirloganu, C. M.; Luo, H.; Klimov, V. I.; Pietryga, J. M. Design and Synthesis of Heterostructured Quantum Dots with Dual Emission in the Visible and Infrared. *ACS Nano* **2015**, *9*, 539−547.
(212) Grodzińska, D.; Pietra, F.; Van Huis, M. A.; Vanmaekelbergh, D.; De Mello Donegá, C. Thermally induced Atomic Reconstruction of PbSe/CdSe Core/Shell Quantum Dots into PbSe/CdSe Bi-Hemisphere Hetero-Nanocrystals. *J. Mater. Chem.* **2011**, *21*, 11556−11565.
(213) Casavola, M.; Van Huis, M. A.; Bals, S.; Lambert, K.; Hens, Z.; Vanmaekelbergh, D. Anisotropic Cation Exchange in PbSe/CdSe Core/Shell Nanocrystals of Different Geometry. *Chem. Mater.* **2012**, *24*, 294−302.
(214) Lee, D. C.; Robel, I. N.; Pietryga, J. M.; Klimov, V. I. Infrared-Active Heterostructured Nanocrystals with Ultralong Carrier Lifetimes. *J. Am. Chem. Soc.* **2010**, *132*, 9960−9962.
(215) Saruyama, M.; So, Y.-G.; Kimoto, K.; Taguchi, S.; Kanemitsu, Y.; Teranishi, T. Spontaneous Formation of Wurzite-CdS/Zinc Blende-CdTe Heterodimers Through a Partial Anion Exchange Reaction. *J. Am. Chem. Soc.* **2011**, *133*, 17598−17601.
(216) Akkerman, Q. A.; D'innocenzo, V.; Accornero, S.; Scarpellini, A.; Petrozza, A.; Prato, M.; Manna, L. Tuning the Optical Properties of Cesium Lead Halide Perovskite Nanocrystals by Anion Exchange Reactions. *J. Am. Chem. Soc.* **2015**, *137*, 10276−10281.
(217) Nedelcu, G.; Protesescu, L.; Yakunin, S.; Bodnarchuk, M. I.; Grotevent, M. J.; Kovalenko, M. V. Fast Anion-Exchange in Highly Luminescent Nanocrystals of Cesium Lead Halide Perovskites (CsPbX3, X= Cl, Br, I). *Nano Lett.* **2015**, *15*, 5635−5640.
(218) García-Santamaría, F.; Brovelli, S.; Viswanatha, R.; Hollingsworth, J. A.; Htoon, H.; Crooker, S. A.; Klimov, V. I. Breakdown of Volume Scaling in Auger Recombination in CdSe/CdS Heteronanocrystals: The Role of the Core−Shell Interface. *Nano Lett.* **2011**, *11*, 687−693.
(219) Mahler, B.; Spinicelli, P.; Buil, S.; Quelin, X.; Hermier, J.-P.; Dubertret, B. Towards Non-Blinking Colloidal Quantum Dots. *Nat. Mater.* **2008**, *7*, 659−664.
(220) Weller, H.; Koch, U.; Gutierrez, M.; Henglein, A. Photochemistry of Colloidal Metal Sulfides 7. Absorption and Fluorescence of Extremely Small ZnS Particles (the World of the Neglected Dimensions). *Ber. Bunsen. Phys. Chem.* **1984**, *88*, 649−656.
(221) Spanhel, L.; Weller, H.; Fojtik, A.; Henglein, A. Photochemistry of Semiconductor Colloids 17. Strong Luminescing CdS and CdS-Ag2S Particles. *Ber. Bunsen. Phys. Chem.* **1987**, *91*, 88−94.
(222) Schooss, D.; Mews, A.; Eychmüller, A.; Weller, H. Quantum-Dot Quantum Well CdS/HgS/CdS: Theory and Experiment. *Phys. Rev. B: Condens. Matter Mater. Phys.* **1994**, *49*, 17072−17078.
(223) Chin, P. T.; De Mello Donegá, C.; Van Bavel, S. S.; Meskers, S. C.; Sommerdijk, N. A.; Janssen, R. A. Highly Luminescent CdTe/CdSe

DOI: 10.1021/acs.chemrev.6b00169
Chem. Rev. 2016, 116, 10513−10622

Colloidal Heteronanocrystals With Temperature-Dependent Emission Color. *J. Am. Chem. Soc.* **2007**, *129*, 14880−14886.
(224) Zhang, W.; Chen, G.; Wang, J.; Ye, B.-C.; Zhong, X. Design and Synthesis of Highly Luminescent Near-infrared-Emitting Water-Soluble CdTe/CdSe/ZnS Core/Shell/Shell Quantum Dots. *Inorg. Chem.* **2009**, *48*, 9723−9731.
(225) Oron, D.; Kazes, M.; Banin, U. Multiexcitons in Type-II Colloidal Semiconductor Quantum Dots. *Phys. Rev. B: Condens. Matter Mater. Phys.* **2007**, *75*, 035330−035337.
(226) Piryatinski, A.; Ivanov, S. A.; Tretiak, S.; Klimov, V. I. Effect of Quantum and Dielectric Confinement On the Exciton-Exciton interaction Energy in Type-II Core/Shell Semiconductor Nanocrystals. *Nano Lett.* **2007**, *7*, 108−115.
(227) Blackman, B.; Battaglia, D. M.; Mishima, T. D.; Johnson, M. B.; Peng, X. Control of the Morphology of Complex Semiconductor Nanocrystals With a Type II Heterojunction, Dots Vs Peanuts, By Thermal Cycling. *Chem. Mater.* **2007**, *19*, 3815−3821.
(228) Cheng, C.-T.; Chen, C.-Y.; Lai, C.-W.; Liu, W.-H.; Pu, S.-C.; Chou, P.-T.; Chou, Y.-H.; Chiu, H.-T. Syntheses and Photophysical Properties of Type-II CdSe/ZnTe/ZnS (Core/Shell/Shell) Quantum Dots. *J. Mater. Chem.* **2005**, *15*, 3409−3414.
(229) Nanda, J.; Ivanov, S. A.; Achermann, M.; Bezel, I.; Piryatinski, A.; Klimov, V. I. Light Amplification in the Single-Exciton Regime Using Exciton-Exciton Repulsion in Type-II Nanocrystal Quantum Dots. *J. Phys. Chem. C* **2007**, *111*, 15382−15390.
(230) Ivanov, S. A.; Piryatinski, A.; Nanda, J.; Tretiak, S.; Zavadil, K. R.; Wallace, W. O.; Werder, D.; Klimov, V. I. Type-II Core/Shell CdS/ZnSe Nanocrystals: Synthesis, Electronic Structures, and Spectroscopic Properties. *J. Am. Chem. Soc.* **2007**, *129*, 11708−11719.
(231) Nemchinov, A.; Kirsanova, M.; Hewa-Kasakarage, N. N.; Zamkov, M. Synthesis and Characterization of Type II ZnSe/CdS Core/Shell Nanocrystals. *J. Phys. Chem. C* **2008**, *112*, 9301−9307.
(232) Bang, J.; Park, J.; Lee, J. H.; Won, N.; Nam, J.; Lim, J.; Chang, B. Y.; Lee, H. J.; Chon, B.; Shin, J. ZnTe/ZnSe (Core/Shell) Type-II Quantum Dots: Their Optical and Photovoltaic Properties. *Chem. Mater.* **2010**, *22*, 233−240.
(233) Dennis, A. M.; Mangum, B. D.; Piryatinski, A.; Park, Y.-S.; Hannah, D. C.; Casson, J. L.; Williams, D. J.; Schaller, R. D.; Htoon, H.; Hollingsworth, J. A. Suppressed Blinking and Auger Recombination in Near-Infrared Type-II InP/CdS Nanocrystal Quantum Dots. *Nano Lett.* **2012**, *12*, 5545−5551.
(234) Blackman, B.; Battaglia, D.; Peng, X. Bright and Water-Soluble Near IR-Emitting CdSe/CdTe/ZnSe Type-II/Type-I Nanocrystals, Tuning the Efficiency and Stability by Growth. *Chem. Mater.* **2008**, *20*, 4847−4853.
(235) Wang, J.; Mora-Seró, I.; Pan, Z.; Zhao, K.; Zhang, H.; Feng, Y.; Yang, G.; Zhong, X.; Bisquert, J. Core/Shell Colloidal Quantum Dot Exciplex States for the Development of Highly Efficient Quantum-Dot-Sensitized Solar Cells. *J. Am. Chem. Soc.* **2013**, *135*, 15913−15922.
(236) Zhu, H.; Song, N.; Lian, T. Wave Function Engineering for Ultrafast Charge Separation and Slow Charge Recombination in Type II Core/Shell Quantum Dots. *J. Am. Chem. Soc.* **2011**, *133*, 8762−8771.
(237) Chen, C. Y.; Cheng, C. T.; Lai, C. W.; Hu, Y. H.; Chou, P. T.; Chou, Y. H.; Chiu, H. T. Type-II CdSe/CdTe/ZnTe (Core−Shell−Shell) Quantum Dots With Cascade Band Edges: the Separation of Electron (at CdSe) and Hole (at ZnTe) by the CdTe Layer. *Small* **2005**, *1*, 1215−1220.
(238) De Geyter, B.; Justo, Y.; Moreels, I.; Lambert, K.; Smet, P. F.; Van Thourhout, D.; Houtepen, A. J.; Grodzinska, D.; De Mello Donega, C.; Meijerink, A. The Different Nature of Band Edge Absorption and Emission in Colloidal PbSe/CdSe Core/Shell Quantum Dots. *ACS Nano* **2011**, *5*, 58−66.
(239) Wu, K.; Song, N.; Liu, Z.; Zhu, H.; Rodríguez-Córdoba, W.; Lian, T. Interfacial Charge Separation and Recombination in InP and Quasi-Type II InP/CdS Core/Shell Quantum Dot-Molecular Acceptor Complexes. *J. Phys. Chem. A* **2013**, *117*, 7561−7570.
(240) Nanda, J.; Ivanov, S.; Htoon, H.; Bezel, I.; Piryatinski, A.; Tretiak, S.; Klimov, V. Absorption Cross Sections and Auger Recombination Lifetimes in Inverted Core-Shell Nanocrystals: Implications for Lasing Performance. *J. Appl. Phys.* **2006**, *99*, 034309.
(241) Kim, S.; Kim, T.; Kang, M.; Kwak, S. K.; Yoo, T. W.; Park, L. S.; Yang, I.; Hwang, S.; Lee, J. E.; Kim, S. K. Highly Luminescent InP/GaP/ZnS Nanocrystals and Their Application to White Light-Emitting Diodes. *J. Am. Chem. Soc.* **2012**, *134*, 3804−3809.
(242) Panda, S. K.; Hickey, S. G.; Waurisch, C.; Eychmüller, A. Gradated Alloyed CdZnSe Nanocrystals With High Luminescence Quantum Yields and Stability for Optoelectronic and Biological Applications. *J. Mater. Chem.* **2011**, *21*, 11550−11555.
(243) Bae, W. K.; Nam, M. K.; Char, K.; Lee, S. Gram-Scale One-Pot Synthesis of Highly Luminescent Blue Emitting Cd1−XZnXS/ZnS Nanocrystals. *Chem. Mater.* **2008**, *20*, 5307−5313.
(244) Chen, Y.; Vela, J.; Htoon, H.; Casson, J. L.; Werder, D. J.; Bussian, D. A.; Klimov, V. I.; Hollingsworth, J. A. Giant" Multishell CdSe Nanocrystal Quantum Dots With Suppressed Blinking. *J. Am. Chem. Soc.* **2008**, *130*, 5026−5027.
(245) Cragg, G. E.; Efros, A. L. Suppression of Auger Processes in Confined Structures. *Nano Lett.* **2010**, *10*, 313−317.
(246) Lim, J.; Bae, W. K.; Lee, D.; Nam, M. K.; Jung, J.; Lee, C.; Char, K.; Lee, S. InP@ZnSeS, Core Composition Gradient Shell Quantum Dots with Enhanced Stability. *Chem. Mater.* **2011**, *23*, 4459−4463.
(247) Smith, A. M.; Mohs, A. M.; Nie, S. Tuning the Optical and Electronic Properties of Colloidal Nanocrystals by Lattice Strain. *Nat. Nanotechnol.* **2009**, *4*, 56−63.
(248) Maiti, S.; Debnath, T.; Maity, P.; Ghosh, H. N. Lattice-Strain-Induced Slow Electron Cooling Due To Quasi-Type-II Behavior in Type-I CdTe/ZnS Nanocrystals. *J. Phys. Chem. C* **2015**, *119*, 8410−8416.
(249) *CRC Handbook of Chemistry and Physics*, 96th (Internet Version 2015) ed.; Haynes, W. M., Ed.; CRC Press/Taylor and Francis: Boca Raton, FL.
(250) Cho, K.-S.; Talapin, D. V.; Gaschler, W.; Murray, C. B. Designing PbSe Nanowires and Nanorings Through Oriented Attachment of Nanoparticles. *J. Am. Chem. Soc.* **2005**, *127*, 7140−7147.
(251) Koh, W.-K.; Bartnik, A. C.; Wise, F. W.; Murray, C. B. Synthesis of Monodisperse PbSe Nanorods: A Case For Oriented Attachment. *J. Am. Chem. Soc.* **2010**, *132*, 3909−3913.
(252) Schliehe, C.; Juarez, B. H.; Pelletier, M.; Jander, S.; Greshnykh, D.; Nagel, M.; Meyer, A.; Foerster, S.; Kornowski, A.; Klinke, C.; et al. Ultrathin PbS Sheets by Two-Dimensional Oriented Attachment. *Science* **2010**, *329*, 550−553.
(253) Erwin, S. C.; Zu, L. J.; Haftel, M. I.; Efros, A. L.; Kennedy, T. A.; Norris, D. J. Doping Semiconductor Nanocrystals. *Nature* **2005**, *436*, 91−94.
(254) Norris, D. J.; Efros, A. L.; Erwin, S. C. Doped Nanocrystals. *Science* **2008**, *319*, 1776−1779.
(255) Buck, M. R.; Bondi, J. F.; Schaak, R. E. A Total-Synthesis Framework for the Construction of High-Order Colloidal Hybrid Nanoparticles. *Nat. Chem.* **2011**, *4*, 37−44.
(256) Khanal, B. P.; Pandey, A.; Li, L.; Lin, Q.; Bae, W. K.; Luo, H.; Klimov, V. I.; Pietryga, J. M. Generalized Synthesis of Hybrid Metal−Semiconductor Nanostructures Tunable from the Visible to the Infrared. *ACS Nano* **2012**, *6*, 3832−3840.
(257) Beattie, A.; Landsberg, P. Auger Effect in Semiconductors. *Proc. R. Soc. London, Ser. A* **1959**, *249*, 16−29.
(258) Chepic, D. I.; Efros, A. L.; Ekimov, A. I.; Vanov, M. G.; Kharchenko, V. A.; Kudriavtsev, I. A.; Yazeva, T. V. Auger Ionization of Semiconductor Quantum Drops in a Glass Matrix. *J. Lumin.* **1990**, *47*, 113−127.
(259) Wang, L.-W.; Califano, M.; Zunger, A.; Franceschetti, A. Pseudopotential Theory of Auger Processes in CdSe Quantum Dots. *Phys. Rev. Lett.* **2003**, *91*, 056404.
(260) Pietryga, J. M.; Zhuravlev, K. K.; Whitehead, M.; Klimov, V. I.; Schaller, R. D. Evidence for Barrierless Auger Recombination in PbSe Nanocrystals: A Pressure-Dependent Study of Transient Optical Absorption. *Phys. Rev. Lett.* **2008**, *101*, 217401.
(261) Park, Y.-S.; Bae, W. K.; Baker, T.; Lim, J.; Klimov, V. I. Effect of Auger Recombination on Lasing in Heterostructured Quantum Dots

DOI: 10.1021/acs.chemrev.6b00169
Chem. Rev. 2016, 116, 10513−10622

with Engineered Core/Shell interfaces. *Nano Lett.* **2015**, *15*, 7319−7328.
(262) Klimov, V. I.; Mikhailovsky, A. A.; Xu, S.; Malko, A.; Hollingsworth, J. A.; Leatherdale, C. A.; Eisler, H.-J.; Bawendi, M. G. Optical Gain and Stimulated Emission in Nanocrystal Quantum Dots. *Science* **2000**, *290*, 314−317.
(263) Lee, J.; Sundar, V. C.; Heine, J. R.; Bawendi, M. G.; Jensen, K. F. Full Color Emission from II−VI Semiconductor Quantum Dot−Polymer Composites. *Adv. Mater.* **2000**, *12*, 1102−1105.
(264) Mcguire, J. A.; Sykora, M.; Joo, J.; Pietryga, J. M.; Klimov, V. I. Apparent Versus True Carrier Multiplication Yields in Semiconductor Nanocrystals. *Nano Lett.* **2010**, *10*, 2049−2057.
(265) Klimov, V. I. Multicarrier interactions in Semiconductor Nanocrystals in Relation to the Phenomena of Auger Recombination and Carrier Multiplication. *Annu. Rev. Condens. Matter Phys.* **2014**, *5*, 285−316.
(266) Park, Y.-S.; Bae, W. K.; Pietryga, J. M.; Klimov, V. I. Auger Recombination of Biexcitons and Negative and Positive Trions in Individual Quantum Dots. *ACS Nano* **2014**, *8*, 7288−7296.
(267) Koh, W.-K.; Koposov, A. Y.; Stewart, J. T.; Pal, B. N.; Robel, I.; Pietryga, J. M.; Klimov, V. I. Heavily Doped n-Type PbSe and PbS Nanocrystals Using Ground-State Charge Transfer From Cobaltocene. *Sci. Rep.* **2013**, *3*, 2004 DOI: 10.1038/srep02004.
(268) Klimov, V. I.; Mcguire, J. A.; Schaller, R. D.; Rupasov, V. I. Scaling of Multiexciton Lifetimes in Semiconductor Nanocrystals. *Phys. Rev. B: Condens. Matter Mater. Phys.* **2008**, *77*, 195324.
(269) Schaller, R. D.; Petruska, M. A.; Klimov, V. I. Tunable Near-infrared Optical Gain and Amplified Spontaneous Emission Using PbSe Nanocrystals. *J. Phys. Chem. B* **2003**, *107*, 13765−13768.
(270) Jha, P. P.; Guyot-Sionnest, P. Trion Decay in Colloidal Quantum Dots. *ACS Nano* **2009**, *3*, 1011−1015.
(271) Cohn, A. W.; Rinehart, J. D.; Schimpf, A. M.; Weaver, A. L.; Gamelin, D. R. Size Dependence of Negative Trion Auger Recombination in Photodoped CdSe Nanocrystals. *Nano Lett.* **2014**, *14*, 353−358.
(272) Achermann, M.; Hollingsworth, J. A.; Klimov, V. I. Multiexcitons Confined within a Subexcitonic Volume: Spectroscopic and Dynamical Signatures of Neutral and Charged Biexcitons in Ultrasmall Semiconductor Nanocrystals. *Phys. Rev. B: Condens. Matter Mater. Phys.* **2003**, *68*, 245302−245301−245305.
(273) Fidler, A. F.; Makarov, N. S.; Robel, I.; Klimov, V. I. Size-Dependence of Multi-Carrier Auger Recombination in CdSe Nanocrystals. Submitted.
(274) Robel, I.; Gresback, R.; Kortshagen, U.; Schaller, R. D.; Klimov, V. I. Universal Size-Dependent Trend in Auger Recombination in Direct-Gap and indirect-Gap Semiconductor Nanocrystals. *Phys. Rev. Lett.* **2009**, *102*, 177404.
(275) Stewart, J. T.; Padilha, L. A.; Bae, W. K.; Koh, W.-K.; Pietryga, J. M.; Klimov, V. I. Carrier Multiplication in Quantum Dots Within the Framework of Two Competing Energy Relaxation Mechanisms. *J. Phys. Chem. Lett.* **2013**, *4*, 2061−2068.
(276) Galland, C.; Ghosh, Y.; Steinbruck, A.; Sykora, M.; Hollingsworth, J. A.; Klimov, V. I.; Htoon, H. Two Types of Luminescence Blinking Revealed By Spectroelectrochemistry of Single Quantum Dots. *Nature* **2011**, *479*, 203−207.
(277) Rabouw, F. T.; Lunnemann, P.; Van Dijk-Moes, R. J. A.; Frimmer, M.; Pietra, F.; Koenderink, A. F.; Vanmaekelbergh, D. Reduced Auger Recombination in Single CdSe/CdS Nanorods By One-Dimensional Electron Delocalization. *Nano Lett.* **2013**, *13*, 4884−4892.
(278) Zavelani-Rossi, M.; Lupo, M. G.; Tassone, F.; Manna, L.; Lanzani, G. Suppression of Biexciton Auger Recombination in CdSe/CdS Dot/Rods: Role of the Electronic Structure in the Carrier Dynamics. *Nano Lett.* **2010**, *10*, 3142−3150.
(279) Sitt, A.; Sala, F. D.; Menagen, G.; Banin, U. Multiexciton Engineering in Seeded Core/Shell Nanorods: Transfer From Type-I To Quasi-Type-II Regimes. *Nano Lett.* **2009**, *9*, 3470−3476.
(280) Qin, W.; Liu, H.; Guyot-Sionnest, P. Small Bright Charged Colloidal Quantum Dots. *ACS Nano* **2014**, *8*, 283−291.
(281) Climente, J. I.; Movilla, J. L.; Planelles, J. Auger Recombination Suppression in Nanocrystals With Asymmetric Electron−Hole Confinement. *Small* **2012**, *8*, 754−759.
(282) Park, Y. S.; Malko, A. V.; Vela, J.; Chen, Y.; Ghosh, Y.; García-Santamaría, F.; Hollingsworth, J. A.; Klimov, V. I.; Htoon, H. Near-Unity Quantum Yields of Biexciton Emission from CdSe/CdS Nanocrystals Measured Using Single-Particle Spectroscopy. *Phys. Rev. Lett.* **2011**, *106*, 187401.
(283) Nair, G.; Zhao, J.; Bawendi, M. G. Biexciton Quantum Yield of Single Semiconductor Nanocrystals From Photon Statistics. *Nano Lett.* **2011**, *11*, 1136−1140.
(284) Park, Y.-S.; Bae, W. K.; Padilha, L. A.; Pietryga, J. M.; Klimov, V. I. Effect of the Core/Shell Interface on Auger Recombination Evaluated By Single-Quantum-Dot Spectroscopy. *Nano Lett.* **2014**, *14*, 396.
(285) Bae, W. K.; Park, Y.-S.; Lim, J.; Lee, D.; Padilha, L. A.; McDaniel, H.; Robel, I.; Lee, C.; Pietryga, J. M.; Klimov, V. I. Controlling the Influence of Auger Recombination on the Performance of Quantum-Dot Light-Emitting Diodes. *Nat. Commun.* **2013**, *4*, 3661.
(286) Basche, T.; Kummer, S.; Brauchle, C. Direct Spectroscopic Observation of Quantum Jumps of a Single Molecule. *Nature* **1995**, *373*, 132−134.
(287) Bout, D. A. V.; Yip, W.-T.; Hu, D.; Fu, D.-K.; Swager, T. M.; Barbara, P. F. Discrete Intensity Jumps and Intramolecular Electronic Energy Transfer in the Spectroscopy of Single Conjugated Polymer Molecules. *Science* **1997**, *277*, 1074−1077.
(288) Dickson, R. M.; Cubitt, A. B.; Tsien, R. Y.; Moerner, W. E. On/Off Blinking and Switching Behaviour of Single Molecules of Green Fluorescent Protein. *Nature* **1997**, *388*, 355−358.
(289) Hoogenboom, J. P.; Van Dijk, E. M. H. P.; Hernando, J.; Van Hulst, N. F.; García-Parajó, M. F. Power-Law-Distributed Dark States Are the Main Pathway for Photobleaching of Single Organic Molecules. *Phys. Rev. Lett.* **2005**, *95*, 097401.
(290) Yeow, E. K. L.; Melnikov, S. M.; Bell, T. D. M.; De Schryver, F. C.; Hofkens, J. Characterizing the Fluorescence intermittency and Photobleaching Kinetics of Dye Molecules Immobilized On A Glass Surface. *J. Phys. Chem. A* **2006**, *110*, 1726−1734.
(291) Htoon, H.; O'Connell, M. J.; Cox, P. J.; Doorn, S. K.; Klimov, V. I. Low Temperature Emission Spectra of Individual Single-Walled Carbon Nanotubes: Multiplicity of Subspecies within Single-Species Nanotube Ensembles. *Phys. Rev. Lett.* **2004**, *93*, 027401.
(292) Cognet, L.; Tsyboulski, D. A.; Rocha, J.-D. R.; Doyle, C. D.; Tour, J. M.; Weisman, R. B. Stepwise Quenching of Exciton Fluorescence in Carbon Nanotubes by Single-Molecule Reactions. *Science* **2007**, *316*, 1465−1468.
(293) Wang, S.; Querner, C.; Emmons, T.; Drndic, M.; Crouch, C. H. Fluorescence Blinking Statistics from CdSe Core and Core/Shell Nanorods. *J. Phys. Chem. B* **2006**, *110*, 23221−23227.
(294) Wang, S.; Querner, C.; Fischbein, M. D.; Willis, L.; Novikov, D. S.; Crouch, C. H.; Drndic, M. Blinking Statistics Correlated With Nanoparticle Number. *Nano Lett.* **2008**, *8*, 4020−4026.
(295) Glennon, J. J.; Tang, R.; Buhro, W. E.; Loomis, R. A. Synchronous Photoluminescence intermittency (Blinking) Along Whole Semiconductor Quantum Wires. *Nano Lett.* **2007**, *7*, 3290−3295.
(296) Efros, A. L.; Rosen, M. Random Telegraph Signal in the Photoluminescence intensity of A Single Quantum Dot. *Phys. Rev. Lett.* **1997**, *78*, 1110−1113.
(297) Kuno, M.; Fromm, D. P.; Hamann, H. F.; Gallagher, A.; Nesbitt, D. J. "On"/"Off" Fluorescence Intermittency of Single Semiconductor Quantum Dots. *J. Chem. Phys.* **2001**, *115*, 1028−1040.
(298) Cichos, F.; Von Borczyskowski, C.; Orrit, M. Power-Law intermittency of Single Emitters. *Curr. Opin. Colloid Interface Sci.* **2007**, *12*, 272−284.
(299) Gomez, D. E.; Califano, M.; Mulvaney, P. Optical Properties of Single Semiconductor Nanocrystals. *Phys. Chem. Chem. Phys.* **2006**, *8*, 4989−5011.
(300) Banin, U.; Bruchez, M.; Alivisatos, A. P.; Ha, T.; Weiss, S.; Chemla, D. S. Evidence for a Thermal Contribution to Emission Intermittency in Single CdSe/CdS Core/Shell Nanocrystals. *J. Chem. Phys.* **1999**, *110*, 1195−1201.

DOI: 10.1021/acs.chemrev.6b00169
Chem. Rev. 2016, 116, 10513−10622

(301) Shimizu, K. T.; Neuhauser, R. G.; Leatherdale, C. A.; Empedocles, S. A.; Woo, W. K.; Bawendi, M. G. Blinking Statistics in Single Semiconductor Nanocrystal Quantum Dots. *Phys. Rev. B: Condens. Matter Mater. Phys.* **2001**, *63*, 205316.
(302) Stefani, F. D.; Knoll, W.; Kreiter, M.; Zhong, X.; Han, M. Y. Quantification of Photoinduced and Spontaneous Quantum-Dot Luminescence Blinking. *Phys. Rev. B: Condens. Matter Mater. Phys.* **2005**, *72*, 125304.
(303) Knappenberger, K. L.; Wong, D. B.; Romanyuk, Y. E.; Leone, S. R. Excitation Wavelength Dependence of Fluorescence Intermittency in CdSe/ZnS Core/Shell Quantum Dots. *Nano Lett.* **2007**, *7*, 3869−3874.
(304) Peterson, J. J.; Nesbitt, D. J. Modified Power Law Behavior in Quantum Dot Blinking: A Novel Role for Biexcitons and Auger Ionization. *Nano Lett.* **2009**, *9*, 338−345.
(305) Tang, J.; Marcus, R. A. Diffusion-Controlled Electron Transfer Processes and Power-Law Statistics of Fluorescence Intermittency of Nanoparticles. *Phys. Rev. Lett.* **2005**, *95*, 107401.
(306) Verberk, R.; Van Oijen, A. M.; Orrit, M. Simple Model for the Power-Law Blinking of Single Semiconductor Nanocrystals. *Phys. Rev. B: Condens. Matter Mater. Phys.* **2002**, *66*, 233202.
(307) Margolin, G.; Protasenko, V.; Kuno, M.; Barkai, E. Power-Law Blinking Quantum Dots: Stochastic and Physical Models. *Adv. Chem. Phys.* **2005**, *133*, 327−356.
(308) Zhao, J.; Nair, G.; Fisher, B. R.; Bawendi, M. G. Challenge to the Charging Model of Semiconductor-Nanocrystal Fluorescence Intermittency from Off-State Quantum Yields and Multiexciton Blinking. *Phys. Rev. Lett.* **2010**, *104*, 157403.
(309) Rosen, S.; Schwartz, O.; Oron, D. Transient Fluorescence of the Off State in Blinking CdSe/Cds/Zns Semiconductor Nanocrystals Is Not Governed By Auger Recombination. *Phys. Rev. Lett.* **2010**, *104*, 157404.
(310) Frantsuzov, P. A.; Marcus, R. A. Explanation of Quantum Dot Blinking without the Long-Lived Trap Hypothesis. *Phys. Rev. B: Condens. Matter Mater. Phys.* **2005**, *72*, 155321.
(311) Hohng, S.; Ha, T. Near-Complete Suppression of Quantum Dot Blinking in Ambient Conditions. *J. Am. Chem. Soc.* **2004**, *126*, 1324−1325.
(312) He, H.; Qian, H.; Dong, C.; Wang, K.; Ren, J. Single Nonblinking CdTe Quantum Dots Synthesized in Aqueous Thiopropionic Acid. *Angew. Chem., Int. Ed.* **2006**, *45*, 7588−7591.
(313) Hammer, N. I.; Early, K. T.; Sill, K.; Odoi, M. Y.; Emrick, T.; Barnes, M. D. Coverage-Mediated Suppression of Blinking in Solid State Quantum Dot Conjugated Organic Composite Nanostructures. *J. Phys. Chem. B* **2006**, *110*, 14167−14171.
(314) Kundu, J.; Ghosh, Y.; Dennis, A. M.; Htoon, H.; Hollingsworth, J. A. Giant Nanocrystal Quantum Dots: Stable Down-Conversion Phosphors that Exploit a Large Stokes Shift and Efficient Shell-To-Core Energy Relaxation. *Nano Lett.* **2012**, *12*, 3031−3037.
(315) Shirasaki, Y.; Supran, G. J.; Bawendi, M. G.; Bulovic, V. Emergence of Colloidal Quantum-Dot Light-Emitting Technologies. *Nat. Photonics* **2013**, *7*, 13−23.
(316) Takahashi, D. Samsung Unveils New Lineup of SUHD TVs With Quantum Dot Displays. http://Venturebeat.Com/2016/01/05/Samsung-Unveils-New-Line-Up-Of-SUHD-TVs-With-Quantum-Dot-Displays (accessed March 3, 2016).
(317) Kwak, J.; Bae, W. K.; Lee, D.; Park, I.; Lim, J.; Park, M.; Cho, H.; Woo, H.; Yoon, D. Y.; Char, K.; et al. Bright and Efficieny Full-Color Colloidal Quantum Dot Light-Emitting Diodes Using An inverted Device Structure. *Nano Lett.* **2012**, *12*, 2362−2366.
(318) Dai, X.; Zhang, Z.; Jin, Y.; Niu, Y.; Cao, H.; Liang, X.; Chen, L.; Wang, J.; Peng, X. Solution-Processed, High-Performance Light-Emitting Diodes Based On Quantum Dots. *Nature* **2014**, *515*, 96−99.
(319) Yang, Y.; Zheng, Y.; Cao, W.; Titov, A.; Hyvonen, J.; Mandersjesse, R.; Xue, J.; Holloway, P. H.; Qian, L. High-Efficiency Light-Emitting Devices Based on Quantum Dots with Tailored Nanostructures. *Nat. Photonics* **2015**, *9*, 259−266.
(320) Lim, J.; Jeong, B. G.; Park, M.; Kim, J. K.; Pietryga, J. M.; Park, Y.-S.; Klimov, V. I.; Lee, C.; Lee, D. C.; Bae, W. K. Influence of Shell Thickness on the Performance of Light-Emitting Devices Based On CdSe/Zn1-XCdxS Core/Shell Heterostructured Quantum Dots. *Adv. Mater.* **2014**, *26*, 8034−8040.
(321) Shen, H.; Cao, W.; Shewmon, N. T.; Yang, C.; Li, L. S.; Xue, J. High-Efficiency, Low Turn-On Voltage Blue-Violet Quantum-Dot-Based Light-Emitting Diodes. *Nano Lett.* **2015**, *15*, 1211−1216.
(322) Cho, K.-S.; Lee, E. K.; Joo, W.-J.; Jang, E.; Kim, T.-H.; Lee, S. J.; Kwon, S.-J.; Han, J. Y.; Kim, B.-K.; Choi, B. L.; et al. High-Performance Crosslinked Colloidal Quantum-Dot Light-Emitting Diodes. *Nat. Photonics* **2009**, *3*, 341−345.
(323) Kim, T.-H.; Cho, K.-S.; Lee, E. K.; Lee, S. J.; Chae, J.; Kim, J. W.; Kim, D. H.; Kwon, J.-Y.; Amaratunga, G.; Lee, S. Y.; et al. Full-Colour Quantum Dot Displays Fabricated by Transfer Printing. *Nat. Photonics* **2011**, *5*, 176−182.
(324) Coropceanu, I.; Bawendi, M. G. Core/Shell Quantum Dot Based Luminescent Solar Concentrators with Reduced Reabsorption and Enhanced Efficiency. *Nano Lett.* **2014**, *14*, 4097−4101.
(325) Bronstein, N. D.; Yao, Y.; Xu, L.; O'Brien, E.; Powers, A. S.; Ferry, V. E.; Alivisatos, A. P.; Nuzzo, R. G. Quantum Dot Luminescent Concentrator Cavity Exhibiting 30-Fold Concentration. *ACS Photonics* **2015**, *2*, 1576.
(326) Galland, C.; Ghosh, Y.; Steinbrück, A.; Hollingsworth, J. A.; Htoon, H.; Klimov, V. I. Lifetime Blinking in Nonblinking Nanocrystal Quantum Dots. *Nat. Commun.* **2012**, *3*, 908.
(327) Htoon, H.; Hollingsworth, J.; Dickerson, R.; Klimov, V. Effect of Zero-To One-Dimensional Transformation on Multiparticle Auger Recombination in Semiconductor Quantum Rods. *Phys. Rev. Lett.* **2003**, *91*, 227401.
(328) Garcia-Santamaria, F.; Chen, Y. F.; Vela, J.; Schaller, R. D.; Hollingsworth, J. A.; Klimov, V. I. Suppressed Auger Recombination in "Giant" Nanocrystals Boosts Optical Gain Performance. *Nano Lett.* **2009**, *9*, 3482−3488.
(329) Orfield, N. J.; Mcbride, J. R.; Wang, F.; Buck, M. R.; Keene, J. D.; Reid, K. R.; Htoon, H.; Hollingsworth, J. A.; Rosenthal, S. J. Quantum Yield Heterogeneity Among Single Nonblinking Quantum Dots Revealed by Atomic Structure-Quantum Optics Correlation. *ACS Nano* **2016**, *10*, 1960−1968.
(330) Hall, R. N.; Fenner, G. E.; Kingsley, J. D.; Soltys, T. J.; Carlson, R. O. Coherent Light Emission From GaAs Junctions. *Phys. Rev. Lett.* **1962**, *9*, 366−368.
(331) Nathan, M. I.; Dumke, W. P.; Burns, G.; Dill, F. H.; Lasher, G. Stimulated Emission of Radiation from GaAs p-n Junctions. *Appl. Phys. Lett.* **1962**, *1*, 62−64.
(332) Arakawa, Y.; Sakaki, H. Multidimensional Quantum Well Laser and Temperature-Dependence of its Threshold Current. *Appl. Phys. Lett.* **1982**, *40*, 939−941.
(333) Asada, M.; Miyamoto, Y.; Suematsu, Y. Gain and the Threshold of 3-Dimensional Quantum-Box Lasers. *IEEE J. Quantum Electron.* **1986**, *22*, 1915−1921.
(334) Ekimov, A. Growth and Optical Properties of Semiconductor Nanocrystals in a Glass Matrix. *J. Lumin.* **1996**, *70*, 1−20.
(335) Ledentsov, N. N.; Ustinov, V. M.; Egorov, A. Y.; Zhukov, A. E.; Maksimov, M. V.; Tabatadze, I. G.; Kopev, P. S. Optical-Properties of Heterostructures with InGaAs-GaAs Quantum Clusters. *Semiconductors* **1994**, *28*, 832.
(336) Kirstaedter, N.; Ledentsov, N. N.; Grundmann, M.; Bimberg, D.; Ustinov, V. M.; Ruvimov, S. S.; Maximov, M. V.; Kopev, P. S.; Alferov, Z. I.; Richter, U.; et al. Low-Threshold, Large T-O Injection-Laser Emission from (InGa)As Quantum Dots. *Electron. Lett.* **1994**, *30*, 1416−1417.
(337) Grundmann, M. The Present Status of Quantum Dot Lasers. *Phys. E* **1999**, *5*, 167−184.
(338) Butty, J.; Hu, Y. Z.; Peyghambarian, N.; Kao, Y. H.; Mackenzie, J. D. Quasicontinuous Gain in Sol-Gel Derived CdS Quantum Dots. *Appl. Phys. Lett.* **1995**, *67*, 2672.
(339) Gindele, F.; Westphaeling, R.; Woggon, U.; Spanhel, L.; Ptatschek, V. Optical Gain and High Quantum Efficiency of Matrix-Free, Closely Packed CdSe Quantum Dots. *Appl. Phys. Lett.* **1997**, *71*, 2181.

DOI: 10.1021/acs.chemrev.6b00169
Chem. Rev. 2016, 116, 10513−10622

(340) Benisty, H.; Sotomayor-Torres, C. M.; Weisbuch, C. Intrinsic Mechanism for the Poor Luminescence Properties of Quantum-Box Systems. *Phys. Rev. B: Condens. Matter Mater. Phys.* **1991**, *44*, 10945−10948.
(341) inoshita, T.; Sakaki, H. Electron Relaxation in Quantum Dot: Significance of Multiphonon Processes. *Phys. Rev. B: Condens. Matter Mater. Phys.* **1992**, *46*, 7260−7263.
(342) Klimov, V. I.; Bawendi, M. G. Ultrafast Carrier Dynamics, Optical Amplification, and Lasing in Nanocrystal Quantum Dots. *MRS Bull.* **2001**, *26*, 998.
(343) Malko, A. V.; Mikhailovsky, A. A.; Petruska, M. A.; Hollingsworth, J. A.; Klimov, V. I. Interplay Between Optical Gain and Photoinduced Absorption in CdSe Nanocrystals. *J. Phys. Chem. B* **2004**, *108*, 5250−5255.
(344) Sosnowski, T. S.; Norris, T. B.; Jiang, H.; Singh, J.; Kamat, K.; Bhattacharya, P. Rapid Carrier Relaxation in In0.4Ga0.6As/GaAs Quantum Dots Characterized by Differential Transmission Spectroscopy. *Phys. Rev. B: Condens. Matter Mater. Phys.* **1998**, *57*, 9423−9426.
(345) Hendry, E.; Koeberg, M.; Wang, F.; Zhang, H.; Donega, C. D.; Vanmaekelbergh, D.; Bonn, M. Direct Observation of Electron-to-Hole Energy Transfer in CdSe Quantum Dots. *Phys. Rev. Lett.* **2006**, *96*, 057408.
(346) Klimov, V. I.; Mikhailovsky, A. A.; McBranch, D. W.; Leatherdale, C. A.; Bawendi, M. G. Mechanisms for intraband Energy Relaxation in Semiconductor Quantum Dots: The Role of Electron-Hole interactions. *Phys. Rev. B: Condens. Matter Mater. Phys.* **2000**, *61*, 13349−13352.
(347) Guyot-Sionnest, P.; Wehrenberg, B.; Yu, D. Intraband Relaxation in CdSe Nanocrystals and the Strong influence of the Surface Ligands. *J. Chem. Phys.* **2005**, *123*, 074709.
(348) Kambhampati, P. Unraveling the Structure and Dynamics of Excitons in Semiconductor Quantum Dots. *Acc. Chem. Res.* **2011**, *44*, 1−13.
(349) Schaller, R. D.; Pietryga, J. M.; Goupalov, S. V.; Petruska, M. A.; Ivanov, S. A.; Klimov, V. I. Breaking the Phonon Bottleneck in Semiconductor Nanocrystals Via Multiphonon Emission Induced by Intrinsic Nonadiabatic interactions. *Phys. Rev. Lett.* **2005**, *95*, 196401−196404.
(350) Pandey, A.; Guyot-Sionnest, P. Slow Electron Cooling in Colloidal Quantum Dots. *Science* **2008**, *322*, 929−932.
(351) Eisler, H.-J.; Sundar, V. C.; Bawendi, M. G.; Walsh, M.; Smith, H. I.; Klimov, V. I. Color-Selective Semiconductor Nanocrystal Laser. *Appl. Phys. Lett.* **2002**, *80*, 4614−4616.
(352) Kazes, M.; Lewis, D. Y.; Evenstein, Y.; Mokari, T.; Banin, U. Lasing From Semiconductor Quantum Rods in a Cylindrical Microcavity. *Adv. Mater.* **2002**, *14*, 317−321.
(353) Malko, A. V.; Mikhailovsky, A. A.; Petruska, M. A.; Hollingsworth, J. A.; Htoon, H.; Bawendi, M. G.; Klimov, V. I. From Amplified Spontaneous Emission To Microring Lasing Using Nanocrystal Quantum Dot Solids. *Appl. Phys. Lett.* **2002**, *81*, 1303−1305.
(354) Mcguire, J. A.; Joo, J.; Pietryga, J. M.; Schaller, R. D.; Klimov, V. I. New Aspects of Carrier Multiplication in Semiconductor Nanocrystals. *Acc. Chem. Res.* **2008**, *41*, 1810−1819.
(355) Htoon, H.; Malko, A. V.; Bussian, D.; Vela, J.; Chen, Y.; Hollingsworth, J. A.; Klimov, V. I. Highly Emissive Multiexcitons in Steady-State Photoluminescence of Individual "Giant" CdSe/CdS Core/Shell Nanocrystals. *Nano Lett.* **2010**, *10*, 2401−2407.
(356) Mikhailovsky, A. A.; Malko, A. V.; Hollingsworth, J. A.; Bawendi, M. G.; Klimov, V. I. Multiparticle Interactions and Stimulated Emission in Chemically Synthesized Quantum Dots. *Appl. Phys. Lett.* **2002**, *80*, 2380−2382.
(357) Svelto, O. *Principles of Lasers*; Springer: New York, 2010.
(358) Sundar, V. C.; Eisler, H.-J.; Bawendi, M. G. Room-Temperature, Tunable Gain Media From Novel II-VI Nanocrystal-Titania Composite Matrices. *Adv. Mater.* **2002**, *14*, 739.
(359) Petruska, M. A.; Bartko, A. P.; Klimov, V. I. An Amphiphilic Approach to Nanocrystal Quantum Dot-Titania Nanocomposites. *J. Am. Chem. Soc.* **2004**, *126*, 714−715.
(360) Bae, W. K.; Brovelli, S.; Klimov, V. I. Spectroscopic Insights into the Performance of Quantum Dot Light-Emitting Diodes. *MRS Bull.* **2013**, *38*, 721−730.
(361) Klimov, V. I.; Ivanov, S. A.; Nanda, J.; Achermann, M.; Bezel, I.; McGuire, J. A.; Piryatinski, A. Single-Exciton Optical Gain in Semiconductor Nanocrystals. *Nature* **2007**, *447*, 441−446.
(362) Klimov, V. I. Spectral and Dynamical Properties of Multiexcitons in Semiconductor Nanocrystals. *Annu. Rev. Phys. Chem.* **2007**, *58*, 635−673.
(363) Dang, C.; Lee, J.; Breen, C.; Steckel, J. S.; Coe-Sullivan, S.; Nurmikko, A. Red, Green and Blue Lasing Enabled By Single-Exciton Gain in Colloidal Quantum Dot Films. *Nat. Nanotechnol.* **2012**, *7*, 335−339.
(364) Grivas, C.; Li, C. Y.; Andreakou, P.; Wang, P. F.; Ding, M.; Brambilla, G.; Manna, L.; Lagoudakis, P. Single-Mode Tunable Laser Emission in the Single-Exciton Regime From Colloidal Nanocrystals. *Nat. Commun.* **2013**, *4*, 2376.
(365) Zavelani-Rossi, M.; Lupo, M. G.; Krahne, R.; Manna, L.; Lanzani, G. Lasing in Self-Assembled Microcavities of CdSe/CdS Core/Shell Colloidal Quantum Rods. *Nanoscale* **2010**, *2*, 931−935.
(366) Gollner, C.; Ziegler, J.; Protesescu, L.; Dirin, D. N.; Lechner, R. T.; Fritz-Popovski, G.; Sytnyk, M.; Yakunin, S.; Rotter, S.; Amin, A. A. Y.; et al. Random Lasing with Systematic Threshold Behavior in Films of CdSe/CdS Core/Thick-Shell Colloidal Quantum Dots. *ACS Nano* **2015**, *9*, 9792.
(367) He, T. C.; Chen, R.; Lin, W. W.; Huang, F.; Sun, H. D. Two-Photon-Pumped Stimulated Emission From ZnO Single Crystal. *Appl. Phys. Lett.* **2011**, *99*, 081902.
(368) Xing, G. C.; Liao, Y. L.; Wu, X. Y.; Chakrabortty, S.; Liu, X. F.; Yeow, E. K. L.; Chan, Y.; Sum, T. C. Ultralow-Threshold Two-Photon Pumped Amplified Spontaneous Emission and Lasing from Seeded CdSe/CdS Nanorod Heterostructures. *ACS Nano* **2012**, *6*, 10835−10844.
(369) Htoon, H.; Hollingsworth, J. A.; Dickerson, R.; Klimov, V. I. Zero- to One-Dimensional Transition and Auger Recombination in Semiconductor Quantum Rods. *Phys. Rev. Lett.* **2003**, *91*, 227401−227404.
(370) Htoon, H.; Hollingsworth, J. A.; Malko, A. V.; Dickerson, R.; Klimov, V. I. Light Amplification in Semiconductor Nanocrystals: Quantum Rods Vs. Quantum Dots. *Appl. Phys. Lett.* **2003**, *82*, 4776−4778.
(371) Liao, Y.; Xing, G.; Mishra, N.; Sum, T. C.; Chan, Y. Low Threshold, Amplified Spontaneous Emission From Core-Seeded Semiconductor Nanotetrapods incorporated into A Sol−Gel Matrix. *Adv. Mater.* **2012**, *24*, OP159−OP164.
(372) Krahne, R.; Zavelani-Rossi, M.; Lupo, M. G.; Manna, L.; Lanzani, G. Amplified Spontaneous Emission From Core and Shell Transitions in CdSe/CdS Nanorods Fabricated By Seeded Growth. *Appl. Phys. Lett.* **2011**, *98*, 063105.
(373) Moreels, I.; Rainò, G.; Gomes, R.; Hens, Z.; Stöferle, T.; Mahrt, R. F. Nearly Temperature-independent Threshold For Amplified Spontaneous Emission in Colloidal CdSe/CdS Quantum Dot-in-Rods. *Adv. Mater.* **2012**, *24*, OP231−OP235.
(374) Guzelturk, B.; Kelestemur, Y.; Olutas, M.; Delikanli, S.; Demir, H. V. Amplified Spontaneous Emission and Lasing in Colloidal Nanoplatelets. *ACS Nano* **2014**, *8*, 6599−6605.
(375) She, C.; Fedin, I.; Dolzhnikov, D. S.; Demortière, A.; Schaller, R. D.; Pelton, M.; Talapin, D. V. Low-Threshold Stimulated Emission Using Colloidal Quantum Wells. *Nano Lett.* **2014**, *14*, 2772−2777.
(376) Grim, J. Q.; Christodoulou, S.; Di Stasio, F.; Krahne, R.; Cingolani, R.; Manna, L.; Moreels, I. Continuous-Wave Biexciton Lasing at Room Temperature Using Solution-Processed Quantum Wells. *Nat. Nanotechnol.* **2014**, *9*, 891−895.
(377) Gao, S.; Zhang, C.; Liu, Y.; Su, H.; Wei, L.; Huang, T.; Dellas, N.; Shang, S.; Mohney, S. E.; Wang, J.; et al. Lasing from Colloidal InP/ZnS Quantum Dots. *Opt. Express* **2011**, *19*, 5528−5535.
(378) Guzelturk, B.; Kelestemur, Y.; Akgul, M. Z.; Sharma, V. K.; Demir, H. V. Ultralow Threshold One-Photon- and Two-Photon-

DOI: 10.1021/acs.chemrev.6b00169
Chem. Rev. 2016, 116, 10513−10622

Pumped Optical Gain Media of Blue-Emitting Colloidal Quantum Dot Films. *J. Phys. Chem. Lett.* **2014**, *5*, 2214−2218.
(379) Wang, Y.; Fong, K. E.; Yang, S.; Ta; Van, D.; Gao, Y.; Wang, Z.; Nalla, V.; Demir, H. V.; Sun, H. Unraveling the Ultralow Threshold Stimulated Emission From CdZnS/ZnS Quantum Dot and Enabling High-Q Microlasers. *Laser & Photonics Reviews* **2015**, *9*, 507−516.
(380) She, C.; Fedin, I.; Dolzhnikov, D. S.; Dahlberg, P. D.; Engel, G. S.; Schaller, R. D.; Talapin, D. V. Red, Yellow, Green, and Blue Amplified Spontaneous Emission and Lasing Using Colloidal CdSe Nanoplatelets. *ACS Nano* **2015**, *9*, 9475−9485.
(381) Yakunin, S.; Protesescu, L.; Krieg, F.; Bodnarchuk, M. I.; Nedelcu, G.; Humer, M.; De Luca, G.; Fiebig, M.; Heiss, W.; Kovalenko, M. V. Low-Threshold Amplified Spontaneous Emission and Lasing From Colloidal Nanocrystals of Caesium Lead Halide Perovskites. *Nat. Commun.* **2015**, *6*, 8056.
(382) Park, Y.-S.; Guo, S.; Makarov, N.; Klimov, V. I. Room Temperature Single-Photon Emission From Individual Perovskite Quantum Dots. *ACS Nano* **2015**, *9*, 10386.
(383) Makarov, N. S.; Guo, S.; Isaienko, O.; Liu, W.; Robel, I.; Klimov, V. I. Spectral and Dynamical Properties of Single Excitons, Biexcitons, and Trions in Cesium−Lead-Halide Perovskite Quantum Dots. *Nano Lett.* **2016**, *16*, 2349−2362.
(384) Zhong, X.; Feng, Y.; Knoll, W.; Han, M. Alloyed Znxcd1-Xs Nanocrystals With Highly Narrow Luminescence Spectral Width. *J. Am. Chem. Soc.* **2003**, *125*, 13559−13563.
(385) Chen, O.; Zhao, J.; Chauhan, V. P.; Cui, J.; Wong, C.; Harris, D. K.; Wei, H.; Han, H.-S.; Fukumura, D.; Jain, R. K.; et al. Compact High-Quality CdSe−CdS Core−Shell Nanocrystals With Narrow Emission Linewidths and Suppressed Blinking. *Nat. Mater.* **2013**, *12*, 445−451.
(386) Baldo, M. A.; O'Brien, D. F.; You, Y.; Shoustikov, A.; Sibley, S.; Thompson, M. E.; Forrest, S. R. Highly Efficient Phosphorescent Emission From Organic Electroluminescent Devices. *Nature* **1998**, *395*, 151−154.
(387) Ma, Y.; Zhang, H.; Shen, J.; Che, C. Electroluminescence from Triplet Metal—Ligand Charge-Transfer Excited State of Transition Metal Complexes. *Synth. Met.* **1998**, *94*, 245−248.
(388) Adachi, C.; Baldo, M. A.; Thompson, M. E.; Forrest, S. R. Nearly 100% Internal Phosphorescence Efficiency in an Organic Light-Emitting Device. *J. Appl. Phys.* **2001**, *90*, 5048−5051.
(389) Endo, A.; Sato, K.; Yoshimura, K.; Kai, T.; Kawada, A.; Miyazaki, H.; Adachi, C. Efficient Up-Conversion of Triplet Excitons into a Singlet State and its Application for Organic Light Emitting Diodes. *Appl. Phys. Lett.* **2011**, *98*, 083302.
(390) Goushi, K.; Yoshida, K.; Sato, K.; Adachi, C. Organic Light-Emitting Diodes Employing Efficient Reverse Intersystem Crossing for Triplet-To-Singlet State Conversion. *Nat. Photonics* **2012**, *6*, 253−258.
(391) Zhang, Q.; Li, B.; Huang, S.; Nomura, H.; Tanaka, H.; Adachi, C. Efficient Blue Organic Light-Emitting Diodes Employing Thermally Activated Delayed Fluorescence. *Nat. Photonics* **2014**, *8*, 326−332.
(392) Chamarro, M.; Gourdon, C.; Lavallard, P.; Lublinskaya, O.; Ekimov, A. I. Enhancement of Electron-Hole Exchange Interaction in CdSe Nanocrystals: A Quantum Confinement Effect. *Phys. Rev. B: Condens. Matter Mater. Phys.* **1996**, *53*, 1336−1342.
(393) Coe, S.; Woo, W.-K.; Bawendi, M.; Bulovic, V. Electroluminescence from Single Monolayers of Nanocrystals in Molecular Organic Devices. *Nature* **2002**, *420*, 800−803.
(394) Mueller, A. H.; Petruska, M. A.; Achermann, M.; Werder, D. J.; Akhadov, E. A.; Koleske, D. D.; Hoffbauer, M. A.; Klimov, V. I. Multicolor Light-Emitting Diodes Based on Semiconductor Nanocrystals Encapsulated in GaN Charge injection Layers. *Nano Lett.* **2005**, *5*, 1039−1044.
(395) Bae, W. K.; Lim, J.; Lee, D.; Park, M.; Lee, H.; Kwak, J.; Char, K.; Lee, C.; Lee, S. R/G/B/Natural White Light Thin Colloidal Quantum Dot-Based Light-Emitting Devices. *Adv. Mater.* **2014**, *26*, 6387−6393.
(396) Qian, L.; Zheng, Y.; Xue, J.; Holloway, P. H. Stable and Efficient Quantum-Dot Light-Emitting Diodes Based On Solution-Processed Multilayer Structures. *Nat. Photonics* **2011**, *5*, 543−548.
(397) Scholz, S.; Kondakov, D.; Lüssem, B.; Leo, K. Degradation Mechanisms and Reactions in Organic Light-Emitting Devices. *Chem. Rev.* **2015**, *115*, 8449−8503.
(398) Bae, W. K.; Kwak, J.; Lim, J.; Lee, D.; Nam, M. K.; Char, K.; Lee, C.; Lee, S. Multicolored Light-Emitting Diodes Based on All-Quantum-Dot Multilayer Films Using Layer-By-Layer Assembly Method. *Nano Lett.* **2010**, *10*, 2368−2373.
(399) Achermann, M.; Petruska, M. A.; Kos, S.; Smith, D. L.; Koleske, D. D.; Klimov, V. I. Energy-Transfer Pumping of Semiconductor Nanocrystals Using an Epitaxial Quantum Well. *Nature* **2004**, *429*, 642−646.
(400) Coe-Sullivan, S.; Woo, W.-K.; Steckel, J. S.; Bawendi, M.; Bulović, V. Tuning the Performance of Hybrid Organic/inorganic Quantum Dot Light-Emitting Devices. *Org. Electron.* **2003**, *4*, 123−130.
(401) Coe-Sullivan, S.; Steckel, J. S.; Woo, W. K.; Bawendi, M. G.; Bulović, V. Large-Area Ordered Quantum-Dot Monolayers via Phase Separation During Spin-Casting. *Adv. Funct. Mater.* **2005**, *15*, 1117−1124.
(402) Steckel, J. S.; Snee, P.; Coe-Sullivan, S.; Zimmer, J. P.; Halpert, J. E.; Anikeeva, P.; Kim, L.-A.; Bulovic, V.; Bawendi, M. G. Color-Saturated Green-Emitting QD-LEDs. *Angew. Chem., Int. Ed.* **2006**, *45*, 5796−5799.
(403) Niu, Y. H.; Munro, A. M.; Cheng, Y. J.; Tian, Y. Q.; Liu, M. S.; Zhao, J. L.; Bardecker, J. A.; Jen-La Plante, I.; Ginger, D. S.; Jen, A. K. Y. Improved Performance From Multilayer Quantum Dot Light-Emitting Diodes via Thermal Annealing of the Quantum Dot Layer. *Adv. Mater.* **2007**, *19*, 3371−3376.
(404) Anikeeva, P. O.; Madigan, C. F.; Halpert, J. E.; Bawendi, M. G.; Bulović, V. Electronic and Excitonic Processes in Light-Emitting Devices Based on Organic Materials and Colloidal Quantum Dots. *Phys. Rev. B: Condens. Matter Mater. Phys.* **2008**, *78*, 085434.
(405) Anikeeva, P. O.; Halpert, J. E.; Bawendi, M. G.; Bulović, V. Quantum Dot Light-Emitting Devices with Electroluminescence Tunable Over the Entire Visible Spectrum. *Nano Lett.* **2009**, *9*, 2532−2536.
(406) Castelli, A.; Meinardi, F.; Pasini, M.; Galeotti, F.; Pinchetti, V.; Lorenzon, M.; Manna, L.; Moreels, I.; Giovanella, U.; Brovelli, S. High-Efficiency All-Solution-Processed Light-Emitting Diodes Based on Anisotropic Colloidal Heterostructures with Polar Polymer Injecting Layers. *Nano Lett.* **2015**, *15*, 5455−5464.
(407) Steckel, J. S.; Zimmer, J. P.; Coe-Sullivan, S.; Stott, N. E.; Bulović, V.; Bawendi, M. G. Blue Luminescence From (CdS)ZnS Core−Shell Nanocrystals. *Angew. Chem., Int. Ed.* **2004**, *43*, 2154−2158.
(408) Wood, V.; Panzer, M. J.; Halpert, J. E.; Caruge, J. M.; Bawendi, M. G.; Bulović, V. Selection of Metal Oxide Charge Transport Layers for Colloidal Quantum Dot LEDs. *ACS Nano* **2009**, *3*, 3581−3586.
(409) Caruge, J. M.; Halpert, J. E.; Wood, V.; Bulovic, V.; Bawendi, M. G. Colloidal Quantum-Dot Light-Emitting Diodes with Metal-Oxide Charge Transport Layers. *Nat. Photonics* **2008**, *2*, 247−250.
(410) Caruge, J.-M.; Halpert, J. E.; Bulović, V.; Bawendi, M. G. NiO as an Inorganic Hole-Transporting Layer in Quantum-Dot Light-Emitting Devices. *Nano Lett.* **2006**, *6*, 2991−2994.
(411) Ho, S.; Liu, S.; Chen, Y.; So, F. Review of Recent Progress in Multilayer Solution-Processed Organic Light-Emitting Diodes. *J. Photonics Energy* **2015**, *5*, 057611−057611.
(412) Chaudhary, S.; Ozkan, M.; Chan, W. C. W. Trilayer Hybrid Polymer-Quantum Dot Light-Emitting Diodes. *Appl. Phys. Lett.* **2004**, *84*, 2925−2927.
(413) Bae, W. K.; Kwak, J.; Park, J. W.; Char, K.; Lee, C.; Lee, S. Highly Efficient Green-Light-Emitting Diodes Based on CdSe@ZnS Quantum Dots with a Chemical-Composition Gradient. *Adv. Mater.* **2009**, *21*, 1690−1694.
(414) Sun, Q.; Wang, Y. A.; Li, L. S.; Wang, D.; Zhu, T.; Xu, J.; Yang, C.; Li, Y. Bright, Multicoloured Light-Emitting Diodes Based on Quantum Dots. *Nat. Photonics* **2007**, *1*, 717−722.
(415) Stouwdam, J. W.; Janssen, R. A. J. Red, Green, and Blue Quantum Dot LEDs with Solution Processable ZnO Nanocrystal Electron Injection Layers. *J. Mater. Chem.* **2008**, *18*, 1889.

DOI: 10.1021/acs.chemrev.6b00169
Chem. Rev. 2016, 116, 10513−10622

(416) Mashford, B. S.; Stevenson, M.; Popovic, Z.; Hamilton, C.; Zhou, Z.; Breen, C.; Steckel, J.; Bulovic, V.; Bawendi, M.; Coe-Sullivan, S.; et al. High-Efficiency Quantum-Dot Light-Emitting Devices With Enhanced Charge injection. *Nat. Photonics* **2013**, *7*, 407−412.
(417) Meerheim, R.; Furno, M.; Hofmann, S.; Lüssem, B.; Leo, K. Quantification of Energy Loss Mechanisms in Organic Light-Emitting Diodes. *Appl. Phys. Lett.* **2010**, *97*, 253305.
(418) Saxena, K.; Jain, V. K.; Mehta, D. S. A Review On the Light Extraction Techniques in Organic Electroluminescent Devices. *Opt. Mater.* **2009**, *32*, 221−233.
(419) Kim, J.-S.; Ho, P. K. H.; Greenham, N. C.; Friend, R. H. Electroluminescence Emission Pattern of Organic Light-Emitting Diodes: Implications for Device Efficiency Calculations. *J. Appl. Phys.* **2000**, *88*, 1073−1081.
(420) Kagan, C. R.; Murray, C. B.; Nirmal, M.; Bawendi, M. G. Electronic Energy Transfer in CdSe Quantum Dot Solids. *Phys. Rev. Lett.* **1996**, *76*, 1517−1520.
(421) Crooker, S. A.; Hollingsworth, J. A.; Tretiak, S.; Klimov, V. I. Spectrally Resolved Dynamics of Energy Transfer in Quantum-Dot Assemblies: Towards Engineered Energy Flows in Artificial Materials. *Phys. Rev. Lett.* **2002**, *89*, 186802.
(422) Pal, B. N.; Ghosh, Y.; Brovelli, S.; Laocharoensuk, R.; Klimov, V. I.; Hollingsworth, J. A.; Htoon, H. 'Giant' CdSe/Cds Core/Shell Nanocrystal Quantum Dots as Efficient Electroluminescent Materials: Strong Influence of Shell Thickness on Light-Emitting Diode Performance. *Nano Lett.* **2012**, *12*, 331−336.
(423) Dabbousi, B. O.; Bawendi, M. G.; Onitsuka, O.; Rubner, M. F. Electroluminescence from CdSe Quantum-Dot/Polymer Composites. *Appl. Phys. Lett.* **1995**, *66*, 1316−1318.
(424) Rowland, C. E.; Schaller, R. D. Exciton Fate in Semiconductor Nanocrystals at Elevated Temperatures: Hole Trapping Outcompetes Exciton Deactivation. *J. Phys. Chem. C* **2013**, *117*, 17337−17343.
(425) Rowland, C. E.; Liu, W.; Hannah, D. C.; Chan, M. K. Y.; Talapin, D. V.; Schaller, R. D. Thermal Stability of Colloidal InP Nanocrystals: Small Inorganic Ligands Boost High-Temperature Photoluminescence. *ACS Nano* **2014**, *8*, 977−985.
(426) Shirasaki, Y.; Supran, G. J.; Tisdale, W. A.; Bulović, V. Origin of Efficiency Roll-Off in Colloidal Quantum-Dot Light-Emitting Diodes. *Phys. Rev. Lett.* **2013**, *110*, 217403.
(427) Huang, H.; Dorn, A.; Nair, G. P.; Bulović, V.; Bawendi, M. G. Bias-induced Photoluminescence Quenching of Single Colloidal Quantum Dots Embedded in Organic Semiconductors. *Nano Lett.* **2007**, *7*, 3781−3786.
(428) Bozyigit, D.; Yarema, O.; Wood, V. Origins of Low Quantum Efficiencies in Quantum Dot LEDs. *Adv. Funct. Mater.* **2013**, *23*, 3024−3029.
(429) Choi, M. K.; Yang, J.; Kang, K.; Kim, D. C.; Choi, C.; Park, C.; Kim, S. J.; Chae, S. I.; Kim, T.-H.; Kim, J. H.; et al. Wearable Red-Green-Blue Quantum Dot Light-Emitting Diode Array Using High-Resolution Intaglio Transfer Printing. *Nat. Commun.* **2015**, *6*, 7149.
(430) Apple, Inc. IPhone 6 Technical Specifications. http://www.apple.com/iphone-6/specs (accessed March 7, 2016).
(431) Samsung Electronics Co., Ltd. Galaxy S6 Edge: Next is Now. http://www.samsung.com/global/galaxy/galaxys6/galaxy-s6-edge (accessed March 7, 2016).
(432) Kim, B. H.; Onses, M. S.; Lim, J. B.; Nam, S.; Oh, N.; Kim, H.; Yu, K. J.; Lee, J. W.; Kim, J.-H.; Kang, S.-K.; et al. High-Resolution Patterns of Quantum Dots Formed By Electrohydrodynamic Jet Printing For Light-Emitting Diodes. *Nano Lett.* **2015**, *15*, 969−973.
(433) Kim, L.; Anikeeva, P. O.; Coe-Sullivan, S. A.; Steckel, J. S.; Bawendi, M. G.; Bulović, V. Contact Printing of Quantum Dot Light-Emitting Devices. *Nano Lett.* **2008**, *8*, 4513−4517.
(434) Rizzo, A.; Mazzeo, M.; Biasiucci, M.; Cingolani, R.; Gigli, G. White Electroluminescence From A Microcontact-Printing-Deposited CdSe/ZnS Colloidal Quantum-Dot Monolayer. *Small* **2008**, *4*, 2143−2147.
(435) Rizzo, A.; Mazzeo, M.; Palumbo, M.; Lerario, G.; D'Amone, S.; Cingolani, R.; Gigli, G. Hybrid Light-Emitting Diodes From Microcontact-Printing Double-Transfer of Colloidal Semiconductor CdSe/ZnS Quantum Dots Onto Organic Layers. *Adv. Mater.* **2008**, *20*, 1886−1891.
(436) Zhu, T.; Shanmugasundaram, K.; Price, S. C.; Ruzyllo, J.; Zhang, F.; Xu, J.; Mohney, S. E.; Zhang, Q.; Wang, A. Y. Mist Fabrication of Light Emitting Diodes With Colloidal Nanocrystal Quantum Dots. *Appl. Phys. Lett.* **2008**, *92*, 023111.
(437) DOE SSL Program, "R&D Plan"; Prepared by Bardsley Consulting, SB Consulting, SSLS, Inc., LED Lighting Advisors, and Navigant Consulting, Inc., May 2015. http://energy.gov/sites/prod/files/2015/06/f22/ssl_rd-plan_may2015_0.pdf (accessed March 7, 2016).
(438) Haverinen, H. M.; Myllylä, R. A.; Jabbour, G. E. Inkjet Printing of Light Emitting Quantum Dots. *Appl. Phys. Lett.* **2009**, *94*, 073108.
(439) Brovelli, S.; Bae, W. K.; Galland, C.; Giovanella, U.; Meinardi, F.; Klimov, V. I. Dual-Color Electroluminescence From Dot-in-Bulk Nanocrystals. *Nano Lett.* **2014**, *14*, 486−494.
(440) Haverinen, H. M.; Myllyla, R. A.; Jabbour, G. E. Inkjet Printed RGB Quantum Dot-Hybrid LED. *J. Disp. Technol.* **2010**, *6*, 87−89.
(441) De Almeida, A.; Santos, B.; Paolo, B.; Quicheron, M. Solid State Lighting Review − Potential and Challenges in Europe. *Renewable Sustainable Energy Rev.* **2014**, *34*, 30−48.
(442) Conner, M. Measuring Light Quality for Philips and Cree LED Bulbs with the MK350 Spectrometer. http://www.designingwithleds.com/measuring-light-quality-philips-cree-led-bulbs-spectrometer (accessed March 16, 2016).
(443) Schubert, E. F. *Light Emitting Diodes*, 2nd ed.; Cambridge University Press: 2006.
(444) Li, Y. Q.; Rizzo, A.; Cingolani, R.; Gigli, G. Bright White-Light-Emitting Device From Ternary Nanocrystal Composites. *Adv. Mater.* **2006**, *18*, 2545−2548.
(445) Anikeeva, P. O.; Halpert, J. E.; Bawendi, M. G.; Bulović, V. Electroluminescence from a Mixed Red−Green−Blue Colloidal Quantum Dot Monolayer. *Nano Lett.* **2007**, *7*, 2196−2200.
(446) Kim, T.-H.; Chung, D.-Y.; Ku, J.; Song, I.; Sul, S.; Kim, D.-H.; Cho, K.-S.; Choi, B. L.; Min Kim, J.; Hwang, S. Heterogeneous Stacking of Nanodot Monolayers By Dry Pick-And-Place Transfer and Its Applications in Quantum Dot Light-Emitting Diodes. *Nat. Commun.* **2013**, *4*, 2637 DOI: 10.1038/ncomms3637.
(447) Lee, K.-H.; Han, C.-Y.; Kang, H.-D.; Ko, H.; Lee, C.; Lee, J.; Myoung, N.; Yim, S.-Y.; Yang, H. Highly Efficient, Color-Reproducible Full-Color Electroluminescent Devices Based on Red/Green/Blue Quantum Dot-Mixed Multilayer. *ACS Nano* **2015**, *9*, 10941.
(448) Reineke, S.; Thomschke, M.; Lüssem, B.; Leo, K. White Organic Light-Emitting Diodes: Status and Perspective. *Rev. Mod. Phys.* **2013**, *85*, 1245−1293.
(449) Wong, J. I.; Mishra, N.; Xing, G.; Li, M.; Chakrabortty, S.; Sum, T. C.; Shi, Y.; Chan, Y.; Yang, H. Y. Dual Wavelength Electroluminescence From CdSe/CdS Tetrapods. *ACS Nano* **2014**, *8*, 2873−2879.
(450) Nizamoglu, S.; Mutlugun, E.; Özel, T.; Demir, H. V.; Sapra, S.; Gaponik, N.; Eychmüller, A. Dual-Color Emitting Quantum-Dot-Quantum-Well CdSe-ZnS Heteronanocrystals Hybridized On InGaN/GaN Light Emitting Diodes For High-Quality White Light Generation. *Appl. Phys. Lett.* **2008**, *92*, 113110.
(451) Sapra, S.; Mayilo, S.; Klar, T. A.; Rogach, A. L.; Feldmann, J. Bright White-Light Emission From Semiconductor Nanocrystals: By Chance and By Design. *Adv. Mater.* **2007**, *19*, 569−572.
(452) Liu, S.; Borys, N. J.; Sapra, S.; Eychmüller, A.; Lupton, J. M. Localization and Dynamics of Long-Lived Excitations in Colloidal Semiconductor Nanocrystals With Dual Quantum Confinement. *ChemPhysChem* **2015**, *16*, 1663−1669.
(453) Parliament, T. E. Directive 2011/65/EU of the European Parliament and of the Council of 8 June 2011 On the Restriction of the Use of Certain Hazardous Substances in Electrical and Electronic Equipment. http://eur-lex.europa.eu/legal-content/EN/TXT/PDF/?uri=CELEX:32011L0065=EN; 2011.
(454) Van De Walle, C. G.; Neugebauer, J. Universal Alignment of Hydrogen Levels in Semiconductors, insulators and Solutions. *Nature* **2003**, *423*, 626−628.

DOI: 10.1021/acs.chemrev.6b00169
Chem. Rev. 2016, 116, 10513−10622

(455) Wei, S.-H.; Zunger, A. Calculated Natural Band Offsets of All II−VI and III−V Semiconductors: Chemical Trends and the Role of Cation d Orbitals. *Appl. Phys. Lett.* **1998**, *72*, 2011−2013.
(456) Wei, S. H.; Zunger, A. Band Offsets and Optical Bowings of Chalcopyrites and Zn-Based II-VI Alloys. *J. Appl. Phys.* **1995**, *78*, 3846−3856.
(457) Wang, A.; Shen, H.; Zang, S.; Lin, Q.; Wang, H.; Qian, L.; Niu, J.; Song Li, L. Bright, Efficient, and Color-Stable Violet ZnSe-Based Quantum Dot Light-Emitting Diodes. *Nanoscale* **2015**, *7*, 2951−2959.
(458) Lim, J.; Park, M.; Bae, W. K.; Lee, D.; Lee, S.; Lee, C.; Char, K. Highly Efficient Cadmium-Free Quantum Dot Light-Emitting Diodes Enabled by the Direct Formation of Excitons Within InP@ZnSeS Quantum Dots. *ACS Nano* **2013**, *7*, 9019−9026.
(459) Jurbergs, D.; Rogojina, E.; Mangolini, L.; Kortshagen, U. Silicon Nanocrystals with Ensemble Quantum Yields Exceeding 60%. *Appl. Phys. Lett.* **2006**, *88*, 233116.
(460) Yang, X.; Zhao, D.; Leck, K. S.; Tan, S. T.; Tang, Y. X.; Zhao, J.; Demir, H. V.; Sun, X. W. Full Visible Range Covering InP/ZnS Nanocrystals with High Photometric Performance and Their Application to White Quantum Dot Light-Emitting Diodes. *Adv. Mater.* **2012**, *24*, 4180−4185.
(461) Kim, J.-H.; Han, C.-Y.; Lee, K.-H.; An, K.-S.; Song, W.; Kim, J.; Oh, M. S.; Do, Y. R.; Yang, H. Performance Improvement of Quantum Dot-Light-Emitting Diodes Enabled by an Alloyed Znmgo Nanoparticle Electron Transport Layer. *Chem. Mater.* **2015**, *27*, 197−204.
(462) Cheng, K.-Y.; Anthony, R.; Kortshagen, U. R.; Holmes, R. J. High-Efficiency Silicon Nanocrystal Light-Emitting Devices. *Nano Lett.* **2011**, *11*, 1952−1956.
(463) Supran, G. J.; Song, K. W.; Hwang, G. W.; Correa, R. E.; Scherer, J.; Dauler, E. A.; Shirasaki, Y.; Bawendi, M. G.; Bulović, V. High-Performance Shortwave-infrared Light-Emitting Devices Using Core−Shell (PbS−CdS) Colloidal Quantum Dots. *Adv. Mater.* **2015**, *27*, 1437−1442.
(464) Madigan, C. F.; Lu, M.-H.; Sturm, J. C. Improvement of Output Coupling Efficiency of Organic Light-Emitting Diodes By Backside Substrate Modification. *Appl. Phys. Lett.* **2000**, *76*, 1650−1652.
(465) Möller, S.; Forrest, S. R. Improved Light Out-Coupling in Organic Light Emitting Diodes Employing Ordered Microlens Arrays. *J. Appl. Phys.* **2002**, *91*, 3324−3327.
(466) Yamasaki, T.; Sumioka, K.; Tsutsui, T. Organic Light-Emitting Device With An Ordered Monolayer of Silica Microspheres As A Scattering Medium. *Appl. Phys. Lett.* **2000**, *76*, 1243−1245.
(467) Riel, H.; Karg, S.; Beierlein, T.; Rieß, W.; Neyts, K. Tuning the Emission Characteristics of Top-Emitting Organic Light-Emitting Devices By Means of A Dielectric Capping Layer: An Experimental and Theoretical Study. *J. Appl. Phys.* **2003**, *94*, 5290−5296.
(468) Yokoyama, D.; Sakaguchi, A.; Suzuki, M.; Adachi, C. Horizontal Orientation of Linear-Shaped Organic Molecules Having Bulky Substituents in Neat and Doped Vacuum-Deposited Amorphous Films. *Org. Electron.* **2009**, *10*, 127−137.
(469) Yang, X.; Dev, K.; Wang, J.; Mutlugun, E.; Dang, C.; Zhao, Y.; Liu, S.; Tang, Y.; Tan, S. T.; Sun, X. W.; et al. Light Extraction Efficiency Enhancement of Colloidal Quantum Dot Light-Emitting Diodes Using Large-Scale Nanopillar Arrays. *Adv. Funct. Mater.* **2014**, *24*, 5977−5984.
(470) Liang, H.; Zhu, R.; Dong, Y.; Wu, S.-T.; Li, J.; Wang, J.; Zhou, J. Enhancing the Outcoupling Efficiency of Quantum Dot LEDs With internal Nano-Scattering Pattern. *Opt. Express* **2015**, *23*, 12910−12922.
(471) Nam, S.; Oh, N.; Zhai, Y.; Shim, M. High Efficiency and Optical Anisotropy in Double-Heterojunction Nanorod Light-Emitting Diodes. *ACS Nano* **2015**, *9*, 878−885.
(472) Hikmet, R. A. M.; Chin, P. T. K.; Talapin, D. V.; Weller, H. Polarized-Light-Emitting Quantum-Rod Diodes. *Adv. Mater.* **2005**, *17*, 1436−1439.
(473) Rizzo, A.; Nobile, C.; Mazzeo, M.; Giorgi, M. D.; Fiore, A.; Carbone, L.; Cingolani, R.; Manna, L.; Gigli, G. Polarized Light Emitting Diode By Long-Range Nanorod Self-Assembling On A Water Surface. *ACS Nano* **2009**, *3*, 1506−1512.
(474) Choudhary, S.; Qureshi, S. *TENCON 2008 - 2008 IEEE Region 10 Conference* 2008; pp 1−4.
(475) Ridley, B. K. *Quantum Processes in Semiconductors*; Oxford University Press: 2013.
(476) Hanna, M.; Nozik, A. Solar Conversion Efficiency of Photovoltaic and Photoelectrolysis Cells With Carrier Multiplication Absorbers. *J. Appl. Phys.* **2006**, *100*, 074510.
(477) Koc, S. The Quantum Efficiency of the Photo-Electric Effect in Germanium for the 0.3−2 M Wavelength Region. *Czech. J. Phys.* **1957**, *7*, 91−95.
(478) Beard, M. C. Multiple Exciton Generation in Semiconductor Quantum Dots. *J. Phys. Chem. Lett.* **2011**, *2*, 1282−1288.
(479) Beard, M. C.; Midgett, A. G.; Hanna, M. C.; Luther, J. M.; Hughes, B. K.; Nozik, A. J. Comparing Multiple Exciton Generation in Quantum Dots to Impact Ionization in Bulk Semiconductors: Implications for Enhancement of Solar Energy Conversion. *Nano Lett.* **2010**, *10*, 3019−3027.
(480) Alig, R. C.; Bloom, S. Electron-Hole-Pair Creation Energies in Semiconductors. *Phys. Rev. Lett.* **1975**, *35*, 1522−1525.
(481) Klein, C. A. Bandgap Dependence and Related Features of Radiation Ionization Energies in Semiconductors. *J. Appl. Phys.* **1968**, *39*, 2029−2038.
(482) Auston, D.; Shank, C.; Lefur, P. Picosecond Optical Measurements of Band-To-Band Auger Recombination of High-Density Plasmas in Germanium. *Phys. Rev. Lett.* **1975**, *35*, 1022.
(483) Klimov, V. I. Mechanisms for Photogeneration and Recombination of Multiexcitons in Semiconductor Nanocrystals: Implications for Lasing and Solar Energy Conversion. *J. Phys. Chem. B* **2006**, *110*, 16827.
(484) Schaller, R. D.; Petruska, M. A.; Klimov, V. I. Effect of Electronic Structure on Carrier Multiplication Efficiency: Comparative Study of PbSe and CdSe Nanocrystals. *Appl. Phys. Lett.* **2005**, *87*, 253102.
(485) Schaller, R. D.; Pietryga, J. M.; Klimov, V. I. Carrier Multiplication in InAs Nanocrystal Quantum Dots with an Onset Defined by the Energy Conservation Limit. *Nano Lett.* **2007**, *7*, 3469−3476.
(486) Stubbs, S. K.; Hardman, S. J. O.; Graham, D. M.; Spencer, B. F.; Flavell, W. R.; Glarvey, P.; Masala, O.; Pickett, N. L.; Binks, D. J. Efficient Carrier Multiplication in InP Nanoparticles. *Phys. Rev. B: Condens. Matter Mater. Phys.* **2010**, *81*, 081303.
(487) Saeed, S.; De Weerd, C.; Stallinga, P.; Spoor, F. C.; Houtepen, A. J.; Siebbeles, L. D.; Gregorkiewicz, T. Carrier Multiplication in Germanium Nanocrystals. *Light: Sci. Appl.* **2015**, *4*, E251.
(488) Stolle, C. J.; Schaller, R. D.; Korgel, B. A. Efficient Carrier Multiplication in Colloidal CuInSe2 Nanocrystals. *J. Phys. Chem. Lett.* **2014**, *5*, 3169−3174.
(489) Stewart, J. T.; Padilha, L. A.; Qazilbash, M. M.; Pietryga, J. M.; Midgett, A. G.; Luther, J. M.; Beard, M. C.; Nozik, A. J.; Klimov, V. I. Comparison of Carrier Multiplication Yields in PbS and PbSe Nanocrystals: The Role of Competing Energy-Loss Processes. *Nano Lett.* **2012**, *12*, 622−628.
(490) Trinh, M. T.; Limpens, R.; De Boer, W. D. A. M.; Schins, J. M.; Siebbeles, L. D. A.; Gregorkiewicz, T. Direct Generation of Multiple Excitons in Adjacent Silicon Nanocrystals Revealed by induced Absorption. *Nat. Photonics* **2012**, *6*, 316−321.
(491) Shabaev, A.; Hellberg, C. S.; Efros, A. L. Efficiency of Multiexciton Generation in Colloidal Nanostructures. *Acc. Chem. Res.* **2013**, *46*, 1242−1251.
(492) Witzel, W. M.; Shabaev, A.; Hellberg, C. S.; Jacobs, V. L.; Efros, A. L. Quantum Simulation of Multiple-Exciton Generation in a Nanocrystal by a Single Photon. *Phys. Rev. Lett.* **2010**, *105*, 137401.
(493) Ellingson, R. J.; Beard, M. C.; Johnson, J. C.; Yu, P.; Micic, O. I.; Nozik, A. J.; Shabaev, A.; Efros, A. L. Highly Efficient Multiple Exciton Generation in Colloidal PbSe and PbS Quantum Dots. *Nano Lett.* **2005**, *5*, 865−871.
(494) Shabaev, A.; Efros, A. L.; Nozik, A. J. Multiexciton Generation by a Single Photon in Nanocrystals. *Nano Lett.* **2006**, *6*, 2856−2863.
(495) Schaller, R. D.; Agranovich, V. M.; Klimov, V. I. High-Efficiency Carrier Multiplication Through Direct Photogeneration of Multi-Excitons via Virtual Single-Exciton States. *Nat. Phys.* **2005**, *1*, 189−194.

DOI: 10.1021/acs.chemrev.6b00169
Chem. Rev. 2016, 116, 10513−10622

(496) Rupasov, V. I.; Klimov, V. I. Carrier Multiplication in Semiconductor Nanocrystals via Intraband Optical Transitions involving Virtual Biexciton States. *Phys. Rev. B: Condens. Matter Mater. Phys.* **2007**, *76*, 125321.
(497) Berestetskii, V. B.; Lifshitz, E. M.; Pitaevskiĭ, L. P. *Quantum Electrodynamics*; Butterworth-Heinemann: 1982.
(498) Allan, G.; Delerue, C. Role of Impact Ionization in Multiple Exciton Generation in PbSe Nanocrystals. *Phys. Rev. B: Condens. Matter Mater. Phys.* **2006**, *73*, 205423.
(499) Franceschetti, A.; An, J. M.; Zunger, A. Impact Ionization Can Explain Carrier Multiplication in PbSe Quantum Dots. *Nano Lett.* **2006**, *6*, 2191−2195.
(500) Delerue, C.; Allan, G.; Pijpers, J.; Bonn, M. Carrier Multiplication in Bulk and Nanocrystalline Semiconductors: Mechanism, Efficiency, and Interest for Solar Cells. *Phys. Rev. B: Condens. Matter Mater. Phys.* **2010**, *81*, 125306.
(501) Califano, M.; Zunger, A.; Franceschetti, A. Direct Carrier Multiplication Due to Inverse Auger Scattering in CdSe Quantum Dots. *Appl. Phys. Lett.* **2004**, *84*, 2409−2411.
(502) Klimov, V. I.; Mcbranch, D. W.; Leatherdale, C. A.; Bawendi, M. G. Electron and Hole Relaxation Pathways in Semiconductor Quantum Dots. *Phys. Rev. B: Condens. Matter Mater. Phys.* **1999**, *60*, 13740.
(503) Wehrenberg, B. L.; Wang, C. J.; Guyot-Sionnest, P. Interband and Intraband Optical Studies of PbSe Colloidal Quantum Dots. *J. Phys. Chem. B* **2002**, *106*, 10634−10640.
(504) Cho, B.; Peters, W. K.; Hill, R. J.; Courtney, T. L.; Jonas, D. M. Bulklike Hot Carrier Dynamics in Lead Sulfide Quantum Dots. *Nano Lett.* **2010**, *10*, 2498−2505.
(505) Klimov, V. I. Detailed-Balance Power Conversion Limits of Nanocrystal-Quantum-Dot Solar Cells in the Presence of Carrier Multiplication. *Appl. Phys. Lett.* **2006**, *89*, 123118.
(506) Hanna, M. C.; Beard, M. C.; Nozik, A. J. Effect of Solar Concentration On the Thermodynamic Power Conversion Efficiency of Quantum-Dot Solar Cells Exhibiting Multiple Exciton Generation. *J. Phys. Chem. Lett.* **2012**, *3*, 2857−2862.
(507) Shockley, W.; Queisser, H. J. Detailed Balance Limit of Efficiency of p-n Junction Solar Cells. *J. Appl. Phys.* **1961**, *32*, 510.
(508) Ji, M.; Park, S.; Connor, S. T.; Mokari, T.; Cui, Y.; Gaffney, K. J. Efficient Multiple Exciton Generation Observed in Colloidal PbSe Quantum Dots with Temporally and Spectrally Resolved intraband Excitation. *Nano Lett.* **2009**, *9*, 1217−1222.
(509) Pijpers, J.; Hendry, E.; Milder, M.; Fanciulli, R.; Savolainen, J.; Herek, J.; Vanmaekelbergh, D.; Ruhman, S.; Mocatta, D.; Oron, D. Carrier Multiplication and its Reduction by Photodoping in Colloidal InAs Quantum Dots. *J. Phys. Chem. C* **2008**, *112*, 4783−4784.
(510) Nair, G.; Geyer, S. M.; Chang, L.-Y.; Bawendi, M. G. Carrier Multiplication Yields in PbS and PbSe Nanocrystals Measured by Transient Photoluminescence. *Phys. Rev. B: Condens. Matter Mater. Phys.* **2008**, *78*, 125325.
(511) Schaller, R. D.; Klimov, V. I. Non-Poissonian Exciton Populations in Semiconductor Nanocrystals via Carrier Multiplication. *Phys. Rev. Lett.* **2006**, *96*, 097402.
(512) Nair, G.; Bawendi, M. G. Carrier Multiplication Yields of CdSe and Cdte Nanocrystals By Transient Photoluminescence Spectroscopy. *Phys. Rev. B: Condens. Matter Mater. Phys.* **2007**, *76*, 081304 DOI: 10.1103/PhysRevB.76.081304.
(513) Fisher, B.; Caruge, J. M.; Zehnder, D.; Bawendi, M. Room-Temperature Ordered Photon Emission From Multiexciton States in Single CdSe Core-Shell Nanocrystals. *Phys. Rev. Lett.* **2005**, *94*, 087403.
(514) Trinh, M. T.; Houtepen, A. J.; Schins, J. M.; Hanrath, T.; Piris, J.; Knulst, W.; Goossens, A. P.; Siebbeles, L. D. in Spite of Recent Doubts Carrier Multiplication Does Occur in PbSe Nanocrystals. *Nano Lett.* **2008**, *8*, 1713−1718.
(515) Schaller, R. D.; Sykora, M.; Pietryga, J. M.; Klimov, V. I. Seven Excitons At A Cost of One: Redefining the Limits For Conversion Efficiency of Photons into Charge Carriers. *Nano Lett.* **2006**, *6*, 424−429.
(516) Ben-Lulu, M.; Mocatta, D.; Bonn, M.; Banin, U.; Ruhman, S. On the Absence of Detectable Carrier Multiplication in A Transient Absorption Study of InAs/CdSe/ZnSe Core/Shell1/Shell2 Quantum Dots. *Nano Lett.* **2008**, *8*, 1207−1211.
(517) Tyagi, P.; Kambhampati, P. False Multiple Exciton Recombination and Multiple Exciton Generation Signals in Semiconductor Quantum Dots Arise From Surface Charge Trapping. *J. Chem. Phys.* **2011**, *134*, 094706.
(518) Mcguire, J. A.; Sykora, M.; Robel, I.; Padilha, L. A.; Joo, J.; Pietryga, J. M.; Klimov, V. I. Spectroscopic Signatures of Photocharging Due To Hot-Carrier Transfer in Solutions of Semiconductor Nanocrystals Under Low-intensity Ultraviolet Excitation. *ACS Nano* **2010**, *4*, 6087−6097.
(519) Midgett, A. G.; Hillhouse, H. W.; Hughes, B. K.; Nozik, A. J.; Beard, M. C. Flowing Versus Static Conditions For Measuring Multiple Exciton Generation in PbSe Quantum Dots. *J. Phys. Chem. C* **2010**, *114*, 17486−17500.
(520) Sandberg, R. L.; Padilha, L. A.; Qazilbash, M. M.; Bae, W. K.; Schaller, R. D.; Pietryga, J. M.; Stevens, M. J.; Baek, B.; Nam, S. W.; Klimov, V. I. Multiexciton Dynamics in infrared-Emitting Colloidal Nanostructures Probed By A Superconducting Nanowire Single-Photon Detector. *ACS Nano* **2012**, *6*, 9532−9540.
(521) Midgett, A. G.; Luther, J. M.; Stewart, J. T.; Smith, D. K.; Padilha, L. A.; Klimov, V. I.; Nozik, A. J.; Beard, M. C. Size and Composition Dependent Multiple Exciton Generation Efficiency in PbS, PbSe, and PbSxSe1-X Alloyed Quantum Dots. *Nano Lett.* **2013**, *13*, 3078−3085.
(522) Padilha, L. A.; Stewart, J. T.; Sandberg, R. L.; Bae, W. K.; Koh, W. K.; Pietryga, J. M.; Klimov, V. I. Carrier Multiplication in Semiconductor Nanocrystals: Influence of Size, Shape, and Composition. *Acc. Chem. Res.* **2013**, *46*, 1261−1269.
(523) Padilha, L. A.; Robel, I.; Lee, D. C.; Nagpal, P.; Pietryga, J. M.; Klimov, V. I. Spectral Dependence of Nanocrystal Photoionization Probability: the Role of Hot-Carrier Transfer. *ACS Nano* **2011**, *5*, 5045−5055.
(524) Padilha, L. A.; Stewart, J. T.; Sandberg, R. L.; Bae, W. K.; Koh, W. K.; Pietryga, J. M.; Klimov, V. I. Aspect Ratio Dependence of Auger Recombination and Carrier Multiplication in PbSe Nanorods. *Nano Lett.* **2013**, *13*, 1092−1099.
(525) Gao, J.; Fidler, A. F.; Klimov, V. I. Carrier Multiplication Detected Through Transient Photocurrent in Device-Grade Films of Lead Selenide Quantum Dots. *Nat. Commun.* **2015**, *6*, 8185.
(526) Pijpers, J.; Ulbricht, R.; Tielrooij, K.; Osherov, A.; Golan, Y.; Delerue, C.; Allan, G.; Bonn, M. Assessment of Carrier-Multiplication Efficiency in Bulk PbSe and PbS. *Nat. Phys.* **2009**, *5*, 811−814.
(527) Nair, G.; Chang, L.-Y.; Geyer, S. M.; Bawendi, M. G. Perspective On the Prospects of a Carrier Multiplication Nanocrystal Solar Cell. *Nano Lett.* **2011**, *11*, 2145−2151.
(528) Lin, Z.; Franceschetti, A.; Lusk, M. T. Size Dependence of the Multiple Exciton Generation Rate in CdSe Quantum Dots. *ACS Nano* **2011**, *5*, 2503−2511.
(529) Rabani, E.; Baer, R. Distribution of Multiexciton Generation Rates in CdSe and InAs Nanocrystals. *Nano Lett.* **2008**, *8*, 4488−4492.
(530) Timmerman, D.; Izeddin, I.; Stallinga, P.; Yassievich, I.; Gregorkiewicz, T. Space-Separated Quantum Cutting With Silicon Nanocrystals For Photovoltaic Applications. *Nat. Photonics* **2008**, *2*, 105−109.
(531) Timmerman, D.; Valenta, J.; Dohnalová, K.; De Boer, W.; Gregorkiewicz, T. Step-Like Enhancement of Luminescence Quantum Yield of Silicon Nanocrystals. *Nat. Nanotechnol.* **2011**, *6*, 710−713.
(532) Govoni, M.; Marri, I.; Ossicini, S. Carrier Multiplication Between Interacting Nanocrystals for Fostering Silicon-Based Photovoltaics. *Nat. Photonics* **2012**, *6*, 672−679.
(533) Beard, M. C.; Knutsen, K. P.; Yu, P. R.; Luther, J. M.; Song, Q.; Metzger, W. K.; Ellingson, R. J.; Nozik, A. J. Multiple Exciton Generation in Colloidal Silicon Nanocrystals. *Nano Lett.* **2007**, *7*, 2506−2512.
(534) Svrcek, V.; Dohnalova, K.; Mariotti, D.; Trinh, M. T.; Limpens, R.; Mitra, S.; Gregorkiewicz, T.; Matsubara, K.; Kondo, M. Dramatic Enhancement of Photoluminescence Quantum Yields for Surface-Engineered Si Nanocrystals Within the Solar Spectrum. *Adv. Funct. Mater.* **2013**, *23*, 6051−6058.

DOI: 10.1021/acs.chemrev.6b00169
Chem. Rev. 2016, 116, 10513−10622

(535) Schmitt-Rink, S.; Chemla, D.; Miller, D. Linear and Nonlinear Optical Properties of Semiconductor Quantum Wells. *Adv. Phys.* **1989**, *38*, 89−188.
(536) Keldysh, L. Coulomb interaction in Thin Semiconductor and Semimetal Films. *JETP Lett.* **1979**, *29*, 658.
(537) Loudon, R. One-Dimensional Hydrogen Atom. *Am. J. Phys.* **1959**, *27*, 649−655.
(538) Haines, L. K.; Roberts, D. H. One-Dimensional Hydrogen Atom. *Am. J. Phys.* **1969**, *37*, 1145−1154.
(539) Bartnik, A.; Efros, A. L.; Koh, W.-K.; Murray, C.; Wise, F. Electronic States and Optical Properties of PbSe Nanorods and Nanowires. *Phys. Rev. B: Condens. Matter Mater. Phys.* **2010**, *82*, 195313.
(540) Penn, R. L.; Banfield, J. F. Imperfect Oriented Attachment: Dislocation Generation in Defect-Free Nanocrystals. *Science* **1998**, *281*, 969−971.
(541) Pacholski, C.; Kornowski, A.; Weller, H. Self-Assembly of Zno: From Nanodots to Nanorods. *Angew. Chem., Int. Ed.* **2002**, *41*, 1188−1191.
(542) Yang, J.; Hyun, B.-R.; Basile, A. J.; Wise, F. W. Exciton Relaxation in PbSe Nanorods. *ACS Nano* **2012**, *6*, 8120−8127.
(543) Aerts, M.; Spoor, F. C.; Grozema, F. C.; Houtepen, A. J.; Schins, J. M.; Siebbeles, L. D. Cooling and Auger Recombination of Charges in PbSe Nanorods: Crossover from Cubic to Bimolecular Decay. *Nano Lett.* **2013**, *13*, 4380−4386.
(544) Wang, F.; Wu, Y.; Hybertsen, M. S.; Heinz, T. F. Auger Recombination of Excitons in One-Dimensional Systems. *Phys. Rev. B: Condens. Matter Mater. Phys.* **2006**, *73*, 245424.
(545) Aerts, M.; Bielewicz, T.; Klinke, C.; Grozema, F. C.; Houtepen, A. J.; Schins, J. M.; Siebbeles, L. D. Highly Efficient Carrier Multiplication in PbS Nanosheets. *Nat. Commun.* **2014**, *5*, 3789 DOI: 10.1038/ncomms4789.
(546) Cirloganu, C. M.; Padilha, L. A.; Lin, Q.; Makarov, N. S.; Velizhanin, K. A.; Luo, H.; Robel, I.; Pietryga, J. M.; Klimov, V. I. Enhanced Carrier Multiplication in Engineered Quasi-Type-II Quantum Dots. *Nat. Commun.* **2014**, *5*, 4148 DOI: 10.1038/ncomms5148.
(547) Beard, M. C.; Midgett, A. G.; Law, M.; Semonin, O. E.; Ellingson, R. J.; Nozik, A. J. Variations in the Quantum Efficiency of Multiple Exciton Generation for a Series of Chemically Treated PbSe Nanocrystal Films. *Nano Lett.* **2009**, *9*, 836−845.
(548) Ten Cate, S.; Liu, Y.; Suchand Sandeep, C.; Kinge, S.; Houtepen, A. J.; Savenije, T. J.; Schins, J. M.; Law, M.; Siebbeles, L. D. Activating Carrier Multiplication in PbSe Quantum Dot Solids by infilling with Atomic Layer Deposition. *J. Phys. Chem. Lett.* **2013**, *4*, 1766−1770.
(549) Ten Cate, S.; Sandeep, C. S. S.; Liu, Y.; Law, M.; Kinge, S.; Houtepen, A. J.; Schins, J. M.; Siebbeles, L. D. A. Generating Free Charges By Carrier Multiplication in Quantum Dots for Highly Efficient Photovoltaics. *Acc. Chem. Res.* **2015**, *48*, 174.
(550) Talgorn, E.; Gao, Y.; Aerts, M.; Kunneman, L. T.; Schins, J. M.; Savenije, T.; Van Huis, M. A.; Van Der Zant, H. S.; Houtepen, A. J.; Siebbeles, L. D. Unity Quantum Yield of Photogenerated Charges and Band-Like Transport in Quantum-Dot Solids. *Nat. Nanotechnol.* **2011**, *6*, 733−739.
(551) Sandeep, C. S. S.; Ten Cate, S.; Schins, J. M.; Savenije, T. J.; Liu, Y.; Law, M.; Kinge, S.; Houtepen, A. J.; Siebbeles, L. D. A. High Charge-Carrier Mobility Enables Exploitation of Carrier Multiplication in Quantum-Dot Films. *Nat. Commun.* **2013**, *4*, 2360 DOI: 10.1038/ncomms3360.
(552) Miller, A.; Abrahams, E. Impurity Conduction At Low Concentrations. *Phys. Rev.* **1960**, *120*, 745.
(553) Auston, D. H. Impulse-Response of Photoconductors in Transmission-Lines. *IEEE J. Quantum Electron.* **1983**, *19*, 639−648.
(554) Keldysh, L. Concerning the Theory of Impact Ionization in Semiconductors. *Sov. Phys. JETP* **1965**, *21*, 1135−1144.
(555) Maes, W.; De Meyer, K.; Van Overstraeten, R. Impact Ionization in Silicon: A Review and Update. *Solid-State Electron.* **1990**, *33*, 705−718.
(556) Bude, J.; Hess, K.; Iafrate, G. Impact Ionization in Semiconductors: Effects of High Electric Fields and High Scattering Rates. *Phys. Rev. B: Condens. Matter Mater. Phys.* **1992**, *45*, 10958.
(557) Carey, G. H.; Abdelhady, A. L.; Ning, Z.; Thon, S. M.; Bakr, O. M.; Sargent, E. H. Colloidal Quantum Dot Solar Cells. *Chem. Rev.* **2015**, *115*, 12732.
(558) Stolle, C. J.; Harvey, T. B.; Pernik, D. R.; Hibbert, J. I.; Du, J.; Rhee, D. J.; Akhavan, V. A.; Schaller, R. D.; Korgel, B. A. Multiexciton Solar Cells of CuInSe2 Nanocrystals. *J. Phys. Chem. Lett.* **2014**, *5*, 304−309.
(559) Sambur, J. B.; Novet, T.; Parkinson, B. A. Multiple Exciton Collection in A Sensitized Photovoltaic System. *Science* **2010**, *330*, 63−66.
(560) Zhitomirsky, D.; Voznyy, O.; Levina, L.; Hoogland, S.; Kemp, K. W.; Ip, A. H.; Thon, S. M.; Sargent, E. H. Engineering Colloidal Quantum Dot Solids Within and Beyond the Mobility-Invariant Regime. *Nat. Commun.* **2014**, *5*, 3803.
(561) Sukhovatkin, V.; Hinds, S.; Brzozowski, L.; Sargent, E. H. Colloidal Quantum-Dot Photodetectors Exploiting Multiexciton Generation. *Science* **2009**, *324*, 1542−1544.
(562) Currie, M. J.; Mapel, J. K.; Heidel, T. D.; Goffri, S.; Baldo, M. A. High-Efficiency Organic Solar Concentrators For Photovoltaics. *Science* **2008**, *321*, 226−228.
(563) Debije, M. G.; Verbunt, P. P. C. Solar Concentrators: Thirty Years of Luminescent Solar Concentrator Research: Solar Energy For the Built Environment. *Adv. Eng. Mater.* **2012**, *2*, 12−35.
(564) Van Sark, W. G. J. H. M.; Barnham, K. W. J.; Slooff, L. H.; Chatten, A. J.; Buchtemann, A.; Meyer, A.; Mccormack, S. J.; Koole, R.; Farrell, D. J.; Bose, R.; et al. Luminescent Solar Concentrators - A Review of Recent Results. *Opt. Express* **2008**, *16*, 21773−21792.
(565) Chemisana, D. Building Integrated Concentrating Photovoltaics: A Review. *Renewable Sustainable Energy Rev.* **2011**, *15*, 603−611.
(566) Chatten, A. J.; Barnham, K. W. J.; Buxton, B. F.; Ekins-Daukes, N. J.; Malik, M. A. Quantum Dot Solar Concentrators. *Semiconductors* **2004**, *38*, 909−917.
(567) Meinardi, F.; Mcdaniel, H.; Carulli, F.; Colombo, A.; Velizhanin, K. A.; Makarov, N. S.; Simonutti, R.; Klimov, V. I.; Brovelli, S. Highly Efficient Large-Area Colourless Luminescent Solar Concentrators Using Heavy-Metal-Free Colloidal Quantum Dots. *Nat. Nanotechnol.* **2015**, *10*, 878−885.
(568) Swanson, R. M. the Promise of Concentrators. *Prog. Photovoltaics* **2000**, *8*, 93−111.
(569) Van Sark, W. G. J. H. M. Luminescent Solar Concentrators − A Low Cost Photovoltaics Alternative. *Renewable Energy* **2013**, *49*, 207−210.
(570) Goetzberger, A.; Greubel, W. Solar Energy Conversion with Fluorescent Collectors. *Appl. Phys.* **1977**, *14*, 123−139.
(571) Hermann, A. M. Luminescent Solar Concentrators - A Review. *Sol. Energy* **1982**, *29*, 323−329.
(572) Batchelder, J. S.; Zewai, A. H.; Cole, T. Luminescent Solar Concentrators. 1: Theory of Operation and Techniques for Performance Evaluation. *Appl. Opt.* **1979**, *18*, 3090−3110.
(573) Yablonovitch, E. Thermodynamics of the Fluorescent Planar Concentrator. *J. Opt. Soc. Am.* **1980**, *70*, 1362−1363.
(574) Weber, W. H.; Lambe, J. Luminescent Greenhouse Collector for Solar Radiation. *Appl. Opt.* **1976**, *15*, 2299−2300.
(575) Roncali, J.; Garnier, F. Photon-Transport Properties of Luminescent Solar Concentrators - Analysis and Optimization. *Appl. Opt.* **1984**, *23*, 2809−2817.
(576) Reisfeld, R. Fluorescent Dyes in Sol-Gel Glasses. *J. Fluoresc.* **2002**, *12*, 317−325.
(577) Gallagher, S. J.; Norton, B.; Eames, P. C. Quantum Dot Solar Concentrators: Electrical Conversion Efficiencies and Comparative Concentrating Factors of Fabricated Devices. *Sol. Energy* **2007**, *81*, 813−821.
(578) Gallagher, S. J.; Rowan, B. C.; Doran, J.; Norton, B. Quantum Dot Solar Concentrator: Device Optimisation Using Spectroscopic Techniques. *Sol. Energy* **2007**, *81*, 540−547.

DOI: 10.1021/acs.chemrev.6b00169
Chem. Rev. 2016, 116, 10513−10622

(579) Slooff, L. H.; Bende, E. E.; Burgers, A. R.; Budel, T.; Pravettoni, M.; Kenny, R. P.; Dunlop, E. D.; Büchtemann, A. A Luminescent Solar Concentrator with 7.1% Power Conversion Efficiency. *Phys. Status Solidi RRL* **2008**, *2*, 257−259.
(580) Bradshaw, L. R.; Knowles, K. E.; Mcdowall, S.; Gamelin, D. R. Nanocrystals for Luminescent Solar Concentrators. *Nano Lett.* **2015**, *15*, 1315−1323.
(581) Krumer, Z.; Pera, S. J.; Van Dijk-Moes, R. J. A.; Zhao, Y.; De Brouwer, A. F. P.; Groeneveld, E.; Van Sark, W. G. J. H. M.; Schropp, R. E. I.; Donega, C. D. M. Tackling Self-Absorption in Luminescent Solar Concentrators With Type-II Colloidal Quantum Dots. *Sol. Energy Mater. Sol. Cells* **2013**, *111*, 57−65.
(582) Şahin, D.; Ilan, B.; Kelley, D. F. Monte-Carlo Simulations of Light Propagation in Luminescent Solar Concentrators Based On Semiconductor Nanoparticles. *J. Appl. Phys.* **2011**, *110*, 033108.
(583) Klimov, V. I.; Baker, T. A.; Lim, J.; Velizhanin, K. A.; McDaniel, H. Quality Factor of Luminescent Solar Concentrators and Practical Concentration Limits Attainable with Semiconductor Quantum Dots. *ACS Photonics* **2016**, *3*, 1138−1148.
(584) Rau, U.; Einsele, F.; Glaeser, G. C. Efficiency Limits of Photovoltaic Fluorescent Collectors. *Appl. Phys. Lett.* **2005**, *87*, 171101.
(585) Giebink, N. C.; Wiederrecht, G. P.; Wasielewski, M. R. Resonance-Shifting to Circumvent Reabsorption Loss in Luminescent Solar Concentrators. *Nat. Photonics* **2011**, *5*, 694−701.
(586) Mulder, C. L.; Reusswig, P. D.; Beyler, A. P.; Kim, H.; Rotschild, C.; Baldo, M. A. Dye Alignment in Luminescent Solar Concentrators: II. Horizontal Alignment for Energy Harvesting in Linear Polarizers. *Opt. Express* **2010**, *18*, A91−A99.
(587) Wang, T.; Zhang, J.; Ma, W.; Luo, Y.; Wang, L.; Hu, Z.; Wu, W.; Wang, X.; Zou, G.; Zhang, Q. Luminescent Solar Concentrator Employing Rare Earth Complex with Zero Self-Absorption Loss. *Sol. Energy* **2011**, *85*, 2571−2579.
(588) Sanguineti, A.; Monguzzi, A.; Vaccaro, G.; Meinardi, F.; Ronchi, E.; Moret, M.; Cosentino, U.; Moro, G.; Simonutti, R.; Mauri, M.; et al. NIR Emitting Ytterbium Chelates for Colourless Luminescent Solar Concentrators. *Phys. Chem. Chem. Phys.* **2012**, *14*, 6452−6455.
(589) Debije, M. G.; Verbunt, P. P. C.; Nadkarni, P. J.; Velate, S.; Bhaumik, K.; Nedumbamana, S.; Rowan, B. C.; Richards, B. S.; Hoeks, T. L. Promising Fluorescent Dye For Solar Energy Conversion Based on a Perylene Perinone. *Appl. Opt.* **2011**, *50*, 163−169.
(590) Desmet, L.; Ras, A. J. M.; De Boer, D. K. G.; Debije, M. G. Monocrystalline Silicon Photovoltaic Luminescent Solar Concentrator With 4.2% Power Conversion Efficiency. *Opt. Lett.* **2012**, *37*, 3087−3089.
(591) Knowles, K. E.; Kilburn, T. B.; Alzate, D. G.; Mcdowall, S.; Gamelin, D. R. Bright CuInS2/CdS Nanocrystal Phosphors For High-Gain Full-Spectrum Luminescent Solar Concentrators. *Chem. Commun.* **2015**, *51*, 9129−9132.
(592) Purcell-Milton, F.; Gun'ko, Y. K. Quantum Dots For Luminescent Solar Concentrators. *J. Mater. Chem.* **2012**, *22*, 16687−16697.
(593) Shcherbatyuk, G. V.; inman, R. H.; Wang, C.; Winston, R.; Ghosh, S. Viability of Using Near-Infrared PbS Quantum Dots as Active Materials in Luminescent Solar Concentrators. *Appl. Phys. Lett.* **2010**, *96*, 191901.
(594) Hyldahl, M. G.; Bailey, S. T.; Wittmershaus, B. P. Photo-Stability and Performance of CdSe/ZnS Quantum Dots in Luminescent Solar Concentrators. *Sol. Energy* **2009**, *83*, 566−573.
(595) Petruska, M. A.; Malko, A. V.; Voyles, P. M.; Klimov, V. I. High-Performance, Quantum Dot Nanocomposites for Nonlinear Optical and Optical Gain Applications. *Adv. Mater.* **2003**, *15*, 610−613.
(596) Tamborra, M.; Striccoli, M.; Comparelli, R.; Curri, M. L.; Petrella, A.; Agostiano, A. Optical Properties of Hybrid Composites Based On Highly Luminescent CdS Nanocrystals in Polymer. *Nanotechnology* **2004**, *15*, S240−S244.
(597) Otto, T.; Müller, M.; Mundra, P.; Lesnyak, V.; Demir, H. V.; Gaponik, N.; Eychmüller, A. Colloidal Nanocrystals Embedded in Macrocrystals: Robustness, Photostability, and Color Purity. *Nano Lett.* **2012**, *12*, 5348−5354.
(598) Semonin, O. E.; Johnson, J. C.; Luther, J. M.; Midgett, A. G.; Nozik, A. J.; Beard, M. C. Absolute Photoluminescence Quantum Yields of IR-26 Dye, PbS, and PbSe Quantum Dots. *J. Phys. Chem. Lett.* **2010**, *1*, 2445−2450.
(599) Bomm, J.; Büchtemann, A.; Fiore, A.; Manna, L.; Nelson, J. H.; Hill, D.; Van Sark, W. G. J. H. M. Fabrication and Spectroscopic Studies On Highly Luminescent CdSe/CdS Nanorod Polymer Composites. *Beilstein J. Nanotechnol.* **2010**, *1*, 94−100.
(600) Brovelli, S.; Schaller, R. D.; Crooker, S. A.; García-Santamaría, F.; Chen, Y.; Viswanatha, R.; Hollingsworth, J. A.; Htoon, H.; Klimov, V. I. Nano-Engineered Electron-Hole Exchange Interaction Controls Exciton Dynamics in Core-Shell Semiconductor Nanocrystals. *Nat. Commun.* **2011**, *2*, 280.
(601) Reiss, P.; Protière, M.; Li, L. Core/Shell Semiconductor Nanocrystals. *Small* **2009**, *5*, 154−168.
(602) Aeberhard, U.; Vaxenburg, R.; Lifshitz, E.; Tomic, S. Fluorescence of Colloidal PbSe/PbS QDs in NIR Luminescent Solar Concentrators. *Phys. Chem. Chem. Phys.* **2012**, *14*, 16223−16228.
(603) De Mello Donega, C. Synthesis and Properties of Colloidal Heteronanocrystals. *Chem. Soc. Rev.* **2011**, *40*, 1512−1546.
(604) Brovelli, S.; Bae, W. K.; Meinardi, F.; Santiago González, B.; Lorenzon, M.; Galland, C.; Klimov, V. I. Electrochemical Control of Two-Color Emission from Colloidal Dot-in-Bulk Nanocrystals. *Nano Lett.* **2014**, *14*, 3855−3863.
(605) Christodoulou, S.; Vaccaro, G.; Pinchetti, V.; De Donato, F.; Grim, J. Q.; Casu, A.; Genovese, A.; Vicidomini, G.; Diaspro, A.; Brovelli, S.; et al. Synthesis of Highly Luminescent Wurtzite CdSe/Cds Giant-Shell Nanocrystals Using a Fast Continuous Injection Route. *J. Mater. Chem. C* **2014**, *2*, 3439−3447.
(606) Galland, C.; Brovelli, S.; Bae, W. K.; Padilha, L. A.; Meinardi, F.; Klimov, V. I. Dynamic Hole Blockade Yields Two-Color Quantum and Classical Light From Dot-in-Bulk Nanocrystals. *Nano Lett.* **2013**, *13*, 321−328.
(607) Nasilowski, M.; Spinicelli, P.; Patriarche, G.; Dubertret, B. Gradient CdSe/CdS Quantum Dots With Room Temperature Biexciton Unity Quantum Yield. *Nano Lett.* **2015**, *15*, 3953−3958.
(608) Cassette, E.; Mahler, B.; Guigner, J.-M.; Patriarche, G.; Dubertret, B.; Pons, T. Colloidal CdSe/CdS Dot-in-Plate Nanocrystals With 2D-Polarized Emission. *ACS Nano* **2012**, *6*, 6741−6750.
(609) Rainò, G.; Stöferle, T.; Moreels, I.; Gomes, R.; Kamal, J. S.; Hens, Z.; Mahrt, R. F. Probing the Wave Function Delocalization in CdSe/CdS Dot-in-Rod Nanocrystals by Time- and Temperature-Resolved Spectroscopy. *ACS Nano* **2011**, *5*, 4031−4036.
(610) Christodoulou, S.; Rajadell, F.; Casu, A.; Vaccaro, G.; Grim, J.; Genovese, A.; Manna, L.; Climente, J. I.; Meinardi, F.; Rainò, G.; et al. Band Structure Engineering via Piezo-Electric Fields in Strained Anisotropic CdSe/CdS Nanocrystals. *Nat. Commun.* **2015**, *6*, 7905.
(611) Sitt, A.; Salant, A.; Menagen, G.; Banin, U. Highly Emissive Nano Rod-in-Rod Heterostructures with Strong Linear Polarization. *Nano Lett.* **2011**, *11*, 2054−2060.
(612) Talapin, D. V.; Nelson, J. H.; Shevchenko, E. V.; Aloni, S.; Sadtler, B.; Alivisatos, A. P. Seeded Growth of Highly Luminescent CdSe/CdS Nanoheterostructures with Rod and Tetrapod Morphologies. *Nano Lett.* **2007**, *7*, 2951−2959.
(613) Kim, M. R.; Miszta, K.; Povia, M.; Brescia, R.; Christodoulou, S.; Prato, M.; Marras, S.; Manna, L. Influence of Chloride Ions on the Synthesis of Colloidal Branched CdSe/Cds Nanocrystals by Seeded Growth. *ACS Nano* **2012**, *6*, 11088−11096.
(614) Mahler, B.; Nadal, B.; Bouet, C.; Patriarche, G.; Dubertret, B. Core/Shell Colloidal Semiconductor Nanoplatelets. *J. Am. Chem. Soc.* **2012**, *134*, 18591−18598.
(615) Tessier, M. D.; Mahler, B.; Nadal, B.; Heuclin, H.; Pedetti, S.; Dubertret, B. Spectroscopy of Colloidal Semiconductor Core/Shell Nanoplatelets with High Quantum Yield. *Nano Lett.* **2013**, *13*, 3321−3328.
(616) Tessier, M. D.; Spinicelli, P.; Dupont, D.; Patriarche, G.; Ithurria, S.; Dubertret, B. Efficient Exciton Concentrators Built From Colloidal Core/Crown CdSe/CdS Semiconductor Nanoplatelets. *Nano Lett.* **2014**, *14*, 207−213.

DOI: 10.1021/acs.chemrev.6b00169
Chem. Rev. 2016, 116, 10513−10622

(617) Javaux, C.; Mahler, B.; Dubertret, B.; Shabaev, A.; Rodina, A. V.; Efros, A. L.; Yakovlev, D. R.; Liu, F.; Bayer, M.; Camps, G.; et al. Thermal Activation of Non-Radiative Auger Recombination in Charged Colloidal Nanocrystals. *Nat. Nanotechnol.* **2013**, *8*, 206−212.
(618) Norris, D. J.; Yao, N.; Charnock, F. T.; Kennedy, T. A. High-Quality Manganese-Doped ZnSe Nanocrystals. *Nano Lett.* **2001**, *1*, 3−7.
(619) Liu, J.; Zhao, Q.; Liu, J.-L.; Wu, Y.-S.; Cheng, Y.; Ji, M.-W.; Qian, H.-M.; Hao, W.-C.; Zhang, L.-J.; Wei, X.-J.; et al. Heterovalent-Doping-Enabled Efficient Dopant Luminescence and Controllable Electronic Impurity via a New Strategy of Preparing II−VI Nanocrystals. *Adv. Mater.* **2015**, *27*, 2753−2761.
(620) Chen, D.; Viswanatha, R.; Ong, G. L.; Xie, R.; Balasubramaninan, M.; Peng, X. Temperature Dependence of "Elementary Processes" in Doping Semiconductor Nanocrystals. *J. Am. Chem. Soc.* **2009**, *131*, 9333−9339.
(621) Bryan, J. D.; Gamelin, D. R. Doped Semiconductor Nanocrystals: Synthesis, Characterization, Physical Properties, and Applications. *Prog. inorg. Chem.* **2005**, *54*, 47−126.
(622) Bussian, D. A.; Crooker, S. A.; Yin, M.; Brynda, M.; Efros, A. L.; Klimov, V. I. Tunable Magnetic Exchange Interactions in Manganese-Doped Inverted Core−Shell Znse−CdSe Nanocrystals. *Nat. Mater.* **2009**, *8*, 35−40.
(623) Ochsenbein, S. T.; Gamelin, D. R. Quantum Oscillations in Magnetically Doped Colloidal Nanocrystals. *Nat. Nanotechnol.* **2011**, *6*, 112−115.
(624) Viswanatha, R.; Pietryga, J. M.; Klimov, V. I.; Crooker, S. A. Spin-Polarized Mn^{2+} Emission from Mn-Doped Colloidal Nanocrystals. *Phys. Rev. Lett.* **2011**, *107*, 067402.
(625) Beaulac, R.; Schneider, L.; Archer, P. I.; Bacher, G.; Gamelin, D. R. Light-Induced Spontaneous Magnetization in Doped Colloidal Quantum Dots. *Science* **2009**, *325*, 973−976.
(626) Corrado, C.; Hawker, M.; Livingston, G.; Medling, S.; Bridges, F.; Zhang, J. Z. Enhanced Cu Emission in ZnS:Cu,Cl/ZnS Core-Shell Nanocrystals. *Nanoscale* **2010**, *2*, 1213.
(627) Gul, S.; Cooper, J. K.; Corrado, C.; Vollbrecht, B.; Bridges, F.; Guo, J. H.; Zhang, J. Z. Synthesis, Optical and Structural Properties, and Charge Carrier Dynamics of Cu-Doped ZnSe Nanocrystals. *J. Phys. Chem. C* **2011**, *115*, 20864−20875.
(628) Jana, S.; Srivastava, B. B.; Jana, S.; Bose, R.; Pradhan, N. Multifunctional Doped Semiconductor Nanocrystals. *J. Phys. Chem. Lett.* **2012**, *3*, 2535−2540.
(629) Meulenberg, R. W.; Van Buuren, T.; Hanif, K. M.; Willey, T. M.; Strouse, G. F.; Terminello, L. J. Structure and Composition of Cu-Doped CdSe Nanocrystals Using Soft X-Ray Absorption Spectroscopy. *Nano Lett.* **2004**, *4*, 2277−2285.
(630) Panda, S. K.; Hickey, S. G.; Demir, H. V.; Eychmüller, A. Bright White-Light Emitting Manganese and Copper Co-Doped ZnSe Quantum Dots. *Angew. Chem., Int. Ed.* **2011**, *50*, 4432−4436.
(631) Pradhan, N.; Battaglia, D. M.; Liu, Y.; Peng, X. Efficient, Stable, Small, and Water-Soluble Doped ZnSe Nanocrystal Emitters as Non-Cadmium Biomedical Labels. *Nano Lett.* **2007**, *7*, 312−317.
(632) Srivastava, B. B.; Jana, S.; Pradhan, N. Doping Cu in Semiconductor Nanocrystals: Some Old and Some New Physical insights. *J. Am. Chem. Soc.* **2011**, *133*, 1007−1015.
(633) Stouwdam, J. W.; Janssen, R. A. J. Electroluminescent Cu-Doped Cds Quantum Dots. *Adv. Mater.* **2009**, *21*, 2916−2920.
(634) Sahu, A.; Kang, M. S.; Kompch, A.; Notthoff, C.; Wills, A. W.; Deng, D.; Winterer, M.; Frisbie, C. D.; Norris, D. J. Electronic Impurity Doping in CdSe Nanocrystals. *Nano Lett.* **2012**, *12*, 2587−2594.
(635) Viswanatha, R.; Brovelli, S.; Pandey, A.; Crooker, S. A.; Klimov, V. I. Copper-Doped Inverted Core/Shell Nanocrystals With "Permanent" Optically Active Holes. *Nano Lett.* **2011**, *11*, 4753−4758.
(636) Pradhan, N.; Goorskey, D.; Thessing, J.; Peng, X. An Alternative of CdSe Nanocrystal Emitters: Pure and Tunable Impurity Emissions in ZnSe Nanocrystals. *J. Am. Chem. Soc.* **2005**, *127*, 17586−17587.
(637) Mocatta, D.; Cohen, G.; Schattner, J.; Millo, O.; Rabani, E.; Banin, U. Heavily Doped Semiconductor Nanocrystal Quantum Dots. *Science* **2011**, *332*, 77−81.
(638) Jana, S.; Srivastava, B. B.; Acharya, S.; Santra, P. K.; Jana, N. R.; Sarma, D. D.; Pradhan, N. Prevention of Photooxidation in Blue-Green Emitting Cu Doped ZnSe Nanocrystals. *Chem. Commun.* **2010**, *46*, 2853−2855.
(639) Xie, R.; Peng, X. Synthesis of Cu-Doped inp Nanocrystals (D-Dots) With ZnSe Diffusion Barrier as Efficient and Color-Tunable NIR Emitters. *J. Am. Chem. Soc.* **2009**, *131*, 10645−10651.
(640) Brovelli, S.; Galland, C.; Viswanatha, R.; Klimov, V. I. Tuning Radiative Recombination in Cu-Doped Nanocrystals via Electrochemical Control of Surface Trapping. *Nano Lett.* **2012**, *12*, 4372−4379.
(641) Broser, I.; Schulz, H. J. A Comparative Study of Infrared Luminescence and Some Other Optical and Electrical Properties of Zn-Cu Single Crystals. *J. Electrochem. Soc.* **1961**, *108*, 545−548.
(642) Peka, P.; Schulz, H. J. Empirical One-Electron Model of Optical-Transitions in Cu-Doped ZnS and CdS. *Phys. B* **1994**, *193*, 57−65.
(643) Stringfellow, G. B.; Bube, R. H. Photoelectronic Properties of ZnSe Crystals. *Phys. Rev.* **1968**, *171*, 903−915.
(644) Grandhi, G. K.; Tomar, R.; Viswanatha, R. Study of Surface and Bulk Electronic Structure of II−VI Semiconductor Nanocrystals Using Cu as a Nanosensor. *ACS Nano* **2012**, *6*, 9751−9763.
(645) Hu, X.; Kang, R.; Zhang, Y.; Deng, L.; Zhong, H.; Zou, B.; Shi, L.-J. Ray-Trace Simulation of CuIns(Se)2 Quantum Dot Based Luminescent Solar Concentrators. *Opt. Express* **2015**, *23*, A858−A867.
(646) Tan, Z.; Zhang, Y.; Xie, C.; Su, H.; Liu, J.; Zhang, C.; Dellas, N.; Mohney, S. E.; Wang, Y.; Wang, J.; et al. Near-Band-Edge Electroluminescence from Heavy-Metal-Free Colloidal Quantum Dots. *Adv. Mater.* **2011**, *23*, 3553−3558.
(647) Aldakov, D.; Lefrancois, A.; Reiss, P. Ternary and Quaternary Metal Chalcogenide Nanocrystals: Synthesis, Properties and Applications. *J. Mater. Chem. C* **2013**, *1*, 3756−3776.
(648) Kolny-Olesiak, J.; Weller, H. Synthesis and Application of Colloidal Cuins2 Semiconductor Nanocrystals. *ACS Appl. Mater. Interfaces* **2013**, *5*, 12221−12237.
(649) Akkerman, Q. A.; Genovese, A.; George, C.; Prato, M.; Moreels, I.; Casu, A.; Marras, S.; Curcio, A.; Scarpellini, A.; Pellegrino, T.; et al. From Binary Cu2S to Ternary Cu−In−S and Quaternary Cu−In−Zn−S Nanocrystals With Tunable Composition via Partial Cation Exchange. *ACS Nano* **2015**, *9*, 521.
(650) Panthani, M. G.; Akhavan, V.; Goodfellow, B.; Schmidtke, J. P.; Dunn, L.; Dodabalapur, A.; Barbara, P. F.; Korgel, B. A. Synthesis of CuInS2, CuInSe2, and Cu(InxGa1-X)Se2 (CIGS) Nanocrystal "Inks" for Printable Photovoltaics. *J. Am. Chem. Soc.* **2008**, *130*, 16770−16777.
(651) Pan, Z.; Mora-Seró, I.; Shen, Q.; Zhang, H.; Li, Y.; Zhao, K.; Wang, J.; Zhong, X.; Bisquert, J. High-Efficiency "Green" Quantum Dot Solar Cells. *J. Am. Chem. Soc.* **2014**, *136*, 9203−9210.
(652) McDaniel, H.; Fuke, N.; Pietryga, J. M.; Klimov, V. I. Engineered CuInSexS2−X Quantum Dots for Sensitized Solar Cells. *J. Phys. Chem. Lett.* **2013**, *4*, 355−361.
(653) Yarema, O.; Bozyigit, D.; Rousseau, I.; Nowack, L.; Yarema, M.; Heiss, W.; Wood, V. Highly Luminescent, Size- and Shape-Tunable Copper Indium Selenide Based Colloidal Nanocrystals. *Chem. Mater.* **2013**, *25*, 3753−3757.
(654) Riha, S. C.; Schaller, R. D.; Gosztola, D. J.; Wiederrecht, G. P.; Martinson, A. B. F. Photoexcited Carrier Dynamics of Cu2S Thin Films. *J. Phys. Chem. Lett.* **2014**, *5*, 4055−4061.
(655) Panthani, M. G.; Khan, T. A.; Reid, D. K.; Hellebusch, D. J.; Rasch, M. R.; Maynard, J. A.; Korgel, B. A. In Vivo Whole Animal Fluorescence Imaging of a Microparticle-Based Oral Vaccine Containing (CuInSeXS2−X)/ZnS Core/Shell Quantum Dots. *Nano Lett.* **2013**, *13*, 4294−4298.
(656) Zhu, M.; Peng, X.; Wang, Z.; Bai, Z.; Chen, B.; Wang, Y.; Hao, H.; Shao, Z.; Zhong, H. Highly Transparent and Colour-Tunable Composite Films with Increased Quantum Dot Loading. *J. Mater. Chem. C* **2014**, *2*, 10031−10036.
(657) Chen, B.; Zhong, H.; Zhang, W.; Tan, Z. A.; Li, Y.; Yu, C.; Zhai, T.; Bando, Y.; Yang, S.; Zou, B. Highly Emissive and Color-Tunable CuInS2-Based Colloidal Semiconductor Nanocrystals: Off-Stoichiometry Effects and Improved Electroluminescence Performance. *Adv. Funct. Mater.* **2012**, *22*, 2081−2088.

DOI: 10.1021/acs.chemrev.6b00169
Chem. Rev. 2016, 116, 10513−10622

(658) De Trizio, L.; Prato, M.; Genovese, A.; Casu, A.; Povia, M.; Simonutti, R.; Alcocer, M. J. P.; D'Andrea, C.; Tassone, F.; Manna, L. Strongly Fluorescent Quaternary Cu−In−Zn−S Nanocrystals Prepared From Cu1-XInS2 Nanocrystals By Partial Cation Exchange. *Chem. Mater.* **2012**, *24*, 2400−2406.
(659) Witt, E.; Kolny-Olesiak, J. Recent Developments in Colloidal Synthesis of CuInSe2 Nanoparticles. *Chem. - Eur. J.* **2013**, *19*, 9746−9753.
(660) Rice, W. D.; McDaniel, H.; Klimov, V. I.; Crooker, S. A. Magneto-Optical Properties of CuInS2 Nanocrystals. *J. Phys. Chem. Lett.* **2014**, *5*, 4105−4109.
(661) Pandey, A.; Brovelli, S.; Viswanatha, R.; Li, L.; Pietryga, J. M.; Klimov, V. I.; Crooker, S. A. Long-Lived Photoinduced Magnetization in Copper-Doped ZnSe-CdSe Core-Shell Nanocrystals. *Nat. Nanotechnol.* **2012**, *7*, 792−797.
(662) Binsma, J. J. M.; Giling, L. J.; Bloem, J. Luminescence of CuInS2: I. The Broad Band Emission and its Dependence on the Defect Chemistry. *J. Lumin.* **1982**, *27*, 35−53.
(663) Huynh, W. U.; Peng, X. G.; Alivisatos, A. P. CdSe Nanocrystal Rods/Poly(3-Hexylthiophene) Composite Photovoltaic Devices. *Adv. Mater.* **1999**, *11*, 923.
(664) Progelhof, R. C.; Franey, J.; Haas, T. W. Absorption Coefficient of Unpigmented Poly(Methyl Methacrylate), Polystyrene, Polycarbonate, and Poly(4-Methylpentene-1) Sheets. *J. Appl. Polym. Sci.* **1971**, *15*, 1803−1807.
(665) Wanwanichai, P.; Junkasem, J.; Saimaneewong, B.; Mahasan, R.; Tantivess, P.; Magaraphan, R.; Vanichvarakij, Y.; Petiraksakul, P.; Supaphol, P. Sheet-Cast Poly(Methyl Methacrylate): One-Step (Water) Versus Two-Step (Water-Air) Isothermal Processes. *Iran. Polym. J.* **2005**, *14*, 61−69.
(666) Colombo, A.; Tassone, F.; Santolini, F.; Contiello, N.; Gambirasio, A.; Simonutti, R. Nanoparticle-Doped Large Area PMMA Plates With Controlled Optical Diffusion. *J. Mater. Chem. C* **2013**, *1*, 2927.
(667) Koike, Y.; Tanio, N.; Ohtsuka, Y. Light Scattering and Heterogeneities in Low-Loss Poly(Methyl Methacrylate) Glasses. *Macromolecules* **1989**, *22*, 1367−1373.
(668) Demir, M. M.; Koynov, K.; Akbey, Ü.; Bubeck, C.; Park, I.; Lieberwirth, I.; Wegner, G. Optical Properties of Composites of PMMA and Surface-Modified Zincite Nanoparticles. *Macromolecules* **2007**, *40*, 1089−1100.
(669) Beiner, M.; Schroter, K.; Hempel, E.; Reissig, S.; Donth, E. Multiple Glass Transition and Nanophase Separation in Poly(N-Alkyl Methacrylate) Homopolymers. *Macromolecules* **1999**, *32*, 6278−6282.
(670) Puig, J.; Williams, R. J. J.; Hoppe, C. E. Poly-(dodecylmethacrylate) as Solvent of Paraffins for Phase Change Materials and Thermally Reversible Light Scattering Films. *ACS Appl. Mater. Interfaces* **2013**, *5*, 9180−9185.
(671) Zvaigzne, M.; Martynov, I.; Samokhvalov, P.; Mochalov, K.; Chistyakov, A. influence of Surface Ligands on the Luminescent Properties of Cadmium Selenide Quantum Dots in a Polymethylmethacrylate Matrix. *Phys. Procedia* **2015**, *73*, 150−155.
(672) Woelfle, C.; Claus, R. O. Transparent and Flexible Quantum Dot−Polymer Composites Using an Ionic Liquid as Compatible Polymerization Medium. *Nanotechnology* **2007**, *18*, 025402.
(673) Inman, R. H.; Shcherbatyuk, G. V.; Medvedko, D.; Gopinathan, A.; Ghosh, S. Cylindrical Luminescent Solar Concentrators with Near-Infrared Quantum Dots. *Opt. Express* **2011**, *19*, 24308−24313.
(674) Lin, H.; Xie, P.; Liu, Y.; Zhou, X.; Li, B. Tuning Luminescence and Reducing Reabsorption of CdSe Quantum Disks for Luminescent Solar Concentrators. *Nanotechnology* **2015**, *26*, 335401.
(675) Goldschmidt, J. C.; Peters, M.; Bösch, A.; Helmers, H.; Dimroth, F.; Glunz, S. W.; Willeke, G. Increasing the Efficiency of Fluorescent Concentrator Systems. *Sol. Energy Mater. Sol. Cells* **2009**, *93*, 176−182.
(676) Co, M. C. *A Color Notation*: Boston, 1919.
(677) Li, H.; Wu, K.; Lim, J.; Song, H. J.; Klimov, V. I. Low-Loss, Large-Area Luminescent Solar Concentrators Fabricated by Doctor-Blade Deposition of Quantum Dots Onto Standard Window Glass. *Nat. Energy* **2016**, in press.
(678) Michalet, X.; Pinaud, F. F.; Bentolila, L. A.; Tsay, J. M.; Doose, S.; Li, J. J.; Sundaresan, G.; Wu, A. M.; Gambhir, S. S.; Weiss, S. Quantum Dots for Live Cells, in Vivo Imaging, and Diagnostics. *Science* **2005**, *307*, 538−544.
(679) Ning, Z.; Ren, Y.; Hoogland, S.; Voznyy, O.; Levina, L.; Stadler, P.; Lan, X.; Zhitomirsky, D.; Sargent, E. H. All-inorganic Colloidal Quantum Dot Photovoltaics Employing Solution-Phase Halide Passivation. *Adv. Mater.* **2012**, *24*, 6295−6299.
(680) Lan, X.; Voznyy, O.; Kiani, A.; García De Arquer, F. P.; Abbas, A. S.; Kim, G.-H.; Liu, M.; Yang, Z.; Walters, G.; Xu, J.; et al. Passivation Using Molecular Halides Increases Quantum Dot Solar Cell Performance. *Adv. Mater.* **2016**, *28*, 299−304.

DOI: 10.1021/acs.chemrev.6b00169
Chem. Rev. 2016, 116, 10513−10622